



HAL
open science

Numerical modelling of large-scale transcurrent faulting and compression effects - Examples from West Africa and New Zealand

Xiaojun Feng

► **To cite this version:**

Xiaojun Feng. Numerical modelling of large-scale transcurrent faulting and compression effects - Examples from West Africa and New Zealand. Earth Sciences. Université Toulouse 3 Paul Sabatier (UT3 Paul Sabatier), 2016. English. NNT: . tel-01467225

HAL Id: tel-01467225

<https://theses.hal.science/tel-01467225>

Submitted on 14 Feb 2017

HAL is a multi-disciplinary open access archive for the deposit and dissemination of scientific research documents, whether they are published or not. The documents may come from teaching and research institutions in France or abroad, or from public or private research centers.

L'archive ouverte pluridisciplinaire **HAL**, est destinée au dépôt et à la diffusion de documents scientifiques de niveau recherche, publiés ou non, émanant des établissements d'enseignement et de recherche français ou étrangers, des laboratoires publics ou privés.



THÈSE

En vue de l'obtention du

DOCTORAT DE L'UNIVERSITÉ DE TOULOUSE

Délivré par :

Université Toulouse 3 Paul Sabatier (UT3 Paul Sabatier)

Présentée et soutenue par :

Xiaojun FENG

le mardi 22 novembre 2016

Titre :

Modélisation numérique des failles décrochantes et des effets de compression à grande échelle - Cas d'étude en Afrique de l'Ouest et Nouvelle Zélande

École doctorale et discipline ou spécialité :

ED SDU2E : Sciences de la Terre et des Planètes Solides

Unité de recherche :

Géoscience Environnement Toulouse (UMR 5563)

Directeur/trice(s) de Thèse :

Mark JESSELL
Roland MARTIN

Jury :

Nicolas COLTICE

Jean- François MOYEN

Olivier VANDERHAEGHE

Bing BAI

Lenka BARATOUX

Roland MARTIN

Mark JESSELL

Jérôme GANNE

Professeur UCB Lyon1, Lyon

Professeur UJM, Saint-Etienne

Professeur UPS, Toulouse

Prof associé CAS-IRSM, Wuhan

CR1, IRD-GET, Toulouse

IR1, CNRS-GET, Toulouse

Professeur UWA, Perth

CR1, IRD-GET, Toulouse

Rapporteur

Rapporteur

Examineur

Examineur

Examineur

Co-directeur de thèse

Invité, directeur de thèse

Invité, co-encadrant de thèse

ACKNOWLEDGEMENTS

The priority of my acknowledgements is to give my foremost gratitude to my supervisors Prof. Mark Walter Jessell and Dr. Roland Martin for guidance and encouragements during the entire PhD study. Throughout this thesis, it contains their thousands of corrections, thoughtful exploration and constructive suggestions. A very special thanks goes to Dr. Jérôme Ganne for fruitful discussions on the Geology of the West African Craton and numerical modelling. I can't thank him enough for his patience, extraordinary insights, guidance and critical comments on my different papers. A thanks goes to Dr. Muriel Gerbault for very helpful discussions and comments on my first paper, otherwise I could not have published it. I also acknowledge Dr. Lenka Baratoux, Dr. Shaobin Hu, Mr. Daqing Liu, Dr. Prince Ofori Amponsah, Dr. Sylvian Block and Miss. Helen McFarlane for helps and discussions during the Ph.D study.

I also want to thank all my Chinese friends I met in Toulouse for having many week-end parties together during my PhD study, Chuanbo Guo; Rui Xue; Ruixi Zhao; Yu Zhao; Yingning He; Jing Sheng; Ping Li; Bing Zhou; Wei Feng; Yi Wang; Hongmei Xu; Xu Yang; Le Yao; Xing Huang; Zukun Qu; Ruoyu Sun; Caiyan Feng; Jing Ye; Chuxian Li; Buyun Du; Youcun Liu; Huihui Li; Wei Yuan; Ran Zhao; He Huang; Yan Huang etc.

Most of the numerical models in this thesis were performed on different cluster machines: Yang, Nuwa and Eos. I would like to thank Didier Gazen, Nicolas Renon for very patient technical support on different machines. I also need to mention the people at the Victorian Partnership for Advanced Computing (VPAC) and Monash University for patient assistance with the numerical code *Underworld* over years. Figures in this thesis are plotted using open source package *Visit* developed by the Lawrence Livermore National Laboratory, they are thanked for providing some helpful suggestions on producing different figures.

The Chinese Scholarship Council (CSC) and the research support from the WAXI project (West African eXploration Initiative) are greatly acknowledged for providing me four years of PhD scholarship. This work would not have been made possible without the aid and support of the WAXI project.

I would like to say '辛苦了' to my lovely wife, Mrs. Yu Chen for her always supports, patience and encouragements.

Finally, say '谢谢' to my baby boy coming on 25th October 2016, Lucas FENG for making me a father!!!!

ABSTRACT

The objective of this thesis is to explore the role shear zones play in localization of deformation and exhumation of the lower crust by using a series of 2D and 3D thermo-mechanical numerical models using the West African Craton (WAC) and the Alpine Fault zones as study areas. With respect to the localization of deformation in the upper crust, different orientations of a system of branched strike-slip faults were studied. Under compression boundary conditions, the results show that the internal fault zones as well as the host rocks in between the faults behave as relatively weaker domains than the external regions. Under simple shear boundary conditions, we explored the process of self-organization of the Australian-Pacific plate boundary fault in southern New Zealand. The models show that deformation is focused along narrow high-strain shear zones in the centre of the model when the softening coefficients are high, whereas the strain is more diffuse with many shear zones spread over the model and possibly some high-strain shear zones focused near one border at lower softening coefficients.

Regarding the role pre-existing faults and basins play in exhumation of the partially molten lower crust, 2D and 3D models with different boundary conditions were tested (including extension, transtension and compression).

- Under extension, in the Eastern and Western parts of the high grade rock corridors in NW Ghana, partially molten rocks exhumed from the lower into middle-upper crustal levels are interpreted to have been dominantly facilitated by the km-scale high-strain corridors. In the central part of the Bole-Bulenga domain, the high grade rocks are interpreted to have been exhumed as a result of a coupling between two mechanisms: (1) the concentration of partially molten rocks between the Jirapa and Bole-Nangodi faults increases due to the reduction in space from north to south; (2) the concentration of lower partially molten rocks in the central part, as a result of inherited orthogonal (E-W) faults.
- Under transtension, in the Sefwi terrane of SW Ghana, the Kukuom-Juaboso domain (KJD) composed of up to amphibolite-migmatite facies could result from the concentration of upwelling partially molten rocks in the relay zone between the Ketesso and Kenyase shear zones during transtension. The two shear zones probably underwent two main stages for growth and maturation from the D1 to D2 deformation phases. The regional exhumation of the high grade rocks in the Sefwi terrane probably occurred within a duration of less than 5 Ma.
- Under compression, the role of volcano-sedimentary basin on spatial-temporal evolution of the lower crust exhumation was tested. The models suggest that a series of sheet-like

granitoids possibly derived from either subducted mélanges, lower crust and/or mantle melting accumulated at depths of the subcontinental mantle would channel along diapirs before feeding the upper crust. When the granitoids arrive at the solidified lids of the diapirs, they would favour migrating horizontally and intruding into the upper crust through weakening zones between the diapirs. This model also suggests an asymmetry of structures between the upper and middle-lower crust, with the dome-like granitoids overlying high-grade sedimentary synforms and high-grade diapirs underlying low-grade greenstone belts.

Key words: Numerical modelling; The West African Craton; The Alpine Fault zones; Transcurrent faults; Localization of deformation; Exhumation

RÉSUMÉ

L'objectif de cette thèse est d'étudier le rôle joué par les zones de cisaillement sur la localisation de la déformation et de l'exhumation de la croûte inférieure grâce à une série de modèles numériques thermomécaniques 2D et 3D que nous avons appliqué à deux cas d'étude: le craton ouest-africain (WAC) et les zones de failles alpines en Nouvelle Zélande. En ce qui concerne la localisation de la déformation dans la croûte supérieure, différentes orientations pour un système de décrochement en ramification ont été testées. Sous un régime compressif, les résultats montrent que les zones de failles internes, ainsi que les unités de roches présentes entre ces failles réagissent de façon plus fragile que les unités rocheuses présentes à l'extérieur de ces domaines. Pour le cas d'un régime de déformation en cisaillement simple, nous avons exploré le processus de réorganisation qui s'est produit aux limites de deux plaques (i.e. Australie et Pacifique) au sud de la Nouvelle-Zélande. Les modèles montrent que la déformation se concentre le long des zones de cisaillement étroites, situées au centre du modèle, lorsque les coefficients d'amollissement sont élevés. Inversement, la contrainte cisailante ressort de façon plus diffuse à travers le modèle lorsque les coefficients d'amollissement sont faibles. Les cisaillements s'expriment alors sur l'ensemble du modèle bien que les taux de cisaillement restent les plus élevés sur les bordures du modèle.

Afin de tester l'impact de failles héritées et de bassins préexistants sur l'exhumation de la croûte inférieure, des modèles 2D et 3D ont été testés avec différentes conditions aux limites (traduisant extension, transtension et compression).

- En contexte extensif, dans les portions Est et Ouest des corridors fortement métamorphisés du Nord-Ouest Ghana, des roches partiellement fondues, issues de la croûte inférieure, ont pu être exhumées au sein des croûtes moyenne à supérieure. Dans la partie centrale du domaine de Bolé-Bulenga, des roches très métamorphisées ont été exhumées grâce au couplage de deux mécanismes: (1) la concentration de roches partiellement fondues entre les failles de Jirapa et de Bolé-Nangodi; ces failles convergent vers le sud, induisant un rétrécissement de l'espace disponible pour accueillir ce matériel fondu; (2) la concentration de roches partiellement fondues dans la partie centrale, induite par un jeu de failles héritées d'orientation Est-Ouest.
- En contexte de transtension, dans le terrane de Sefwi au Sud-Ouest Ghana, le domaine de Kukuom-Juaboso (KJD), composé majoritairement par des roches à faciès de type amphibolite à migmatitique, semble s'être mis en place sous forme d'intrusions au sein d'une zone relais située entre les zones de cisaillements de Kenyase et de Ketéso. Ces deux zones de cisaillement sont marquées par un stade de croissance puis de maturation qui semblent être

reliés aux phases de déformation D1 puis D2 reconnues régionalement. L'exhumation régionale des roches très métamorphisées dans le terrane de Sefwi s'est probablement produite en moins de 5 Ma.

- En régime compressif, l'impact joué par les bassins volcano-sédimentaires sur le processus d'exhumation de la croûte inférieure a été testé numériquement. Les modèles suggèrent que de multiples injections de magmas granitoïdiques, dérivant soit de matériaux subductés, soit d'une fusion de produits crustaux ou de matériel mantellique accumulés en profondeur, ont pu être canalisées au sein de diapirs avant de venir nourrir la croûte supérieure. Ce modèle suggère également une asymétrie des structures entre la croûte supérieure d'une part, et la croûte inférieure à moyenne d'autre part: i.e. (i) les bassins de roches vertes faiblement métamorphisés de la croûte supérieure reposent sur les diapirs métamorphisés et (ii) les bassins de roches vertes très métamorphisés constituent le soubassement des dômes granitoïdiques de la croûte supérieure.

Mots clés: Modélisation numérique; Le craton ouest-africain; Les zones de failles alpines; Failles décrochantes; Localisation de la déformation; Exhumation

Content

ACKNOWLEDGEMENTS.....	I
ABSTRACT.....	III
RÉSUMÉ.....	V
INTRODUCTION.....	1
Chapter 1 Rheology and deformation mechanisms of the lithosphere.....	5
Introduction.....	6
1.1 Mechanical Behaviour of materials.....	6
1.1.1 Elasticity.....	6
1.1.2 Elastic-plasticity.....	7
1.1.3 Visco-elasticity.....	7
1.1.4 Visco-plasticity.....	8
1.2 Deformation styles.....	9
1.2.1 Tectonic and gravitational forces.....	9
1.2.1.1 Tectonic forces.....	9
1.2.1.2 Gravitational force.....	11
1.3 Rheological profiles in the lithosphere.....	12
1.4 Temperature.....	14
1.4.1 Conduction and convection.....	14
1.4.1.1 Conduction.....	14
1.4.1.2 Convection.....	15
1.4.2 Thermal history of the Earth.....	17
1.4.3 Geodynamic implications.....	18
1.5 The <i>Underworld</i> Numerical code.....	21
1.5.1 Overview.....	21
1.5.2 General equations.....	22
1.5.3 Performance.....	23
1.6 References.....	25
Chapter 2 Geological settings of the study areas.....	35

Introduction.....	36
2.1 Summary of geological framework of the WAC.....	36
2.1.1 Leo-Man Shield	37
2.1.1.1 Geological summary of South-Western Burkina Faso.....	38
2.1.1.2 Geological summary of North-West Ghana	39
2.1.2 Debates on the WAC.....	41
2.1.2.1 Geodynamic settings	41
2.1.2.2 Deformation phases	42
2.1.2.3 Tectonic models in the WAC	44
2.2 Geological setting in Southern New Zealand	46
2.2.1 Geodynamic evolution (110 Ma-0 Ma).....	46
2.2.2 Summary of geological framework of the South New Zealand	47
2.2.3 Ongoing topics	48
2.2.3.1 The Alpine Fault expressions in lower crust and mantle.	48
2.2.3.2 Mechanism of shear localization.....	50
2.3 References.....	53
Chapter 3 The role of interacting fault systems on the localization of deformation in the upper crust.....	63
3.1 Interacting fault systems in NW Ghana.....	64
Introduction	64
3.1.1 3-D numerical modelling of the influence of pre-existing faults and boundary conditions on the distribution of deformation: Example of North-Western Ghana	64
3.1.2 Appendix	85
3.2 Interacting fault systems in southern New Zealand.....	86
Introduction	86
3.2.1 Effect of strain-weakening on Oligocene-Miocene self-organization of the Australian-Pacific plate boundary fault in southern New Zealand: Insights from numerical modelling	86
3.2.2 Appendix	102
Chapter 4 The role of interacting fault systems on the exhumation of the lower crust	103
Introduction.....	104

4.1 Influence of pre-existing faults on the distribution of lower crust exhumation under extension: Numerical modelling and Implications for NW Ghana.....	105
Highlights	106
Abstract.....	107
4.1.1 Introduction	108
4.1.2 Geological setting	109
4.1.2.1 The West African Craton (WAC).....	109
4.1.2.2 The Leo-Man Shield.....	109
4.1.2.3 Summary of the Bole-Bulenga Terrane (BBT)	110
4.1.3 Numerical method and assumptions for the model.....	112
4.1.4 Results.....	117
4.1.4.1 2D models.....	118
4.1.4.2 Exhumation of lower crust in the 3D models.....	122
4.1.5 Discussion	125
4.1.5.1 Distribution of lower crust	125
4.1.5.2 Distribution of finite strain	126
4.1.5.3 Model implications for the BBT.....	128
4.1.5.4 Limitations and perspectives.....	130
4.1.6 Conclusions	130
4.1.7 Acknowledgements	131
4.1.8 Appendix	131
4.1.9 References	135
4.2 3D numerical modelling of the re-distribution of partially molten lower crust rocks in relay zones between faults during transtension: Implications for the Sefwi terrane, SW Ghana	142
Abstract.....	143
Highlights	144
4.2.1 Introduction	145
4.2.2 Geological setting	146
4.2.3 Method and model setup	148

4.2.4 Results.....	153
4.2.4.1 The upper surface of the partially molten lower crust	153
4.2.4.2 Surface relief.....	156
4.2.4.3 Particles motion: extension versus transtension	158
4.2.5 Discussion	161
4.2.5.1 Migration of particles: extension versus transtension.....	161
4.2.5.2 Exhumation rate	162
4.2.5.3 Model implications for the Ghanaian Sefwi terrane	165
4.2.5.4 Limitations and perspectives.....	167
4.2.6 Conclusions	168
4.2.7 Acknowledgements	170
4.2.8 References	171
Chapter 5 A numerical study of exhumation modes in the WAC during regional compression	179
Introduction.....	180
5 Role of volcano-sedimentary basin on spatial-temporal evolution of lower crust exhumation in the West African Craton (ca. 2.20-2.00 Ga): A numerical model.....	181
Highlights	182
Abstract	183
5.1 Introduction.....	184
5.2 Geological setting	185
5.2.1 Geological framework in the Leo-Man Shield	185
5.2.2 Geological summary in South-Western Burkina Faso	185
5.2.3 Gravimetric responses	187
5.3 Tectonic models: the deformation of greenstone-granitoid belts.....	187
5.4 Ambient mantle temperature (Tp).....	189
5.5 Numerical method and model assumptions	193
5.6 Thermo-mechanical modelling results	196
5.6.1 Model200 and Model250	196
5.6.2 Model290.....	197
5.6.3 Model350 and Model400	197
5.6.4 Mode450.....	198

5.7. Discussion	205
5.7.1 The mantle potential temperature.....	205
5.7.2 A new tectonic scenario.....	206
5.7.3 Implications for the Birimian crust	209
5.7.4 Limitations and perspectives	210
5.8 Conclusions.....	211
5.9 Acknowledgements	212
5.10 Appendix.....	213
5.11 References	214
Chapter 6 General conclusions and perspectives	223
6.1 General conclusions.....	224
6.1.1 Localization of deformation.....	224
6.1.2 Exhumation of the lower crust	224
6.2 Limitations of the models and Perspectives.....	225
6.3 References	225
6.4 Conclusions générales	226
6.4.1 La localisation de la déformation.....	226
6.4.2 Exhumation de la croûte inférieure.....	226
Chapter 7 Appendix	229
7.1 List of publications associated with this thesis	230

INTRODUCTION

Les structures héritées au sein de la croûte peuvent jouer un rôle important dans l'initialisation de la distribution et le contrôle de l'évolution de la déformation et du relief. Ces structures héritées peuvent offrir des sites privilégiés pour l'accumulation de contraintes en raison de leur fonction de concentrateur de contraintes par rapport à la roche hôte. La croissance des failles est principalement influencée par les champs de contraintes hétérogènes, caractérisés par une augmentation systématique des déplacements et des durées relatives des événements de type glissements sismiques sur une échelle régionale ou par le mouvement relatif des plaques sur une plus grande échelle. Au cours de la croissance et la propagation des failles, une liaison souple peut mûrir et se durcir via la propagation de fracture à l'extrémité des failles et la répétition des interactions entre les failles. La dynamique crustale d'un système de failles en interaction représente un problème complexe en raison de la variation de l'orientation du décrochement le long de la faille sur des échelles de temps géologiques.

Le processus de formation des corps métamorphiques complexes (MCC) est généralement lié à une tectonique en extension à l'échelle continentale. Il est caractérisé par l'exhumation des matériaux partiellement fondus de la croûte inférieure jusqu'aux niveaux de la croûte supérieure. La mise en place des roches partiellement fondues est essentiellement conduite par les contrastes de densité et de viscosité par rapport aux roches solides environnantes (encaissantes). L'orientation des failles héritées, le gradient géothermique et l'épaisseur de la lithosphère jouent tous un rôle important en influençant l'évolution et la distribution de l'exhumation de la croûte inférieure lors des processus d'extension.

L'objectif principal de cette recherche est de comprendre et de comparer le rôle que jouent les zones de cisaillement héritées dans la localisation de la déformation et de l'exhumation de la croûte inférieure en utilisant une série de modèles numériques thermomécaniques 2D et 3D en prenant le Craton Ouest Africain (WAC) et les zones de failles alpines en Nouvelle Zélande comme zones d'étude. Dans le WAC, des zones de cisaillement à l'échelle du craton marquent souvent les frontières, dans le Nord-Ouest et le Sud-Ouest du Ghana, entre les ceintures de roches vertes faiblement métamorphisées et des roches métamorphiques de haute grade allant jusqu'à des faciès de type amphibolitique-migmatitique. Dans les zones de failles alpines, l'histoire des déformations précoces peut être observée dans l'île plus récente de South Island. Son expression structurale est compatible avec les segments de crête régionaux orientés Nord-Est et les failles orientées Nord-Ouest. Ces fabriques héritées sont supposées jouer un rôle important dans le contrôle de l'évolution de la

localisation des déformations au cours du développement précoce, à l'époque Oligocène-Miocène, des conditions aux limites décrochantes dextres modernes à travers la faille Alpine. Cette thèse de doctorat est structurée en trois grands chapitres afin d'aborder les points soulignés ci-dessus:

Dans le chapitre trois, nous utilisons le craton ouest-africain (WAC) et les zones de failles alpines en Nouvelle Zélande comme zones d'étude afin d'explorer le rôle des failles pré-existantes sur l'initialisation, la distribution et le contrôle de la déformation. Différentes orientations d'un système de décrochement ramifié ont été testées. Dans un régime soumis à des conditions aux limites en compression, les résultats montrent que les zones de failles internes, ainsi que les unités de roches présentes entre ces failles réagissent de façon plus fragile que les unités rocheuses présentes à l'extérieur de ces domaines. Pour le cas d'un régime de déformation en cisaillement simple, nous avons exploré le processus de réorganisation qui s'est produit aux limites de deux plaques (i.e. Australie et Pacifique) au sud de la Nouvelle-Zélande. Les modèles montrent que la déformation se concentre le long des zones de cisaillement étroites, situées au centre du modèle, lorsque les coefficients d'amollissement sont élevés. Inversement, la contrainte cisailante ressort de façon plus diffuse à travers le modèle lorsque les coefficients d'amollissement sont faibles. Les cisaillements s'expriment alors sur l'ensemble du modèle bien que les taux de cisaillement restent les plus élevés sur les bordures du modèle.

Dans le chapitre quatre, nous prenons le Nord-Ouest et le Sud-Ouest Ghana comme zones d'étude afin de comprendre le rôle joué par les zones de cisaillement pré-existantes dans le processus d'exhumation de la croûte inférieure sous conditions aux limites en extension et en transtension. En contexte extensif, dans les portions Est et Ouest des corridors fortement métamorphisés du Nord-Ouest Ghana, des roches partiellement fondues, issues de la croûte inférieure, ont pu être exhumées au sein des croûtes moyenne à supérieure. Dans la partie centrale du domaine de Bolé-Bulenga, des roches très métamorphisées ont été exhumées grâce au couplage de deux mécanismes: (1) la concentration de roches partiellement fondues entre les failles de Jirapa et de Bolé-Nangodi augmente à cause du fait que ces failles convergent vers le sud, induisant un rétrécissement de l'espace disponible pour accueillir ce matériel fondu; (2) la concentration de roches partiellement fondues dans la partie centrale, induite par un jeu de failles héritées orthogonales d'orientation Est-Ouest. En contexte de transtension, dans le terrane de Sefwi au Sud-Ouest Ghana, le domaine de Kukuom-Juaboso (KJD), composé majoritairement par des roches à faciès de type amphibolite à migmatitique, semble s'être mis en place sous forme d'intrusions de roches partiellement fondues au sein d'une zone relais située entre les zones de cisaillements de Kenyase et de Ketéso. Ces deux zones de cisaillement sont marquées par un stade de croissance puis de maturation qui semblent être reliés aux phases de

déformation D1 puis D2 reconnues régionalement. L'exhumation régionale des roches très métamorphisées dans le terrane de Sefwi s'est probablement produit en moins de 5 Ma.

Dans le chapitre 5, nous visons à apporter un nouvel éclairage sur l'évolution des ceintures de type «granitoïde-Greenstone» à partir d'une étude numérique. Dans cette partie, en régime compressif, l'impact joué par les bassins volcano-sédimentaires sur l'évolution spatio-temporelle du processus d'exhumation de la croûte inférieure a été testé numériquement. Les modèles suggèrent que de multiples injections de magmas granitoïdiques, dérivant soit de matériaux subductés, soit d'une fusion de produits crustaux et/ou de matériel mantellique accumulés en profondeur, ont pu être canalisées au sein de diapirs avant de venir nourrir la croûte supérieure. Lorsque les granitoïdes ont rencontré le toit solidifié des diapirs, ils ont probablement migré latéralement puis sont venus pratiquer une intrusion dans la croûte supérieure via des zones de faiblesse situées entre les diapirs. Ce modèle suggère également une asymétrie des structures entre la croûte supérieure d'une part, et les croûtes inférieure à moyenne d'autre part: i.e. (i) les bassins de roches vertes faiblement métamorphisés de la croûte supérieure reposent sur les diapirs métamorphisés et (ii) les bassins de roches vertes très métamorphisés constituent le soubassement des dômes granitoïdiques de la croûte supérieure.

Le chapitre 6 synthétise les principaux résultats et aborde quelques perspectives de recherche ouvertes par ces travaux.

Le chapitre 7 énumère les publications liées à cette thèse, en outre, un papier publié à la revue *American Mineralogist* (By Jérôme Ganne, Xiaojun Feng, Patrice Rey, and Vincent De Andrade. «Statistical Petrology Reveals a Link Between Supercontinents Cycle and Mantle Global Climate», 2016, doi: 10.2138/am-2016-5868) dans lequel nous nous sommes intéressés à la géostatistique, à l'extraction de données, à la température du manteau et aux cycles supercontinentaux.

La thèse a été financée par une bourse du CSC (China Scholarship Council, No. 201206420020, 2012-2016). Les frais de fonctionnement de la recherche ont été pris en charge par le projet WAXI, lors de sa seconde phase (WAXI II), à partir de septembre 2011. Cette initiative, qui a débuté en Novembre 2006, est principalement financée par l'industrie minière internationale et par AusAID, via un consortium international, AMIRA. AMIRA International est une association industrielle dédiée au soutien de la recherche collaborative industrielle des minéraux. L'objectif principal de WAXI est d'accroître le potentiel d'exploration du Craton Ouest Africain à travers un programme intégré de recherche et de collecte de données, et d'augmenter la capacité des institutions locales à entreprendre ce type de travail.

Chapter 1

Rheology and deformation mechanisms of the lithosphere

Introduction

This chapter introduces the rheology and deformation mechanisms in the lithosphere starting with a basic review of the mechanical behaviour of materials. This is followed by a short introduction to the role gravitational and tectonic forces play in influencing the deformation styles. Subsequently, different rheological profiles in the lithosphere are discussed, together with some physical constraints on the deformation mechanisms and viscosities according to experimental studies. Two basic patterns of heat transfer (conduction and convection) in the Earth are introduced. As an extension, the thermal history of the mantle (particularly the mantle potential temperature, T_p) is introduced and its geodynamic consequence is subsequently discussed.

Finally, the numerical code ‘*Underworld*’ is introduced together with a basic model for testing the physical performances.

1.1 Mechanical Behaviour of materials

1.1.1 Elasticity

Elasticity is the ability of a material to recover its original shape and size after the removal of an external stress on the material. For small-scale deformation within a short time period, most materials exhibit linear elasticity that can be expressed as a linear relationship between force and displacement (1.1) or stress and strain (1.2) as follows:

$$F = -KX \quad (1.1)$$

$$\sigma = E\varepsilon \quad (1.2)$$

where F is the external force, K is the spring constant, X is the displacement, σ is the stress, ε is the strain and E is a material constant known as the Young’s modulus.

For an isotropic medium, the elastic property at any point O , is independent of direction. The material’s linear elasticity can be expressed as equations (1.3) and (1.4). The relationship between the shear modulus, Young’s modulus and Poisson’s ratio is given in equation (1.5).

$$\sigma_{ij} = \lambda\delta_{ij}\varepsilon_{kk} + 2\mu\varepsilon_{ij} \quad (1.3)$$

$$\varepsilon_{ij} = \frac{1}{2\mu}\sigma_{ij} - \frac{\nu}{E}\delta_{ij}\sigma_{kk} \quad (1.4)$$

$$\mu = \frac{E}{2(1+\nu)} \quad (1.5)$$

where σ_{ij} is the stress tensor, ε_{ij} is the strain tensor, δ_{ij} is the Kronecker delta, λ is the Lamé’s first parameter ($\lambda = K - \frac{2}{3}\mu$, K is the bulk modulus), μ is the shear modulus and ν is the Poisson’s ratio.

1.1.2 Elastic-plasticity

Elastic-plasticity is widely used to model the large-scale deformation of crust and upper mantle. The deformation includes non-permanent (elastic component, ε_e) and permanent (plastic component, ε_p) components. The non-permanent deformation is totally recoverable after the applied force is removed. Plasticity, is when a material is undergoing irreversible changes of shape and size during deformation as a consequence of the applied force beyond the elastic limit within a longer time period. Total strain can be expressed as follows:

$$\varepsilon = \varepsilon_e + \varepsilon_p \quad (1.6)$$

In geology, this term (elastic-plasticity) is in general equated to a rock acquiring a permanently distortional strain in response to external (tectonic and gravitational) forces.

In this thesis, the pressure-dependent Drucker-Prager (DP) yield criterion (Drucker and Prager, 1952) is employed to determine a material has failed or undergone plastic yielding. The Drucker-Prager yield criterion is generally expressed in terms of cohesion, pressure and coefficient of internal friction angle (equation 1.7). According to the equation, a higher applied stress will be required to cause a material to yield as buried depth increases.

$$\tau_{II} = P \cdot \tan \varphi + \delta_c \quad (1.7)$$

where τ_{II} is the second invariant of the deviatoric stress tensor, P is the local pressure, φ is the effective internal friction angle and δ_c is the effective cohesion. Under a hydrostatic condition, the local pressure can be written in terms of three principle stresses, as $P = \frac{1}{3}(\sigma_1 + \sigma_2 + \sigma_3)$.

1.1.3 Visco-elasticity

Visco-elasticity is the ability of a material or medium to exhibit both elastic and viscous characteristics when deformation occurs in response to applied force. The viscosity of a material is a property that is used to quantify its resistance to a shear or tensional stress. A viscoelastic behaviour indicates a process of losing energy (Meyers and Chawla, 2009) in a cycle of loading and unloading (Figure 1.1) and takes into account the past history of the material stress. The elastic component has been mentioned through equation (1.2). The viscous component can be modelled by a dashpot and the stress-strain relationship can be written as follows:

$$\sigma = \eta \frac{d\varepsilon}{dt} \quad (1.8)$$

where σ is the stress, η is the dynamic viscosity and $\frac{d\varepsilon}{dt}$ is the rate of shear deformation.

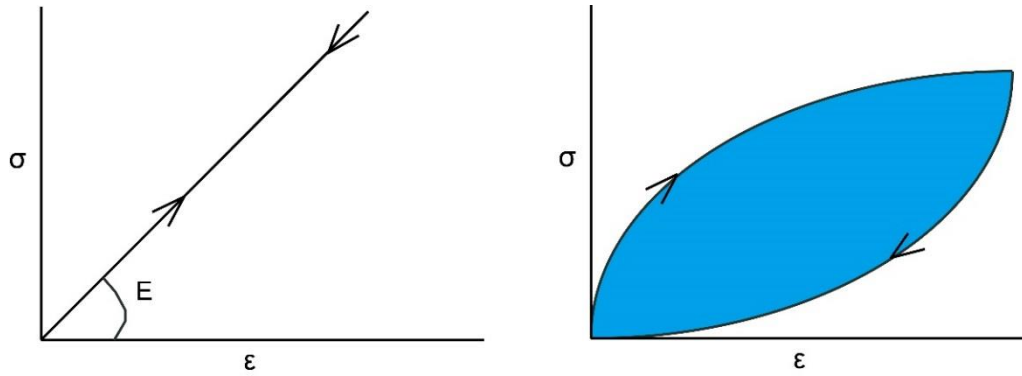


Figure 1.1: Stress (σ)-strain (ϵ) curves for an elastic material (left) and a viscoelastic material (right), respectively. Blue area shows the amount of energy lost in a cycle of loading and unloading.

To model viscoelastic materials, the best starting point is to invoke the three principal models composed of springs and dashpots: the Kelvin-Voigt, the Maxwell and the standard linear solid models. The sketch models are plotted in Figure 1.2. The Kelvin-Voigt model is composed of a dashpot and a Hook law type elastic spring connected in parallel, the Maxwell model consists of a dashpot and a Hookean elastic spring connected in series, and the standard linear solid model is a parallel connection of the Maxwell's full components and a Hookean elastic spring.

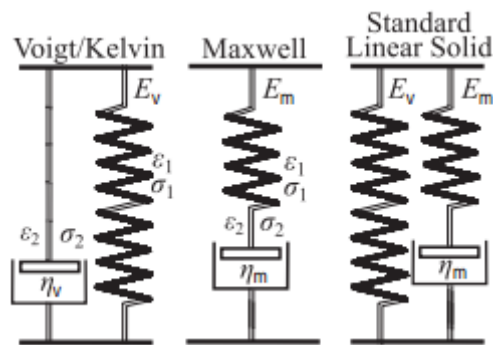


Figure 1.2: Different linear viscoelastic models (the Kelvin-Voigt, the Maxwell and the Standard Linear Solid models), diagrammed by using springs and dashpots (Source: Vincent, 2012).

1.1.4 Visco-plasticity

Visco-plasticity is generally used to describe the rate-dependent inelastic behaviour of a solid material. The present thesis aims to explore the evolution of large deformation within a long time period. Therefore, a visco-plastic rheology is employed for all models without taking into account elastic components. Most rocks deform according to a non-linear fashion, as a result of high temperature and high pressure at depths.

Creep is the tendency of a material to move slowly or deform permanently as a result of long-term exposure to high stress that is still below the yield strength. A representative creep law for describing the behaviour of olivine-rich rocks was firstly introduced by Kirby and Kronenberg, (1987):

$$\dot{\epsilon} = A (\sigma_1 - \sigma_3)^n \exp(-Q/RT) \quad (1.9)$$

where $\dot{\epsilon}$ is the steady-state creep rate, A is a pre-exponential constant (property of a rock), n is a power law exponent (rocks generally range between 2 and 5, Gerbault, 1999), Q is the activation energy, R is the universal gas constant and T is the local temperature.

For an incompressible material (Chen and Morgan, 1990), the following equation (1.10) is used:

$$\dot{\epsilon} = \frac{4}{3} \cdot \dot{\epsilon}_2 = \frac{4}{3} \cdot \frac{\dot{\epsilon}_1 - \dot{\epsilon}_3}{2} \quad (1.10)$$

An isotropic tensor stress-strain rate relationship is assumed and expressed as follows:

$$\tau_{ij} = 2 \cdot \eta \cdot \epsilon_{ij} \quad (1.11)$$

Matching equations (1.9) and (1.11), the effective viscosity can be expressed as follows:

$$\eta = \frac{1}{4} (0.75 \cdot A)^{(-1/n)} \cdot \dot{\epsilon}_2^{\left(\frac{1}{n}-1\right)} \cdot \exp\left(\frac{Q}{nRT}\right) \quad (1.12)$$

In the subsequent chapters, equation (1.12) is employed to model the dislocation creep flow in all cases.

1.2 Deformation styles

Deformation is a change in form or shape (including rigid and non-rigid body), which can be measured by identifying the positions of material particles before and after the deformation (Figure 1.3). Rocks can be deformed in many different ways and this is dominantly determined by the magnitudes and orientations of three principle stresses. This indicates that strain information together with observed structures in rocks can provide the paleo-stress information that the rocks have experienced. There are two most potent forces for deformation: tectonic and gravitational forces. Tectonic forces generally act in a sub-horizontal way, whereas gravitational force near the surface of the Earth acts essentially vertically.

1.2.1 Tectonic and gravitational forces

1.2.1.1 Tectonic forces

Tectonic forces are commonly responsible for large-scale lithospheric plate motion, as well as accountable for the bending, warping, fracturing of the upper crust on both continental (regional) and

local scales. Tectonic forces can be classified into three different categories: compressional, tensional and shearing tectonic forces (Figure 1.4).

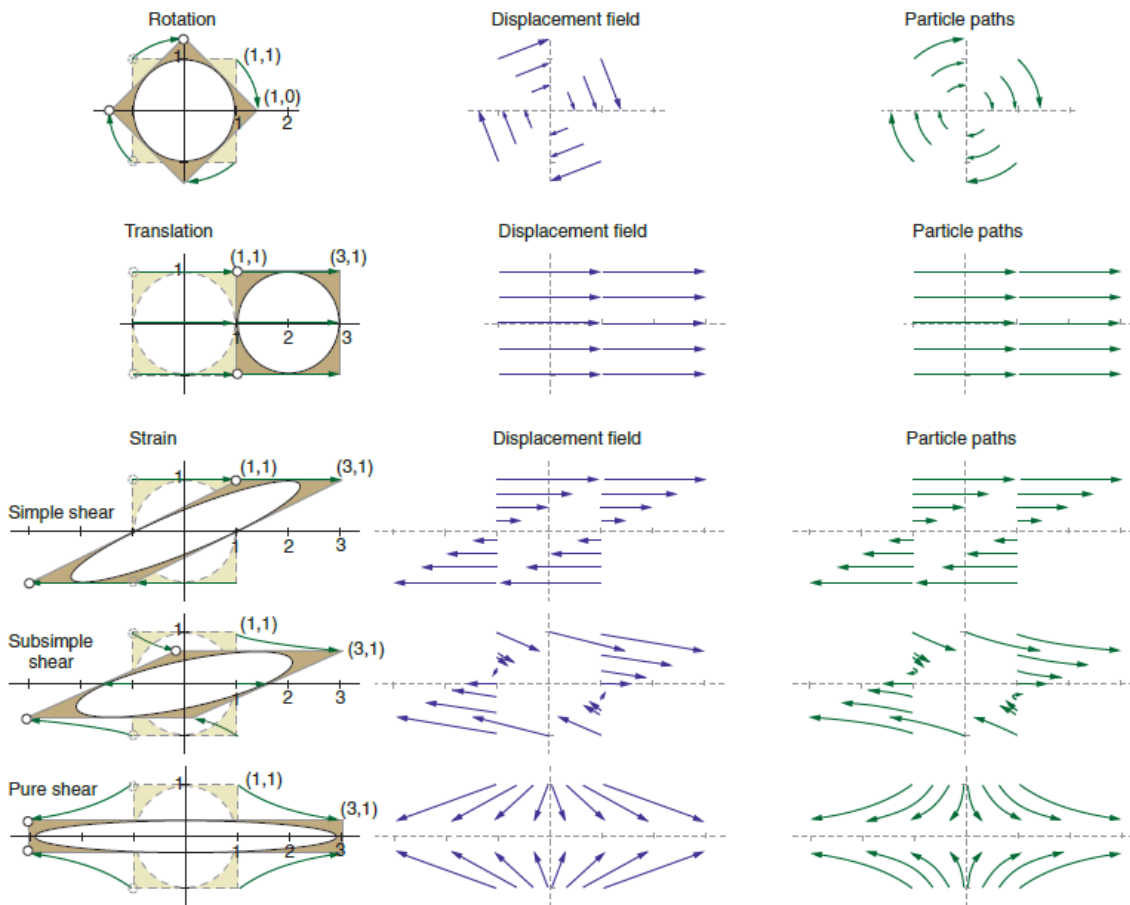


Figure 1.3: Displacement field and particles paths under rotation, translation and strain related to simple shear, sub-simple shear and pure shear (Source: Fossen, 2010).

Compressional tectonic forces

Compressional tectonic forces push two continental blocks together resulting in thickening and shortening the crust. Rocks near the Earth's surface typically break and move along fractures. High temperature-pressure lower crustal rocks typically fold rather than breaking abruptly in response to compressional forces.

Tensional tectonic forces

On a global scale, tensional tectonic forces are mainly responsible for the separation of lithospheric plates. This process is generally named as a continental rifting. On a regional scale, tensional forces frequently form a series of parallel normal faults termed as horsts and grabens.

Shearing tectonic forces

Shearing tectonic force slides parts of the Earth's crust past each other. The process of shearing can occur within brittle, brittle-ductile and ductile rocks. On a global scale, simple shear typically occurs at transform boundaries. Transpression regime is a result of an oblique collision of tectonic plates during non-orthogonal subduction (e.g. the Alpine Fault of New Zealand). Transtension regime results from an oblique tensional environment (e.g. the Dead Sea), which is related to both strike-slip and extensional structures.

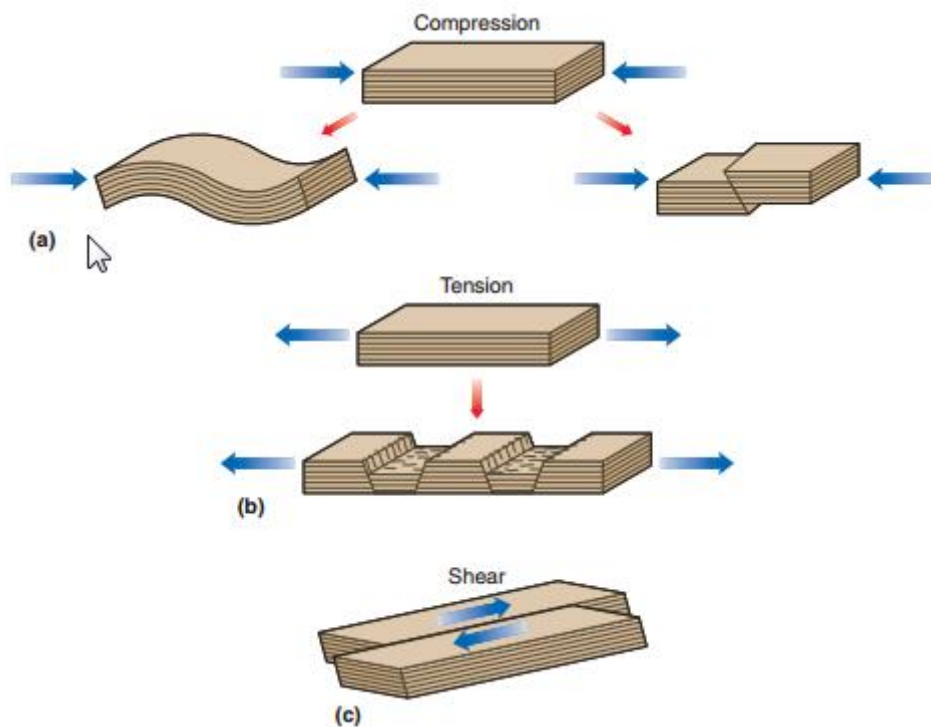


Figure 1.4: Diagrammatic sketches for various tectonic deformation styles. The deformation styles result from different tectonic forces (Source: Gabler et al., 2009): (a) compression, (b) tension and (c) shear.

1.2.1.2 Gravitational force

Gravitational force influences all kinds of large-scale deformation. Its role becomes noticeable when the size of the structure is increased (regional scale structures). On a local scale, gravitational force has little influence on folds, usually few centimetres to metres in size. Whereas on a global scale, gravity is the main driving force responsible for plate tectonics, for instance, when a dense oceanic lithosphere moves beneath a continental plate and sinks into the mantle (i.e. subduction). Gravity tectonics is strictly associated with downward motion, as this is the way that gravity is perceived to operate. The gravity tectonics was firstly introduced by De Wijkerslooth de Weerdesteryn, (1934) to explain the formation of folds and thrusts in the foreland zones of mountain belts.

Gravity-driven ductile flow can effectively reduce the lateral contrast in gravitational potential energy (Rey et al., 2001) and the lateral contrast in density (Fleitout and Froideveaux, 1982; Ganne et al.,

2014). The strength profile (Rey et al., 2001) of the deforming lithosphere also plays a major role in controlling gravitational instabilities.

1.3 Rheological profiles in the lithosphere

Bürgmann and Dresen, (2008) used food analogies to sketch the distribution of strength and rheological parameters in the lithosphere, thus shown as “Jelly Sandwich”, “Crème Brulée” and “Banana Split-like” models (Figure 1.5). In panel (a), a weak middle and lower crust (Indian-Asian type, Burov, 2011) is sandwiched between the strong upper crust and the strong lithospheric mantle. Compared to panel (a), model (b) has a lower crust with a high strength as a result of the absence of water. The strength of the lithospheric mantle becomes weak as a result of a high geothermal gradient (Jackson, 2002). When crustal fault zones are included in the lithosphere, the differential stress is significantly reduced throughout the whole lithosphere. This is attributed to a “Banana Split-like” model (Panel c in Figure 1.5).

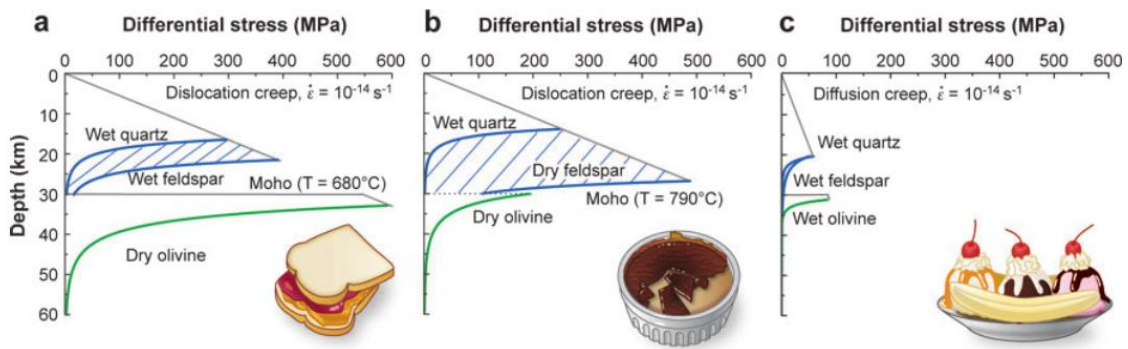


Figure 1.5: Schematic view of the strength profiles through the lithosphere (Source: Bürgmann and Dresen, 2008). The Moho interface is assumed at a depth of 30 km. (a) Jelly Sandwich model. (b) Crème Brulée model. (c) Banana Split model.

From laboratory experiments, the rheological behavior of rocks pertaining to the lower crust and upper mantle (Figure 1.6) is controlled by a series of important parameters such as grain size, hydrous (saturated in water)/anhydrous conditions, temperature, melt fraction and mineral phase content (Figure 1.6). Silicate rocks are usually mechanically weaker under the hydrous condition than that under the anhydrous condition. The differences in strength and viscosity between wet and dry rocks can reach an order of 10^4 , depending on the conditions of temperature and deformation mechanisms. Figure 1.6 shows that the differential stress and viscosity decrease with increasing temperature. The creep pattern is dominantly controlled by grain boundary conditions. Diffusion creep is linear in stress with a stress component of $n = 1$. The deformation in the upper mantle is dominantly controlled by olivine (Figure 1.6d). The stress component of $n = 3.5 \pm 0.5$ was suggested by Hirth and Kohlstedt, (2003) for the dislocation creep of olivine rich rocks under the hydrous/anhydrous conditions. An

1. Rheology and deformation mechanisms of the lithosphere

activation energy of 529 kJ mol^{-1} was estimated by Dohmen et al. (2002) for the dislocation creep under both the hydrous and anhydrous conditions. In the present thesis, the parameters used to model the upper mantle are similar to the estimates given above.

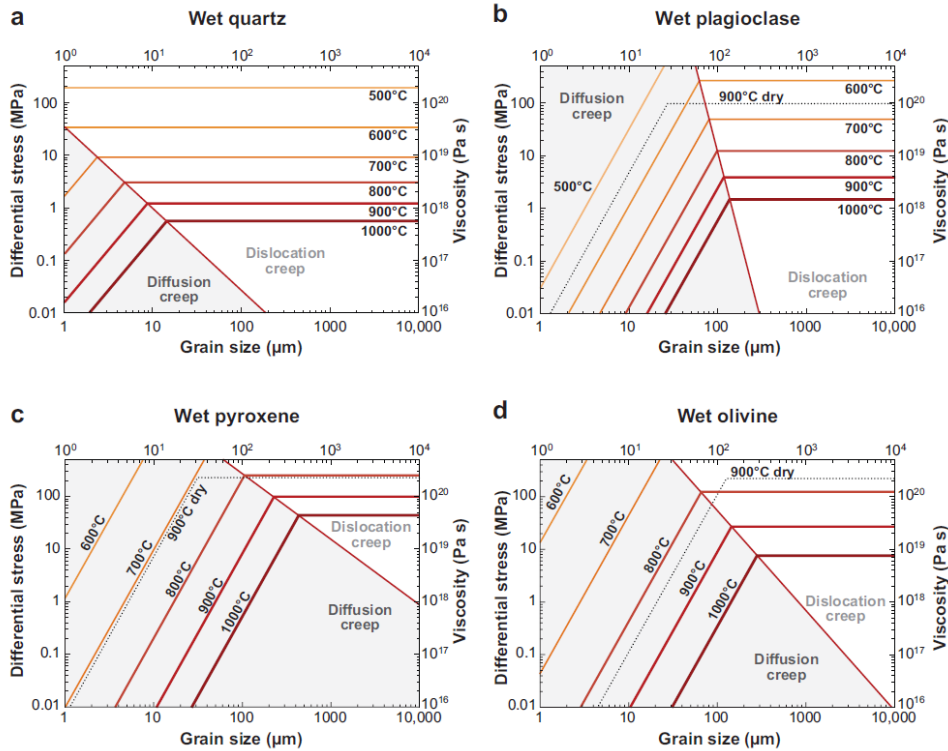


Figure 1.6: Deformation mechanism and rheological behaviour influenced by different parameters on a laboratory scale (Source: Bürgmann and Dresen, 2008): (a) Wet quartz (Rutter and Brodie, 2004a, 2004b) (b) Wet plagioclase (Rybacki et al., 2006). (c) Wet pyroxene (Dimanov and Dresen, 2005), dry pyroxene (Bystricky and Maxwell, 2001). (d) Olivine (Hirth and Kohlstedt, 2003).

Throughout crustal thickening process during plate convergence, rocks pertaining to lower crust and upper mantle may contain varying amount of partial melts. The presence of a melt phase can significantly affect the viscosity, density and strength of rocks (Renner et al., 2000; Vanderhaeghe, 2001; Vanderhaeghe and Teyssier, 2001). The decreases in density and viscosity (Figure 1.7) due to the involvement of partial melts during crustal thickening can result in gravitational instabilities of lower crust (Ganne et al., 2014). In order to explain the transition from crustal thickening to crustal thinning, Vanderhaeghe and Teyssier, (2001) concluded three main mechanisms:

- (1) A sudden increase of gravitational potential energy resulting from asthenosphere upwelling (convective removal and delamination).
- (2) A decrease in the tectonic force related to a decrease in plate convergence.
- (3) A decrease in the strength at the base of the zone of thickened crust due to thermal weakening.

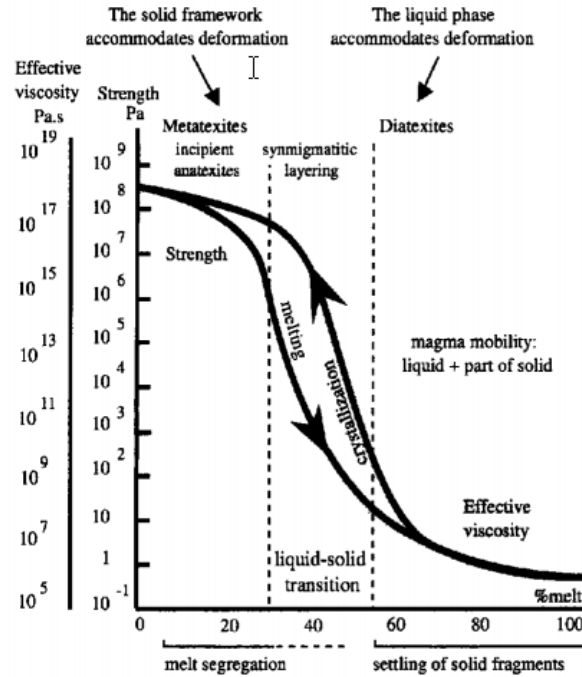


Figure 1.7: Rheological behaviour of partially molten rocks (Source: Vanderhaeghe, 2001), which is derived from a compilation of previous experimental data and theoretical rheological laws (Roscoe, 1952; Arzi, 1978; Van Der Molten and Paterson, 1979; Rutter and Neumann, 1995; Philpotts and Carroll, 1996).

1.4 Temperature

The heat from the Earth's interior is transferred to the surface by the combined effect of radiation, conduction and convection/advection. Temperature changes with depth and tectonic setting. In the lithospheric continent, thermal conduction is the prominent heat transfer mechanism among the three heat transfer styles (Clauser and Huenges, 1995). In other words, the lithospheric crust exhibits both mechanical and thermal behaviours in the Earth. In the mantle, thermal convection plays a dominant role in heat transport and is the main driving force responsible for plate tectonics.

1.4.1 Conduction and convection

1.4.1.1 Conduction

Thermal conduction describes the process of heat transfer through an object when it has a temperature difference at the adjacent sides of the body. The basic equation governing conduction is the Fourier's Law, and is expressed as follows:

$$q = -k \frac{\Delta T}{\Delta z} = -k \frac{\partial T}{\partial z} \quad (1.13)$$

where q is the heat flux (the average heat flow of the Earth is approximately 80 mWm^{-2}), k is the thermal conductivity (conductivity of a surficial rock ranges between 1 and $4 \text{ Wm}^{-1}\text{K}^{-1}$) and z is the distance of heat transfer.

For the Earth, heat is transferred by conduction in the lithospheric crust where rocks are rigid and cannot flow, and at the same time, where the geothermal gradient is also markedly higher than the one in the mantle.

With respect to the thermal conductivity of various rocks (Clauser and Huenges, 1995), volcanic and sedimentary rocks with a high porosity are skewed towards low conductivity. Plutonic rocks with a low feldspar content (less than 60 %) have a higher thermal conductivity. Regarding metamorphic rocks, a high quartz content significantly increases the thermal conductivity.

Regarding the distribution of heat flux in lithospheric continents, the average heat flux is about 65 mWm^{-2} , while the average heat flux for oceans ranges between 100 and 450 mWm^{-2} . The map of global heat flux is shown in Figure 1.8 (Davies and Davies, 2010).

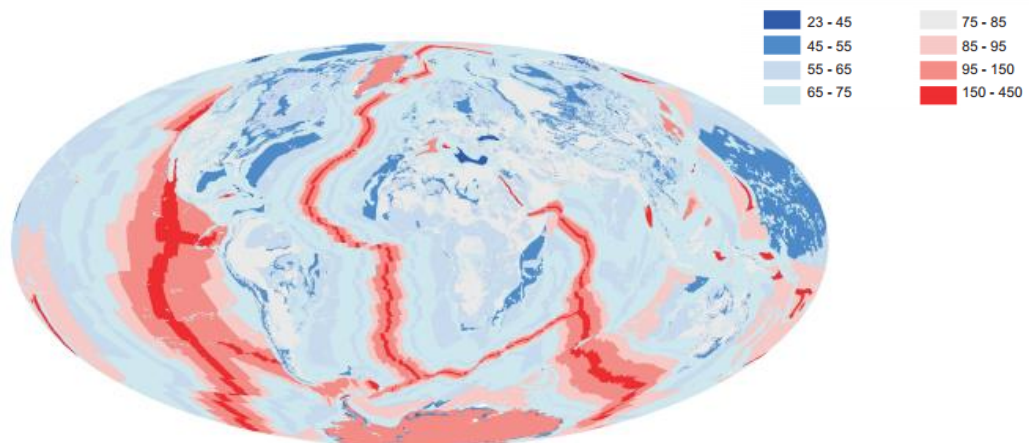


Figure 1.8: Map of global heat flux (mWm^{-2}) (Source: Davies and Davies, 2010).

1.4.1.2 Convection

Thermal convection in the mantle and in the cores is the fundamental mechanism of cooling of the Earth, characterized by transporting heat from the interior to the surface. The small-scale convection occurring in the lithospheric mantle is faster than that near the core of the Earth (Zhong and Zhang, 2005). A shallow convection cycle may take about a duration of around 50 Ma, while for the convection near the boundary between the mantle and core may take around 200 Ma.

Regarding the mechanisms accounting for driving plate motion, two mantle convection models are widely recognized (Figures 1.9 and 1.10). They are known as the whole mantle convection model (Davies et al., 1976; Takley, 2000; Bercovici and Karato, 2003) and the double-layer convection model separated by the discontinuous interface located at a depth of about 660 km (Olson, 1984; Cserepes

1. Rheology and deformation mechanisms of the lithosphere

and Rabinowicz, 1985; Stein et al., 1994). The difference between the two models is the role that the lower mantle plays in driving plate tectonics. Arguments against the double-layer mantle convection model have been reinforced by showing the mantle velocity structures. This is obtained by using seismic tomography (Van der Hilst et al., 1997; Grand et al., 1997), and shows the existence of downgoing slabs in the lower mantle. In many cases (Creager and Jordan, 1984; Christensen, 1996; Steinberger, 2000; Goes et al., 2008; Van der Meer et al., 2010), the slabs tend to temporarily flatten out above the discontinuous plane before descending into the lower mantle, a major mineralogical phase transition is expected to occur at this horizon.

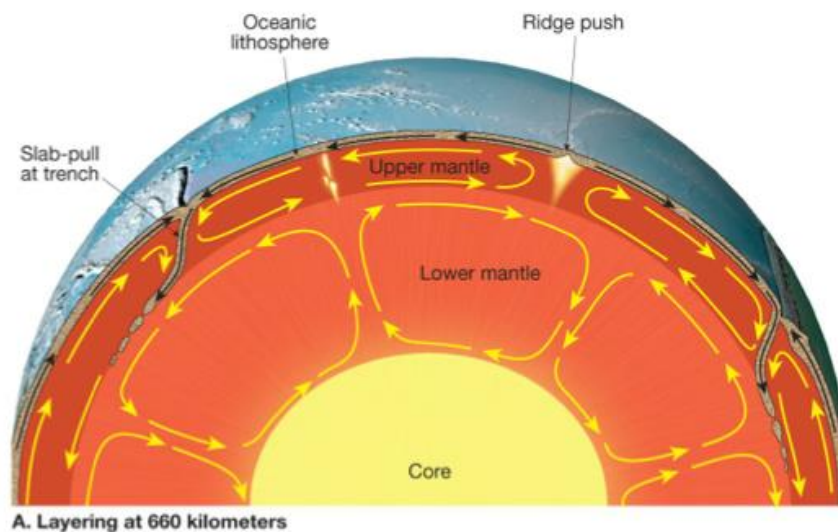


Figure 1.9: The double-layer mantle convection model (Source: USGS)

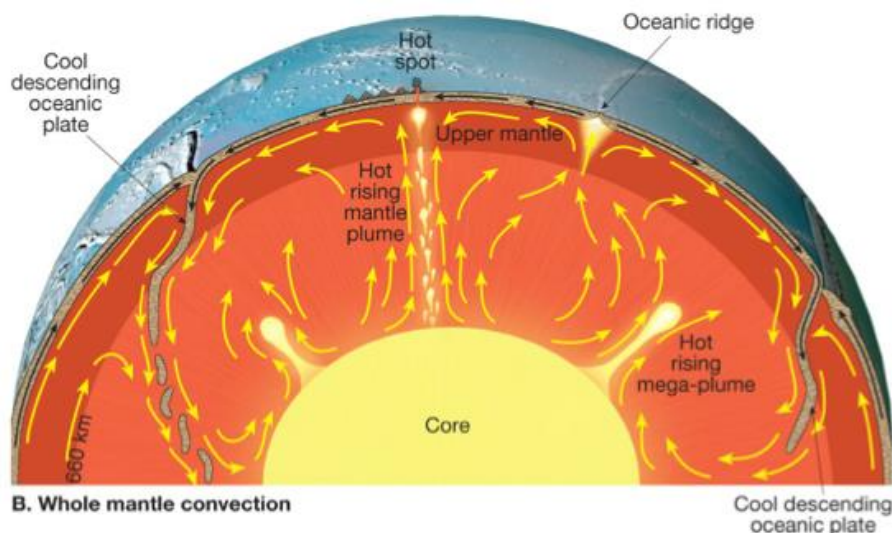


Figure 1.10: The whole-mantle convection model (Source: USGS).

1.4.2 Thermal history of the Earth

Magmatism and tectonic activities of the Earth are the surface expression of heat loss and heat transfer from the mantle and core. It is widely recognised that the mantle was hotter during the Archaean time compared to the present day, as evident by two lines of evidences:

- (1) Twice the amount of heat loss than the present day
- (2) The presence of high-MgO content komatiites in Archaean greenstone belts (Condie, 2005).

Basalts are thought to be a temperature probe of the upper mantle, as their chemical compositions significantly change with the mantle potential temperature (T_p) through geological time (Thompson and Gibson, 2000; Herzberg et al., 2007; Herzberg, 2011; Putirka et al., 2007). Herzberg et al. (2010) explored the thermal evolution (T_p) over time (0-4 Ga) by using a multi-dimensional database, their results show that the T_p decreases from 1500-1600 °C at 2.5-3.0 Ga to 1350 °C at the present day (Figure 1.11).

Korenaga, (2008a, 2008b) explored the secular cooling through the Earth's history by using the ratio of heat production from radiogenic elements over the heat loss by the mantle convection. The Urey ratios of 0.08, 0.23 and 0.38 (sluggish plate tectonic) were used to estimate the T_p through geological time (Figure 1.11), on the basis of assuming the present-day T_p of 1350 °C. However, Davies, (2009) presented that the less than 100 °C of the T_p decreases over the past 4 Ga (Figure 1.11) based on the convectonal heat-flow (more rapid plate tectonic in the past) scaling and a very high present day Urey ratio of 0.8.

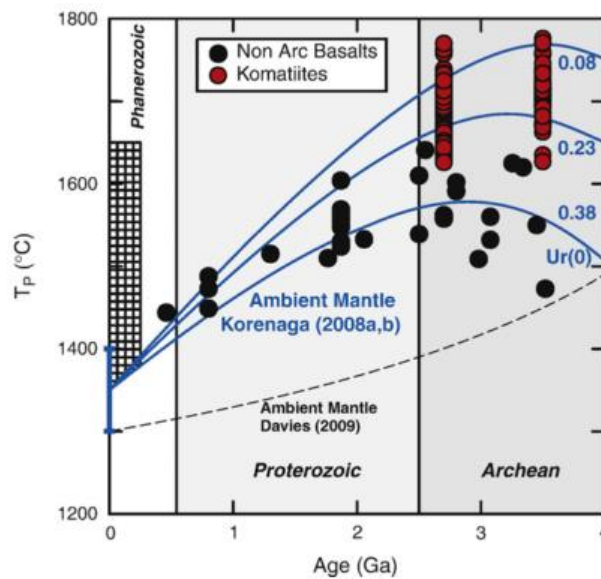


Figure 1.11: The T_p values through geological time (Source: Herzberg et al., 2010). Secular cooling model indicated by blue lines is from Korenaga, (2008a, 2008b), corresponding to the Urey ratios (mantle heat

production from radiogenic elements divided by heat loss as result of mantle convection) of 0.08, 0.2 and 0.38, respectively. Davis, (2009) assumed a present-day Urey ratio of 0.8.

1.4.3 Geodynamic implications

Temperature in the Earth can be estimated according to the global surface heat flow, heat production and conductivity. In the lithospheric mantle and asthenosphere, thermal convection is the dominant mechanism responsible for heat transport. Temperature increases with depth at different rates according to different geological settings (Figure 1.12, Condie, 2005). For most cases, geothermal gradient ranges between 10-30 °C/km at a depth of no greater than 50 km. With the exception of ocean-ridge settings (A, in Figure 1.12), the geotherm steeply intersects with the wet mantle solidus at a depth of less than 50 km. After that, the geotherm rapidly decreases in order to avoid producing a huge amount of melting in the upper mantle. For most Archean shields (D, in Figure 1.12), their geotherm does not intersect with the mantle solidus temperature. For other continental settings (C, in Figure 1.12), the geotherm slightly intersects the mantle solidus temperature at a depth of about 150-200 km.

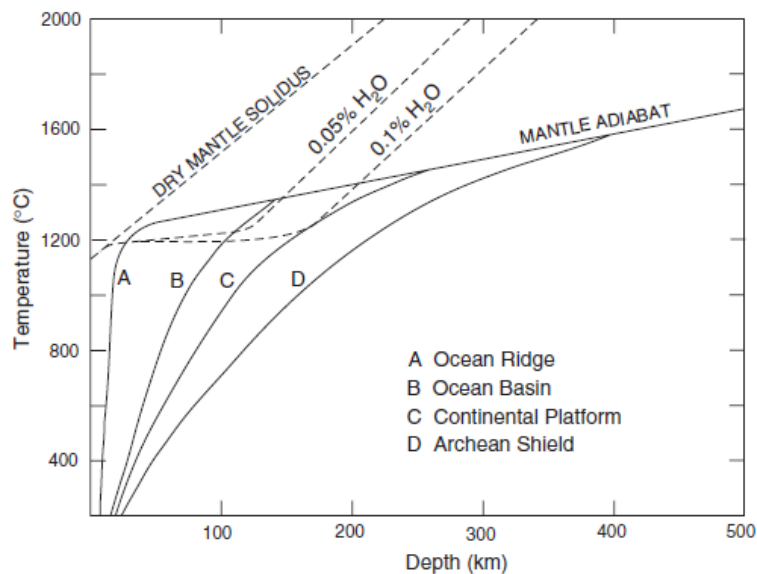


Figure 1.12: Lithospheric geotherms with respect to different geological settings. Dry mantle, 0.1% H₂O and 0.05 % H₂O mantle solidus are shown (Source: Condie, 2005).

The mechanical strength of the lithosphere evolves over geological time and space scales, which is primarily influenced by the evolution of the T_p (Willett et al., 1993; Burg and Ford, 1997; Anderson, 2005; Mckenzie et al., 2005). Modern orogenic belts are the loci of singular mineral transformations, such as the Alpine or Himalayan orogenic belts, proceeding at high-pressure and low-temperature conditions. The conditions are usually within the blueschist and greenschist facies series. (Maluski and Matte, 1984; Okay, 1989; Maruyama et al., 1996; Prelević et al., 2013). The apparent lack of high-

pressure rocks before the Neoproterozoic Era (1000-540 Ma) remains a key debate challenging the existence of modern-style plate subduction during the Archaean (4.0-2.5 Ga) and Paleoproterozoic (2.5-1.8 Ga) times. Owing to the elevated T_p (Choukroune et al., 1997; Korenaga, 2008b; Hertzberg et al., 2009, 2010), plate might move faster and slab might dip shallower than the present/modern subduction zones (Sleep and Windley, 1982; Hargraves, 1986; Van Hunen and Van den Berg, 2008). This suggests that plate tectonics in the Archaean time probably operated in a different pattern compared to the modern subduction (Cawood et al., 2006).

Van Hunen and Van den Berg, (2008) tested the role the T_p plays in altering the patterns of subduction using numerical modelling (Figure 1.13). With an elevated T_p , slab detachment occurs very fast at a relatively shallow depth. After that, no slab-pull exists anymore to drive the process of subduction, and subduction ceases completely.

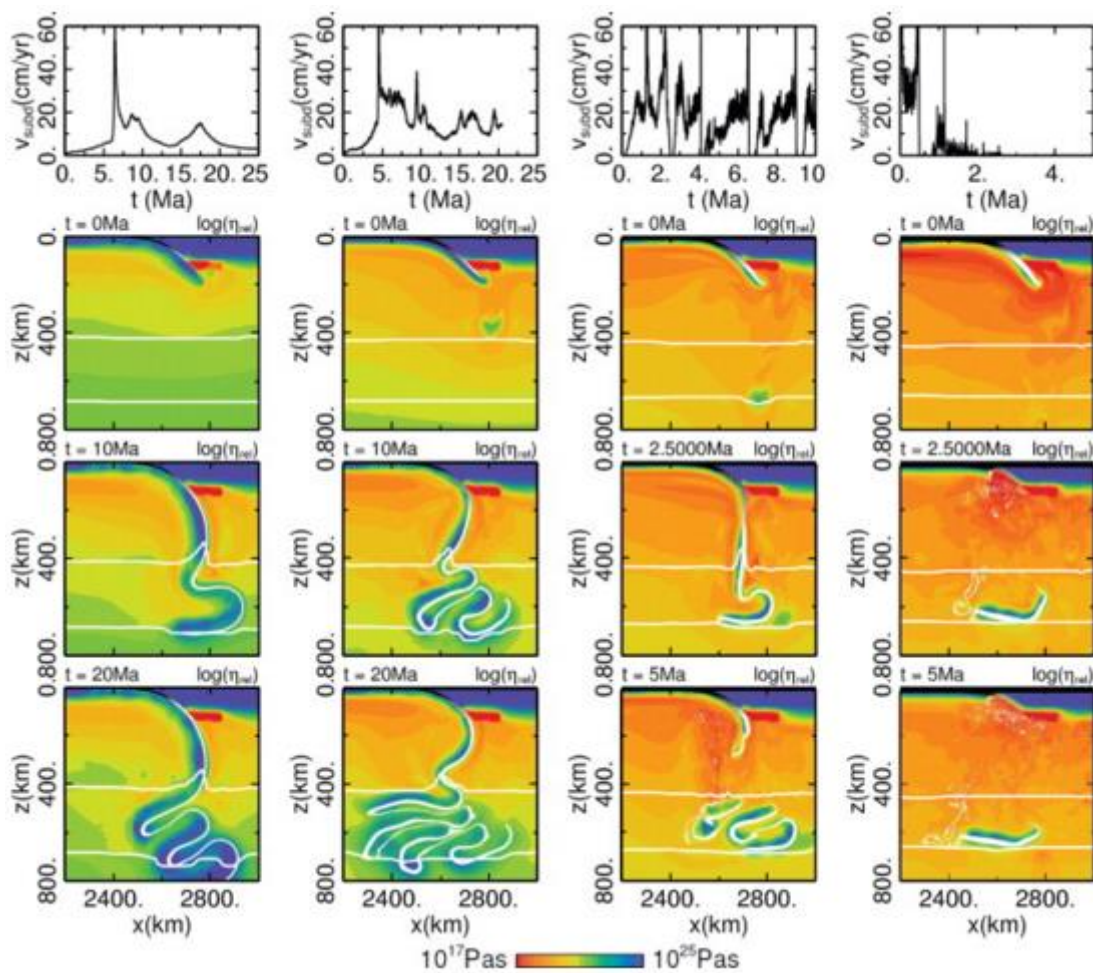


Figure 1.13: Subduction modes controlled by the different T_p (Source: Van Hunen and Van den Berg, 2008). The first column shows the behaviour of subduction using the T_p of 1350 °C, which is approximate to the value at the present day. The second, third and fourth columns exhibit different modes of subduction when the increased T_p

1. Rheology and deformation mechanisms of the lithosphere

difference (ΔT_p) is respectively set to 100 K, 200 K and 300 K compared to the present value of 1350 °C ($\Delta T_p = T - T_p$).

The T_p is also thought to play a dominant role in the evolutionary thickness of the lithosphere through geological time (Boyd, 1989; Anderson, 1995; Artemieva and Mooney, 2001), as the effective viscosity of rocks decreases with increasing temperature (burial depth). High geothermal gradient and melting degree (Foley et al., 2003) lead to the formation of thicker and smaller (Martin, 1986) portions of lithosphere and crust.

The Archaean and early Proterozoic lithosphere are generally divided into thinner and thicker groups (Doin et al., 1997; Artemieva and Mooney, 2001). The cratons of the thinner group are generally found in South Africa, Western Australia, South America, India and part of Canadian Shield (Mackenzie and Canil, 1999; Rudnick and Nyblade, 1999; Jaupart et al., 1998), ranging between 200-220 km depth. The cratons of the thicker group are mostly found in Baltic Shield, Siberian Platform and West Africa (Artemieva and Mooney, 2001).

The thickness distribution of the lithosphere probably could reflect how the continental roots were affected by the Archaean superplumes (Artemieva and Mooney, 2001) or clusters of regional plumes heads. The maximum lithospheric thickness in the WAC is estimated between 300 and 350 km in the Archaean time and decreases to 200±50 km in the early Proterozoic lithosphere (Clouser and Langston, 1990; Qiu et al., 1996; Artemieva and Mooney, 2001). This decrease probably results from delamination processes (Eglinger et al., 2015).

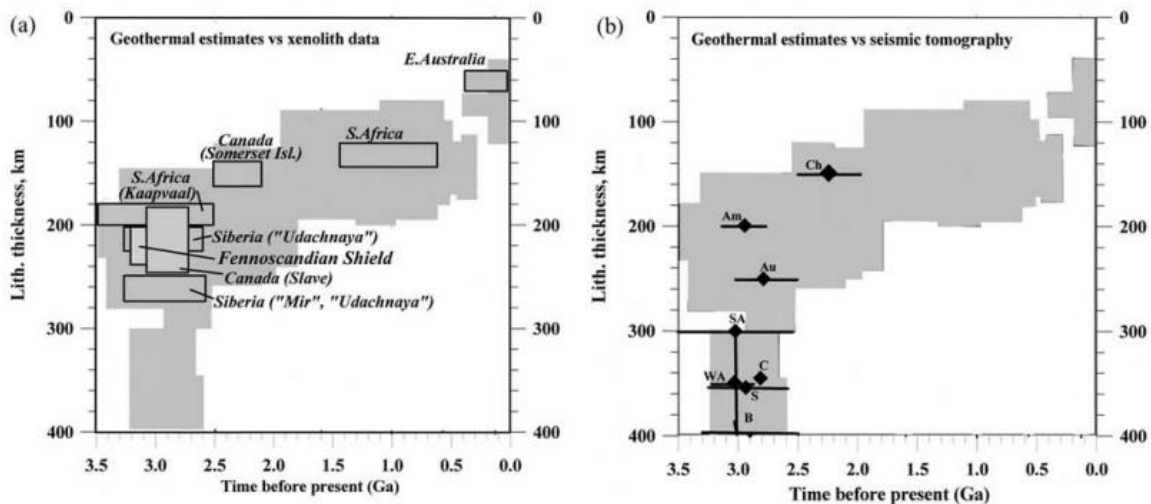


Figure 1.14: Thermal lithosphere thickness estimated by using xenolith and seismic tomography data (Source: Artemieva and Mooney, 2001). The shaded areas show the thickness of the lithosphere versus time estimated by geothermal modelling. The boxes are estimated by using xenolith data, for south Africa from Boyd et al. (1985); Boyd and Gurney, (1986); Ryan et al. (1996); for the Canadian shield from Mackenzie and Canil, (1997); Rudnick,

(1998); Schmidberger and Francis, (1999); Kjarsgaard and Peterson, (1992); and Kopylova et al. (1999); for the Siberian shield from Boyd et al. (1985, 1995); Boyd, (1994); Griffin et al. (1993, 1996); Pokhilenko et al. (1993); and Ryan et al. (1996); for eastern Australia from Griffin et al. (1987); and O'Reilly and Griffin, (1985); and for the Baltic Shield from Kukkonen and Peltonen, (1999). The horizontal and vertical sizes of the boxes indicates the variations of age (Goodwin, 1996) and thickness, respectively. In the right panel, diamonds and lines are collected from seismic tomography data from Grand, (1994) and Zhang and Tanimoto, (1993). Am=Amazonian craton; Au=Western Australian craton, B=Baltic shield; C=Canadian Shield; Ch = Cathaysian craton; S = Siberian craton; SA=South African craton; WA= West African Craton.

1.5 The *Underworld* Numerical code

1.5.1 Overview

The Underworld code (Moresi et al., 2003, 2007) is a 3D parallel geodynamic modelling platform capable of viscous/viscoplastic rheologies. The code uses a hybrid Lagrangian Particle-in-Cell (*PIC*) finite element scheme and is written in C in an object oriented style. It aims to solve thermal and thermo-mechanical models with the involvement of tectonic processes, such as the processes of slab subduction, mantle convection and lithospheric deformation over large time and spatial scales.

Hierarchically, *Underworld* is a program that sits at the top of other programs (Figure 1.15), including Particle-in-Cellerator, StGDomian, StGFEM, gLucifer and StGermain components. Each of the programs relies on the previous components, as an extension of scientific or/and computational capacity of the underlying programs.

The StGermain component sits on the base level of the hierarchical structures, which is used to manage the CPU parallel programming architecture, memory and object oriented frameworks. Depending on this component, models files can be transferred to multiple cores for further uses by higher end users (cluster machines).

The StGDomian component is used to define the geometry and meshing and some basic mathematical formulas. The associations between a mesh and the storage of a value on that mesh (field) are also coupled by this component.

The StGFEM component is one that allows users to simply compose finite element problems from a series of linear equations. The PETScs package is well leveraged against for vector operation, parallel matrix, equation solver and other linear algebra tools (Moresi et al., 2007).

The Particle-in-Cellerator component uses a Particle-in-Cell approach, with the collection of particles and associated properties. It handles the problems of locating to which cell a given particle belongs to

and population control (as particles may be advected in and out of the modelling domain), particularly across multiple processors.

The gLucifer component is a visualization framework, which can render and explore the results immediately as the simulation processes, which allows users to specify visualization elements in the XML script that defines the model.

The *Underworld* component is the top layer of the hierarchical structure, which is used to handle the models governing various geophysical rheologies.

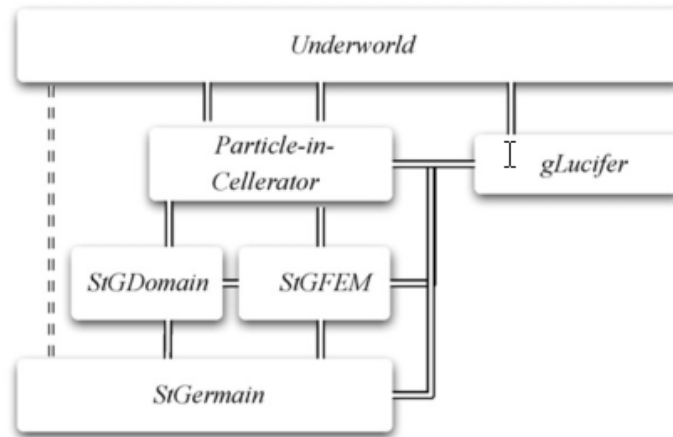


Figure 1.15: *Underworld* hierarchical structure, including the *Underworld* (Source: Moresi et al., 2007), Particle-in-Cellerator, StGDomian, StGFEM, gLucifer and StGermain components.

1.5.2 General equations

Underworld solves the Stokes flow problem and the energy (advection/diffusion) equations. For an incompressible material, the governing equations of momentum (1.14), mass (1.15) and energy equations (1.16) are expressed as follows, the equations can be customized for modelling complex geophysical behaviours. More details on the method description and other computational equations can be found in Moresi et al. (2003, 2007).

$$\frac{\partial \sigma_{ij}}{\partial x_j} = \rho_{eff} \cdot g_i \quad (1.14)$$

$$\nabla \cdot u = 0 \quad (1.15)$$

$$\frac{\partial T}{\partial t} + (u \cdot \nabla)T = \frac{\partial}{\partial x_i} \left(\frac{k_i \partial T}{\partial x_i} \right) + Q \quad (1.16)$$

where ρ_{eff} is the effective density, k_i is the thermal diffusion and Q is the radiogenic heat production ($Q = \rho H$, H is the radiogenic heat production per mass unit).

1.5.3 Performance

In simulations performed using the Particle-in-Cell method (*PIC*), the number of particles in each cell significantly influences the results. As an example, a simple 3D model consisting of two vertical faults is pre-explored. The number of particles in each cell is fixed, ranging between 10 and 50 at a gradient of 10. The modelling domain has a size of 200 km × 200 km × 50 km with free-slip boundary conditions shown in Figure 1.16.

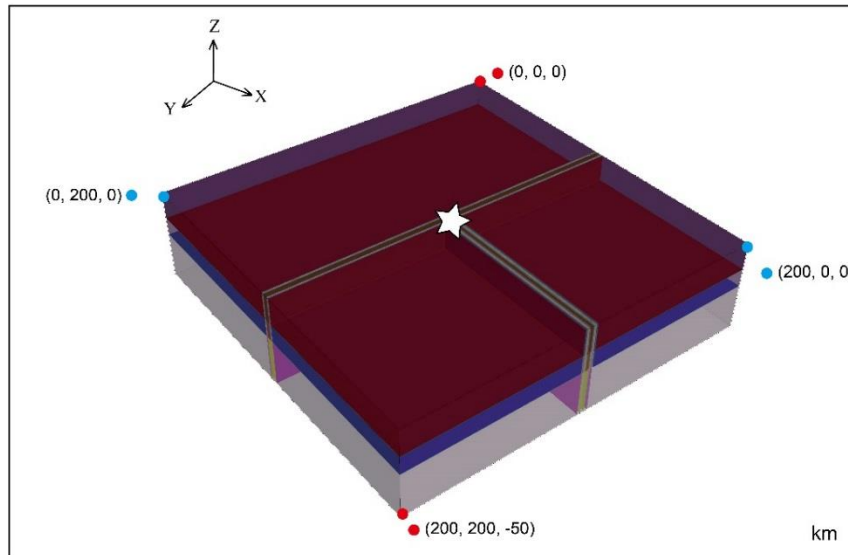


Figure 1.16: Modelling domain contains two vertical faults (purple plane). The space coordinates of the white star is (100 km, 100 km, -1 km). The performance of vertical velocity (white star) when employing different numbers of particles for each cell is explored and shown in Figure 1.17.

Figure 1.17 shows that the numerical fluctuation of vertical velocity at the point located at (100 km, 100 km, -1 km) decreases with increasing particles in each cell. The performance is satisfactory when employing 30-50 particles. Regarding the consumption of computing time when containing different particles (Figure. 1.18), the case with 10 particles in each cell yields a huge consumption. This indicates that the numerical fluctuation increases with decreasing particles. In the present thesis, 30 particles are placed in each cell for modelling as a compromise between performance and stability.

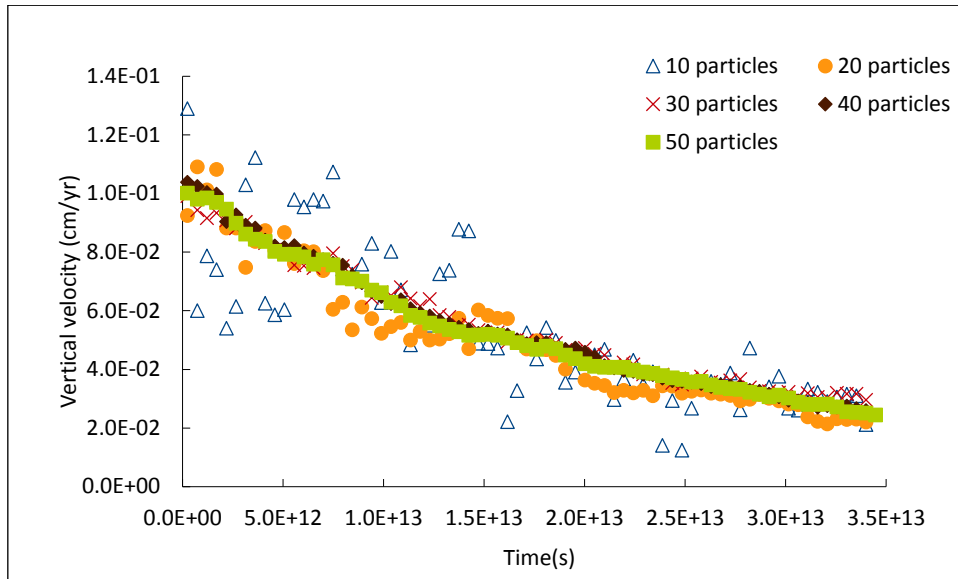


Figure 1.17: The performance of vertical velocity at the point of (100 km, 100 km, -1 km) when using different numbers of particles for each cell. The point is indicated by white star in Figure 1.13.

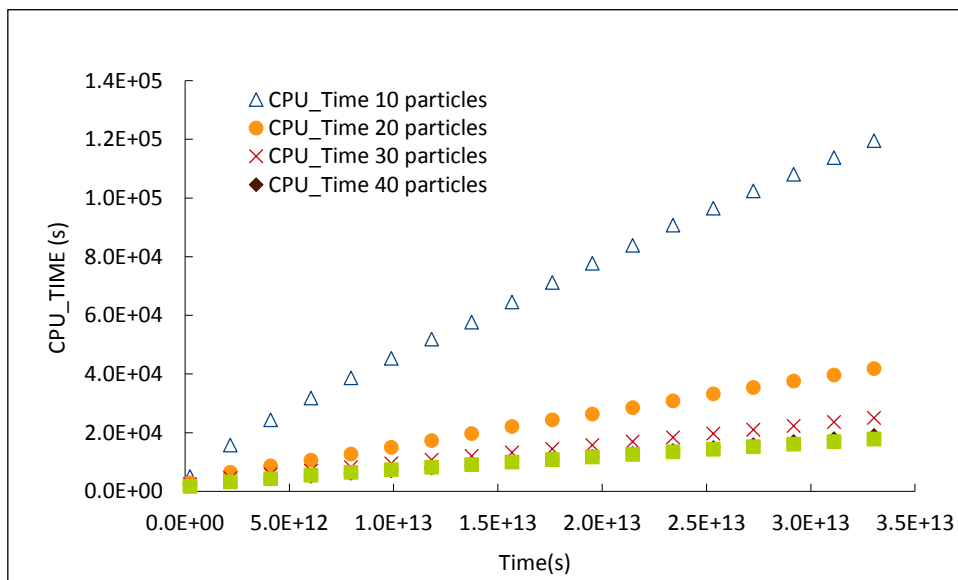


Figure 1.18: The consumption of computing time using different numbers of particles for each cell.

Regarding the computing time using 128 cores in parallel for the model (Figure 1.19), the computing time increases with increasing elements (resolution). Mesh sizes are divided by $72 \times 72 \times 36$ to $144 \times 144 \times 72$ elements. Computing time increases slowly and linearly. For mesh sizes divided by $192 \times 192 \times 96$, computing time is three time more expensive than the mesh size divided by $144 \times 144 \times 72$ is required. This is probably caused by requirement of more MPI buffers (Peter et al., 2011) and limit of data-transfer speeds between computer nodes (Ichimura et al., 2013).

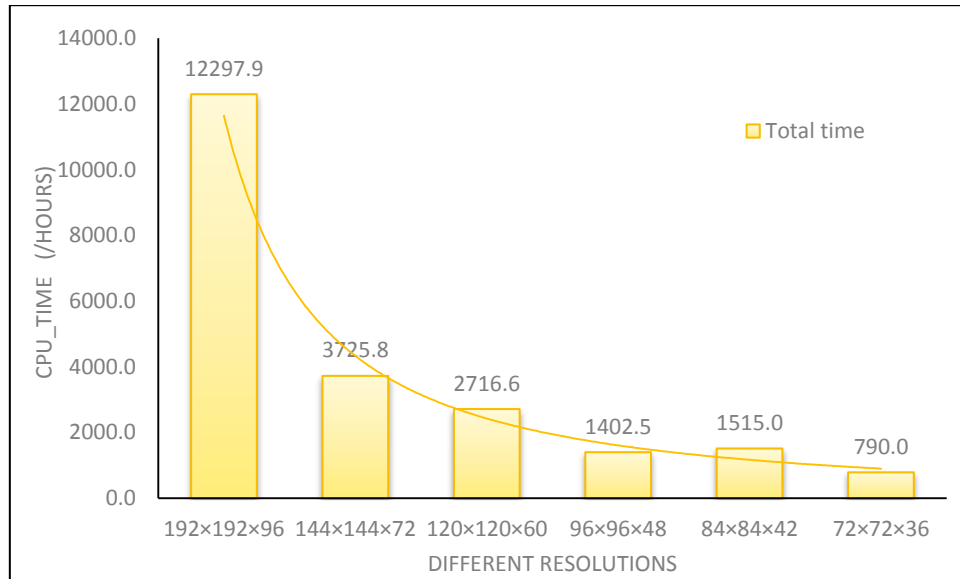


Figure 1.19: Computing time using different resolutions.

1.6 References

- Abbott, D., Burgess, L., Longhi, J., Smith, W. H., 1994. An empirical thermal history of the Earth's upper mantle. *Journal of Geophysical Research*, 99, 835-13.
- Abbott, D., Mooney, W., 1995. The structural and geochemical evolution of the continental crust: support for the oceanic plateau model of continental growth. *Reviews of Geophysics*, 33, 231-242.
- Anderson, D. L., 1995. Lithosphere, asthenosphere, and perisphere. *Reviews of Geophysics*, 33, 125-149.
- Artemieva, I. M., Mooney, W. D., 2001. Thermal thickness and evolution of Precambrian lithosphere: a global study. *Journal of Geophysical Research: Solid Earth (1978–2012)*, 106 (B8), 16387-16414.
- Arzi, A. A., 1978. Critical phenomena in the rheology of partially melted rocks. *Tectonophysics*, 44 (1), 173-184.
- Bercovici, D., Karato, S. I., 2003. Whole-mantle convection and the transition-zone water filter. *Nature*, 425 (6953), 39-44.
- Boyd, F. R., Gurney, J. J., Richardson, S. H., 1985. Evidence for a 150–200-km thick Archaean lithosphere from diamond inclusion thermobarometry. *Nature*, 315 (6018), 387-389.
- Boyd, F. R., Gurney, J. J., 1986. Diamonds and the African lithosphere. *Science*, 232 (4749), 472-477.

- Boyd, F. R., 1989. Compositional distinction between oceanic and cratonic lithosphere. *Earth and Planetary Science Letters*, 96, 15-26.
- Boyd, F. R., N. P. Pokhilenko, D. G. Pearson, N. V. Sobolev, Peridotite xenoliths from the Udachnaya kimberlite pipe, paper presented at 6th International Kimberlite Conference, Inst. of Geol and Geophys., Russ. Acad. of Sci., Novosibirsk, Russia, Aug. 1995.
- Brace, W. F., Kohlstedt, D. L., 1980. Limits on lithospheric stress imposed by laboratory experiments. *Journal of geophysical research*, 85 (B11), 6248-6252.
- Burg, J. P., Ford, M., 1997. Orogeny through time: an overview. Geological Society, London, Special Publications, 121, 1-17.
- Burov, E. B., 2011. Rheology and strength of the lithosphere. *Marine and Petroleum Geology*, 28 (8), 1402-1443.
- Bystricky, M., Mackwell, S., 2001. Creep of dry clinopyroxene aggregates. *Journal of Geophysical Research: Solid Earth (1978–2012)*, 106 (B7), 13443-13454.
- Cawood, P.A., Kroener, A., Pisarevsky, S., 2006. Precambrian plate tectonics: criteria and evidence. *GSA Today*, 16, 4–11.
- Chen, Y., Morgan, W. J., 1990. A nonlinear rheology model for mid-ocean ridge axis topography. *Journal of Geophysical Research: Solid Earth (1978–2012)*, 95 (B11), 17583-17604.
- Christensen, U. R., 1996. The influence of trench migration on slab penetration into the lower mantle. *Earth and Planetary Science Letters*, 140 (1), 27-39.
- Clauser, C., Huenges, E., 1995. Thermal conductivity of rocks and minerals. *Rock physics & phase relations: A handbook of physical constants*, 105-126.
- Clouser, R. H. Langston, C. A., 1990. Upper mantle structure of southern Africa from P waves. *Journal of Geophysical Research: Solid Earth (1978–2012)* 95, B11, 17403-17415.
- Condie, K. C., 1981. *Archaean greenstone belts*. Elsevier.
- Condie, K. C., 1986. Origin and early growth rate of continents. *Precambrian Research*, 32, 261-278.
- Condie, K. C., 2005. *Earth as an evolving planetary system*. Academic Press.
- Creager, K. C., Jordan, T. H., 1984. Slab penetration into the lower mantle. *Journal of Geophysical Research: Solid Earth (1978–2012)*, 89 (B5), 3031-3049.
- Cserepes, L., Rabinowicz, M., 1985. Gravity and convection in a two-layer mantle. *Earth and planetary science letters*, 76 (1), 193-207.

- Davies, G. F., 1977. Whole-mantle convection and plate tectonics. *Geophysical Journal International*, 49 (2), 459-486.
- Davies, J. H., Davies, D. R., 2010. Earth's surface heat flux. *Solid Earth*, 1 (1), 5-24.
- De Beer, J. H., Meyer, R., 1984. Geophysical characteristics of the Namaqua-Natal Belt and its boundaries, South Africa. *Journal of geodynamics*, 1, 473-494.
- De Wijkerslooth de Weerdesteyn, 1934. *Bau und Entwicklung des Apennins besonders der Gebirge Toscanas*, Geologisch Institut, Amsterdam (1934) 426 p.
- Dewey, J. F., Burke, K. C., 1973. Tibetan, Variscan, and Precambrian basement reactivation: products of continental collision. *The Journal of Geology*, 683-692.
- Dimanov, A., Dresen, G., 2005. Rheology of synthetic anorthite-diopside aggregates: Implications for ductile shear zones. *Journal of Geophysical Research: Solid Earth (1978–2012)*, 110(B7).
- Dioh, E., Béziat, D., Debat, P., Grégoire, M., Ngom, P.M., 2006. Diversity of the Palaeoproterozoic granitoids of the Kédougou inlier (eastern Sénégal): Petrographical and geochemical constraints. *Journal of African Earth Science*, 44, 351–371.
- Drucker, D. C. and Prager, W., 1952. Soil mechanics and plastic analysis for limit design. *Quarterly of Applied Mathematics*, 10 (2), pp. 157–165.
- Durrheim, R. J., Mooney, W. D., 1994. Evolution of the Precambrian lithosphere: seismological and geochemical constraints. *Journal of Geophysical Research: Solid Earth (1978–2012)*, 99 (B8), 15359-15374.
- Eglinger, A., Thébaud, N., Davis, J., Miller, J., Zeh, A., McCuaig, C., & Belousova, E. (2015, August). High-K to shoshonitic magmatism across the northern Archean Kéména Man margin (Guinea): implications for the Eburnean orogenic gold mineralizations. In SGA meeting Nancy, August 2015.
- Fleitout, L., Froidevaux, C., 1982. Tectonics and topography for a lithosphere containing density heterogeneities. *Tectonics*, 1 (1), 21-56.
- Foley, S. F., Buhre, S., Jacob, D. E., 2003. Evolution of the Archaean crust by delamination and shallow subduction. *Nature*, 421, 249-252.
- Fossen, H., 2010. *Structural geology*. Cambridge University Press, P22.
- Gabler, R., Petersen, J., Trapasso, L., Sack, D., 2008. *Physical geography*. Cengage Learning, p394.

- Ganne, J., Gerbault, M., Block, S., 2014. Thermo-mechanical modeling of lower crust exhumation— Constraints from the metamorphic record of the Palaeoproterozoic Eburnean orogeny, West African Craton. *Precambrian Research*, 243, 88-109.
- Gerbault, M., 1999. Modélisation numérique de la naissance des déformations localisées: exemple du flambage lithosphérique (Doctoral dissertation, Université Montpellier II-Sciences et Techniques du Languedoc).
- Goes, S., Capitanio, F. A., Morra, G., 2008. Evidence of lower-mantle slab penetration phases in plate motions. *Nature*, 451 (7181), 981-984.
- Goetze, C., Brace, W. F., 1972. Laboratory observations of high-temperature rheology of rocks. *Tectonophysics*, 13 (1), 583-600.
- Goodwin, A. M. 1996. Principles of Precambrian geology. Academic Press.
- Grand, S. P. 1994. Mantle shear structure beneath the Americas and surrounding oceans. *Journal of Geophysical Research: Solid Earth (1978–2012)*, 99 (B6), 11591-11621.
- Grand, S. P., van der Hilst, R. D., Widiyantoro, S., 1997. High resolution global tomography: a snapshot of convection in the Earth. *Geological Society of America Today*, 7 (4).
- Griffin, W. L., Sutherland, F. L., Hollis, J. D. 1987. Geothermal profile and crust-mantle transition beneath east-central Queensland: volcanology, xenolith petrology and seismic data. *Journal of Volcanology and Geothermal Research*, 31 (3), 177-203.
- Hargraves, R. B., 1986. Faster spreading or greater ridge length in the Archaean? *Geology* 14, 750-752.
- Herzberg, C., Gazel, E., 2009. Petrological evidence for secular cooling in mantle plumes. *Nature*, 458, 619–622.
- Herzberg, C., Condie, K., Korenaga, J., 2010. Thermal history of the Earth and its petrological expression. *Earth Planetary Science Letters*, 292, 79–88.
- Hirth, G., Kohlstedt, D. L., 1996. Water in the oceanic upper mantle: implications for rheology, melt extraction and the evolution of the lithosphere. *Earth and Planetary Science Letters*, 144 (1), 93-108.
- Hirth, G., 2002. Laboratory constraints on the rheology of the upper mantle. *Reviews in mineralogy and geochemistry*, 51 (1), 97-120.
- Hirth, G., Kohlstedt, D., 2003. Rheology of the upper mantle and the mantle wedge: A view from the experimentalists. *Inside the subduction Factory*, 83-105.

- Hoffman, P. F., 1989. Precambrian geology and tectonic history of North America. The geology of North America—an overview, 447-512.
- Ichimura, T., Agata, R., Hori, T., Hirahara, K., Hori, M., 2013. Fast numerical simulation of crustal deformation using a three-dimensional high-fidelity model. *Geophysical Journal International*, 195 (3), 1730-1744.
- Jaupart, C., Mareschal, J. C., Guillou-Frottier, L., Davaille, A., 1998. Heat flow and thickness of the lithosphere in the Canadian Shield. *Journal of Geophysical Research: Solid Earth (1978–2012)*, 103 (B7), 15269-15286.
- Kirby, S. H., Kronenberg, A. K., 1983. Rheology of the lithosphere. *Reviews of Geophysics*, 21 (6), 1458-1487.
- Kjarsgaard, B. A., Peterson, T. D., 1992. Kimberlite-derived ultramafic xenoliths from the diamond stability field: a new Cretaceous geotherm for Somerset Island, Northwest Territories. *Current Research, Part B*, 1-6.
- Kohlstedt, D. L., Evans, B., Mackwell, S. J., 1995. Strength of the lithosphere: constraints imposed by laboratory experiments. *Journal of geophysical research-all series-100*, 17-587.
- Kopylova, M. G., Russell, J. K., Cookenboo, H., 1999. Petrology of peridotite and pyroxenite xenoliths from the Jericho kimberlite: implications for the thermal state of the mantle beneath the Slave craton, northern Canada. *Journal of Petrology*, 40 (1), 79-104.
- Korenaga, J., 2006. Archaean geodynamics and the thermal evolution of Earth. *Geophysical Monograph-American Geophysical Union*, 164, 7-32.
- Korenaga, J., 2008a. Plate tectonics, flood basalts, and the evolution of Earth's oceans. *Terra Nova*, 20, 419–439.
- Korenaga, J., 2008b. Urey ratio and the structure and evolution of Earth's mantle. *Reviews of Geophysics*, 46 (2).
- Kukkonen, I. T., Peltonen, P., 1999. Xenolith-controlled geotherm for the central Fennoscandian Shield: implications for lithosphere–asthenosphere relations. *Tectonophysics*, 304 (4), 301-315.
- Mackenzie, J. M., and D. Canil., 1997, Thermal state of the lower crust and upper mantle of the Archaean Slave Province, NWT, Canada: A xenolith study, paper presented at MIT-Harvard Workshop on Continental Roots, Harvard Univ., Cambridge, Mass., Oct. 1997
- Maluski, H., Matte, P., 1984. Ages of alpine tectonometamorphic events in the northwestern Himalaya (northern Pakistan) by $^{39}\text{Ar}/^{40}\text{Ar}$ method. *Tectonics*, 3, 1–18.

- Martin, H., 1986. Effect of steeper Archean geothermal gradient on geochemistry of subduction–zone magmas. *Geology*, 14, 753–756.
- Maruyama, S., Liou, J.G., Terabayashi, M., 1996. Blueschists and Eclogites of the World and Their Exhumation. *International Geological Review*, 38, 485–594.
- Mckenzie, D., Jackson, J., Priestley, K., 2005. Thermal structure of oceanic and continental lithosphere. *Earth and Planetary Science Letters*, 233, 337–349.
- Meyers, M. A., Chawla, K. K., 2009. *Mechanical behaviour of materials*. Cambridge University Press, 71–160.
- Montési, L. G., Hirth, G., 2003. Grain size evolution and the rheology of ductile shear zones: from laboratory experiments to postseismic creep. *Earth and Planetary Science Letters*, 211 (1), 97–110.
- Moresi, L., Dufour, F., Mühlhaus, H. B., 2003. A Lagrangian integration point finite element method for large deformation modeling of viscoelastic geomaterials. *Journal of Computational Physics*, 184, 476–497.
- Moresi, L., Quenette, S., Lemiale, V., Meriaux, C., Appelbe, B., Mühlhaus, H., 2007. Computational approaches to studying non–linear dynamics of the crust and mantle. *Physics of the Earth and Planetary Interior*, 163, 69–82.
- Okay, A. I., 1989. Alpine–Himalayan blueschists. *Annual Review of Earth and Planetary Sciences*, 17, 55–87.
- Olson, P., 1984. An experimental approach to thermal convection in a two-layered mantle. *Journal of Geophysical Research: Solid Earth (1978–2012)*, 89 (B13), 11293–11301.
- Perry, H. K. C., Mareschal, J. C., Jaupart, C., 2006. Variations of strength and localized deformation in cratons: the 1.9 Ga Kapuskasing uplift, Superior Province, Canada. *Earth and Planetary Science Letters*, 249, 216–228.
- Peter, D., Komatitsch, D., Luo, Y., Martin, R., Le Goff, N., Casarotti, E., Le Loher, P., Magnoni, F., Liu, Q., Blitz, C. and Nissen-Meyer, T., 2011. Forward and adjoint simulations of seismic wave propagation on fully unstructured hexahedral meshes. *Geophysical Journal International*, 186 (2), 721–739.
- Philpotts, A. R., Carroll, M., 1996. Physical properties of partly melted tholeiitic basalt. *Geology*, 24 (11), 1029–1032.

- Polet, J., Anderson, D. L., 1995. Depth extent of cratons as inferred from tomographic studies. *Geology*, 23, 205-208.
- Prelević, D., Jacob, D. E., Foley, S. F., 2013. Recycling plus: a new recipe for the formation of Alpine–Himalayan orogenic mantle lithosphere. *Earth and Planetary Science Letter*, 362, 187–197.
- Qiu, X., Priestley, K., McKenzie, D., 1996. Average lithospheric structure of southern Africa. *Geophysical Journal International*, 127, 563-581.
- Renner, J., Evans, B., Hirth, G., 2000. On the rheologically critical melt fraction. *Earth and Planetary Science Letters*, 181 (4), 585-594.
- Rey, P., Vanderhaeghe, O., Teyssier, C., 2001. Gravitational collapse of the continental crust: definition, regimes and modes. *Tectonophysics*, 342 (3), 435-449.
- Roscoe, R., 1952. The viscosity of suspensions of rigid spheres. *British Journal of Applied Physics*, 3 (8), 267.
- Ross, G. M., Eaton, D. W., Boerner, D. E., Miles, W., 2000. Tectonic entrapment and its role in the evolution of continental lithosphere: an example from the Precambrian of western Canada. *Tectonics*, 19, 116-134.
- Rudnick, R. L., McDonough, W. F., O'Connell, R. J., 1998. Thermal structure, thickness and composition of continental lithosphere. *Chemical Geology*, 145 (3), 395-411.
- Rudnick, R. L., Nyblade, A. A., 1999. The thickness and heat production of Archaean lithosphere: constraints from xenolith thermobarometry and surface heat flow. *Mantle petrology: Field observations and high pressure experimentation: A tribute to Francis R. (Joe) Boyd*, 6, 3-12.
- Rutter, E. H., Neumann, D. H. K., 1995. Experimental deformation of partially molten Westerly granite under fluid-absent conditions, with implications for the extraction of granitic magmas. *Journal of Geophysical Research: Solid Earth (1978–2012)*, 100 (B8), 15697-15715.
- Rutter, E. H., Brodie, K. H., 2004a. Experimental grain size-sensitive flow of hot-pressed Brazilian quartz aggregates. *Journal of Structural Geology*, 26 (11), 2011-2023.
- Rutter, E. H., Brodie, K. H., 2004b. Experimental intracrystalline plastic flow in hot-pressed synthetic quartzite prepared from Brazilian quartz crystals. *Journal of Structural Geology*, 26 (2), 259-270.
- Ryan, C. G., Griffin, W. L., Pearson, N. J., 1996. Garnet geotherms: Pressure-temperature data from Cr-pyrope garnet xenocrysts in volcanic rocks. *Journal of Geophysical Research: Solid Earth (1978–2012)*, 101 (B3), 5611-5625.

- Rybacki, E., Gottschalk, M., Wirth, R., Dresen, G., 2006. Influence of water fugacity and activation volume on the flow properties of fine-grained anorthite aggregates. *Journal of Geophysical Research: Solid Earth* (1978–2012), 111 (B3).
- Schmidberger, S. S., Francis, D., 1999. Nature of the mantle roots beneath the North American craton: mantle xenolith evidence from Somerset Island kimberlites. *Lithos*, 48 (1), 195-216.
- Shirey, S. B., Richardson, S. H., 2011. Start of the Wilson cycle at 3 Ga shown by diamonds from subcontinental mantle. *Science*, 333 (6041), 434-436.
- Sleep, N. H., Windley, B. F., 1982. Archaean plate tectonics: constraints and inferences. *The Journal of Geology*, 90, 363-379.
- Stein, M., Hofmann, A. W., 1994. Mantle plumes and episodic crustal growth. *Nature*, 372 (6501), 63-68.
- Steinberger, B., 2000. Slabs in the lower mantle—results of dynamic modelling compared with tomographic images and the geoid. *Physics of the Earth and Planetary Interiors*, 118 (3), 241-257.
- Tackley, P. J., 2000. Mantle convection and plate tectonics: Toward an integrated physical and chemical theory. *Science*, 288 (5473), 2002-2007.
- Treagus, S. H., Sokoutis, D., 1992. Laboratory modelling of strain variation across rheological boundaries. *Journal of Structural Geology*, 14 (4), 405-424.
- Van der Hilst, R. D., Widiyantoro, S., Engdahl, E. R., 1997. Evidence for deep mantle circulation from global tomography. *Nature*, 386, 578-584.
- Van der Meer, D. G., Spakman, W., van Hinsbergen, D. J., Amaru, M. L., Torsvik, T. H., 2010. Towards absolute plate motions constrained by lower-mantle slab remnants. *Nature Geoscience*, 3 (1), 36-40.
- Van der Molen, I., Paterson, M. S., 1979. Experimental deformation of partially-melted granite. *Contributions to Mineralogy and Petrology*, 70 (3), 299-318.
- Van Hunen, J., Van den Berg, A. P., 2008. Plate tectonics on the early Earth: limitations imposed by strength and buoyancy of subducted lithosphere. *Lithos*, 103 (1), 217-235.
- Vanderhaeghe, O., 2001. Melt segregation, pervasive melt migration and magma mobility in the continental crust: the structural record from pores to orogens. *Physics and Chemistry of the Earth, Part A: Solid Earth and Geodesy*, 26 (4), 213-223.

- Vanderhaeghe, O., Teyssier, C., 2001. Partial melting and flow of orogens. *Tectonophysics*, 342 (3), 451-472.
- Vincent, J., 2012. *Structural biomaterials*. Princeton University Press, P13.
- Willett, S., Beaumont, C., Fullsack, P., 1993. Mechanical model for the tectonics of doubly vergent compressional orogens. *Geology*, 21, 371-374.
- Y O'Reilly, S., Griffin, W. L., 1985. A xenolith-derived geotherm for southeastern Australia and its geophysical implications. *Tectonophysics*, 111, 41-63.
- Zhang, Y. S., Tanimoto, T., 1993. High-resolution global upper mantle structure and plate tectonics. *Journal of Geophysical Research: Solid Earth (1978–2012)*, 98 (B6), 9793-9823.
- Zhong, J. Q., Zhang, J., 2005. Thermal convection with a freely moving top boundary. *Physics of Fluids (1994-present)*, 17 (11), 115105.

Chapter 2

Geological settings of the study areas

Introduction

This chapter presents a summary of geological background for the study areas: the WAC and the Alpine Fault zones. With respect to the WAC, a general overview of the geological framework together with several controversial topics covering geodynamic settings, deformation phases and different tectonic models will be introduced.

As an extension for studying the role pre-existing faults play in influencing the process of localization of deformation, this thesis chapter also investigates the evolution of the Alpine Fault zones in the South Island of New Zealand during the Oligocene-Miocene times. Firstly, the geodynamic evolution during the formation of the Alpine Fault since the Cretaceous times is presented. Subsequently, a geological summary of the South Island of New Zealand is introduced. Finally, two selected topics concerning the Alpine Fault zones in the South Island are presented: (1) the structural expressions in the crust and the upper mantle, (2) the evolution of shear localization.

2.1 Summary of geological framework of the WAC

The WAC consists of two major Archaean to Paleoproterozoic blocks (Figure 2.1), known as the Réguibat Shield to the north, the Leo-Man Shield to the south. The central cratonic depression of the WAC is covered by the Taoudeni basin which divides the WAC into the aforementioned shields. The basin is composed of meso-Proterozoic to early Palaeozoic sediments (Bessoles, 1977; Rooney et al., 2010). The Tindouf Basin outcrops on the northern edge of the Réguibat shield.

The Pan-African orogenic belts surround the WAC on its eastern and western sides. The western margin is composed of the Mauritanides, Bassarides and Rokelides. The Mauritanides and the Bassarides have the same age (660 Ma) but are largely reworked by the Hercynian orogeny (Villeneuve and Dallmeyer, 1987). The 1500 km northern external nappes of the Mauritanides (from Senegal to Morocco) thrust N-S over the Taoudeni Basin (Bassot, 1966; Villeneuve, 2005).

The Leo-Man Shield is characterized by extensive volcano-sedimentary and plutonic belts disposed roughly parallel to each other (N-S to NE-SW trending). This feature is not observed in the Réguibat shield, perhaps resulting from different geodynamic settings. In summary:

- In the Réguibat Shield, two main orogenic stages took place, thus known as a mature island-arc setting at about 2.21-2.18 Ga and followed by an active-margin magmatic setting at around 2.09 Ga (Peucat et al., 2005).
- In the Leo-Man Shield, geodynamic setting is thought to be associated with an immature volcanic arc (Sylvester and Attoh, 1992; Dampare et al., 2008) or an oceanic plateau

2. Geological settings of the study areas

(Abouchami et al., 1990; Boher et al., 1992), this debate will be discussed in detail in section 2.1.2.

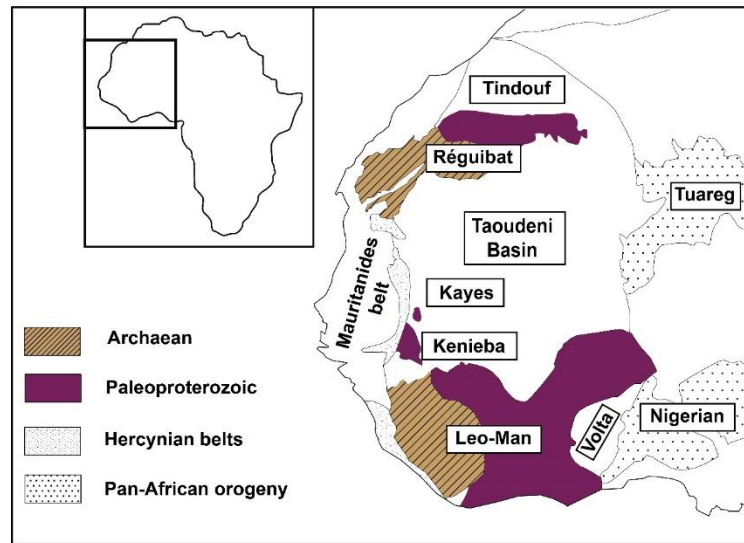


Figure 2.1: Geological sketch map of the WAC, modified after Peucat et al. (2005), showing the various cratonic Archaean and Paleoproterozoic nuclei of the Réguibat and Leo-Man Shields. The late Proterozoic and Paleozoic basins (Taoudeni and Tindouf) and the Pan-African belts flank the craton.

2.1.1 Leo-Man Shield

The Leo-Man Shield is composed of an Archaean and Paleoproterozoic nuclei known as the Kénema-Man domain (KMD) and the Baoulé-Mossi domain (BMD), respectively (Figure 2.2). The two domains are separated each other by a cratonic fault called the Sassandra Fault (SF). The KMD is composed of the oldest rocks in the WAC, ranging between 3540 Ma (Egal et al., 2002; Rollinson, 2016) and 2500 Ma.

The BMD is located to the north and east of the KMD, characterized by extensively distributed N-S to NE-SW trending greenstone belts intruded and separated by several generations of granitoids. The earliest granitoids intrusions contemporaneous with the Birimian mafic volcanic activities took place between 2195 and 2172 Ma (Hirdes et al., 1992; Siegfried et al., 2009; Baratoux et al., 2011; Sakyi et al., 2014). The major magmatic pulses intruded the whole volcanic complexes later, ranging from ~2153 and 2068 Ma (U-Pb and Pb-Pb zircon ages, Hirdes et al., 1996; Egal et al., 2002; Gasquet et al., 2003).

The Eburnean orogeny operated from ~ 2130 (or 2160, Baratoux et al., 2011) to 1980 Ma in the BMD (Davis et al., 1994; Feybesse et al., 2006). In summary, the first Eburnean deformation phase (D1) took place between ca. ~2.20 and 2.10 Ga. This deformation phase was associated with crustal thickening (Allibone et al., 2002; Ledru et al., 1991; Vidal et al., 1996), operated under an E-W to WNW-oriented

2. Geological settings of the study areas

compression (Baratoux, et al., 2011). The D2 tectono-metamorphic deformational phase was responsible for producing most of the large structures observed in the Birimian Province.

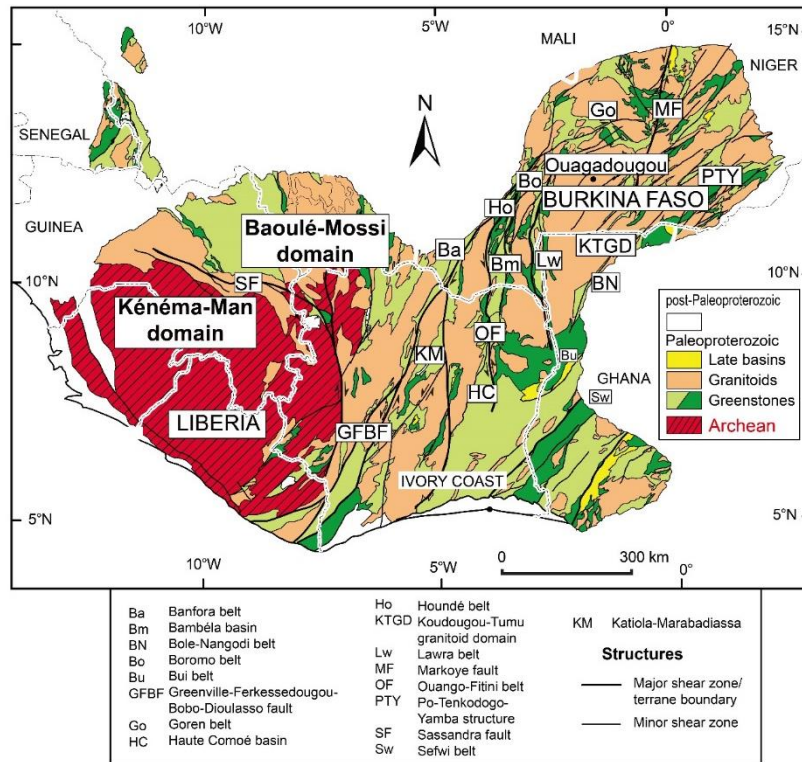


Figure 2.2: Main geological units in the Leo-Man Shield, modified after Milési et al. (2004) and Block et al. (2015).

2.1.1.1 Geological summary of South-Western Burkina Faso

The South-Western part of Burkina Faso consists of a series of sub-parallel N-S to NNE trending Paleoproterozoic greenstone belts. From east to west is the Boromo-Lawra, Houndé-Ouango-Fitini and Banfora greenstone belts (Figure 2.2). These belts are separated and intruded by extensive granitoids provinces (more details on the radiometric ages can be found in Baratoux et al., 2011). The oldest intrusions took place between ca. 2.53 and 2.13 Ga (Hirdes et al., 1996; Koté et al., 2003), and younger intrusions emplaced around ca. 2.12-2.10 Ga (Hirdes et al., 1996; Le Métour et al., 2003). The thickness of volcano-sediments ranges between 5 and 20 km depending on the situations of folding and buckling (Baratoux et al., 2011).

The Banfora greenstone belt extends down to the Greenville-Ferkessedougou-Bobo-Dioulasso Fault (GFBF) zones and the Katiola–Marabadiassa (KM) area. The eastern margin of the Banfora greenstone belt consists of basalt, andesite pyroclastic flow and rhyolite, while the western margin is only composed of volcano-sedimentary rocks (Figure 2.2). The GFBF structures characterize the dominant structures in the region, which have been massively intruded by several episodes of granitoids. In the

KM area, the belts have been intruded by the main pulses of granitoids between 2123±3 and 2097±3 Ma (Doumbia et al., 1998).

The Houndé-Ouango-Fitini (HOF) greenstone belt is located in between the Boromo-Lawra and Banfora-KM-GFBF greenstone belts, which is further divided into eastern and western halves. The eastern portion of the belt is mainly composed of andesite pyroclastic flow and volcano-sediments in the centre (Baratoux et al., 2011), and some rhyolites at the base. The western part of the belt extends down to Ivory Coast, known as Ouango-Fitini belt (Hirdes et al., 1996; Pouclet et al., 1996). It is predominantly composed of intermediate to acid calc-alkaline volcanic series including voluminous basaltic andesites and pyroclastic flows (Hirdes et al., 1996; Baratoux et al., 2011). The belts have been mainly intruded by several generations of granitoids between 2014±3 and 2152±2 Ma (Hirdes et al., 1996; Lüdtke et al., 1998). The eastern, northern and western margins of the belt consist of basalt (up to 6 km thick), with intercalated gabbros (Baratoux et al., 2011)

The Boromo greenstone belt dominantly consists of flysch-like metasediments, tuffs and epiclastic volcano-sediments with occasional intercalations of andesites and rhyolites (Baratoux et al., 2011). This belt extends down to Ghana without major interruptions, where it is named as the Lawra belt (Leube et al., 1990).

2.1.1.2 Geological summary of North-West Ghana

The North-West Ghana straddles the Upper West region, Upper East region and the Northern regions of Ghana and lies near the eastern margin of the Paleoproterozoic BMD of the WAC. The geology of North-Western Ghana are divided into various domains by Block et al. (2015). Thus known as the Wa-Lawra belt, the Koudougou-Tumu domain, the Bole-Bulenga domain, the Julie belt and the Bole-Nangodi belts (Figure 2.3).

The E-W oriented Julie belt is located in the central portion of NW Ghana (Figure 2.1). Bounded to the north of the Julie belt is the Koudougou-Tumu domain, to the south by the Bole-Bulenga domain and to the east by the Bole-Nangodi belts. Bounded to the west of the Koudougou-Tumu domain is the Wa-Lawra belt.

The Wa-Lawra belt is further divided into the eastern and western halves by the crustal scale Jirapa shear zone which exhibits sinistral characteristics (Figure 2.3). The eastern half is composed of mainly 2139±2 Ma metamorphosed sedimentary rocks (volcano-sediments, greywackes, shales) and early syn-tectonic 2212±1 (Sekyi et al., 2014) and 2153±4 Ma (Agyei Duodu et al., 2009) granitoids. These rocks have been intruded by the 2104±1 Ma late kinematic granitoids (Agyei Duodu, 2009; Baratoux et al., 2011; Block et al., 2015). The rocks in the eastern half have experienced up to green schist metamorphism (Block et al., 2015). The western half is composed of the 2187±3 Ma high grade

2. Geological settings of the study areas

gneisses and granitoids (Agyei Duodu et al., 2009). The Koudougou-Tumu domain is composed of the 2162±1 to 2134±1 Ma gneisses and gabbro, which has been intruded by the 2128 Ma late porphyritic granites (Agyei Duodu et al., 2009). The boundary between the Wa-Lawra belt and the Koudougou-Tumu domain is marked by the Jang fault (Block et al., 2015).

The Bole-Bulenga terrane is composed of high grade metamorphic rock termed as Buki gneisses by De Kock et al. (2011). According to Block et al. (2015), the Bole-Bulenga terrane is composed of paragneisses and metabasites usually migmatitic in nature. These rocks have been intruded by orthogneisses with crystallization ages between 2195 and 2135 Ma.

The Julie belt (Figure 2.3) is composed of basalts, silicic volcano-sediments and granitoids (Amponsah et al., 2015). Dating done on the silicic volcano-sediments shows that some of the rocks crystallized at 2129 ± 7 Ma (Block et al., 2015). This indicates that some parts of the belt formed at least at 2130 Ma. The foliation in the volcano-sediments and granitoids within this fault shows a stretching lineation plunging down-dip and towards higher grade rocks (Block et al., 2015).

Bounded to the south of the Bole-Bulenga terrane and east of the Julie belt is the NE-SW trending crustal scale Bole-Nangodi shear zones. The shear zones are composed of volcanoclastic rocks, greywackes, shales, granites, granitoids and gneisses with crystallization ages between 2196±1 and 2118±3 Ma (Agyei Duodu et al., 2009; De Kock et al., 2011).

Structurally, De Kock et al. (2011) proposed an initial short lived pre-Eburnean event which occurred between 2160 and 2150 Ma in NW Ghana. This deformational event was associated with plutonic emplacement and basin contraction. Two main deformation phases are thought to play a dominant role in the formation of the main structures in the Bole-Bulenga domain. The D1 stage was characterized by shortening and mostly marked by thrust faulting (Baratoux et al., 2011). The D2 stage was marked by N-S-directed extension characterized by extensional shear zones along the northern and southern margins of the Bole-Bulenga domain (Block et al., 2015).

Recent investigations performed by Block et al. (2015) in the North-Western part of Ghana highlighted the presence of large scale (> 50 km wide) migmatitic complexes in the Bole-Bulenga terrane formed at ca. 2.13 Ga. They are associated with medium-pressure amphibolite facies rocks that are very similar to those observed by Ganne et al. (2012) in the thermal aureoles of granitic plutons in Burkina Faso, Senegal and Niger. They reveal a clockwise P-T-t path, melting at pressure over 10.0 kbar, then followed by steep decompression and heating to peak temperature of 750 °C at 5-8 kbar.

2. Geological settings of the study areas

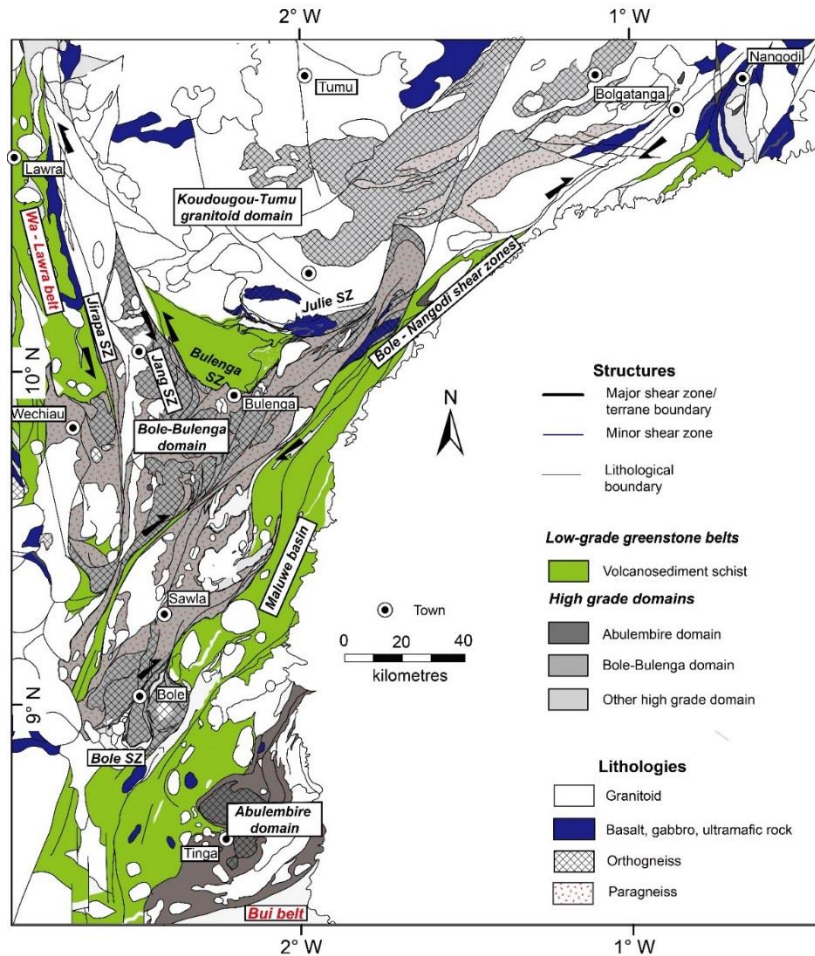


Figure 2.3: High grade Bole-Bulenga terrane, several dominant shear zones separated low grade greenstone belt (volcano-sediment) from high grade tectono-metamorphic terranes (after Block et al., 2015 and Feng et al., 2016)

2.1.2 Debates on the WAC

2.1.2.1 Geodynamic settings

Despite stimulating debates on the WAC in the last 30 years, the geodynamic setting of the Birimian terrane is still not well constrained, in part because there are large uncertainties and growing discussions surrounding the interpretation of geochemical/geochronological information. The processes of magmatism responsible for extracting the crust from the mantle is still under debate. Different geodynamic settings are thought to be involved: thus an immature volcanic arc (Sylvester and Attoh, 1992; Dioh et al., 2006; Dampare et al., 2008) or an oceanic plateau (Abouchami et al., 1990; Boher et al., 1992), or a combination of them (Beziat et al., 2000; Lompo, 2009).

Boher et al. (1992) proposed that there were three main stages responsible for crustal growth during the Eburnean orogeny:

- (1) a stage characterized by plume activities and abundant extractions of the mantle (pillowed basalts, which show a similar geochemical characteristic with modern ocean plateaus)

- (2) an oceanic slab was subducted beneath the plateau, characterized by local productions of calc-alkaline magmas
- (3) The Archaean continent collided the plateau.

Dampare et al. (2008) explored the trace elements of basalts to conclude that the geodynamic regime was related to a subduction process. In the southern Ashanti volcanic belt, the LREE-depleted tholeiitic basalts/basaltic andesites show the geochemical signatures of back-arc basin. The calc-alkaline exhibits the signatures of intra-oceanic island arc. The high Mg basaltic/andesitic evolved in a fore arc regime.

However, some necessary constrains for strengthening this theory (subduction) are not observed, for instance, the age gradient across the sets of sub-parallel granitoid-greenstone belts is not clearly observed (Block, 2015). This possibly indicates that the style of subduction during the Eburnean orogeny may differ from the modern subduction process resulting from the elevated T_p (Van Hunen and Van den Berg, 2008).

2.1.2.2 Deformation phases

The number of deformation phases (Figure 2.4) characterizing the Eburnean orogeny is still under strong debates (Feybesse et al., 2006 and refs. therein). The existence of a S1 fabric developed at the early stages (D1) of the Eburnean Orogeny in the volcano-sedimentary belts is supported by some authors (Hein et al., 2010 and refs. therein) and contested by other ones (Vidal et al., 2009). S1 is often described as a shear foliation.

The subsequent D2 deformation phase was responsible for most of the main structures observed in the Birimian terrane. This deformation regime structured the greenstones basins into linear to arcuate belts and characterized by craton-scale transcurrent shear zones (Jessell et al., 2012). The overall metamorphic facies associated with this deformation are greenschist but locally grades into the amphibolite facies especially around the thermal aureoles of few granitoids (Pons et al., 1995; John et al., 1999; Debat et al., 2003; Ganne et al., 2012).

According to Vidal et al. (2009), the D2 is characterized by sub-vertical magmatic fabrics (Sm2) manifested by compositional layering in the granitoids. The D2 shortening further affected and steepened the D1 structures in greenstone belts within large synforms. The D1 features were strongly obliterated by the D2 structures and it is difficult to distinguish them. The D2 compression switched to transpression during the later stages of the orogenic cycle (Vidal et al., 2009) leading to the development of steep N-S to NE-SW trending transcurrent shear zones (S2/C2).

2. Geological settings of the study areas

Palaeoproterozoic	Age (Ga)	Formation	Tectonic/Metamorphic Event		Process/Cycle/orogeny
	~2.35 - 2.25	BIF bearing volcano-sedimentary formations	greenstone belts	granitoids	Deposition along the margin of the Sao Luis Craton
	2.25 - >2.17	Volcano-plutonism (mafic)	- primary volcanic stratification		Birimian accretion (mostly mafic)
	<2.17 - 2.15	major pulse of plutonism (early granitoids - TTG)			
	2.15 - 2.13 to 2.1 2.13 - 2.105	Detrital sedimentation from greywackes to flysch-type (Comoé basin in Ghana) Syn-kinematic plutonism from - early banded granitoids (TTG)	D1 D2	- sedimentary bedding S0 S1 - early metamorphic foliation (mostly overprinted) M1 parageneses : chlorite-phengite (low temperature/depth ratio - average of 10-12°C/km) S2 - regional dominant foliation (contact metamorphism) (NNE-SSW to NE-SW trending) M2a parageneses : greenschist to amphibolite facies (moderately temperature/depth ratio- average of 25 °C/km)	S2m - magmatic foliation in leucogranite and compositional layering in TTGs
2.095 - 1.98	- late granitoids (leucogranite) in the calc-alkaline suite	- isoclinal folding of S0 (and S1) with subvertical fold axial planes (S2) S2/C2 - Multiple and localized steep shear zones (N-S to NE-SW trending) M2b parageneses : low-P greenschist facies (elevated temperature/depth ratio- >50 °C/km)		S2/C2 - regional shear and strike-slip fault zones	

BIF, banded iron formation

Age are defined according to published data in Feybesse et al (2006) : radiometric age determinations were obtained using the single-zircon lead-evaporation, Sm-Nd , K-Ar and 40Ar/39Ar methods

Figure 2.4: Chronology of Paleoproterozoic events in the WAC, modified after Feybesse et al. (2006) and Vidal et al. (2009) associating with metamorphic data of Ganne et al. (2012, 2014).

2.1.2.3 Tectonic models in the WAC

“Dome and basin” is a representative structure in the Archaean orogeny, which is related to the sagduction of dense supracrustal materials and the uprise of less dense underlying rocks as a result of density contrasts (Gorman et al., 1978). However, the application of this “dome and basin” model to Paleoproterozoic orogeny is still a matter of debate.

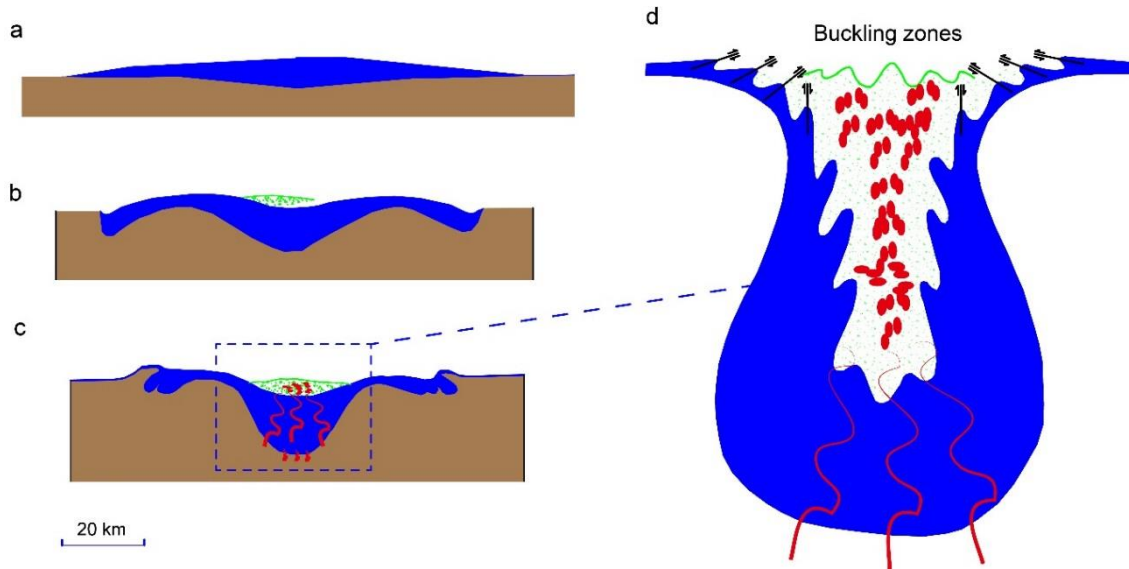


Figure 2.5: A tectonic model accounting for the deformation of greenstone belts in the Archaean time (modified after Gorman et al., 1978). Blue area represents the volcanic succession. Brown area represents the underlying crust of tonalitic composition. Red lines and particles represent the partially molten material derived from lower sources (from upper mantle and lower crust). Green particles represent the volcano-sediment. (a) The volcanic rocks are erupted due to involvements of extensional/tensional tectonic regimes. (b) A central basin forms in the central portion of the volcanic rocks. (c) Calc-alkaline magmas derived from the lower sources (lower crust, mantle) intrude into and infill the central basin. (d) Faulting and buckling zones.

In the South-Western part of Burkina Faso (Figure 2.6a), Baratoux et al. (2011) proposed that the volcanic and meta-sedimentary rocks underwent long-wavelength amplitude buckling during the transition from an ocean crust to a thickened continental crust (~ 30 km). The magmatism simultaneous fed granitoids into the system. The granitoids accumulated at the base of the upper crust or/and intruded into the volcanic islands. Regarding the subduction process, two scenarios were proposed:

- (1) Each greenstone belt (Boromo, Houndé and Banfora greenstone belts) corresponds to a volcanic arc.

2. Geological settings of the study areas

- (2) Only one large volcanic arc existed (at least 400 km in width), which was shortened and folded into the present belts during the Eburnean orogeny under the E-W to WNW-oriented compressions (D1 and D2).

However, in Ivory Coast, Vidal et al. (2009) proposed two deformation stages to explain the orogenic evolution on the basis of “dome and basin” (Figure 2.6c). The D1 stage is characterized by self-development of “dome and basin” only due to the contrast in density without the involvement of any horizontal tectonic forces. This description corresponds well with the mechanisms of diapirism in the Archaean orogeny (Gorman et al., 1978; Chardon et al., 2002). The D2 stage is characterized by coeval ascent of diapirs and horizontal shortening.

Compared to Vidal et al. (2009), an opposing model (crustal thickening by nappe stacking) was proposed by Feybesse et al. (2006) for the Sunyani-Comoé basin according to the geometric relationship between the distribution of upwelling leucogranites and regional shear zones (Figure 2.6d). The D1 stage was responsible for thrusting and accretion. The D2 stage was responsible for leucogranite emplacement, through which two main stages were suggested:

- (1) Initiating brittle deformation in the crust
- (2) Lecugranite emplaced through the brittle fractures during the process of transcurrent shearing.

Regarding a numerical study, Ganne et al. (2014) modelled the post-accretion Eburnean collisional-orogeny (Figure 2.6b). A relatively homogeneous temperature profile was suggested, characterized by a moderate temperature gradient of 20 to 30 °C /km. They proposed that the exhumation of partially molten rocks, characterized by strong lateral metamorphic gradients, was mainly controlled by simultaneous folding/shortening and gravitational instabilities in the crust.

These different tectonic models suggest that the overall tectonic regime in the WAC during the Eburnean Orogeny is still a matter of debate, due to limited outcrop exposures (Baratoux et al., 2011; Jessell et al., 2012; Ganne et al., 2012), uncertain geophysical signatures (Moho depth, Jessell et al., 2016) and vague thermal state of the mantle (Tp). All these uncertainties suggest that the origin of granitoids in the WAC remains incompletely understood.

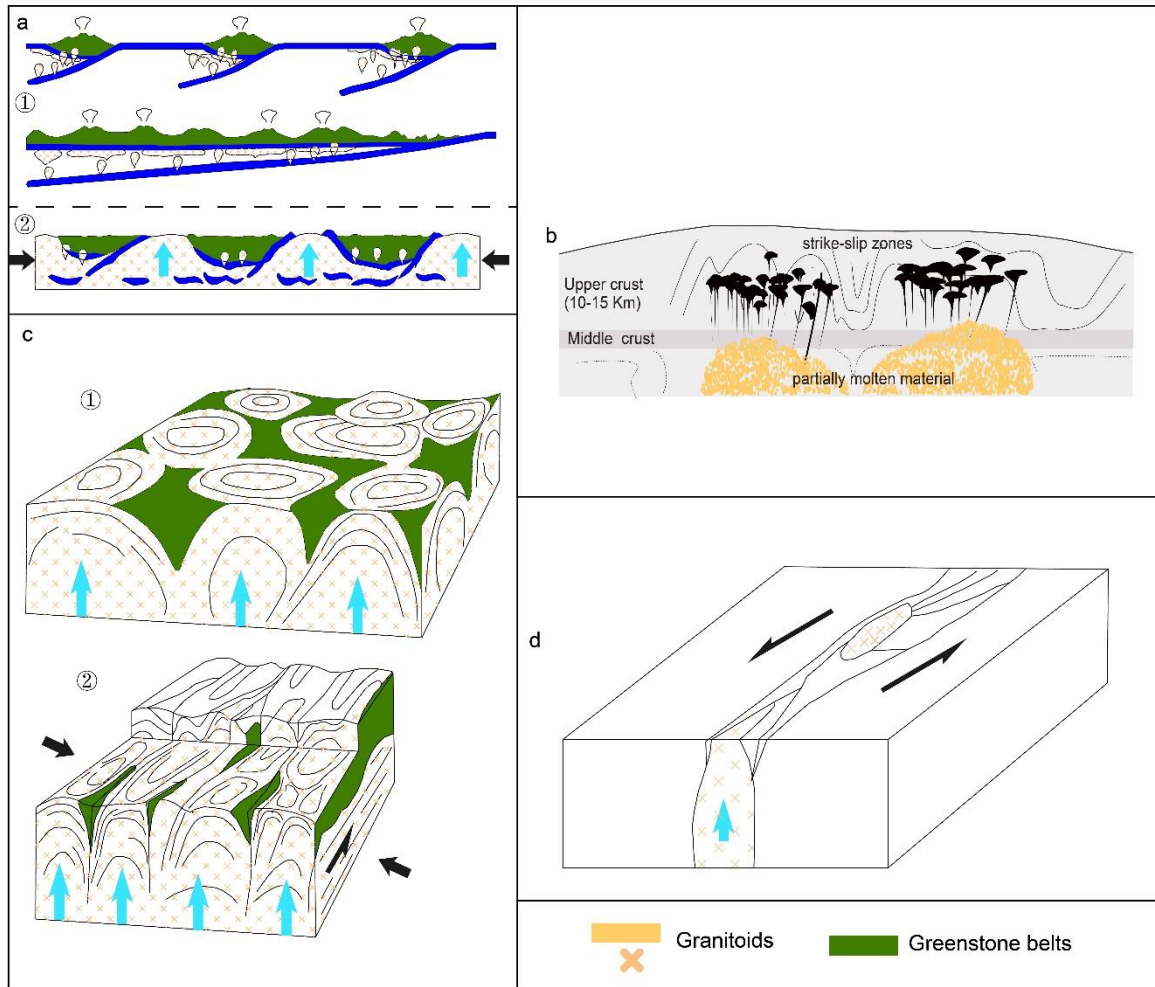


Figure 2.6: Different tectonic models accounting for the deformation of greenstone-granitoid belts in the WAC proposed by (a) Baratoux et al. (2011) (b) Ganne et al. (2014) (c) Vidal et al. (2009) (d) Feybesse et al. (2006), respectively. Boundary tectonic forces are shown in black arrows. Upward movement of granitoids is indicated by blue arrows.

2.2 Geological setting in Southern New Zealand

2.2.1 Geodynamic evolution (110 Ma-0 Ma)

The continental portions of the Australian-New Zealand landmass started to split from the Southern part of Gondwana during the late Cretaceous (Figure 2.7a). Separation of the Zealandia plate from Australia and Antarctica was initiated around 85 Ma (Figure 2.7b), with rifting from south to north to form the new Tasman Sea (Hayes, 1973; Gaina et al., 1998; Sutherland, 1999). At about 45 Ma, the Resolution Ridge rift boundary (Figure 2.7c) is believed to have formed as a consequence of a spreading ridge propagating through the southern New Zealand along the line of the Emerald fracture zone (Sutherland, 1999; Sutherland et al., 2000). From Oligocene to Early Miocene times, the plate boundary developed transform characteristics as the AUS-PAC spreading direction became progressively more

2. Geological settings of the study areas

oblique with respect to the ascent Challenger rift zone, with strike-slip motion dominant through much of the central South Island by around 21 Ma (King et al., 2000). Strike-slip deformation subsequently dominated strain localisation through on land continental New Zealand. A step-change in the AUS-PAC pole of rotation to the west at around 7-8 Ma introduced substantial oblique transpression across the system (Walcott, 1998; King et al., 2000; Batt et al., 2001), leading to rapid uplift of the Southern Alps (Figure 2.7d).

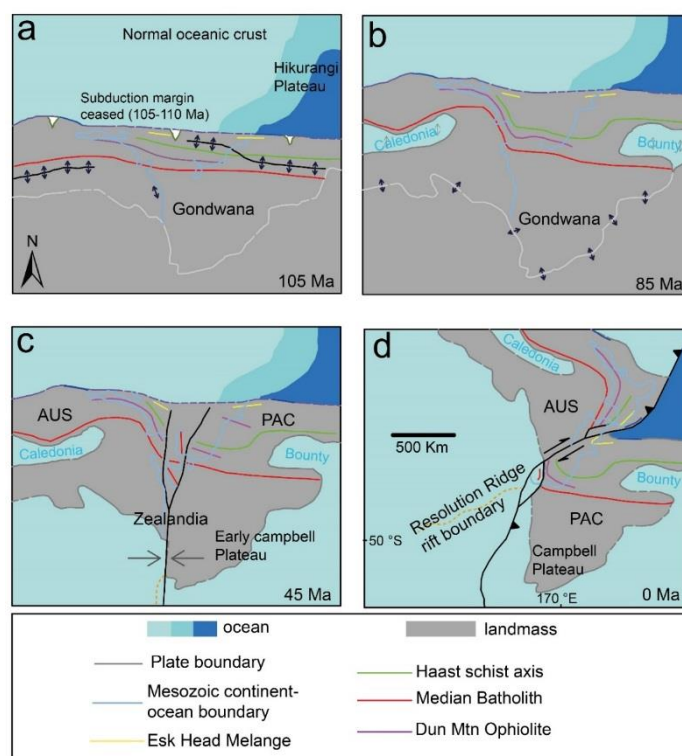


Figure 2.7: Schematic diagram, showing the evolution of the Australian-New Zealand plates from Cretaceous to recent time (modified after Mortimer, 2014).

2.2.2 Summary of geological framework of the South New Zealand

Basement geology (Figure 2.8) of the South Island of New Zealand is divided into Eastern and Western Province domains by the Median Tectonic Zone (Landis and Coombs, 1967; Bradshaw, 1980; Bishop et al., 1985). The Western Province is comprised of fragments of the early-middle Palaeozoic continental margin of Gondwana cut by series of upper Devonian to Lower Carboniferous granitoids (Park, 1921; Grindley, 1961; Suggate, 1965; Ireland and Gibson, 1998; Muir et al., 1998) and gneisses (Mortimer, 2004). The Eastern Province is mostly composed of metagreywacke together with higher-grade (pumpellyite-actinolite to amphibolite facies) equivalents in the Haast Schist group (Mortimer, 2004), resulting from convergent margin processes and corresponding metamorphism from Permian to Cretaceous times (Aronson, 1965). The Western Province is both older (Landis and Coombs, 1967) and for the most part mechanically stronger (Gerbault et al., 2002) than the Eastern province. The Western

2. Geological settings of the study areas

and Eastern Provinces also express contrasting metamorphic histories, with the Eastern Province dominated by the low temperature-high pressure Wakatipu Metamorphic Belt, and the Western Province the high temperature-low pressure Tasman Metamorphic belt (Turner 1938; Miyashiro, 1961; Landis and Coombs, 1967; Coombs, 1985).

The South Island in New Zealand region, is made up of a network of faults and shear zones with the most dominant structure being the Alpine Fault (Figure 2.8). The Alpine Fault operates as the effective tectonic boundary between the Australian and Pacific plates, and transects the western South Island as a variably southeast dipping structure accommodating dextral strike-slip motion of about 3 cm/year (Norris et al., 1990; Berryman et al., 1992; Davey et al., 1995; Walcott, 1998). This structure accommodates about 70% of the current plate boundary motion, and has accounted for more than 50% of the plate displacement at a crustal scale since 45 Ma (Beavan et al., 1999; Sutherland et al., 2000).

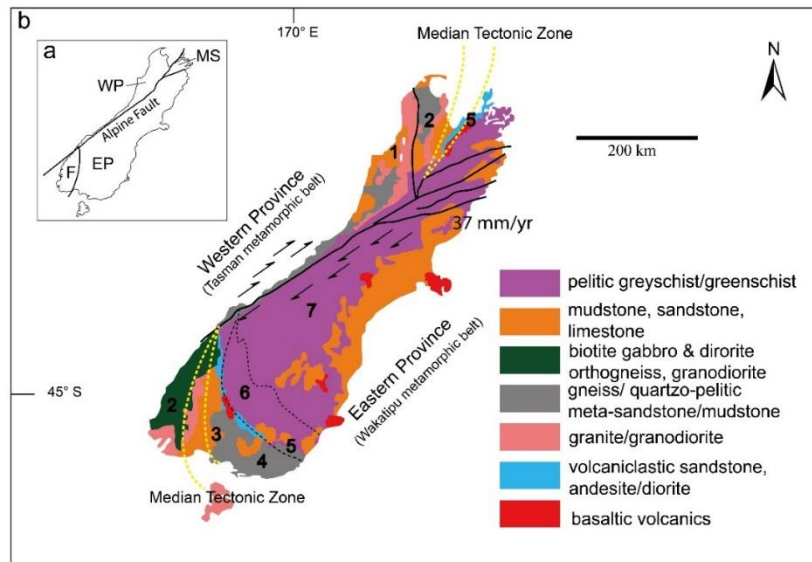


Figure 2.8: (a) Simplified geological map of New Zealand, showing the major structural features related to the AUS-PAC plate boundary through the study area (South Island). MS, WP, EP and F represents Marlborough Sounds, Western Province, Eastern Province and Fiordland, respectively. (b) Simplified litho-structural map of the South Island of New Zealand (Modified after Barth et al., 2013; GNS Science, 2010; Sutherland, 1999). 1 = Buller Terrane, 2= Takaka Terrane, 3 = Brook street Terrane, 4 = Murihiku Terrane, 5 = Maitai Terrane, 6 = Caples Terrane and 7 = Torlesse Terrane.

2.2.3 Ongoing topics

2.2.3.1 The Alpine Fault expressions in lower crust and mantle.

Continental transform faults form as two plates slide past one another, through which large displacements are accommodated onto a single fault. In the upper crust, the structures of faults are

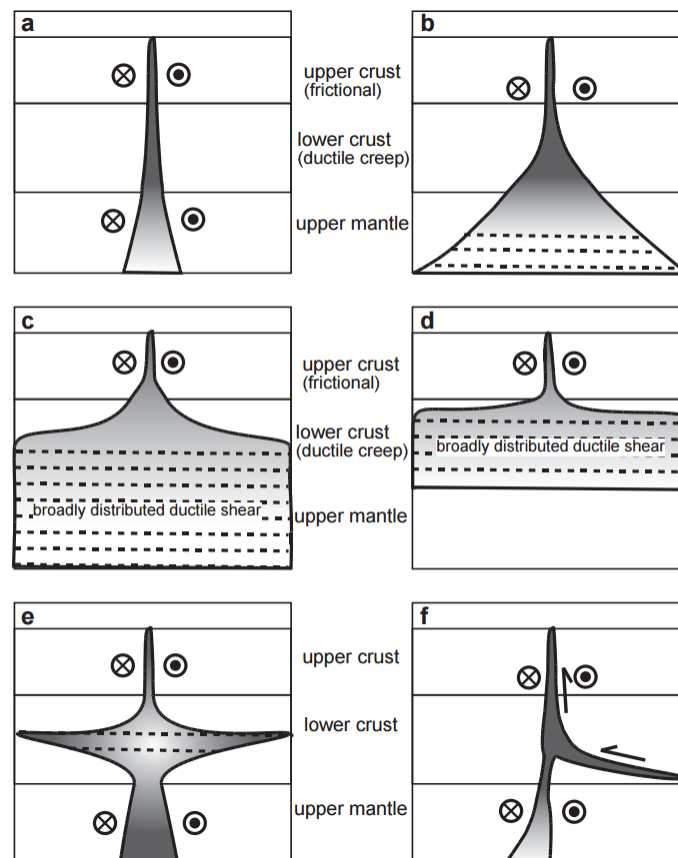
2. Geological settings of the study areas

typically expressed as narrow damage zones. However, in mantle and lower crust, the structures is less constrained. Figure 2.9 shows various models used for accounting for deep structures.

Regarding the structural expression of the Alpine Fault, Norris and Toy, (2014) raised a main concern about the deep structure of the Alpine Fault, and the link between the observed near-surface deformation and the associated deformation in the lower crust and lithospheric mantle.

High grade mylonite is observed in the hanging wall of the Alpine Fault, and the deformation observed in the mylonite is dominantly simple shear (Holm et al., 1989; Toy et al., 2008). This evidence suggests that localized shear zones extend through most of the lower crust (Norris and Toy, 2014).

A recent seismic tremor from the central section of the Alpine Fault was reported by Wech et al. (2012). They defined a zone extending through the ductile lower crust and appearing to steeply descend into the lithospheric mantle (Figure 2.9). Little et al. (2002) suggested that the Pacific plate is still undergoing the processes of delamination along a sub-horizontal interface at a depth of between 20 and 30 km. Rocks above this decollement are exhumed and uplifted due to thermal weakening. This is in good agreement with Koons et al. (2003), they proposed a partitioning of motion between a sub-flat-lying ductile detachment and a highly steep strike-slip shear zone at depth.



2. Geological settings of the study areas

Figure 2.9: Diagram shows different models accounting for the deep structures of a transform fault (source: Norris and Toy, 2014).

In the lithospheric mantle, the structural expression of the Alpine Fault remains uncertain (Morris and Toy, 2014). The main tool to reveal the deep structure is seismic anisotropy. According to the distribution of seismic anisotropy data (Savage et al., 2004; 2007), the South Island can be divided into two domains: the Southern South Island and the Northern South Island. In the Northern domain, Savage et al. (2007) suggested that a 70-100 km wide shear zone is located in the upper mantle. For the Southern domain, it may reflect a wide low-strain zones. It has been suggested that this distribution indicates that simple shear is dominant in the Northern domain, and pure shear is dominant in the Southern domain (Savage et al., 2007). The 80 km width of the distributed shear zone in the lower crust is roughly similar to the estimated width of the high-strain zone in the upper mantle (Norris, 1979; Little et al., 2002, Savage et al., 2007), suggesting that the crust and mantle probably are closely coupled.

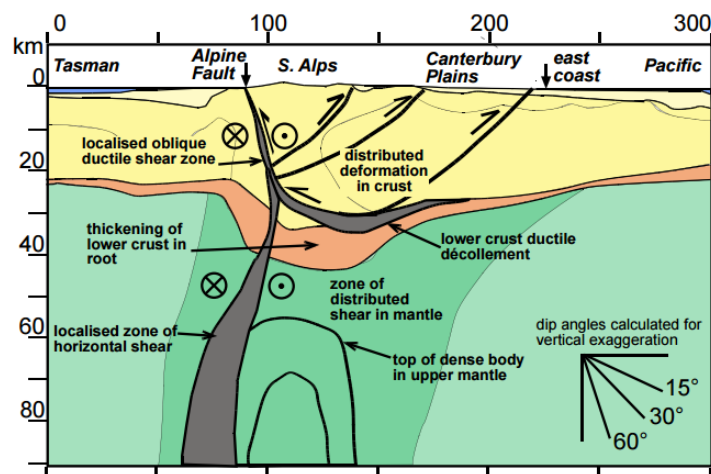


Figure 2.10: Diagram shows the deep structures of the central section of the Alpine Fault (source: Norris and Toy, 2014). Grey areas indicate highly localized shear zones.

2.2.3.2 Mechanism of shear localization

There is still debate concerning the strength distribution in the continental lithosphere, e.g., how inherited structures in the lithosphere and strain weakening of rocks influence the process of strain localization and further initial plate boundaries (Gueydan et al., 2014, Figure 2.11). Rheological heterogeneity and mechanical anisotropy acquired from past tectonic events commonly provide preferential zones for strain localization and accommodation. On a continental scale, the progressive and repeated interactions between strain weakening and strain localization lead to the progressive growth and maturation of new plate boundaries under external boundary conditions, while plate interiors may still remain intact (Jordan, 1978; Gueydan et al., 2014). For instance, during the Pangaea

2. Geological settings of the study areas

breakup, tectonic inheritance on a large scale coincides with the distribution of large transform offsets of the continental margins (e.g. the Bahamas transform margin as discussed in Thomas, 2006; Whalen et al., 2015).

In Southern New Zealand, continental regions inherited intricate fabrics resulting from the accretion, localized uplift, and subsidence of the landmass through geological history (Little and Mortimer, 2001; Claypool et al., 2002; Upton et al., 2014). The early deformation history can be observed in the modern South Island. Their structural expression (Figure 2.12) is consistent with the regional NE trending ridge segments and NW trending faults (Lamarche et al., 1997; Deckert., et al., 2002; Gray and Foster, 2004). These inherited fabrics are thought to play an important role in controlling the evolution of strain localization during the Oligocene-Miocene early development of the modern dextral strike-slip boundary conditions across the Alpine Fault.

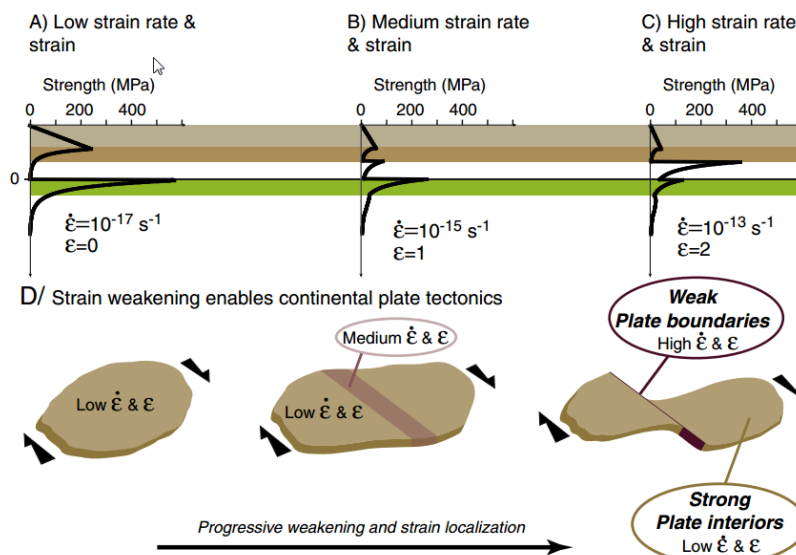


Figure 2.11: Strain localization influenced by strain weakening (Source: Gueydan et al., 2014).

However, the occurrence of this self-organization of strain localization as well as the modern coherent plate boundary resulting from the inherited fabrics in the study area are not completely understood (Barnes, 1994; Lamarche et al., 1997; Sutherland et al., 2000; Upton et al., 2014). Also the manner by which these mechanical and rheological parameters (i.e., viscosity, friction coefficient and cohesion et al., Gueydan et al., 2014; Upton et al., 2014) influence the processes of strain localization at a crustal scale is still not completely defined.

2. Geological settings of the study areas

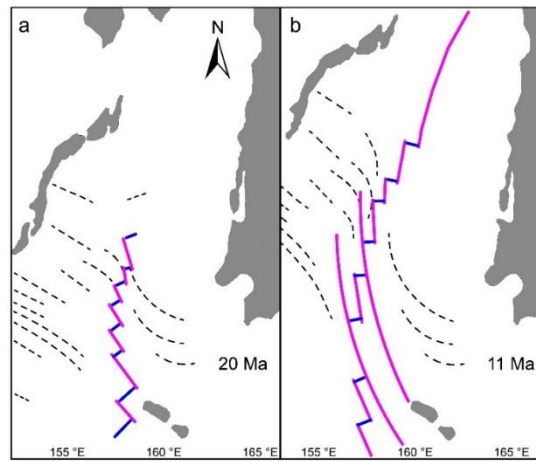


Figure 2.12: The distribution of inherited shear zones of a two stage Australian-Pacific boundary (Panel a, b, modified after Lamarche et al., 1997). Black dashed line = fracture zones; dark solid blue line = inherited NE-trending fabrics (spreading ridges); deep pink solid line = inherited NW-trending fabrics.

2.3 References

- Abouchami, W., Boher, M., Michard, A., Albarede, F., 1990. A major 2.1 Ga event of mafic magmatism in West Africa: an early stage of crustal accretion. *Journal of Geophysical Research: Solid Earth*, 95(B11), 17605-17629.
- Agyei Duodu, J., Loh, G.K., Boamah, K.O., 2009. Geological map of Ghana 1:1 000 000. Geological Survey Department of Ghana (GSD).
- Allibone, A., Teasdale, J., Cameron, G., Etheridge, M., Uttley, P., Soboh, A., Lamb, E., 2002. Timing and structural controls on gold mineralization at the Bogoso gold mine, Ghana, West Africa. *Economic Geology*, 97, 949-969.
- Amponsah, P. O., Salvi, S., Béziat, D., Siebenaller, L., Baratoux, L., Jessell, M. W., 2015. Geology and geochemistry of the shear-hosted Julie gold deposit, NW Ghana. *Journal of African Earth Sciences*, 112, 505-523.
- Aronson, J. L., 1965. Reconnaissance rubidium-strontium geochronology of New Zealand plutonic and metamorphic rocks. *New Zealand journal of geology and geophysics*, 8 (3), 401-423.
- Baratoux, L., Metelka, V., Naba, S., Jessell, M. W., Grégoire, M., Ganne, J., 2011. Juvenile Paleoproterozoic crust evolution during the Eburnean orogeny (~2.2–2.0Ga), western Burkina Faso. *Precambrian Research*, 191, 18–45.
- Barnes, P. M., 1994. Inherited structural control from repeated Cretaceous to Recent extension in the North Mernoo fault zone, western Chatham Rise, New Zealand. *Tectonophysics*, 237 (1), 27-46.
- Barth, N.C., Boulton, C., Carpenter, B.M., Batt, G.E., Toy, V.G., 2013. Slip localization on the southern Alpine Fault New Zealand. *Tectonics*, 32 (3), 620–640.
- Bassot, J. P., 1966. Étude géologique du Sénégal oriental et de ses confins guinéo-maliens. (No. 40). Éditions BRGM.
- Batt, G. E., 2001. The approach to steady state thermochronological distribution following orogenic development in the Southern Alps of New Zealand, *American Journal of Science*, 301, 374-384.
- Batt, G. E., S. L. Baldwin, M. Cottam, P. Fitzgerald, and M. T. Brandon., 2004. Cenozoic Plate Boundary Evolution in the South Island of New Zealand: New Thermochronological Constraints. *Tectonics*, 23, TC4001, doi: 10.1029/ 2003TC001527.

2. Geological settings of the study areas

- Beavan, J., Ellis, S., Wallace, L., Denys, P., 2007. Kinematic constraints from GPS on oblique convergence of the Pacific and Australian plates, central South Island, New Zealand. *A Continental Plate Boundary: Tectonics at South Island, New Zealand*, 75-94.
- Beavan, J., Moore, M., Pearson, C., Henderson, M., Parsons, B., Bourne, S., England, P., Walcott, D., Blick, G., Darby, D., Hodgkinson, K., 1999. Crustal deformation during 1994–1998 due to oblique continental collision in the central Southern Alps, New Zealand, and implications for seismic potential of the Alpine fault. *Journal of Geophysical Research: Solid Earth (1978-2012)*, 104 (B11), 25233-25255.
- Berryman, K.R., Beanland, S., Cooper, A.F., Cutten, H.N., Norris, R.J., and Wood, P.R., 1992, The Alpine Fault, New Zealand: Variation in Quaternary structural style and geomorphic expression: *Annales Tectonicae*, v. VI, p. 126–163.
- Bessoles, B., 1977. Géologie de l'Afrique: le craton ouest africain (No. 88-89). BRGM.
- Béziat, D., Bourges, F., Debat, P., Lompo, M., Martin, F., Tollon, F., 2000. A Paleoproterozoic ultramafic-mafic assemblage and associated volcanic rocks of the Boromo greenstone belt: fractionates originating from island-arc volcanic activity in the West African craton. *Precambrian Research*, 101(1), 25-47.
- Béziat, D., Dubois, M., Debat, P., Nikiéma, S., Salvi, S., Tollon, F., 2008. Gold metallogeny in the Birimian craton of Burkina Faso (West Africa). *Journal of African Earth Sciences*, 50, 215–233.
- Bishop, D. G., J. D. Bradsaw, C. A. Landis., 1985. Provisional terrane map of South Island, New Zealand, in *Tectonostratigraphic Terranes of the Circum-Pacific Region*, Earth Sci. Ser., vol. 1., edited by D. G. Howell, pp. 515-521, AAPG Circum-Pacific Council for Energy and Mineral Resour, Houston, Tex.
- Block, S., Ganne, J., Baratoux, L., Zeh, A., Parra–Avila, A. L., Jessell, M., Ailleres, L., Siebenaller, L., 2015. Petrological and geochronological constraints on lower crust exhumation during Paleoproterozoic (Eburnean) orogeny, NW Ghana, West African craton. *Journal of Metamorphic Geology*, 33, 463-494.
- Boher, M., Abouchami, W., Michard, A., Albarede, F., Arndt, N. T., 1992. Crustal growth in West Africa at 2.1 Ga. *Journal of Geophysical Research: Solid Earth (1978-2012)*, 97, 345-369.
- Bradshaw. J. D, Andrews. P. B, Adams. C. J., 1980. Carboniferous to Cretaceous on the Pacific margin of Gondwana: The Rangitata phase of New Zealand. *Proceedings Fifth Int Gondwana Symposium*, Wellington, New Zealand

2. Geological settings of the study areas

- Chardon, D., Peucat, J. J., Jayananda, M., Choukroune, P., Fanning, C. M., 2002. Archaean granite-greenstone tectonics at Kolar (south India): Interplay of diapirism and bulk inhomogeneous contraction during juvenile magmatic accretion. *Tectonics*, 21(3).
- Chardon, D., Gapais, D., Cagnard, F., 2009. Flow of ultra-hot orogens: A view from the Precambrian, clues for the Phanerozoic. *Tectonophysics*, 477, 105-118.
- Claypool, A. L., Klepeis, K. A., Dockrill, B., Clarke, G. L., Zwingmann, H., Tulloch, A., 2002. Structure and kinematics of oblique continental convergence in northern Fiordland, New Zealand. *Tectonophysics*, 359 (3), 329-358.
- Coombs, D.S., 1985. New Zealand terranes. Third Circum-Pacific Terrane Conference, Geological Society of Australia. Extended abstracts.
- Dallmeyer, R. D., Villeneuve, M., 1987. $^{40}\text{Ar}/^{39}\text{Ar}$ mineral age record of polyphase tectonothermal evolution in the southern Mauritanide orogen, southeastern Senegal. *Geological Society of America Bulletin*, 98 (5), 602-611.
- Dampare, S. B., Shibata, T., Asiedu, D. K., Osaе, S., Banoeng-Yakubo, B., 2008. Geochemistry of Paleoproterozoic metavolcanic rocks from the southern Ashanti volcanic belt, Ghana: petrogenetic and tectonic setting implications. *Precambrian Research*, 162 (3), 403-423.
- Davey, F. J., T. Henyey, S. Kleffman, A. Melhuish, D. Okaya, T. A. Stern, T. A., and D. J. Woodward., 1995. Crustal reflections from the Alpine Fault Zone, South Island, New Zealand. *New Zealand Journal of Geology and Geophysics*, 38, 601-604.
- Davis, D. W., Hirdes, W., Schaltegger, U., Nunoo, E. A., 1994. U-Pb age constraints on deposition and provenance of Birimian and gold-bearing Tarkwaian sediments in Ghana, West Africa. *Precambrian Research*, 67 (1-2), 89-107.
- de Kock, G. S., Armstrong, R. A., Siegfried, H. P., Thomas, E., 2011. Geochronology of the Birim Supergroup of the West African craton in the Wa–Bolé region of west–central Ghana: Implications for the stratigraphic framework. *Journal of African Earth Sciences*, 59, 1–40.
- Debat, P., Nikiéma, S., Mercier, A., Lompo, M., Béziat, D., Bourges, F.,... Wenmenga, U., 2003. A new metamorphic constraint for the Eburnean orogeny from Paleoproterozoic formations of the Man shield (Aribinda and Tampelga countries, Burkina Faso). *Precambrian Research*, 123, 47–65.
- Deckert, H., Ring, U., Mortimer, N., 2002. Tectonic significance of Cretaceous bivergent extensional shear zones in the Torlesse accretionary wedge, central Otago Schist, New Zealand. *New Zealand Journal of Geology and Geophysics*, 45 (4), 537-547.

2. Geological settings of the study areas

- Dioh, E., Béziat, D., Debat, P., Grégoire, M., Ngom, P.M., 2006. Diversity of the Palaeoproterozoic granitoids of the Kédougou inlier (eastern Sénégal): Petrographical and geochemical constraints. *Journal of African Earth Science*, 44, 351–371.
- Doumbia, S., Pouclet, A., Kouamelan, A., Peucat, J. J., Vidal, M., Delor, C., 1998. Petrogenesis of juvenile-type Birimian (Paleoproterozoic) granitoids in Central Côte-d'Ivoire, West Africa: geochemistry and geochronology. *Precambrian Research*, 123, 47–65.
- Egal, E., Thiéblemont, D., Lahondère, D., Guerrot, C., Costea, C.A., Iliescu, D., Delor, C., Goujou, J. C., Lafon, J.M., Tegye, M., Diaby, S., Kolié, P., 2002. Late Eburnean granitization and tectonics along the western and northwestern margin of the Archaean Kénéma-Man domain (Guinea, West African Craton). *Precambrian Research*, 117, 57-84.
- Feybesse, J. L., Billa, M., Guerrot, C., Duguey, E., Lescuyer, J. L., Milesi, J. P., Bouchot, V., 2006. The paleoproterozoic Ghanaian province: Geodynamic model and ore controls, including regional stress modeling. *Precambrian Research*, 149, 149–196.
- Gaina, C., Müller, R. D., Royer, J. Y., Stock, J., Hardebeck, J., Symonds, P., 1998. The tectonic history of the Tasman Sea: a puzzle with 13 pieces. *Journal of Geophysical Research B*, 103 (B6), 12413-12433.
- Ganne, J., De Andrade, V., Weinberg, R.F., Vidal, O., Dubacq, B., Kagambega, N., Naba, S., Baratoux, L., Jessell, M., Allibon, J., 2012. Modern-style plate subduction preserved in the Palaeoproterozoic West African craton. *Nature Geoscience*, 5, 60-65.
- Ganne, J., Gerbault, M., Block, S., 2014. Thermo-mechanical modeling of lower crust exhumation— Constraints from the metamorphic record of the Palaeoproterozoic Eburnean orogeny, West African Craton. *Precambrian Research*, 243, 88-109.
- Gasquet, D., Barbey, P., Adou, M., Paquette, J. L., 2003. Structure, Sr–Nd isotope geochemistry and zircon U–Pb geochronology of the granitoids of the Dabakala area (Côte d'Ivoire): evidence for a 2.3 Ga crustal growth event in the Palaeoproterozoic of West Africa? *Precambrian Research*, 127, 329-354.
- Gerbault, M., Davey, F., Henrys, S., 2002. Three-dimensional lateral crustal thickening in continental oblique collision: an example from the Southern Alps, New Zealand. *Geophysical Journal International*, 150 (3), 770-779.
- GNS Science (2010), 1:1 000 000 Geological Map of New Zealand, Inst. of Geol. and Nucl. Sci., Lower Hutt, New Zealand, <http://portal.onegeology.org/>.

2. Geological settings of the study areas

- Gorman, B.E., Pearce, T.H., Birkett, T.C., 1978. On the structure of Archaean greenstone belts. *Precambrian Research*, 6, 23–41.
- Gray, D.R., Foster, D. A., 2004. $^{40}\text{Ar}/^{39}\text{Ar}$ thermochronologic constraints on deformation, metamorphism and cooling/exhumation of a Mesozoic accretionary wedge, Otago Schist, New Zealand. *Tectonophysics*, 385, 181–210.
- Grindley, G.W., 1961. Geological Map of New Zealand, 1:250,000. New Zealand, Dept. Sci. Ind. Res. Sheet 13, Golden Bay.
- Gueydan, F., Précigout, J., Montési, L.G.J., 2014. Strain weakening enables continental plate tectonics. *Tectonophysics*, 631, 189–196.
- Hayes, D. E., 1973. Seafloor spreading in the Tasman Sea. *Nature*, 243, 454-458.
- Hein, K. A. A., 2010. Succession of structural events in the Goren greenstone belt (Burkina Faso): implications for West African tectonics. *Journal of African Earth Sciences*, 56, 83–94.
- Hirdes, W., Davis, D.W., Eisenlohr, B.N., 1992. Reassessment of Proterozoic granitoid ages in Ghana on the basis of U/Pb zircon and monazite dating. *Precambrian Research*, 56, 89–96.
- Hirdes, W., Davis, D.W., Lüdtke, G., Konan, G., 1996. Two generations of Birimian (Paleoproterozoic) volcanic belts in northeastern Côte d'Ivoire (West Africa): consequences for the "Birimian controversy." *Precambrian Research*, 80, 173–191.
- Holm, D. K., Norris, R. J., Craw, D., 1989. Brittle and ductile deformation in a zone of rapid uplift: Central Southern Alps, New Zealand. *Tectonics*, 8 (2), 153-168.
- Ireland, T., Gibson, G. M., 1998. SHRIMP monazite and zircon geochronology of high-grade metamorphism in New Zealand. *Journal of metamorphic geology*, 16 (2), 149-167.
- Jessell, M. W., Amponsah, P. O., Baratoux, L., Asiedu, D. K., Loh, G. K., Ganne, J., 2012. Crustal-scale transcurrent shearing in the Paleoproterozoic Sefwi-Sunyani-Comoé region, West Africa. *Precambrian Research*, 212-213, 155-168.
- John, T., Klemd, R., Hirdes, W. Loh, G., 1999. The meta-morphic evolution of the Paleoproterozoic (Birimian) volcanic Ashanti belt (Ghana, West Africa). *Precambrian Research*, 98, 11-30.
- Jordan, T. H., 1978. Composition and development of the continental tectosphere. *Nature*, 274 (5671), 544-548.
- King, P. R., 2000. Tectonic reconstructions of New Zealand: 40 Ma to the present. *New Zealand Journal of Geology and Geophysics*, 43 (4), 611-638.

2. Geological settings of the study areas

- Koons, P. O., Norris, R. J., Craw, D., Cooper, A. F., 2003. Influence of exhumation on the structural evolution of transpressional plate boundaries: An example from the Southern Alps, New Zealand. *Geology*, 31 (1), 3-6.
- Koté, S., Ouedraogo, I., Donzeau, M., Le Métour, J., Castaing, C., Egal, E., Thiéblemont, D., Tegye, M., Guerrot, C., Chèvremont, P., Milési, J.P., Billa, M., Itard, Y., Ki, J.C., 2003. Notice explicative de la Carte géologique du Burkina Faso à 1/200,000. Feuille Léo, p. 70.
- Lamarche, G., Collot, J.-Y., Wood, R.A., Sosson, M., Sutherland, R., Delteil, J., 1997. The Oligocene-Miocene Pacific-Australia plate boundary, south of New Zealand: Evolution from oceanic spreading to strike-slip faulting. *Earth and Planetary Science Letters*, 148 (1), 129-139.
- Landis, C. A., Coombs, D. S., 1967. Metamorphic belts and orogenesis in southern New Zealand. *Tectonophysics*, 4 (4), 501-518.
- Le Métour, J., Chèvremont, P., Donzeau, M.E., Thiéblemont, E., Tegye, D., Guerrot, M.C.M., Itard, B., Castaing, Y., Delpont, C., Ki, G., Zunino, J.C.C., 2003. Notice explicative de la Carte géologique du Burkina Faso à 1/200,000. Feuille Houndé, p.82.
- Ledru, P., Pons, J., Milési, J. P., Feybesse, J. L., Johan, V., 1991. Transcurrent tectonics and polycyclic evolution in the Lower Proterozoic of Senegal-Mali. *Precambrian Research*, 50 (3), 337-354.
- Leube, A., Hirdes, W., Mauer, R., Kesse, G.O., 1990. The early Proterozoic Birimian Supergroup of Ghana and some aspects of its associated gold mineralization. *Precambrian Research*, 46, 139-165.
- Little, T. A., Mortimer, N., 2001. Rotation of ductile fabrics across the Alpine Fault and Cenozoic bending of the New Zealand orocline. *Journal of the Geological Society*, 158 (5), 745-756.
- Little, T. A., Holcombe, R. J., Lig, B. R., 2002. Kinematics of oblique collision and ramping inferred from microstructures and strain in middle crustal rocks, central Southern Alps, New Zealand. *Journal of Structural Geology*, 24 (1), 219-239.
- Lompo, M., 2009. Geodynamic evolution of the 2.25-2.0 Ga Palaeoproterozoic magmatic rocks in the Man-Leo Shield of the West African Craton. A model of subsidence of an oceanic plateau. *Geological Society, London, Special Publications*, 323, 231-254.
- Lüdtke, G., Hirdes, W., Konan, G., Koné, Y., Yao, C., Diarra, S., Zamblé, Z., 1998. Géologie de la région Haute Comoé Nord-feuilles Kong (4b et 4d) et Téhini-Bouna (3a à 3d). *Direction de la Géologie Abidjan Bulletin*, 178

2. Geological settings of the study areas

- Metelka, V., Baratoux, L., Naba, S., Jessell, M. W., 2011. A geophysically constrained litho–structural analysis of the Eburnean greenstone belts and associated granitoid domains, Burkina Faso, West Africa. *Precambrian Research*, 190, 48–69.
- Milési, J.P., Feybesse, J.L., Pinna, P., Deschamps, Y., Kampunzu, H., Muhongo, S., Lescuyer, J.L., Le Goff, E., Delor, C., Billa, M., Ralay, F., Henry, C., 2004. Geological map of Africa 1:10,000,000, SIGAfrique project. In: 20th Conference of African Geology, BRGM, Orleans, France, 2–7 June, <http://www.sigafrique.net> (last accessed 14/12/2010).
- Miyashiro, A., 1961. Evolution of metamorphic belts. *Journal of Petrology*, 2 (3), 277-311.
- Moore, M., England, P., Parsons, B., 2002. Relation between surface velocity field and shear wave splitting in the South Island of New Zealand. *Journal of Geophysical Research: Solid Earth* (1978-2012), 107 (B9), ETG-5.
- Mortimer, N., 2004. New Zealand's geological foundations. *Gondwana Research*, 7 (1), 261-272.
- Mortimer, N., 2014. The oroclinal bend in the South Island, New Zealand. *Journal of Structural Geology* 64, 32-38.
- Muir, R. J., Ireland, T. R., Weaver, S. D., Bradshaw, J. D., Evans, J. A., Eby, G. N., Shelley, D. , 1998. Geochronology and geochemistry of a Mesozoic magmatic arc system, Fiordland, New Zealand. *Journal of the Geological Society*, 155 (6), 1037-1053.
- Norris, R. J., Koons, P. O., Cooper, A. F., 1990. The obliquely-convergent plate boundary in the South Island of New Zealand: implications for ancient collision zones. *Journal of structural geology*, 12 (5), 715-725.
- Norris, R. J., Toy, V. G., 2014. Continental transforms: A view from the Alpine Fault. *Journal of Structural Geology*, 64, 3-31.
- Park, J., 1921. Geology and mineral resources of western Southland. *New Zealand Geological Survey Bulletins*, 23, 1-88.
- Peucat, J. J., Capdevila, R., Drareni, A., Mahdjoub, Y., Kahoui, M., 2005. The Eglab massif in the West African Craton (Algeria), an original segment of the Eburnean orogenic belt: petrology, geochemistry and geochronology. *Precambrian Research*, 136, 309-352.
- Pons, J., Barbey, P., Dupuis, D. Leger, J.M., 1995. Mechanisms of pluton emplacement and structural evolution of a 2.1 Ga juvenile continental crust: the Birimian of southwestern Niger. *Precambrian Research*, 70, 281–301.

2. Geological settings of the study areas

- Rooney, A. D., Selby, D., Houzay, J. P., Renne, P. R., 2010. Re-Os geochronology of a Mesoproterozoic sedimentary succession, Taoudeni basin, Mauritania: implications for basin-wide correlations and Re-Os organic-rich sediments systematics. *Earth and Planetary Science Letters*, 289(3), 486-496.
- Sakyi, P. A., Su, B. X., Anum, S., Kwayisi, D., Dampare, S. B., Anani, C. Y., Nude, P. M., 2014. New zircon U–Pb ages for erratic emplacement of 2213–2130Ma Paleoproterozoic calc–alkaline I-type granitoid rocks in the Lawra Volcanic Belt of Northwestern Ghana, West Africa. *Precambrian Research*, 254, 149–168.
- Savage, M. K., Duclos, M., Marson-Pidgeon, K., 2007. Seismic anisotropy in south island, New Zealand. *A Continental Plate Boundary: Tectonics at South Island, New Zealand*, 95-114.
- Siegfried, P., De Kock, G.S., Clarke, B., Agenbacht, A., Delor, C., Van Rooyen, R.C., 2009. Geological Map Explanation—Map Sheet 0903D (1:100 000), Mining Sector Support Programme. CGS, BRGM, Geoman, GSD, Accra.
- Suggate, R. P., 1965. The tempo of events in New Zealand geological history. *New Zealand Journal of Geology and Geophysics*, 8 (6), 1139-1148.
- Sutherland, R., 1999. Basement geology and tectonic development of the greater New Zealand region: an interpretation from regional magnetic data. *Tectonophysics*, 308 (3), 341-362.
- Sutherland, R., Davey, F., Beavan, J., 2000. Plate boundary deformation in South Island, New Zealand, is related to inherited lithospheric structure. *Earth and Planetary Science Letters*, 177 (3), 141-151.
- Sylvester, P. J., Attoh, K., 1992. Litho stratigraphy and composition of 2.1 Ga greenstone belts of the West African Craton and their bearing on crustal evolution and the Archaean-Proterozoic boundary. *The Journal of Geology*, 377-393.
- Thomas, W. A., 2006. Tectonic inheritance at a continental margin. *GSA Today*, 16 (2), 4-11.
- Toy, V. G., Prior, D. J., Norris, R. J., 2008. Quartz fabrics in the Alpine Fault mylonites: Influence of pre-existing preferred orientations on fabric development during progressive uplift. *Journal of Structural Geology*, 30 (5), 602-621.
- Turner, F. J., 1938. Progressive regional metamorphism in southern New Zealand. *Geological magazine*, 75, 160-174.

2. Geological settings of the study areas

- Upton, P., Craw, D., Walcott, R., 2014. Far-field deformation resulting from rheologic differences interacting with tectonic stresses: an example from the Pacific/Australian plate boundary in southern New Zealand. *Geosciences*, 4 (3), 93-113.
- Van Hunen, J., Van den Berg, A. P., 2008. Plate tectonics on the early Earth: limitations imposed by strength and buoyancy of subducted lithosphere. *Lithos*, 103 (1), 217-235.
- Vidal, M., Delor, C., Pouclet, A., Simeon, Y., Alric, G., 1996. Evolution géodynamique de l’Afrique de l’Ouest entre 2.2 Ga et 2 Ga; le style archéen’ des ceintures vertes et des ensembles sédimentaires birimiens du nord-est de la Côte-d’Ivoire. *Bulletin de la Société géologique de France*, 167, 307–319.
- Vignerresse, J. L., Clemens, J. D., 2000. Granitic magma ascent and emplacement: neither diapirism nor neutral buoyancy. *Geological Society, London, Special Publications*, 174 (1), 1-19.
- Villeneuve, M., 2005. Paleozoic basins in West Africa and the Mauritanide thrust belt. *Journal of African Earth Sciences*, 43, 166-195.
- Walcott, R. I., 1998. Modes of oblique compression: Late Cenozoic Tectonics of the South Island of New Zealand. *Reviews of Geophysics*, 36, 1-26.
- Wech, A. G., Boese, C. M., Stern, T. A., Townend, J., 2012. Tectonic tremor and deep slow slip on the Alpine Fault. *Geophysical Research Letters*, 39 (10).
- Whalen, L., Gazel, E., Vidito, C., Puffer, J., Bizimis, M., Henika, W., Caddick, M. J., 2015. Supercontinental inheritance and its influence on supercontinental breakup: The Central Atlantic Magmatic Province and the breakup of Pangea. *Geochemistry, Geophysics, Geosystems*, 16 (10), 3532-3554.

2. Geological settings of the study areas

Chapter 3

The role of interacting fault systems on the localization of deformation in the upper crust

3.1 Interacting fault systems in NW Ghana

Introduction

An interacting fault system commonly presents complex dynamics due to varying orientations and strike-slip instabilities along faults. It is not possible to fully tackle this problem in a simple 2D model as the spatial distribution of high strain zones is an important factor in the understanding of the dynamical effects. In order to explore the role of pre-existing faults playing in the localization of deformation, this chapter section presents a series of 3D numerical models with different orientations of faults to study the evolution and distribution of deformation. The numerical model results are discussed in the context of North-Western Ghana. This part has been published as *Precambrian Research*, 2016, 264, 161-179.

3.1.1 3-D numerical modelling of the influence of pre-existing faults and boundary conditions on the distribution of deformation: Example of North-Western Ghana

High-strain zones bound and separate the high-grade tectono-metamorphic terranes from lower-grade greenstone belts in the North-Western parts of Ghana. These belts are bounded by granitoid domains characterized by two main episodic pulses of magmatic intrusive events, which occurred between 2213 and 2086 Ma. High-strain zones are thought to play a significant role in creating fluid pathways, particularly for partially molten material from lower crustal sources to the upper crust. In this study, a three-dimensional thermo-mechanical model has been used to explore the evolution of high-strain zones and relief under compressional and simple shear boundary conditions. Different orientations of a system of branched strike-slip faults were tested. The effects of the frictional angle and density contrast on the evolution of relief were also compared in this study. The resulting model indicates domains of tensile vs. compressional strain as well as shear zones. This shows that the internal fault zones as well as the host rock in between the faults behave as relatively weaker domains than the external regions. Under both applied compressive and simple shear boundary conditions, these weakened domains constitute preferential zones of tensile and shear strain accommodations in the upper crust, which may favour infilling by deeper partially molten rocks. These processes are suggested to be the most likely to have occurred in pre-existing branched shear zones systems in North-Western Ghana during the Eburnean orogeny (around 2.20-2.10 Ga).

The orientations of faults in these models play an important role in controlling the evolution of relief and localized deformation. In particular, greatest the largest relief is obtained when faults dip parallel to each other and when they are inclined at depth, as they thus facilitate strain rotation and material transfer from depth. The host rock density does not play a primary role in producing relief compared to variations in friction angle at crustal scale of our model. Relief increases by 200-300 m when the

3. Role of interacting fault systems on the localization of deformation in the upper crust

host rock density is increased by 200 kg/m³, whereas relief reduces by about 1200 m when decreasing the host rock friction from $\varphi = 20^\circ$ to 10° . This study suggests a model for interpreting the evolution and locus of exhumation of partially molten rocks in North-Western Ghana.



3-D numerical modelling of the influence of pre-existing faults and boundary conditions on the distribution of deformation: Example of North-Western Ghana



Xiaojun Feng^{a,*}, Prince O. Amponsah^a, Roland Martin^a, Jérôme Ganne^a, Mark W. Jessell^{a,b}

^a Geosciences Environnement Toulouse, Observatoire Midi Pyrénées, 14 av. E. Belin, 31400 Toulouse, France

^b Centre for Exploration Targeting, The University of Western Australia, 35 Stirling Highway, Crawley, Perth, WA 6009, Australia

ARTICLE INFO

Article history:

Received 17 January 2015

Received in revised form 11 June 2015

Accepted 14 June 2015

Available online 28 June 2015

Keywords:

3D numerical modelling

Eburnean orogeny

Strike-slip faults

Deformation

West African Craton

ABSTRACT

High-strain zones bound and separate the high-grade tectono-metamorphic terranes from low-grade greenstone belts in the North-Western parts of Ghana. These belts are bounded by granitoid domains characterized by two main episodic pulses of magmatic intrusive events, which occurred between 2213 Ma and 2086 Ma. High-strain zones are thought to play a significant role in creating fluid pathways, particularly for partially molten material from lower crustal sources to the upper crust. In this study, a three-dimensional thermo-mechanical model has been used to explore the evolution of high-strain zones and relief under compressional and simple shear boundary conditions. Different orientations of a system of branched strike-slip faults were tested. The effects of the frictional angle and density contrast on the evolution of relief were also compared in this study. The resulting model indicates domains of tensile vs. compressional strain as well as shear zones. This shows that the internal fault zones as well as the host rock in between the faults behave as relatively weaker domains than the external regions. Under both applied compressive and simple shear boundary conditions, these weakened domains constitute preferential zones of tensile and shear strain accommodations in the upper crust, which may favour infilling by deeper partially molten rocks. This processes is suggested by the authors as the most likely processes to have occurred in pre-existing branched shear zones systems in North-Western Ghana during the Eburnean orogeny (around 2.20–2.10 Ga).

The orientations of faults in these models play an important role in controlling the evolution of relief and localized deformation. In particular, greatest the largest relief is obtained when faults dip parallel to each other and when they are inclined at depth, as they thus facilitate strain rotation and material transfer from depth. The host rock density does not play a primary role in producing relief compared to variations in friction angle at crustal scale of our model. Relief increases by 200–300 m when the host rock density is increased by 200 kg/m³, whereas relief reduces by about 1200 m when decreasing the host rock friction from $\phi = 20^\circ$ to 10° . This study suggests a model for interpreting the evolution and locus of exhumation of partially molten rocks in North-Western Ghana.

© 2015 Elsevier B.V. All rights reserved.

1. Introduction

It has been previously established that pre-existing shear zones in the crust may be reactivated and act as preferential loci for strain accommodation, when the principal stress field changes or rotates under external boundary conditions (D'Alessio and Martel, 2004; Fialko et al., 2005; Fialko, 2006; Gerbault et al., 2003; Middleton

and Copley, 2013; Nieto-Samaniego, 1999; Scholz, 2007; Sibson, 1977; Tong et al., 2014; Walsh et al., 2002; Zhang et al., 2009). It has also been suggested that shear zones play a significant role in providing fluid pathways for partially molten materials from lower crustal levels to the upper crust (Neves et al., 2000; Pereira et al., 2013; Snoko et al., 1999; Vigneresse and Tikoff, 1999; Weinberg et al., 2006).

Even at constant obliquity of far-field motion, the development of high-strain shear zones results in highly variable structures and fabrics. Whereas numerical modelling studies of oblique tectonics in the crust (e.g. Braun and Beaumont, 1995; Braun and Yamato,

* Corresponding author. Tel.: +33 0664699991.

E-mail address: fxjuncumt@gmail.com (X. Feng).

2010; Gerbault et al., 2002; Le Pourhiet et al., 2012) are still constrained by computational limitations, a large number of analogue modelling studies have investigated aspects of localized deformation in three-dimensional strike-slip settings (e.g., see review by Dooley and Schreurs, 2012, and references therein; Leever et al., 2011). Such numerical and analogue studies reproduce quite well field observations such as evolving Riedel shears, connection with P shears and the building of positive or negative flower structures. All of these structures mentioned above depend on lateral and basal boundary conditions, the initial geometries and the mechanical properties of the modelled crustal material. The orientation, magnitude and shape (flattening vs constriction, etc.) of finite strain ellipsoids tend to change continually as a result of the increasing simple shear component with respect to the coaxial components of deformation (Fossen and Tikoff, 1998; Sanderson and Marchini, 1984; Leever et al., 2011; Dooley and Schreurs, 2012). Further complications arise with heterogeneous deformation, non-steady-state deformation and strain partitioning. Within a shear zone, strain may either increase in intensity towards the central part of the zone, or be preferentially partitioned as a localized simple shear component within the broader high strain zone. In such partitioned shear zones, parts of the terranes may actually move faster than the relative plate motion, while other sections may move slower than or even in an antithetical direction to plate motion (Fossen and Tikoff, 1998; Dooley and Schreurs, 2012). This highlights the difficulty in reconstructing initial geometries and boundary conditions that produce high-strain shear zones, and then in understanding the strain field allowing deeper fluids to flow throughout the solid upper crust.

The crustal dynamics of an interacting fault system represent a complex problem due to varying orientation (Peltzer et al., 2001) and strike-slip instability along fault (Xing et al., 2007) over geological time scales. The spatial and temporal pattern of deformation is controlled by the orientations of pre-existing fault zones with respect to far-field boundary conditions (e.g., Buck and Lavier, 2001; Sibson and Xie, 1998; Tranos, 2012). In particular, new shear zones and localized deformation may develop through time (Alberti, 2010; Avouac and Burov, 1996; Giger et al., 2008; Jessell et al., 2012; Rice, 1993). Two interacting faults can be mutually constrained over a time period, during which faults weaken and also impact on the surrounding host rocks (Imber et al., 2004), possibly initiating new failures (Buck and Lavier, 2001; Leever et al., 2011). Conversely, varying boundary conditions simulate how different paleostress fields affect strain localization of interacting faults over geological time (Naylor et al., 1986; Ueta et al., 2000).

In this study we have investigated the role NE-SW trending crustal scale shear zone architecture plays in controlling the loci of exhumation during the Eburnean Orogeny in the Birimian of North-Western Ghana. According to Block et al. (2015), the high grade Bole-Bulenga terrane in North-Western Ghana, is composed mostly of gneisses, metabasites and monzogranites and located between the craton scale N-S Jirapa and the NE-SW Bole-Nangodi shear zones (Fig. 1). These high strain shear zones separate the high grade tectono-metamorphic Bole-Bulenga terrane from adjacent low grade greenstone belts (i.e. Wa-Lawra and Julie belts) which is mostly characterized by early thrust and late stage kinematic shear deformation. The minimum pressure difference between high grade amphibolite–migmatite facies Bole-Bulenga terrane (lower crust) and the adjacent greenschist facies belts (upper crustal materials) is about 3 kbar, corresponding to over 10 km in thickness.

Although Block et al. (2015) highlighted the significance of extension for exhumation in the Bole-Bulenga terrane; they also indicated that extension is certainly not the only process accounting for the exhumation of lower crust. In addition, Sakyi et al. (2014) concluded that the oldest pulses of granitic emplacement in the Wa-Lawra belt are around 2212 ± 1 Ma. This indicates that the

emplacement of Birimian granitoids in the study area should have commenced much earlier than previous studies have mentioned. All these uncertainties show that insights into the exhumation mechanisms for high grade rocks along and in between these two faults are of interest in this region. Generally, the spatial-temporal evolution of high-strain zones relating to pre-existing branched faults systems is still not completely understood. Simultaneously, fault zones in this area of Ghana are generally treated as vertical or sub-vertical (Adjei, 1992; Harcouët-Menou et al., 2009; Lompo, 2010). These uncertainties associated with the interpretation and geometry of the fault zones provided the motivation to test the influence of fault orientations on the distribution of high-strain zones reactivated in a specific kinematic setting.

The aim of this paper is not to re-produce the exact evolutionary history of geological structures in North-Western Ghana, but rather to use this geology as a basic example for assessing how the orientations of a paired fault zone system influences the distribution of high-strain zones and relief. In this study, we assume that the pre-existing faults interact with hard linkage (Gupta and Scholz, 2000), rather than interacting only through their stress fields (soft linkage), and the choice of soft linkages would significantly alter the results, but were not studied here. We use a three-dimensional thermo-mechanical model to explore the distribution of high-strain zones and relief associated with pre-existing weak domains, by testing various orientations of a system of two strike-slip faults under pure shear as well as simple shear boundary conditions. We also test the relative effects of friction angle and density contrast on the evolution of relief. These tests may shed light on exhumation process of high grade rocks associated with strain, as well as the topographic evolution in North-Western Ghana. According to tomographic models and velocity group dispersion analysis, in the Kaapvaal, Congo, Cameroon and West African/(WAC) cratons, the depth of the Moho has been estimated as 40 km and even deeper towards the south-west margin of the WAC or at about 43–48 km in the Congo Basin (Fishwick and Bastow, 2011; Lebedev et al., 2009; Pasyanos and Nyblade, 2007; Seber et al., 2001; Tokam et al., 2010) while it can reach as high as 30 km in northern Africa (Marone et al., 2003). Similar or complementary data of the Precambrian lithosphere structure has also been detailed in Lebedev et al. (2009). A compilation of Moho depths for the West African Craton (Jessell et al., 2015) reveals considerable uncertainty, and we have taken a thinner crust depth around 30 km in the present 3D modelling studies assuming that this was more or less the Proterozoic Moho depth.

2. Geological setting

2.1. Summary of the Birimian in the West African Craton

Most modern orogenic belts, such as the Alpine or Himalayan chains, display greenschist and blueschist facies metamorphism (Avé Lallemant and Guth, 1990; Maruyama et al., 1996; Ota and Kaneko, 2010), whereas the existence of modern-style plate subduction in ancient orogenic belts remains the subject of debate (Ganne et al., 2011; Stern, 2007, 2008; Condie and Kröner, 2008). Precambrian terranes also display widespread greenschist rocks, characterized by the development of a subvertical foliation, which is also axial-planar to elongated synforms and antiforms in greenstone lithologies (Cagnard et al., 2006a,b, 2007; Rey and Houseman, 2006). Such tectonic features are exemplified by the upper crustal portions of the Archaean crust in India (Chardon et al., 2009; Hansen et al., 1995; Jagadeesh and Rai, 2008; Mall et al., 2012). These Precambrian deformation events are proposed to have occurred in a regime of moderate regional convergence, which involved dominantly horizontal and locally vertical motions of material in the

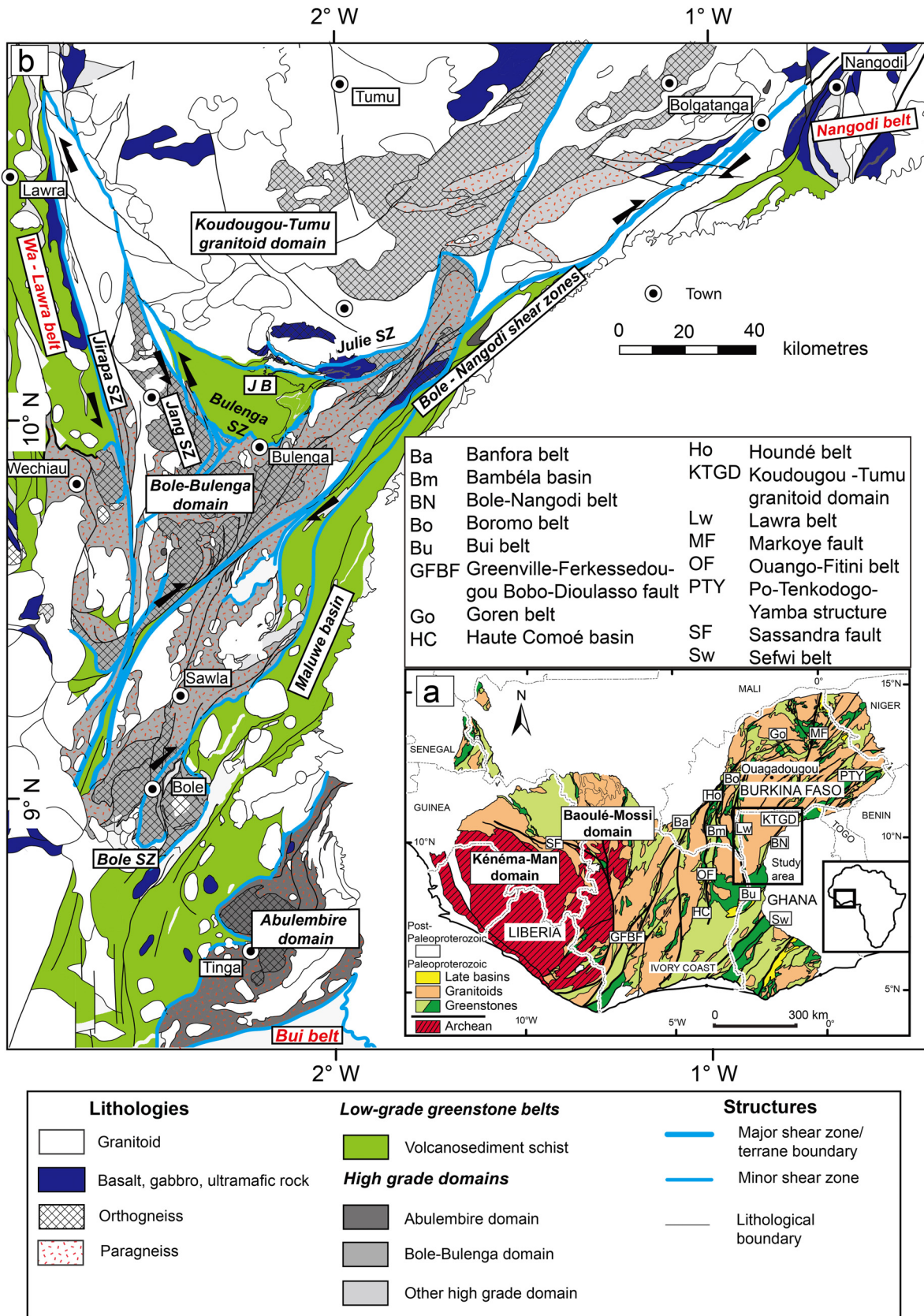


Fig. 1. (a) Simplified geological map of the Leo-Man Craton of the southern part of the West African Craton (WAC) with the zone of interest outlined. Paleoproterozoic greenstones are divided into two groups, light green represents intermediate to acid volcanoclastic and volcano-sediment, and dark green represents mafic to intermediate lavas and volcanic products, with granitoids in orange. (b) Geological setting of the study area (after Block et al., 2015). High-strain zones (blue lines) separate or limit the high-grade tectono-metamorphic terranes from low-grade greenstone belts, high-grade rock assemblages are mainly observed between the Jirapa shear zone and Bole-Nangodi shear zones. (For interpretation of the references to colour in this figure legend, the reader is referred to the web version of the article.)

upper portions of the crust (down-dip mineral lineation), accompanied by localized strike-slip motion (Block et al., 2015; Ganne et al., 2014).

The southern part of the West African Craton (WAC; Fig. 1) is dominated by Birimian terranes of Palaeoproterozoic age (ca. ~2.20–2.00 Ga, Castaing et al., 2003a,b and references therein), which extend to the east and to the north of the Liberian Archaean cratonic nucleus (Fig. 1). The Birimian formations consist of linear or arcuate narrow volcanic belts (greenstones sensu stricto) often associated to narrow volcano-sedimentary basins (greenstones sensu lato). They are intruded by several generations of granitoids (Dioh et al., 2006; Doumbia et al., 1998; Gasquet et al., 2003; Hirdes et al., 1996 and references therein). The Birimian basins is composed of, a thick sequence of tholeiitic basalts, covered by a detrital sedimentary pile which includes inter-bedded calc-alkaline volcanic rocks. Recent studies have shown that the geodynamic settings of the Birimian units was initially formed in an immature volcanic arc setting (Dioh et al., 2006) or plateaus (Boher et al., 1992; Lompo, 2009), and were later deformed and metamorphosed during the Eburnean orogeny, between ~2.15 Ga and 2.00 Ga (Egal et al., 2002). Despite stimulating debate in the last 30 years, the geodynamic setting of the Birimian sequences is not well constrained, in part because there are large uncertainties and growing discussion surrounding the use of geochemical information as an efficient tool for unravelling geodynamical settings in the past.

Structurally, the number of deformation phases characterizing the Eburnean orogeny is still under debate (Feybesse et al., 2006 and refs therein). In summary, the first Eburnean deformation phase (D1) took place between ca. ~2.20 Ga and 2.10 Ga. This phase of deformation is associated with crustal thickening via nappe stacking and burial of rocks (Allibone et al., 2002; Ledru et al., 1991; Vidal et al., 1996), operated under an E-W to WNW-oriented compression (Baratoux et al., 2011). Block et al. (2015) suggest that some aspects of this phase of deformation occurred in high pressure – low temperature conditions. D2 is a tectono-metamorphic deformational phase responsible for most of the large structures observed in the Birimian Province (Greenstones basins were deformed into linear to arcuate belts or transcurrent shear zones) and occurred synchronously with some granitoid emplacement. Transition of D1 to the subsequent D2 deformation phase is likely to have occurred at around 2.13 Ga in Ghana, following a major pulse of granitoid emplacement at ca. 2.15 Ga (Feybesse et al., 2006; Block et al., 2015).

2.2. Geological summary in North-Western Ghana

The geology of North-Western Ghana straddles the Upper West region, Upper East region and the Northern regions of Ghana and lies near the eastern margin of the Paleoproterozoic Baoulé-Mossi domain of the West African Craton (WAC). Block et al. (2015) divided the geology of North-Western Ghana into various domains. Thus the Wa-Lawra belt, the Koudougou-Tumu domain, the Bole-Bulenga domain, the Julie belt and the Bole-Nangodi belt.

The E-W oriented Julie belt is located in the central portion of North-Western Ghana (Fig. 1). Bounded to the north of the Julie belt is the Koudougou-Tumu domain and to the south by the Bole-Bulenga domain and to the east, the Bole-Nangodi belt. Bounded to the west of the Koudougou-Tumu domain is the Wa-Lawra belt.

The Wa-Lawra belt is further divided into the eastern and western halves by the crustal scale Jirapa shear zone which usually exhibits sinistral characteristics (Fig. 1). The eastern half is composed of mainly 2139 ± 2 Ma (detrital zircon ages) metamorphosed sedimentary rocks (volcanosediments, greywackes, shales) and early syn-tectonic 2212 ± 1 Ma (Sakyi et al., 2014) and 2153 ± 4 Ma (Agyei Duodu et al., 2009) granitoids. These rocks have been intruded by the 2104 ± 1 Ma late kinematic granitoids (Agyei

Duodu et al., 2009; Baratoux et al., 2011; Block et al., 2015). The rocks in the eastern half has experienced up to green schist metamorphism (Block et al., 2015). The western half is composed of the 2187 ± 3 Ma mainly high grade gneisses and granitoid (Agyei Duodu et al., 2009). These rocks here have been metamorphosed up to amphibolite facies.

The boundary between the Wa-Lawra belt and the Koudougou-Tumu domain is marked by the Jang fault (Block et al., 2015). The Koudougou-Tumu domain is composed of mainly of the 2162 ± 1 Ma to 2134 ± 1 Ma gneisses and gabbro, which has been intruded by the 2128 Ma late porphyritic granites (Agyei Duodu et al., 2009).

The Julie belt is composed of low grade basalts, silicic volcanosediments and granitoids mostly with tonalitic affinities (Amponsah et al., 2015). Dating done on the silicic volcanosediments showed that some of the rocks crystallized at 2129 ± 7 Ma (Block et al., 2015). This indicates that some part of the belt formed at least at 2130 Ma. The foliation in volcanosediments and granitoids within this fault shows a stretching lineation plunging down-dip and towards higher grade rocks (Block et al., 2015).

The Bole-Bulenga terrane is composed of high grade metamorphic rock termed as Buki gneisses by De Kock et al. (2011). According to Block et al. (2015), the Bole-Bulenga terrane is composed of paragneisses and metabasites usually migmatitic in nature. These rocks have been intruded by orthogneisses with crystallization ages between 2195 Ma and 2135 Ma.

Bounded to the south of the Bole-Bulenga terrane and east of the Julie belt is the Bole-Nangodi belt. Their boundary is marked by the NE-SW trending crustal scale Bole-Nangodi shear zones. This belt is composed of volcanoclastic rocks, greywackes, shales, granites, granitoids and gneisses with crystallization ages between 2196 ± 1 Ma and 2118 ± 3 Ma (Agyei Duodu et al., 2009; De Kock et al., 2011).

Structurally, De Kock et al. (2011) proposed an initial short lived pre-Eburnean event which occurred between 2160 Ma and 2150 Ma in North-Western Ghana. This deformational event is associated with plutonic emplacement and basin contraction. D1 is characterized by shortening and mostly marked by thrust faulting (Baratoux et al., 2011). S1 penetrative metamorphic foliation observed within this deformation event is evidenced within the high grade and low grade rocks in the Bole-Bulenga terrane and Julie belt respectively. D2 is marked by N-S-directed extension which is characterized by extensional shear zones along the northern and southern margins (acting as transition zones with greenstone belts) of the Bole-Bulenga domain (Block et al., 2015).

Recent investigations performed by Block et al. (2015) in the North-Western parts of Ghana highlighted the presence of large scale (>50 km wide) migmatitic complexes in the Bole-Bulenga terrane formed at ca. 2.13 Ga. They are associated with medium-pressure amphibolite facies rocks that are very similar to those observed by Ganne et al. (2011) in the thermal aureoles of granitic plutons in Burkina Faso, Senegal and Niger. They reveal a clockwise P-T-t path, melting at pressure over 10.0 kbar, then followed by decompression and heating to peak temperature of 750°C at 5–8 kbar.

Ganne et al. (2014) proposed that a relatively homogeneous temperature profile existed at ca. 2.15–2.10 Ga, characterized by a moderate temperature gradient of $20\text{--}30^\circ\text{C}/\text{km}$ (that does not correspond to a hot orogeny) (Chardon et al., 2009). Accordingly, a partially molten zone would have formed at a depth of 25 km in the crust, fuelled by progressive burial and heating of felsic material. Once mixed in the lower crust, these melts could have been partially redistributed towards the upper crust, contributing to gravitational instabilities in the middle crust. They proposed that exhumation of this partially molten material, characterized by strong lateral metamorphic gradients, was mainly controlled by simultaneous

Table 1
Model parameters common to all experiments. * ρ_{fault} , * ΔT and * φ indicate the values that change according to different models.

Parameter	Symbol	Value-units
Thickness	H_{upper}	20 km
	H_{lower}	10 km
	* ρ_{upper}	2800 kg/m ³
Density	ρ_{lower}	3000 kg/m ³
	* ρ_{fault}	2600 kg/m ³
Dislocation creep power law pre-exponential factor	A	MPa ⁻ⁿ /s
Dislocation creep power law exponent	n	–
Power law creep activation energy	Q	kJ/mol
Temperature gradient	* ΔT	20 °C/km
Gas constant	R	8.314 J mol ⁻¹ K ⁻¹
Heat capacity	C_p	1000 J/kg K
Thermal diffusivity	γ	m ² /s
Thermal expansion	λ	K ⁻¹
Gravitational acceleration	g	9.81 m/s ²
Friction angle	* φ	2.5–36.5°
Cohesion for Drucker–Prager	σ_c	1–20 MPa
Viscosity limit	η	1e+20 < η < 1e+23 Pa s

Table 2
Rheological properties of crustal layers. The non-Newtonian power law is used for the upper and lower crusts, whereas we employ a constant viscosity for fault zones, yielding a viscosity contrast of about 1/1000 compared to upper crust portions (Malservisi et al., 2003).

Layer	A (MPa ⁻ⁿ /s)	n	Q (kJ/mol)
Upper crust	2.0×10^{-4}	3.4	260
Lower crust	1.3×10^{-3}	2.4	219
Fault		1×10^{20} Pa s	

folding/shortening and gravitational instabilities in the juvenile crust, with the exception of North-Western Ghana where this partially molten material was extruded into the upper crust. It has been blocked and ceased at around 15 km depth in the crust, we might call retention zones, perhaps related to the presence of a competent overlying upper crust (Ganne et al., 2014; Vigneresse and Clemens, 2000).

3. Numerical method and model setup

The mechanical problem is modelled using the numerical code Underworld (Moresi et al., 2003, 2007), which can simulate visco-plastic rheologies in a three-dimensional cartesian geometry. Underworld uses a Lagrangian particle-in-cell finite element scheme which has been extensively used in geological modelling (Lemiale et al., 2008; Mason et al., 2010; Moresi and Mühlhaus, 2006; OzBench et al., 2008; Zlotnik et al., 2013). The governing equations of momentum (1), mass (approximately incompressible materials) (2) and energy (3) conservation are expressed as follows (Moresi et al., 2003, 2007; De Smet et al., 1998):

$$\frac{\partial \sigma_{ij}}{\partial x_j} = \rho g_i \quad (1)$$

$$\nabla \cdot u = 0 \quad (2)$$

$$\rho C_p \frac{DT}{Dt} + (u \cdot \nabla)T = \frac{\partial}{\partial x_i} (k_i \frac{\partial T}{\partial x_i}) + \rho H \quad (3)$$

where σ is the Cauchy stress tensor, u is the velocity, and ρ is the density (which depends on material composition), g is the gravitational acceleration, x_i are the spatial coordinates, k_i is the thermal conductivity and is calculated by the equation $k_i = \gamma \rho C_p$, $\gamma = 10^{-6}$ m²/s is the thermal diffusivity, C_p is the heat capacity at constant pressure and H is the radiogenic heat production per unit mass.

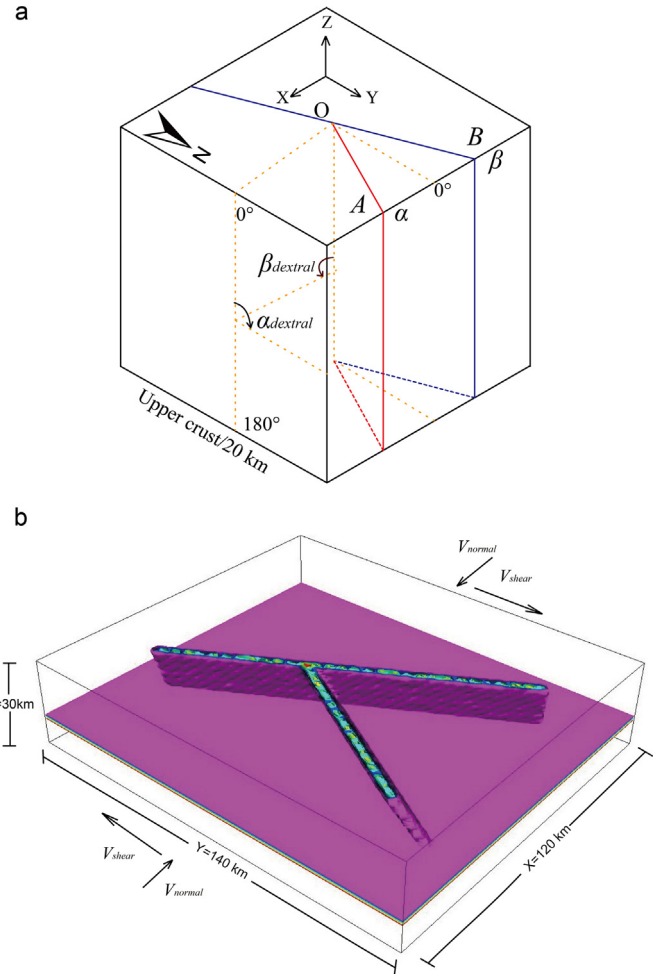


Fig. 2. Schematic geometry and boundary conditions. The domain is 140 km long (Y direction), 120 km wide (X direction) and 30 km thick (Z direction), and contains two neighbouring faults in the upper crust. In figure (a), planes A and B in red and dark blue represent fault A and fault B. The faults' intersection is referred to as point O. In figure (b), the purple plane represents the interface between the upper and lower crust. Boundary conditions are displayed with black arrows. Compressional velocities (V_{normal}) are applied normal to YZ section (East-West direction), whereas simple shear (V_{shear}) is simulated along these YZ borders. The base of the model is fixed, while the surface is set either to free, free-slip or free-remeshing surface boundary conditions. Four angles (α , β , α_{dextral} , β_{dextral}) are used to describe faults' orientations. The angles α , β represent the azimuth of the fault planes. The angles α_{dextral} , β_{dextral} are counted clockwise around the azimuth direction of the fault expressed between N0 and 180°. In all cases, α is fixed to 30° (as in figure (b)). (For interpretation of the references to colour in this figure legend, the reader is referred to the web version of the article.)

The depth dependent Drucker–Prager yield criterion (Eq. (4)) is used to describe the solid yield behaviour of the crust, in which P is the local pressure. φ is the effective friction angle and σ_p is the effective cohesion, by allowing for strain-weakening of materials (Moresi and Mühlhaus, 2006)

$$\tau_{\text{yield}} = P \cdot \tan \varphi + \sigma_p \quad (4)$$

Rock deformation is temperature sensitive and at higher temperatures they preferentially deform by dislocation creep, commonly described by a temperature-dependent non-Newtonian power law viscosity (e.g. Ranalli, 1995 and references therein):

$$\eta_m = 0.25 \cdot (0.75A)^{(-1/n)} \cdot \dot{\epsilon}^{((1/n)-1)} \cdot \exp(Q/nRT) \quad (5)$$

where $\dot{\epsilon}$ is the second invariant of the strain rate, Q is the activation energy, R is the universal gas constant, A is a pre-exponential constant, and n is a power law exponent.

Table 3
Parameters for each model, varying with respect to the reference value (model 1-1).

Exp#	Boundary condition	α	β	$\alpha_{dextral}$	$\beta_{dextral}$	Surface boundary condition	Friction of upper crust	Density contrast ($\rho_{upper} - \rho_{fault}$)
1-1	Compression	30	330	150	30	Remesh	30	200
1-1-1	Compression	30	330	150	30	Free	30	200
1-1-2	Compression	30	330	150	30	Free-slip	30	200
1-2	Compression	30	330	150	30	Remesh	30	100
1-3	Compression	30	330	150	30	Remesh	30	50
1-4	Compression	30	330	150	30	Remesh	30	0
1-5	Compression	30	330	150	30	Remesh	30	400
2-2	Compression	30	330	30	150	Remesh	30	200
2-3	Compression	30	330	30	30	Remesh	30	200
2-4	Compression	30	330	60	150	Remesh	30	200
2-5	Compression	30	315	120	30	Remesh	30	200
2-5-1	Compression	30	315	120	0	Remesh	30	200
2-5-2	Compression	30	315	120	150	Remesh	30	200
2-6	Compression	30	330	60	30	Remesh	30	200
2-7	Compression	30	330	120	30	Remesh	30	200
2-8	Compression	30	330	150	30	Remesh	20	200
2-9	Compression	30	330	150	30	Remesh	10	200
2-10	Compression	30	330	150	150	Remesh	30	200
2-11	Compression	30	330	120	150	Remesh	30	200
2-12	Compression	30	330	150	30	Remesh	15	200
S-1	Simple shear	30	330	150	30	Remesh	30	200
S-2-4	Simple shear	30	330	60	150	Remesh	20	200
S-5	Simple shear	30	330	0	30	Remesh	30	200
S-5-1	Simple shear	30	330	0	30	Remesh	20	200
S-5-2	Simple shear	30	330	0	30	Remesh	10	200
S-2-5	Simple shear	30	315	120	30	Remesh	20	200
S-2-6	Simple shear	30	330	60	30	Remesh	20	200
S-2-7	Simple shear	30	330	60	30	Free	20	200
S-2-8	Simple shear	30	330	60	30	Free-slip	20	200
S-2-9	Simple shear	30	330	120	30	Remesh	20	200
V-S	Simple shear	30	330	0	0	Remesh	20	200
V-C	Compression	30	330	0	0	Remesh	20	200

With progressive loading, elementary stresses increase. We note $\tau = \sqrt{(1/2)\tau_{ij}\tau_{ij}}$ the square root of the second invariant of the stress tensor. When τ is less than the yield stress τ_{yield} , the viscosity remains equal to the material viscosity $\eta = \eta_m$. However, when τ equals yield stress τ_{yield} , the additional plastic deformation is accounted for through reducing the viscosity to an effective viscosity:

$$\eta = \frac{\tau_{yield}}{2\dot{\epsilon}} \quad \text{for } \tau = \tau_{yield} \quad (6)$$

The rheological parameters for the non-Newtonian power-law are given in Table 2.

For the initial thermal conditions, we fixed a temperature $T = 20^\circ\text{C}$ at the top surface ($Z = 30\text{ km}$) and $T = 620^\circ\text{C}$ at the bottom of the computational domain ($Z = 0$), assuming a reference temperature gradient of $20^\circ\text{C}/\text{km}$. Other physical and thermal properties are given in Table 1.

The model domain is composed of a 20 km thick upper crust and a 10 km thick lower crust. In the upper crust, two neighbouring faults A and B (20 km thick) are defined with specific orientations ($\alpha, \alpha_{dextral}, \beta, \beta_{dextral}$). The schematic model is given in Fig. 2. The size of the domain is 140 km long (Y direction), 120 km wide (X direction) and 30 km thick (Z direction), and is modelled at a resolution of $2\text{ km} \times 2\text{ km} \times 1\text{ km}$. We use a random initial particle layout with 30 particles in each cell, and record their positions and other fields' variables at each computing step. All experiments described below were run at similar resolution on an Altix ICE 8200, 2.8 GHz, and 8 Mb per processor cluster.

Four possible conditions to simulate surface: (1) a free surface (Arnold et al., 2001; González et al., 2008; Hall et al., 2003; Schellart, 2008), (2) a sticky air-layer (viscosity set to $\sim 10^{19}\text{ Pa s}$; density set to 1 kg/m^3) overlying the surface to stop particles from escaping from the computing domain (Burov and Gerya, 2014; Gerya and Stöckhert, 2005; Gerya et al., 2008; Ueda et al., 2012) (3) a free-slip surface (Eberle et al., 2002; Mason et al., 2010; OzBench et al., 2008;

Schellart et al., 2010; Stegman et al., 2006; Zlotnik et al., 2013) or (4) a free remeshing surface (Foryan and Rasmussen, 1989; Koshizuka et al., 1998; Moresi et al., 2003; Shyy et al., 2012). We tested the option (1), (3) and (4) in this study. A free surface is completely free, without constraining horizontal and vertical velocities, but within codes such as Underworld, passive markers (particles) are lost when their stored historical data when they escape from the computational domain. The model also needs to refill with new particles in cells that become empty. A free-slip surface in turn does not allow for vertical motion and therefore over constrains this boundary. A free re-meshing surface as the one we have implemented here is one that couples a free surface with a re-meshing technique (Moresi et al., 2003), and which can carry the particles (passive markers) out of the ranges of the old mesh. Their history is stored into a new mesh according to their vertical velocities. We update/re-generate and deform the Eulerian mesh at every solution step. Particles and nodes carry various data used for outputs and subsequent step calculations. The particles located near the surface of the computing domain tend to escape when they store an upward velocity. The outline of the mesh is thus re-meshed and moved to ensure that these escaping particles remain inside the computational domain. Thanks to this procedure, the model can better model topographic evolution under various external boundary conditions, in compression (see case 1-1, case 1-1-1 and case 1-1-2 in Table 3) and simple shear (cases S-2-6, S-2-7, and S-2-8 depicted in Table 3).

In this paper, we test compressional (21 models) and simple shear with periodic boundary conditions (11 models, see the configurations given in Table 3) applied from each YZ wall side, applied at a rate of 5 mm/year respectively for about 4.5 Ma (shortening: 45 km) and 19 Ma (bulk shear strain $\gamma = 1.5$).

4. Results

A total of 32 models have been constructed to test the influence of various orientations of the pre-existing faults on the distribution

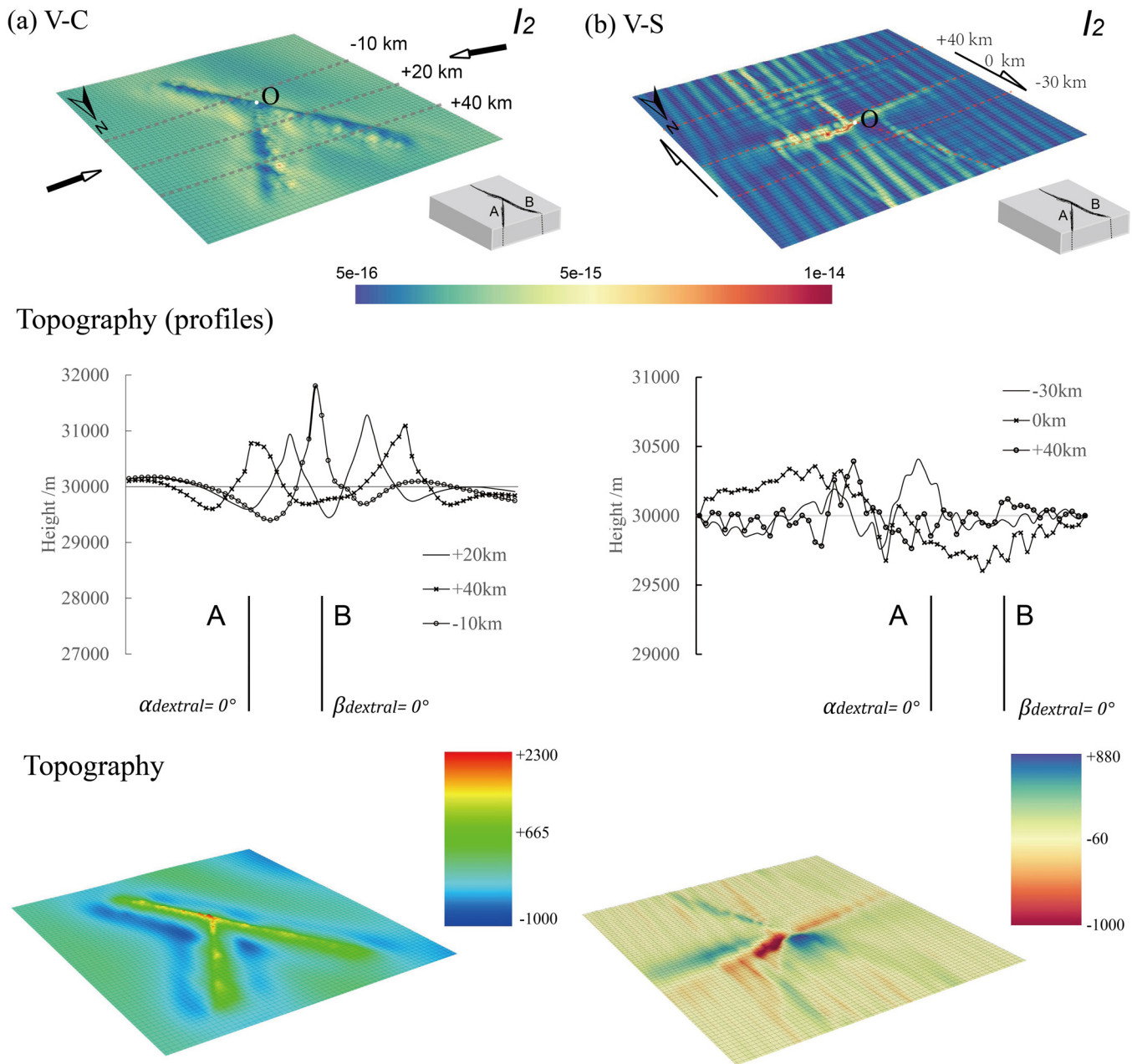


Fig. 3. Contour plots of the second (I_2 , s^{-1} , first row) invariants of strain rate and topographic profiles (second and third rows). For boundary conditions in compression (a) and simple shear (b). The intersection point of both faults is marked as point O in Fig. 2a. Topographic profiles of case V-C are displayed at $Y=+20$ km, $Y=+40$ km and $Y=-10$ km, at $Y=-30$ km, $Y=0$ km and $Y=+40$ km for case V-S, which are indicated by dashed lines in the first row.

of localized deformation and topographic evolution. The parameters are all listed in Table 3.

4.1. Influence of faults orientations

Firstly, we test the simplest system of two vertical faults under compressional (case V-C) and simple shear (case V-S) boundary conditions. The results under compressional boundary conditions are displayed in Fig. 3a, and show that deformation is evenly distributed along faults. Relief at the top surface of the model is approximately symmetrical along profiles at $Y=20$ km and $Y=40$ km, and reaches a maximum height of about 2 km along profile $Y=-10$ km when only fault B is present. When both faults are present, the highest relief reaches about 2300 m close to the faults intersection

zone (point O, $Y=0$). Maximum subsidence occurs along the south segment of fault B and in between both faults (about 500 m).

For the case V-S under simple shear boundary conditions (Fig. 3b), fault A which has an unfavourable orientation to the shearing direction will rotate synchronously to accommodate shear strain. The relief reaches a maximum height of 880 m and subsidence attains about -800 m around the intersection zone.

In Figs. 4–6, the results indicate that the angle of orientations of the pre-existing faults $\alpha_{dextral}$, $\beta_{dextral}$ controls the distribution of strain and relief. For experiments 2-6 and 2-4 in compression, the dip of fault A ($\alpha_{dextral}=60^\circ$) is double that of fault B ($\beta_{dextral}=30^\circ/150^\circ$), and deformation mostly focuses on the foot-wall of fault A, and less along fault B (Figs. 4a and 5a). The topographic profile of fault B in Fig. 4a with $\beta_{dextral}=30^\circ$ shows

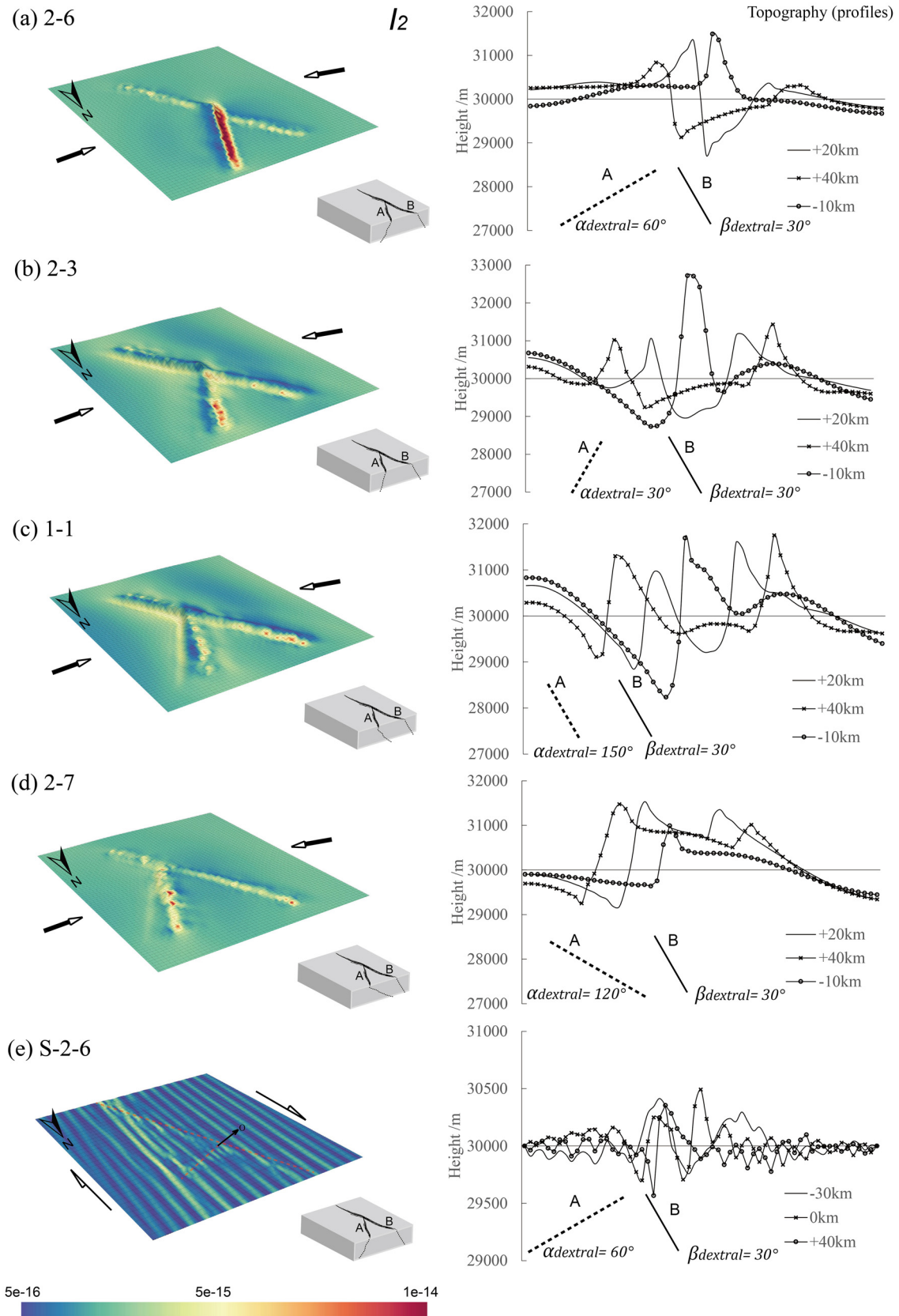


Fig. 4. The second (I_2 , s^{-1} , left column) invariants of strain rate and topography (right column) when using different fault A orientations at $\alpha_{dextral} = 30^\circ$, 60° , 120° , and 150° respectively (Fig. 2), fixing $\beta_{dextral}$ to 30° . In figure (a)–(d), compressional boundary conditions are applied. In figure (e), simple shear boundary conditions are applied. Topographic profiles using the free-remeshing surface boundary condition with legend displayed in Fig. 3. The dashed and solid lines labeled A and B in the right column represent the orientations of fault A and B, respectively. For other model details including model names and parameters, see details in Tables 1–3.

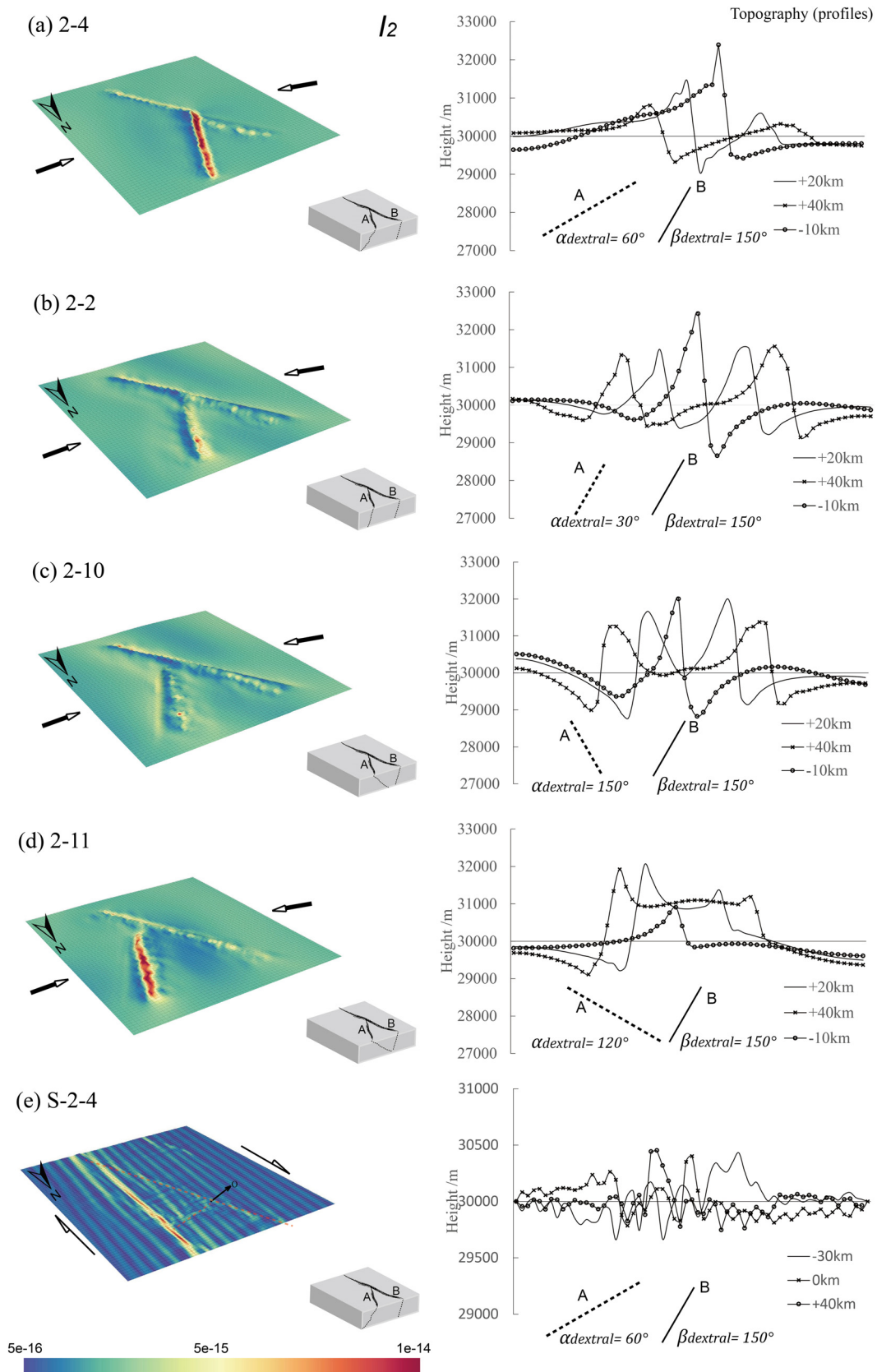


Fig. 5. The second (I_2 , s^{-1} , left column) invariants of strain rate when using different fault A orientations at $\alpha_{dextral} = 30^\circ$, 60° , 120° , and 150° respectively (Fig. 2), fixing $\beta_{dextral}$ to 150° compared to Fig. 4. In figure (a)–(d), compressional boundary conditions are applied. In figure (e), simple shear boundary conditions are applied. The right column shows topographic profiles using the free-remeshing surface boundary condition. Legends for topographic profiles are same as Figs. 3 and 4.

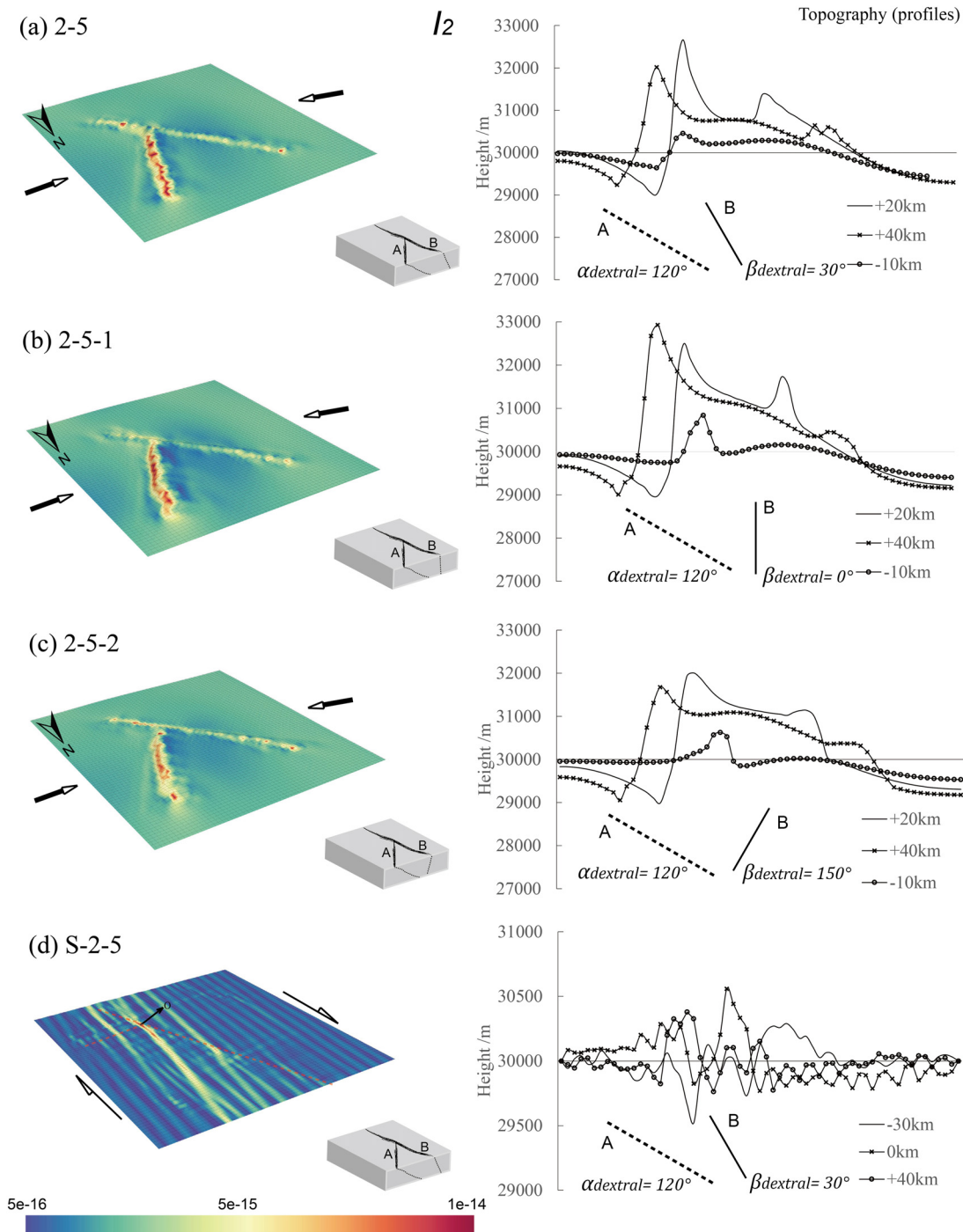


Fig. 6. The second (I_2 , s^{-1} , left column) invariants of strain rate and topography when varying the orientations of fault B ($\beta_{dextral} = 0^\circ$, 30° , and 150° (Fig. 2), and fixing $\alpha_{dextral}$ to 120° compared to Figs. 4 and 5. In figure (a)–(d) compressional boundary conditions are applied, whereas figure (e) displays the results for applied simple shear boundary conditions. See Fig. 3 and Table 3 for additional legend detail.

greater subsidence compared to Fig. 5a, where $\beta_{dextral} = 150^\circ$. Surface uplift primarily focuses in the hanging walls of fault A and B, and decreases when moving away from the intersection zone, as indicated by vertical sections along $Y = +20$ km, $+40$ km and -10 km in Fig. 3a.

Still in compression, we tested the dip of fault A (Figs. 4a–d and 5a–d), and varied $\alpha_{dextral}$ from 30° to 150° and $\beta_{dextral} = 30^\circ/150^\circ$, the variation in the tested dip resulted in different strain localization and topographic evolution. In case 2-7 ($\alpha_{dextral} = 120^\circ$, $\beta_{dextral} = 30^\circ$), subsidence occurs immediately above the intersection of fault A with the topography, and is located

adjacent to the main uplifting topography, which exceeds 1 km in height at a distance of about 10 km away from the southern side of the intersected zone. The orientation of fault A ($\alpha_{dextral}$) influences the subsidence associated with fault B, as shown in Fig. 5 by cases 2-4, 2-2, 2-10 and 2-11 ($\beta_{dextral} = 150^\circ$). The models produce a roughly symmetric topography when dips $\alpha_{dextral}$ and $\beta_{dextral}$ are identical, e.g., cases 2-3 and 2-10. Maximum subsidence of -1.5 km occurs in cases 1-1, where faults dip become parallel ($\alpha_{dextral} = 150^\circ$ and $\beta_{dextral} = 30^\circ$).

Note that in all these experiments, the negative segment (southern segment of point O, in Fig. 2a) contains only fault B. This

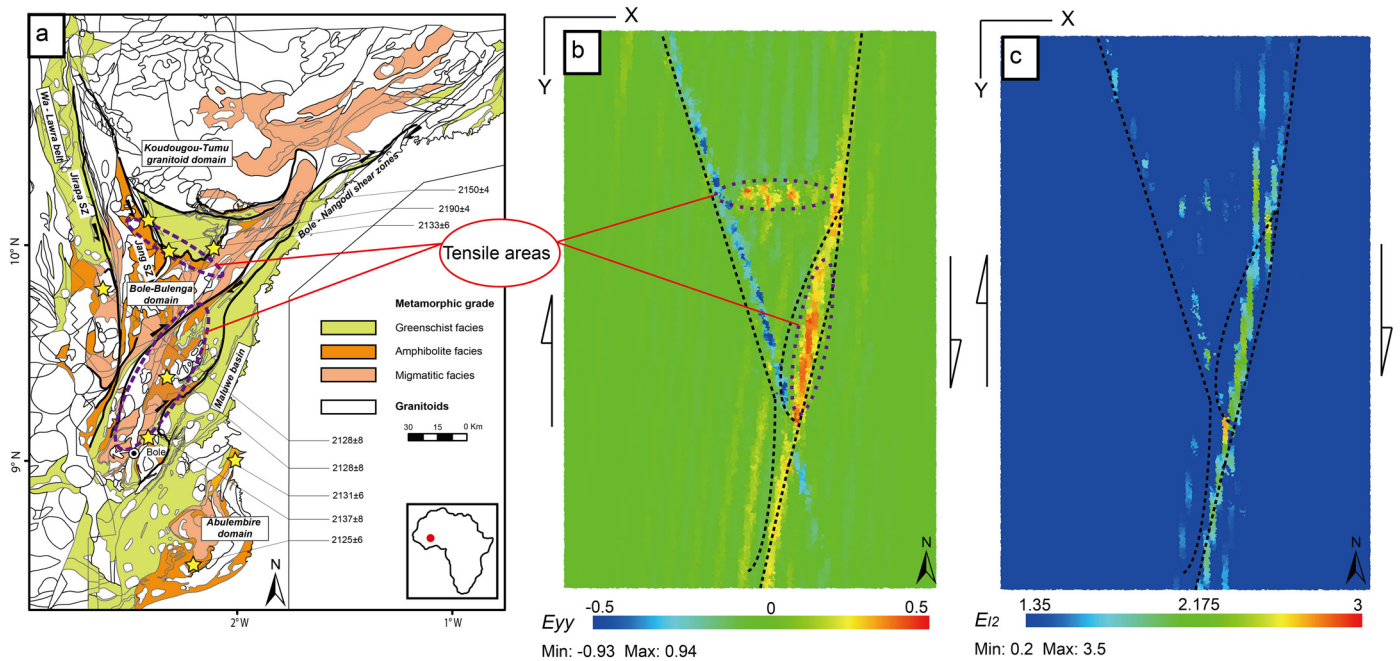


Fig. 7. (a) Metamorphic map of North-Western Ghana in the West African Craton and radiometric ages, modified from Block et al. (2015) and Baratoux et al. (2011). (b) The accumulation (E_{yy}) of strain rate component ϵ_{yy} , which is used as a proxy to indicate the finite strain zones (tensile and compressional areas) under simple shear boundary conditions. The dashed lines bound the major deformed regions. (c) The accumulation (E_{I_2}) of the second invariant of the strain rate (I_2 , s^{-1}). Dotted ellipses are used to indicate the major N-S tensile domains in the study area (figure (a)) by Block et al., 2015 and numerical results in the model (figure (b)). (For interpretation of the references to colour in the text, the reader is referred to the web version of the article.)

motivated another series of comparisons (Fig. 6), in which fault A's orientation is set fixed and equal to $\alpha_{dextral} = 120^\circ$, while fault B's orientation $\beta_{dextral}$ were varied at 0° , 30° and 150° . The resulting models indicate that surface uplift decreases with increasing $\beta_{dextral}$, with maximum height reaching about 3000 m at the faults' intersection zone (point O). In contrast, when the fault flips as for case $\beta_{dextral} > 90^\circ$, relief only reaches about 2000 m with uplift spatially distributed instead of being concentrated around point O.

Four cases in simple shear boundary conditions (Figs. 3b, 4e, 5e and 6d) are tested with variable dips and orientations similar to cases displayed in Figs. 3a, 4a, 5a and 6a. Angle $\alpha_{dextral}$ has a dominating role, with largest strain zones focusing in the internal domain in between both faults when $\alpha_{dextral} = 60^\circ$ (Figs. 4e and 5e). In turn, angle $\beta_{dextral}$ mainly influences the distribution of deformation and relief at the surface along fault B with the highest topographic point or relief reaching 500 m under simple shear (case S-2-6).

4.2. A strain pattern compatible to North-Western Ghana

Case S-2-6 produces a compatible strain pattern with field observation, characterized by two main structures bound the internal high strain domain. We have chosen to display the cumulated values over time (E_{yy} and E_{I_2}) of the strain rate component ϵ_{yy} in N-S direction and the second (I_2) invariant of the strain rate tensor respectively. This helps to identify domains in tensile (Figs. 7b and S1) and shear (Fig. 7c) for case S-2-6. E_{yy} values obtained, was within the interval $[-0.93, 0.94]$, and E_{I_2} ranged between the interval $[0.2, 3.5]$ over 19 Ma under simple shear boundary conditions. Tensile zones focus in the internal domain in between both faults and parallel to the eastern shearing direction ($E_{yy} > 0$, green to red). Compressional zones concentrate around the inherited fault B ($E_{yy} < 0$, green to blue). Shear zones ($E_{I_2} < 1.8$, light blue to red) focus along the inherited fault B and mainly overlap with the tensile areas (parallel to the eastern shearing direction, $E_{I_2} > 2$).

Supplementary Fig. S1 related to this article can be found, in the online version, at <http://dx.doi.org/10.1016/j.precamres.2015.06.006>

The angle ψ (Fig. 8) between the external shearing orientations and the misoriented fault A increases with time (rotating about 60° over 19 Ma, indicated by the grey lines with red arrows in Fig. 8b). The oriented fault B rotates about 15° over 19 Ma (indicated by the dotted black line with blue arrow in Fig. 8b).

4.3. Influences of rock density and host rock friction

Here we use a reference model case 1-1 (under compression, $\alpha_{dextral} = 150^\circ$ and $\beta_{dextral} = 30^\circ$, Fig. 4c). Figs. 9 and 10 show that a more resistant surrounding host rock causes greater localized deformation and higher elevations along faults A and B. Cases 2-12 and 2-9 with lower host rock friction (thus closer to the internal faults friction) generate four new shear bands rooting at the base of the model domain, nearly independent from the pre-existing faults. As expected, the shear bands angle increases towards 45° with decreasing rock friction (e.g. Lemiale et al., 2008). We also document the influence of host rock friction under simple shear boundary conditions (case S-5, S-5-1 and S-5-2). These tests illustrate how a smaller contrast in friction between internal (faults) and external (host) domains tends to destroy the initial geometry and perhaps even the continuity (e.g. coherency) of pre-existing fault systems, relating with the effects of the Drucker-Prager yield criterion and lithostatic pressure.

Density variations do not play a primary role in building topography compared to the effect of host rock friction at the scale of a crustal system. When increasing by 200 kg/m^3 the host rock density, topographic height respectively increases by 200 m and 300 m at the highest uplifted point at the intersection of faults A and B (point O). Fig. 10 shows that using a friction angle 30° or 20° produce a similar height (elliptic domain in light green). While when setting a host rock friction angle to 20° and 10° (respectively in blue and light red ellipses), topography height drops by about 1200 m. In

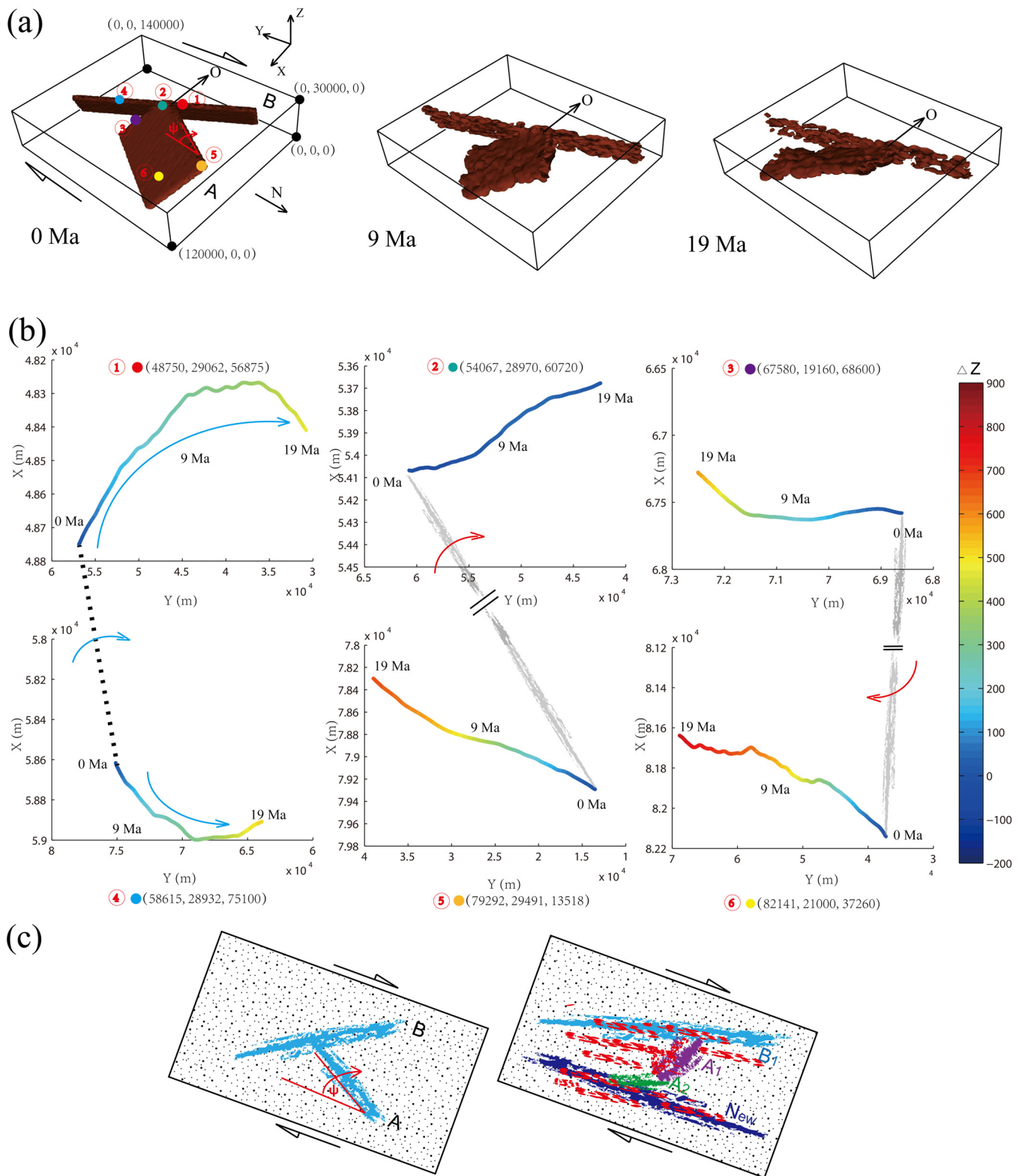


Fig. 8. Analysis of crustal rocks motion under simple shear boundary conditions (case S-2-6). (a) The evolution of faults geometries at 0 Ma, 9 Ma, and 19 Ma. (b) Coordinates of six representative points, initial positions are displayed by a filled colour circle in (figure (a)). Red and blue circles display passive markers (particles) located along fault B (near surface), while green, orange, purple and yellow circles are particles located in fault A. Red and blue arrows sketch the main trends of faults through time. The light grey and dotted lines represent the initial position of fault A and B (joining markers), indicating fault rotation through time. The colour bar for lines in figure (b) represents the uplifted trajectory (ΔZ) of these particles. (c) Sketch showing the evolution of faults geometries. The red dots sketch the possible channels of the upwelling molten material (Figs. 7, 8 and S1). (For interpretation of the references to colour in this figure legend, the reader is referred to the web version of the article.)

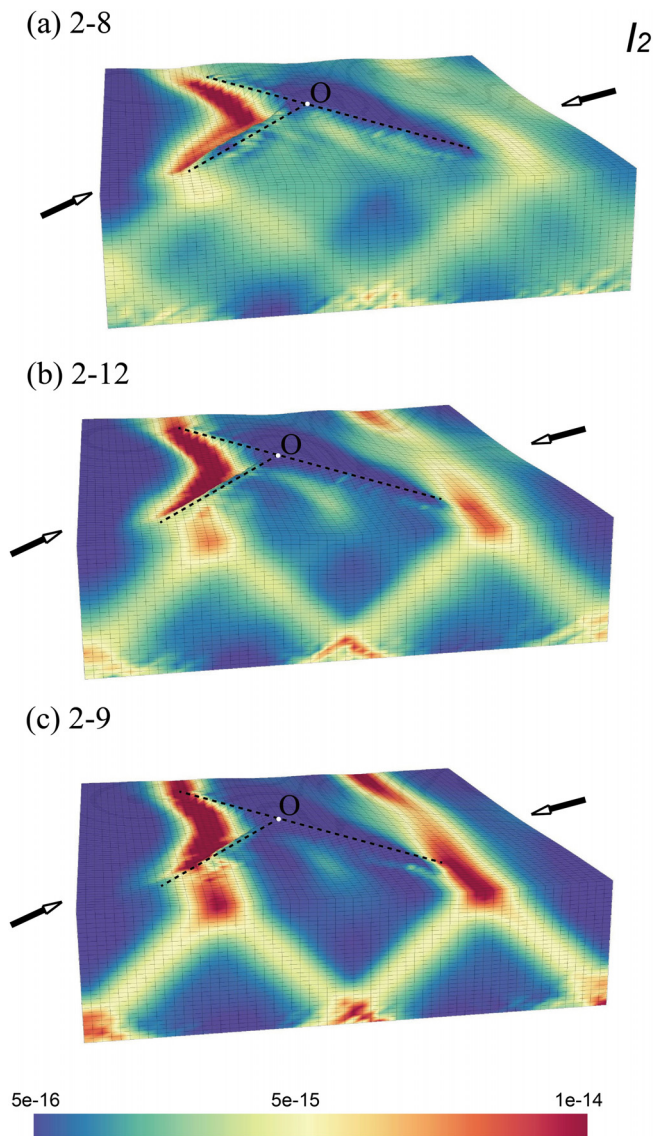


Fig. 9. The second (I_2 , s^{-1}) invariants of strain rate influenced by host rock friction angle under compressional boundary conditions. To the difference with the reference model (case 1-1, friction angle = 30° , Fig. 4c), upper crust friction angles of 20° , 15° , 10° (from top to bottom).

comparison, a variable density of the fault rocks tested in cases 1-2, 1-3, 1-4, produces roughly similar topography (slightly inclined lines in Fig. 10).

4.4. Effect of the top surface boundary condition

In Fig. 11 we have selected four near-surface passive markers (physical particles) to trace field data. The results show that the physical particles, when accounting for a free surface boundary condition, lose their historic data after about 12.5 Ma in simple shear, and after about 1–2 Ma in compression due to escaping (Fig. 11a and d). In the case with a top free-slip boundary condition, the uplifting process is greatly constrained by the fixed vertical motion at the surface (Fig. 11b and e). These tests show the advantages of implementing a free-remeshing surface boundary condition when modelling the evolution of Earth's surface using particle in cell (PIC) method.

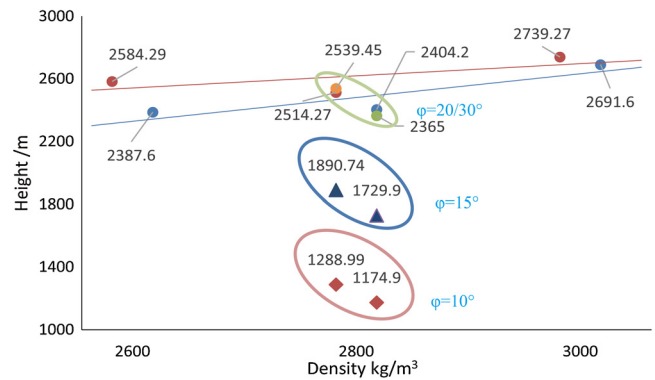


Fig. 10. Relief influenced by host rock friction angle and density contrast under compressional boundary conditions. A representative point at the faults' intersection (point O), as well as the maximum uplifted height of each model. Topographic height respectively increases by 200 m and 300 m at point O when increasing by 200 kg/m^3 the host rock density. Topographic height when using host rock friction angles of 30° or 20° produce similar heights (elliptic domain in light green in figure (d)). Setting a friction angle to 15° and 10° (respectively covered by the blue and light red ellipses), drops the topography by about 600 m. In all experiments, the contrast in density has a smaller effect on topography than the host rock friction angle. (For interpretation of the references to colour in this figure legend, the reader is referred to the web version of the article.)

5. Discussion

5.1. Strain and relief

The second invariant of the strain rate highlights shearing domains (greatest in red, in Figs. 3–7, 9 and 12), following several previous studies that have proposed that high-strain zones (shear and tension zones) could play a significant role in the draining of residual fluids from deeper retention zones at the strain rate of 10^{-15} s^{-1} to $\sim 10^{-10} \text{ s}^{-1}$ indicated by structure (Fernández and Castro, 1999), analogue (Benn et al., 1998) and numerical models (Cruden, 1998; Berdiel et al., 1997), feeding the upper crust with partially molten lower crustal rocks (Fossen and Tikoff, 1998; Neves et al., 1996, 2000; Pereira et al., 2013; Snoke et al., 1999; Weinberg et al., 2006).

Effective strength heterogeneities due to pre-existing faults trigger strain rotation and produce preferential sites for shear strain with respect to the surrounding rocks (e.g. Mair and Abe, 2008; Nieto-Samaniego, 1999). Our numerical models show that high-strain zones focus along and in between both faults A and B. The highest uplifted point is close to the intersection region which may focus fluids flow (Lawley et al., 2013), the peak fluid velocities increase 20–47% when the fault zone intersections enlarge apertures only about 1–8% (Person et al., 2012). Large localized deformation appears at the two faults' intersection zone and along faults using the free-remeshing surface boundary condition. Models with top-free boundary conditions lose a large amount of data due to particles escape out of the domain, whereas those with free-slip boundary conditions limit the accuracy in modelling surface processes because the vertical motion of the surface is prevented, in particular around high strain/uplifted zones (Fig. 11).

Our models, similarly to analogue models which yet assume different initial and boundary conditions, reproduce large block rotations at large amounts of strike-slip motion. Under compression, the host rock domain in between the two faults concentrate shear deformation relatively faster (about 2–5 times) than other domains (case 1-1, in Figs. 4 and 12), which is consistent with the description by Fossen and Tikoff (1998). They discussed the distribution of wrenching into shearing and vertical components, with both constriction and extrusion domains whatever the obliquity of the boundary conditions. In our models, large shearing

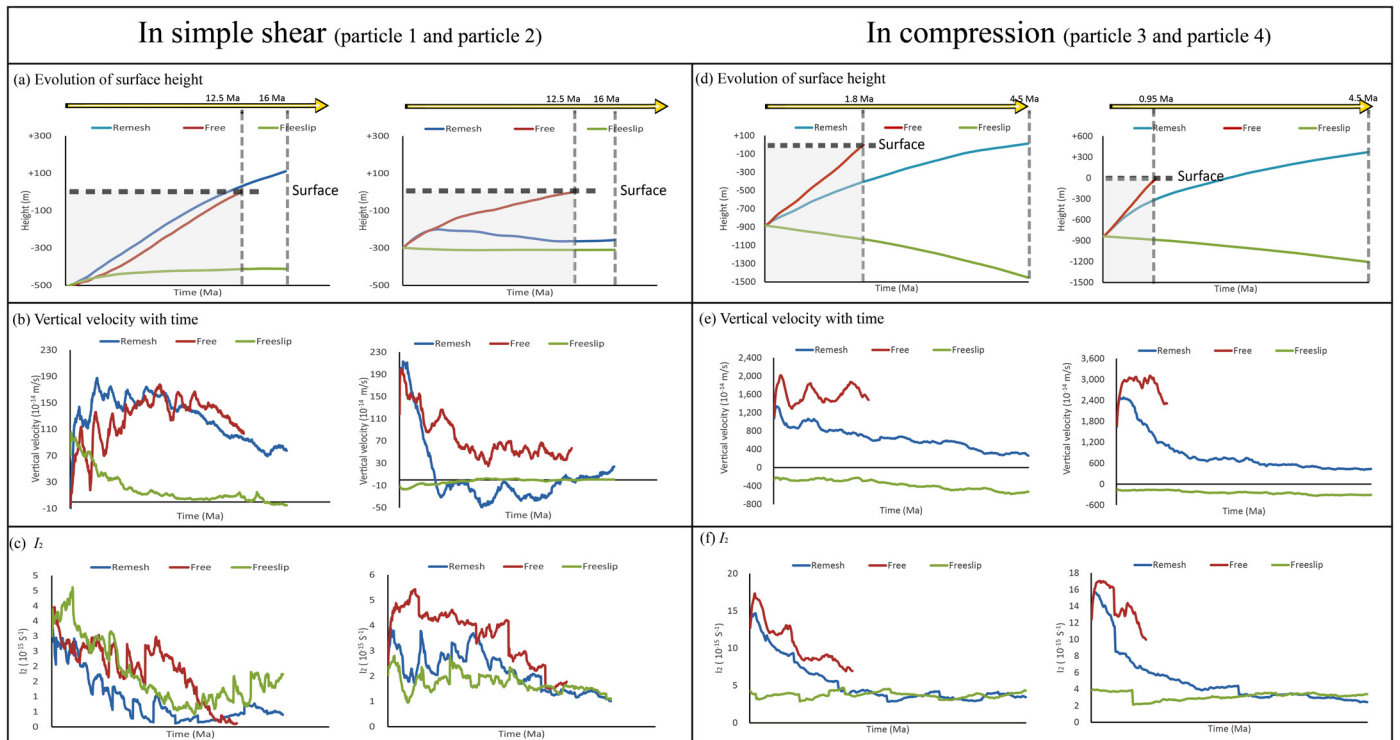


Fig. 11. Effect of top surface boundary conditions (cell particles) in case S-2-6 (left column: simple shear) and case 1-1 (right column: compression) by recording properties of tracers when using a free re-meshing surface, free and free-slip top surface boundary conditions, respectively, see Table 3 for details. Four near-surface particles were selected to trace data (surface height in figure (a) and (d), vertical velocity in figure (b) and (e) and the second invariant of strain rate I_2 in figure (c) and (f)) through time. Their coordinates (Figs. 2 and 8a) in metres are (X, Z, Y): particle 1 (79,292, 29,491, 13,518), particle 2 (73,352, 29,701, 99,471), particle 3 (96,320, 29,115, 28,924), and particle 4 (76,560, 29,163, 93,712). Physical particles under free surface boundary conditions lose their historic data after about 12.5 Ma in simple shear (particle 1 and particle 2) and after about 1.0–2.0 Ma in compression (particle 3 and particle 4) due to their escaping from the mesh domain. For models under free-slip top boundary conditions, surface uplift is over constrained by the imposed 0 vertical motion condition (figure (b) and figure (e)).

deformations develop along and in between faults at depth, which may consequently act as favourable areas to channel molten material from the lower crust and upwelling into the upper crust (Fig. 12) (Rosenberg and Handy, 2000; Katz et al., 2006; Koyi et al., 2013; Lawley et al., 2013; Mourgues et al., 2012). In addition, heterogeneous shearing zones evolving with time at depth would influence the geometry of pathway for channelling partially molten material. Based on our numerical results, we have sketched the evolving deformation and rotation (towards the vertical line) process in compression (Fig. 12b).

For models under simple shear boundary conditions (Figs. 3b, 4e, 5e and 6d), pre-existing faults mainly accommodate strain distribution, as long as they are not too radically misoriented with respect to the external shearing conditions, such as fault B in Fig. 2. When faults are radically misoriented, such as fault A in Fig. 2, they tend to rotate with the overall strain (and stress) field and synchronously accommodate less strain than optimally oriented faults. The noise of simple shear models occurs because the sample boundary is never perfectly flat (as in the real world situation) due to numerical fluctuations in the particle locations, and to a mild interference effect between the array of particles and the underlying grid (Moresi et al., 2001).

Relief is controlled by the rock hardness, homogeneity, external boundary conditions, mantle convection and the geometry of faults systems (Amadei and Stephansson, 1997; Bois et al., 2012; Brown and Scholz, 1985; Brown et al., 1986; Moucha and Forte, 2011). A recent numerical model developed by Braun et al. (2014), showed that rock density also plays an important role in shaping relief at the scale of the Earth. Considering pre-existing faults, structure development and topographic uplift have been shown to be controlled by the reactivation of pre-existing

faults under renewed boundary conditions associated with the rotation of principal forces (Ju et al., 2014; Tong et al., 2014; Wibberley et al., 2008). Testing different orientations show a direct relation with the distribution of uplifted areas. In comparison to the effect of the friction angle, the density contrast does not play a primary role in shaping the relief at the scale of the study area in these models (similarly to sand prism in analogue models, Graveleau et al., 2011, 2012 and references therein).

5.2. Reconstruction: model application to the Bole-Bulenga terrane

High-strain zones (tensile zones in Figs. 7b and S1, corresponding to N-S-directed extension, shear zones in Fig. 7c) mainly focus parallel to the eastern shearing direction and internal domains of both structures, which is similar with the distribution of high grade rock in the Bole-Bulenga terrane in Fig. 3a.

From deformation phase D1 (dominantly characterized by E-W to WNW-directed shortening, evidence from western Burkina Faso by Baratoux et al., 2011) to the subsequent D2 (characterized by N-S directed extension, Block et al., 2015), changes in the direction of principal forces must occur in the study area, resulting in a transition deformation phase for accumulating strain from far field boundary conditions. We suggest that our modelled pre-existing faults grew and developed during this short stage (case S-2-6). Fault A becomes a non-favoured location to accommodate strain from its eastern side (right-hand) as angle ψ increases through time. A large amount of localized deformation will tend to occur parallel to the eastern shearing direction (Figs. 7 and S1). This newly produced tensile and shear zone together with the favourably

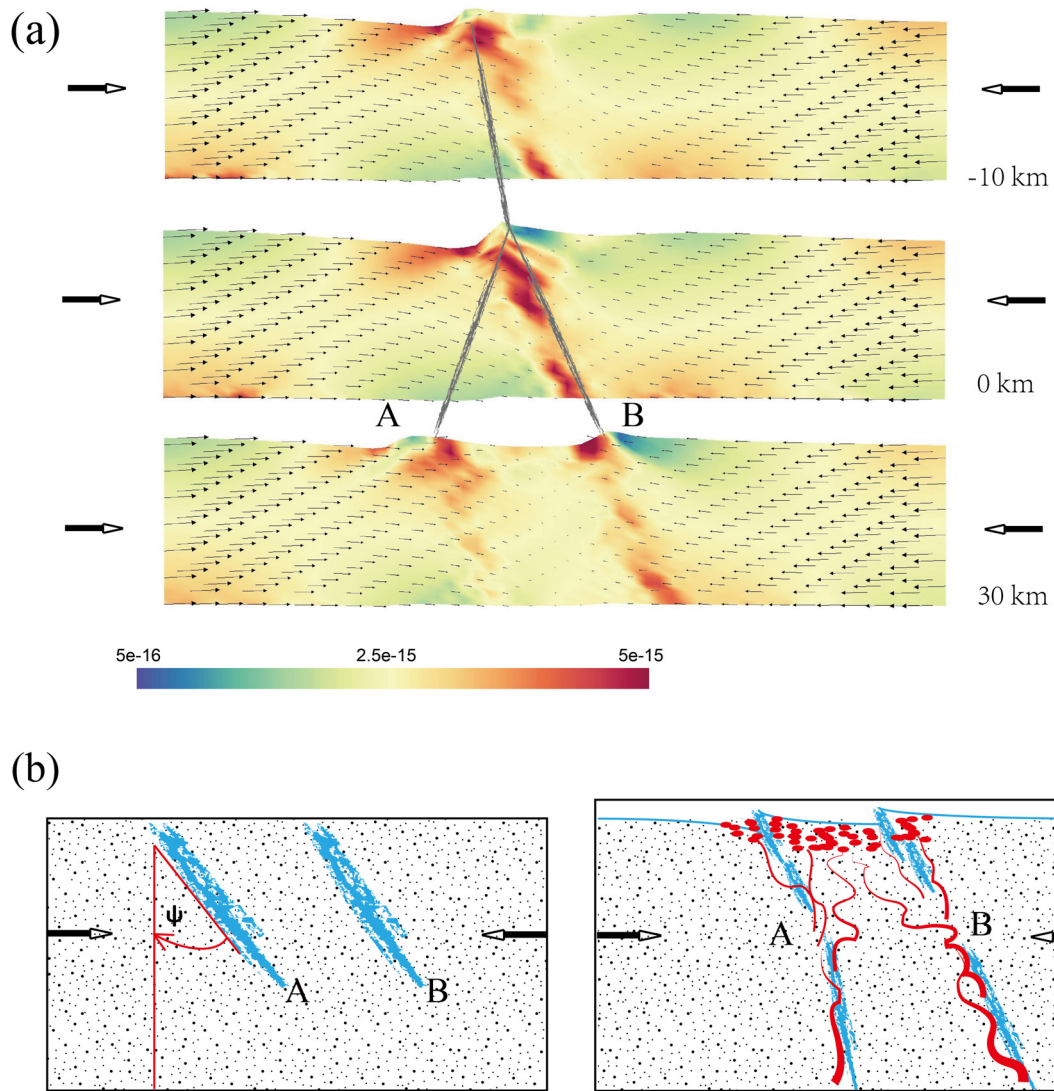


Fig. 12. Profiles of the second (I_2, s^{-1}) invariant of strain rate with velocity vectors (case 1-1) after about 4.5 Ma under compressional boundary conditions, and along selected profiles at $Y = -10$ km, 0 km and 30 km. The outlines of fault A and B are plotted in light grey above these sections. (e) Sketch showing the evolution of faults geometries (in blue) under compressional boundary conditions according to the numerical results. The angle ψ in figure (b) indicates that fault A rotates clockwise with time (towards vertical). The red dots and lines represent inferred favourable areas that would channel partially molten material/fluids from the lower crust and extrude in the upper crust. (For interpretation of the references to colour in this figure legend, the reader is referred to the web version of the article.)

oriented fault B form a compatible strain pattern with the field, characterized by two main high-strain zones with the bounded internal high-strain domain (A1 particles in purple, sketched in Fig. 8c). Fluids or partially molten materials may store in the deepest root of the pre-existing shear zones (Morand, 1992; Berdiel et al., 1997; D'Lemos et al., 1992; Pirajno, 2010). By taking fault

rotation into consideration, this suggests that they may passively migrate and rotate together (Fig. 8b) with the solid matrix under external boundary conditions through geological time, preferentially intruding into the upper crust, which can probably be interpreted as a potential contribution to exhumation in the study area.

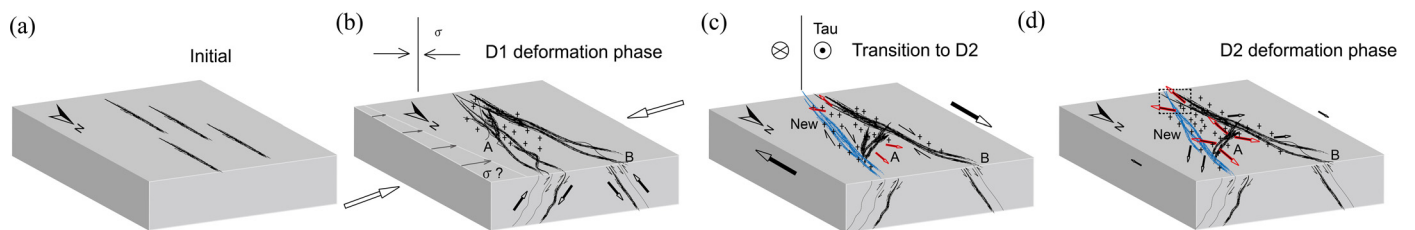


Fig. 13. Reconstruct and sketch the tectonic scenario during D1–D2 deformation phase for the study area. Figures (a)–(d) correspond to initial condition, D1 phase, late-D1 – early D2 transition phase and post-D2 phase, respectively (Block et al., 2015; Baratoux et al., 2011.). The crosses in the figures represent weak domains, the red arrows represent the stretching direction according to the findings of Block et al. (2015). During its N–S-directed extensional process, the fault New in blue transects the internal domains, merges and intersects with the inherited fault B (indicated by the dotted box). (For interpretation of the references to colour in this figure legend, the reader is referred to the web version of the article.)

These cumulative high-strain zones may exhume part of partially molten materials from the lower crust during this transition stage. This is evident by the broad range of crystallization age in the field (in Fig. 7a, 2195 Ma to ~2125 Ma). More importantly, these high-strain zones make a significant contribution to offering preferred/potential zones (tensile and shearing zones) for the major exhumation event during the following post-D2 N-S stretching deformation phase. This theoretical model is consistent with the findings of Block et al. (2015). The P-T paths of samples collected in the Bole-Bulenga terrane indicate that during this late D2 deformation phase, high grade rocks were largely exhumed through the upper crust (>10 km) along the reverse, normal and transcurrent shear zones. According to the numerical results, we reconstruct and sketch the tectonic scenario during D1–D2 deformation phase (Baratoux et al., 2011; Block et al., 2015) for the study area in Fig. 13.

6. Limitations and perspectives

As discussed in Fossen and Tikoff (1998), it is difficult to track the evolution of strain orientations and magnitude within high-strain shear zones, because by definition shearing and constrictional components evolve in time, this becomes worse if the medium is heterogeneous and if deformation is partitioned. The numerical models presented here show how delicate it is to represent the long term evolution of strain components in numerical models, and we aim at improving these representations of strain components in future numerical approaches (e.g. strain ellipsoids as in Gerbault et al., 2002, or lines of maximum finite strain tensor as in Le Pourhiet et al., 2012), in order to better identify constrictional and tensile structural domains. We deliberately did not introduce any melting process in order to first understand the appropriate requirements on the mechanical state of the solid upper crust, although this is a focus of future studies. A number of analogue models have explored this question via significantly different experimental setups in which the modelled crustal layers are underlain by mechanical discontinuities such as strike-slip basement faults or basal weak zones (see reviews by Dooley and Schreurs, 2012, and references therein). It would be delicate but interesting to explore with analogue models the influence of pre-existing systems of weak fault zones as those we have considered here.

In addition, we mostly discussed the role of crustal strength variations and density contrast in producing relief at crustal scale using a viscous material (Cook and Royden, 2008). In the near future, in order to fulfil a completed topography, a crust-mantle coupled interaction should be taken into consideration for including dynamic topography.

7. Conclusion

In this paper, we use a three-dimensional thermo-mechanical model to explore the distribution of high-strain domains associated with pre-existing shear zones, by testing various orientations of a system of two strike-slip faults under pure shear as well as simple shear boundary conditions. We have also tested the effects of the friction angle and density contrast on the evolution of relief.

We reconstructed the evolution of deformation in North-Western Ghana around 2.20–2.10 Ga, the result shows that the Bole-Bulenga terrane may undergo a major transition in association with changes in the directions of principal forces from deformation phase D1 to D2. These cumulative high-strain zones may exhume part of partially molten materials from the lower crust during this stage, this can probably be evidenced by the broad range of crystallization age in the field (In Fig. 7a, 2195 Ma to ~2125 Ma). More

importantly, these high-strain zones make a significant contribution to offering preferred/potential zones (tensile and shearing zones) for the major exhumation event during the following post-D2 N-S stretching deformation phase.

The resulting model shows the formation of domains of tensile vs. compressional strain as well as shear zones, shows that the internal fault zones as well as the host rock in between the faults behave as relatively weaker domains than external regions.

The orientations of faults play an important role in controlling the evolution of relief. Greatest magnitudes of relief are obtained when faults dip parallel to each other and when they are inclined at depth, as they thus facilitate strain rotation and material transfer from depth. Relief increases by 200–300 m when the host rock density is increased by 200 kg/m³, whereas relief reduces by about 1200 m when decreasing the host rock friction from $\varphi = 20^\circ$ to 10° at crustal scale.

Acknowledgements

This work was granted access to the high-performance computing resources of both the French supercomputing centre, CCRT of the French Nuclear Agency, under allocation #2014-046351 awarded by GENCI (Grand Equipement National de Calcul Intensif), and the regional computing centre, CALMIP in Toulouse, France, under allocation #P1403. We would like to thank Muriel Gerbault for kindly providing many helpful comments and discussions at different stages of the project. We also thank the development teams at the Victorian Partnership for Advanced Computing (VPAC) and Monash University for technical assistance with the software Underworld. We gratefully acknowledge John Mansour and Luke Mondy for improving a previous version of the code. Sylvain Block is warmly thanked for providing radiometric ages of some samples and comments. Figures are plotted using open source package Visit developed by the Lawrence Livermore National Laboratory. X.F. thanks the Chinese Scholarship Council for his PhD scholarship. Constructive and valuable comments by Laurent Ailleres, an anonymous reviewer and Editor Peter Cawood are gratefully acknowledged.

References

- Adjei, 1992. The significance of NE-SW parallel fractures in the West African Craton. In: *Proceedings of the International Conferences on Basement Tectonics*, vol. 7, pp. 49–60.
- Agyei Duodu, J., Loh, G.K., Boamah, K.O., 2009. *Geological Map of Ghana 1:1 000 000*. Geological Survey Department of Ghana (GSD).
- Alberti, M., 2010. Analysis of kinematic correlations in faults and focal mechanisms with GIS and Fortran programs. *Comput. Geosci.* 36, 186–194.
- Allibone, A., Teasdale, J., Cameron, G., Etheridge, M., Uttley, P., Soboh, A., Lamb, E., 2002. Timing and structural controls on gold mineralization at the Bogoso gold mine, Ghana, West Africa. *Econ. Geol.* 97, 949–969.
- Amadei, B., Stephansson, O., 1997. *Rock Stress and Its Measurement*. Springer Science Business Media.
- Amponsah, P.O., Salvi, S., Béziat, D., Jessell, M.W., Siebenaller, L., Baratoux, L., 2015. Geology and geochemistry of the shear-hosted Julie deposit, NW Ghana. *J. Afr. Earth Sci.*, <http://dx.doi.org/10.1016/j.jafrearsci.2015.06.013>
- Arnold, J., Jacoby, W.R., Schmeling, H., Schott, B., 2001. Continental collision and the dynamic and thermal evolution of the Variscan orogenic crustal root – numerical models. *J. Geodyn.* 31, 273–291.
- Avé Lallemand, H.G., Guth, L.R., 1990. Role of extensional tectonics in exhumation of eclogites and blueschists in an oblique subduction setting: Northeastern Venezuela. *Geology* 18, 950–953.
- Avouac, J.P., Burov, E.B., 1996. Erosion as a driving mechanism of intracontinental mountain growth. *J. Geophys. Res.* 101, 17747–17769.
- Baratoux, L., Metelka, V., Naba, S., Jessell, M.W., Grégoire, M., Ganne, J., 2011. Juvenile Paleoproterozoic crust evolution during the Eburnean orogeny (<2.2–2.0 Ga), western Burkina Faso. *Precambrian Res.* 191, 18–45.
- Berdiel, T.R., Gapais, D., Brun, J.P., 1997. Granite intrusion along strike-slip zones in experiment and nature. *Am. J. Sci.* 297, 651–678.
- Benn, K., Odonne, F., De Saint Blanquat, M., 1998. Pluton emplacement during transpression in brittle crust: new views from analogue experiments. *Geology* 26, 1079–1082.

- Block, S., Ganne, J., Baratoux, L., Zeh, A., Parra-Avila, A.L., Jessell, M., Ailleres, L., Siebenaller, L., 2015. Petrological and geochronological constraints on lower crust exhumation during Paleoproterozoic (Eburnean) orogeny, NW Ghana, West African craton. *J. Metamorph. Geol.* 33, 463–494.
- Boher, M., Abouchami, W., Michard, A., Albaredo, F., Arndt, N.T., 1992. Crustal growth in West Africa at 2.1 Ga. *J. Geophys. Res.* 97, 345–369.
- Bois, T., Bouissou, S., Jaboyedoff, M., 2012. Influence of structural heterogeneities and of large scale topography on imbricate gravitational rock slope failures: new insights from 3-D physical modeling and geomorphological analysis. *Tectonophysics* 526–529, 147–156.
- Braun, J., Beaumont, C., 1995. Three-dimensional numerical experiments of strain partitioning at oblique plate boundaries: implications for contrasting tectonic styles in the southern Coast Ranges, California, and central South Island, New Zealand. *J. Geophys. Res. Atmos.* 1001, 18059–18074.
- Braun, J., Yamato, P., 2010. Structural evolution of a three-dimensional, finite-width crustal wedge. *Tectonophysics* 484, 181–192.
- Braun, J., Simon-Labric, T., Murray, K.E., Reiners, P.W., 2014. Topographic relief driven by variations in surface rock density. *Nat. Geosci.* 7, 534–540.
- Brown, S.R., Scholz, C.H., 1985. Broad bandwidth study of the topography of natural rock surfaces. *J. Geophys. Res.* 90, 12575–12582.
- Brown, S.R., Kranz, R.L., Bonner, B.P., 1986. Correlation between the surfaces of natural rock joints. *Geophys. Res. Lett.* 13, 1430–1433.
- Buck, W.R., Lavie, L.L., 2001. A tale of two kinds of normal fault: the importance of strain weakening in fault development. *Geol. Soc. Lond. Spec. Publ.* 187, 289–303.
- Burov, E., Gerya, T., 2014. Asymmetric three-dimensional topography over mantle plumes. *Nature* 513, 85–89.
- Cagnard, F., Brun, J.P., Gapais, D., 2006a. Modes of thickening of analogue weak lithospheres. *Tectonophysics* 421, 145–160.
- Cagnard, F., Durrieu, N., Gapais, D., Brun, J.P., Ehlers, C., 2006b. Crustal thickening and lateral flow during compression of hot lithospheres, with particular reference to Precambrian times. *Terra Nova* 18, 72–78.
- Cagnard, F., Gapais, D., Barbey, P., 2007. Collision tectonics involving juvenile crust: the example of the southern Finnish Svecofennides. *Precambrian Res.* 154, 125–141.
- Castaing, C., Billa, M., Milési, J.P., Thiéblemont, D., Le Metour, J., Egal, E., Donzeau, M., (BRGM) (Coordonnateurs) et Guerrot, C., Cocherie, A., Chevremont, P., Tegye, M., Itard, Y., (BRGM), Zida, B., Ouédraogo, I., Koté, S., Kaboré B.E., Ouédraogo C., (ANTEA), 2003a. Notice explicative de la carte géologique et minière du Burkina Faso à 1/1 000 000.
- Castaing, C., Le Metour, J., Billa, M., (Coordonnateurs) Donzeau, M., Chevremont, P., Egal, E., (BRGM) Zida, B., Ouédraogo, I., Koté, S., Kaboré B.E., Ouédraogo, C., (BUMIGEB), Thiéblemont, D., Guerrot, C., Cocherie, A., Tegye, M., Milési J.P., Itard, Y., (BRGM), 2003b. Carte géologique et minière du Burkina Faso à 1/1 000 000.
- Chardon, D., Gapais, D., Cagnard, F., 2009. Flow of ultra-hot orogens: a view from the Precambrian, clues for the Phanerozoic. *Tectonophysics* 477, 105–118.
- Condie, K.C., Kröner, A., 2008. When did plate tectonics begin? Evidence from the geologic record. *Geol. Soc. Am. Spec. Pap.* 440, 281–294.
- Cook, K.L., Royden, L.H., 2008. The role of crustal strength variations in shaping orogenic plateaus, with application to Tibet. *J. Geophys. Res.* 113, B8407.
- Cruden, A.R., 1998. On the emplacement of tabular granites. *J. Geol. Soc. Lond.* 155, 853–862.
- D'Alessio, M.A., Martel, S.J., 2004. Fault terminations and barriers to fault growth. *J. Struct. Geol.* 26, 1885–1896.
- De Kock, G.S., Armstrong, R.A., Siegfried, H.P., Thomas, E., 2011. Geochronology of the Birim Supergroup of the West African craton in the Wa-Bolè region of west-central Ghana: implications for the stratigraphic framework. *J. Afr. Earth Sci.* 59, 1–40.
- D'Lemos, R.S., Brown, M., Strachan, R.A., 1992. Granite magma generation, ascent and emplacement within a transpressional orogen. *J. Geol. Soc.* 149, 487–490.
- Dioh, E., Béziat, D., Debat, P., Grégoire, M., Ngom, P.M., 2006. Diversity of the Palaeoproterozoic granitoids of the Kédougou inlier (eastern Sénégal): petrographical and geochemical constraints. *J. Afr. Earth Sci.* 44, 351–371.
- Dooley, T.P., Schreurs, G., 2012. Analogue modelling of intraplate strike-slip tectonics: a review and new experimental results. *Tectonophysics* 574–575, 1–71.
- Doumbia, S., Pouclet, A., Kouamelan, A., Peucat, J.J., Vidal, M., Delor, C., 1998. Petrogenesis of juvenile-type Birimian (Paleoproterozoic) granitoids in Central Côte-d'Ivoire, West Africa: geochemistry and geochronology. *Precambrian Res.* 123, 47–65.
- Eberle, M.A., Grasset, O., Sotin, C., 2002. A numerical study of the interaction between the mantle wedge, subducting slab, and overriding plate. *Phys. Earth Planet. Inter.* 134, 191–202.
- Egal, E., Thiéblemont, D., Lahondère, D., Guerrot, C., Costea, C.A., Iliescu, D., Delor, C., Goujou, J.C., Lafon, J.M., Tegye, M., Diaby, S., Kolié, P., 2002. Late Eburnean granitization and tectonics along the western and northwestern margin of the Archean Kénéma-Man domain (Guinea, West African Craton). *Precambrian Res.* 117, 57–84.
- Feybesse, J.L., Billa, M., Guerrot, C., Duguey, E., Lescuyer, J.L., Milesi, J.P., Bouchot, V., 2006. The paleoproterozoic Ghanaian province: geodynamic model and ore controls, including regional stress modeling. *Precambrian Res.* 149, 149–196.
- Fernández, C., Castro, A., 1999. Pluton accommodation at high strain rates in the upper continental crust. The example of the Central Extremadura batholith, Spain. *J. Struct. Geol.* 21, 1143–1149.
- Fialko, Y., Rivera, L., Kanamori, H., 2005. Estimate of differential stress in the upper crust from variations in topography and strike along the San Andreas Fault. *Geophys. J. Int.* 160, 527–532.
- Fialko, Y., 2006. Interseismic strain accumulation and the earthquake potential on the southern San Andreas fault system. *Nature* 441, 968–971.
- Fishwick, S., Bastow, I., 2011. Towards a better understanding of African topography: a review of passive-source seismic studies of the African crust and upper mantle. *Geol. Soc. Lond. Spec. Publ.* 357, 343–371.
- Foryan, J.M., Rasmussen, H., 1989. Numerical methods for viscous flows with moving boundaries. *Appl. Mech. Rev.* 42, 323–341.
- Fossen, H., Tikoff, B., 1998. Extended models of transpression and transtension, and application to tectonic settings. *Geol. Soc. Lond. Spec. Publ.* 135, 15–33.
- Ganne, J., De Andrade, V., Weinberg, R.F., Vidal, O., Dubacq, B., Kagambega, N., Naba, S., Baratoux, L., Jessell, M., Allibon, J., 2011. Modern-style plate subduction preserved in the Palaeoproterozoic West African craton. *Nat. Geosci.* 5, 60–65.
- Ganne, J., Gerbault, M., Block, S., 2014. Thermo-mechanical modeling of lower crust exhumation—constraints from the metamorphic record of the Palaeoproterozoic Eburnean orogeny, West African Craton. *Precambrian Res.* 243, 88–109.
- Gasquet, D., Barbey, P., MADou, B., Paquette, J., 2003. Structure, Sr–Nd isotope geochemistry and zircon U–Pb geochronology of the granitoids of the Dabakala area (Côte d'Ivoire): evidence for a 2.3 Ga crustal growth event in the Palaeoproterozoic of West Africa? *Precambrian Res.* 127, 329–354.
- Gerbault, M., Davey, F., Henrys, S., 2002. Three-dimensional lateral crustal thickening in continental oblique collision: an example from the Southern Alps, New Zealand. *Geophys. J. Int.* 150, 770–779.
- Gerbault, M., Henrys, S., Davey, F., 2003. Numerical models of lithospheric deformation forming the Southern Alps of New Zealand. *J. Geophys. Res.* 108 (B7), 2341, <http://dx.doi.org/10.1029/2001JB001716>
- Gerya, T., Stöckhert, B., 2005. Two-dimensional numerical modeling of tectonic and metamorphic histories at active continental margins. *Int. J. Earth Sci.* 95, 250–274.
- Gerya, T.V., Perchuk, L.L., Burg, J.-P., 2008. Transient hot channels: perigrating and regurgitating ultrahigh-pressure, high-temperature crust–mantle associations in collision belts. *Lithos* 103, 236–256.
- Giger, S.B., Cox, S.F., Tenthorey, E., 2008. Slip localization and fault weakening as a consequence of fault gouge strengthening – insights from laboratory experiments. *Earth Planet Sci. Lett.* 276, 73–84.
- González, G., Gerbault, M., Martinod, J., Cembrano, J., Carrizo, D., Allmendinger, R., Espina, J., 2008. Crack formation on top of propagating reverse faults of the Chuculay Fault System, northern Chile: insights from field data and numerical modelling. *J. Struct. Geol.* 30, 791–808.
- Graveleau, F., Hurtrez, J.E., Dominguez, S., Malavielle, J., 2011. A new experimental material for modeling relief dynamics and interactions between tectonics and surface processes. *Tectonophysics* 513, 68–87.
- Graveleau, F., Malavielle, J., Dominguez, S., 2012. Experimental modelling of orogenic wedges: a review. *Tectonophysics* 538, 1–66.
- Gupta, A., Scholz, C.H., 2000. A model of normal fault interaction based on observations and theory. *J. Struct. Geol.* 22, 865–879.
- Hall, C.E., Gurnis, M., Sdrólías, M., Lavie, L.L., Müller, R.D., 2003. Catastrophic initiation of subduction following forced convergence across fracture zones. *Earth Planet Sci. Lett.* 212, 15–30.
- Hansen, E.C., Newton, R.C., Janardhar, A.S., Lindenberg, S., 1995. Differentiation of Late Archean Crust in the Eastern Dharwar Craton, Krishnagiri–Salema Area, South India. *J. Geol.* 103, 629–651.
- Harcouët-Menou, V., Guillou-Frottier, L., Bonneville, A., Adler, P.M., Mourzenko, V., 2009. Hydrothermal convection in and around mineralized fault zones: insights from two- and three-dimensional numerical modeling applied to the Ashanti belt, Ghana. *Geofluids* 9, 116–137.
- Hirdes, W., Davis, D.W., Lüdtke, G., Konan, G., 1996. Two generations of Birimian (Paleoproterozoic) volcanic belts in northeastern Côte d'Ivoire (West Africa): consequences for the Birimian controversy. *Precambrian Res.* 80, 173–191.
- Imber, J., Tuckwell, G.W., Childs, C., Walsh, J.J., Manzocchi, T., Heath, A.E., Bonson, C.G., Strand, J., 2004. Three-dimensional distinct element modelling of relay growth and breaching along normal faults. *J. Struct. Geol.* 26, 1897–1911.
- Jagadeesh, S., Rai, S.S., 2008. Thickness, composition, and evolution of the Indian Precambrian crust inferred from broadband seismological measurements. *Precambrian Res.* 162, 4–15.
- Jessell, M.W., Amponsah, P.O., Baratoux, L., Asiedu, D.K., Loh, G.K., Ganne, J., 2012. Crustal-scale transcurrent shearing in the Paleoproterozoic Sefwi-Sunyani-Comé region, West Africa. *Precambrian Res.* 212–213, 155–168.
- Jessell, M.W., Begg, G.C., Miller, M.S., 2015. The geophysical signatures of the West African Craton. *Precambrian Res.* (under review).
- Ju, W., Hou, G., Zhang, B., 2014. Insights into the damage zones in fault-bend folds from geomechanical models and field data. *Tectonophysics* 610, 182–194.
- Katz, R.F., Spiegelman, M., Holtzman, B., 2006. The dynamics of melt and shear localization in partially molten aggregates. *Nature* 442, 676–679.
- Koshizuka, S., Nobe, A., Oka, Y., 1998. Numerical analysis of breaking waves using the moving particle semi-implicit method. *Int. J. Numer. Methods Fluids* 26, 751–769.

- Koyi, H., Schmeling, H., Burchardt, S., Talbot, C., Mukherjee, S., Sjöström, H., Chemia, Z., 2013. Shear zones between rock units with no relative movement. *J. Struct. Geol.* 50, 82–90.
- Lawley, C., Imber, J., Selby, D., 2013. Structural controls on orogenic and mineralization during transpression: Lupa Goldfield, Southwestern Tanzania. *Econ. Geol.* 108, 1615–1640.
- Le Pourhiet, L., Huet, B., May, D.A., Labrousse, L., Jolivet, L., 2012. Kinematic interpretation of the 3D shapes of metamorphic core complexes. *Geochem. Geophys. Geosyst.* 13, Q09002, <http://dx.doi.org/10.1029/2012GC004271>
- Lebedev, S., Boonen, J., Trampert, J., 2009. Seismic structure of Precambrian lithosphere: new constraints from broad-band surface-wave dispersion. *Lithos* 109, 96–111.
- Leever, K.A., Gabrielsen, R.H., Sokoutis, D., Willingshofer, E., 2011. The effect of convergence angle on the kinematic evolution of strain partitioning in transpressional brittle wedges: insight from analog modeling and high-resolution digital image analysis. *Tectonics* 30, TC2013, <http://dx.doi.org/10.1029/2010TC002823>
- Ledru, P., Pons, J., Milési, J.P., Feybesse, J.L., Johan, V., 1991. Transcurrent tectonics and polycyclic evolution in the Lower Proterozoic of Senegal-Mali. *Precambrian Res.* 50, 337–354.
- Lemiale, V., Mühlhaus, H.-B., Moresi, L., Stafford, J., 2008. Shear banding analysis of plastic models formulated for incompressible viscous flows. *Phys. Earth Planet. Inter.* 171, 177–186.
- Lompo, M., 2009. Geodynamic evolution of the 2.25–2.0 Ga Palaeoproterozoic magmatic rocks in the Man-Leo Shield of the West African Craton. A model of subsidence of an oceanic plateau. *Geol. Soc. Lond. Spec. Publ.* 323, 231–254.
- Lompo, M., 2010. Paleoproterozoic structural evolution of the Man-Leo Shield (West Africa). Key structures for vertical to transcurrent tectonics. *J. Afr. Earth Sci.* 58, 19–36.
- Mair, K., Abe, S., 2008. 3D numerical simulations of fault gouge evolution during shear: grain size reduction and strain localization. *Earth Planet. Sci. Lett.* 274, 72–81.
- Mall, D.M., Chandrakala, K., Sudhir Kumar, A., Sarkar, D., 2012. Sub-crustal LVZ below Dharwar craton, India: an evidence for mantle metasomatism and tectonothermal activity in the Archean crust. *Precambrian Res.* 208–211, 161–173.
- Malservici, R., Gans, C., Furlong, K., 2003. Numerical modeling of strike-slip creeping faults and implications for the Hayward fault, California. *Tectonophysics* 361, 121–137.
- Marone, F., Van Der Meijde, M., Van Der Lee, S., Giardini, D., 2003. Joint inversion of local, regional and teleseismic data for crustal thickness in the Eurasia–Africa plate boundary region. *Geophys. J. Int.* 154, 499–514.
- Maruyama, S., Liou, J.G., Terabayashi, M., 1996. Blueschists and eclogites of the world and their exhumation. *Int. Geol. Rev.* 38, 485–594.
- Mason, W., Moresi, L., Betts, P.G., Miller, M.S., 2010. Three-dimensional numerical models of the influence of a buoyant oceanic plateau on subduction zones. *Tectonophysics* 483, 71–79.
- Middleton, T.A., Copley, A., 2013. Constraining fault friction by re-examining earthquake nodal plane dips. *Geophys. J. Int.* 196, 671–680.
- Morand, V.J., 1992. Pluton emplacement in a strike-slip fault zone: the Doctors Flat Pluton, Victoria, Australia. *J. Struct. Geol.* 14, 205–213.
- Moresi, L., Mühlhaus, H., Dufour, F., 2001. An overview of numerical methods for Earth simulations. In: *Exploration Geodynamics Chapman Conference* 19, pp. 113–119.
- Moresi, L., Dufour, F., Mühlhaus, H.B., 2003. A Lagrangian integration point finite element method for large deformation modeling of viscoelastic geomaterials. *J. Comput. Phys.* 184, 476–497.
- Moresi, L., Mühlhaus, H.B., 2006. Anisotropic viscous models of large-deformation Mohr–Coulomb failure. *Philos. Mag.* 86, 3287–3305.
- Moresi, L., Quenette, S., Lemiale, V., Meriaux, C., Appelbe, B., Mühlhaus, H., 2007. Computational approaches to studying non-linear dynamics of the crust and mantle. *Phys. Earth Planet. Inter.* 163, 69–82.
- Moucha, R., Forte, A.M., 2011. Changes in African topography driven by mantle convection. *Nat. Geosci.* 4, 707–712.
- Mourgues, R., Bureau, D., Bodet, L., Gay, A., Gressier, J.B., 2012. Formation of conical fractures in sedimentary basins: experiments involving pore fluids and implications for sandstone intrusion mechanisms. *Earth Planet. Sci. Lett.* 313–314, 67–78.
- Naylor, M., Mandl, G., Supesteijn, C.H., 1986. Fault geometries in basement-induced wrench faulting under different initial stress states. *J. Struct. Geol.* 8, 737–752.
- Neves, S.P., Vauchez, A., Archanjo, C.J., 1996. Shear zone-controlled magma emplacement or magma-assisted nucleation of shear zones? Insights from northeast Brazil. *Tectonophysics* 262, 349–364.
- Neves, S.P., Vauchez, A., Feraud, G., 2000. Tectono-thermal evolution, magma emplacement, and shear zone development in the Caruaru area (Borborema Province, NE Brazil). *Precambrian Res.* 99, 1–32.
- Nieto-Samaniego, Á.F., 1999. Stress, strain and fault patterns. *J. Struct. Geol.* 21, 1065–1070.
- Ota, T., Kaneko, Y., 2010. Blueschists, eclogites, and subduction zone tectonics: insights from a review of Late Miocene blueschists and eclogites, and related young high-pressure metamorphic rocks. *Gondwana Res.* 18, 167–188.
- OzBench, M., Regenaer-Lieb, K., Stegman, D.R., Morra, G., Farrington, R., Hale, A., May, D.A., Freeman, J., Bourgouin, L., Mühlhaus, H., Moresi, L., 2008. A model comparison study of large-scale mantle-lithosphere dynamics driven by subduction. *Phys. Earth Planet. Inter.* 171, 224–234.
- Pasyanos, M.E., Nyblade, A.A., 2007. A top to bottom lithospheric study of Africa and Arabia. *Tectonophysics* 444, 27–44.
- Pereira, M.F., Chichorro, M., Fernández, C., Silva, J.B., Matias, F.V., 2013. The role of strain localization in magma injection into a transtensional shear zone (Variscan belt, SW Iberia). *J. Geol. Soc.* 170, 93–105.
- Peltzer, G., Crampé, F., Hensley, S., Rosen, P., 2001. Transient strain accumulation and fault interaction in the Eastern California shear zone. *Geology* 29, 975–978.
- Person, M., Hofstra, A., Sweetkind, D., Stone, W., Cohen, D., Gable, C.W., Banerjee, A., 2012. Analytical and numerical models of hydrothermal fluid flow at fault intersections. *Geofluids* 12, 312–326.
- Pirajno, F., 2010. Intracontinental strike-slip faults, associated magmatism, mineral systems and mantle dynamics: examples from NW China and Altay-Sayan (Siberia). *J. Geodyn.* 50, 325–346.
- Ranalli, G., 1995. *Rheology of the Earth*. Springer Science & Business Media, pp. 413.
- Rey, P.F., Houseman, G., 2006. Lithospheric scale gravitational flow: the impact of body forces on orogenic processes from Archaean to Phanerozoic. *Geol. Soc. Lond. Spec. Publ.* 253, 153–167.
- Rice, J., 1993. Spatio-temporal complexity of slip on a fault. *J. Geophys. Res.* 98, 9885–9907.
- Rosenberg, C.L., Handy, M.R., 2000. Syntectonic melt pathways during simple shearing of a partially molten rock analogue (Norcamphor–Benzamide). *J. Geophys. Res.* 105, 3135–3149.
- Sakyi, P.A., Su, B.X., Anum, S., Kwaiyisi, D., Dampare, S.B., Anani, C.Y., Nude, P.M., 2014. New zircon U–Pb ages for erratic emplacement of 2213–2130 Ma Paleoproterozoic calc-alkaline I-type granitoid rocks in the Lawra Volcanic Belt of Northwestern Ghana, West Africa. *Precambrian Res.* 254, 149–168.
- Sanderson, D.J., Marchini, W.R.D., 1984. Transpression. *J. Struct. Geol.* 6, 449–458.
- Schellart, W.P., 2008. Kinematics and flow patterns in deep mantle and upper mantle subduction models: influence of the mantle depth and slab to mantle viscosity ratio. *Geochem. Geophys. Geosyst.* 9, Q03014, <http://dx.doi.org/10.1029/2007GC001656>
- Schellart, W., Stegman, D., Farrington, R., 2010. Cenozoic tectonics of western North America controlled by evolving width of Farallon slab. *Science* 80, 316–319.
- Scholz, C.H., 2007. *Fault mechanics*. Treatise Geophys. 6, 441–483.
- Seber, D., Sandvol, E., Sandvol, C., Brindisi, C., Barazangi, M., 2001. Crustal model for the Middle East and North Africa region: implications for the isostatic compensation mechanism. *Geophys. J. Int.* 147, 630–638.
- Shyy, W., Udaykumar, H.S., Rao, M.M., Smith, R.W., 2012. *Computational Fluid Dynamics with Moving Boundaries*. Taylor & Francis, Inc., Bristol, PA.
- Sibson, R.H., 1977. Fault rocks and fault mechanisms. *J. Geol. Soc.* 133, 191–213.
- Sibson, R.H., Xie, G.Y., 1998. Dip range for intracontinental reverse fault ruptures: truth not stranger than fiction? *Bull. Seismol. Soc. Am.* 88, 1014–1022.
- De Smet, J.H., Van Den Berg, A.P., Vlaar, N.J., 1998. Stability and growth of continental shields in mantle convection models including recurrent melt production. *Tectonophysics* 296, 15–29.
- Snoko, A.W., Kalakay, T.J., Quick, J.E., Sinigoi, S., 1999. Development of a deep-crustal shear zone in response to syntectonic intrusion of mafic magma into the lower crust, Ivrea-Verbano zone, Italy. *Earth Planet. Sci. Lett.* 166, 31–45.
- Stegman, D.R., Freeman, J., Schellart, W.P., Moresi, L., May, D., 2006. Influence of trench width on subduction hinge retreat rates in 3-D models of slab rollback. *Geochem. Geophys. Geosyst.* 7, Q03012, <http://dx.doi.org/10.1029/2005GC001056>
- Stern, R.J., 2007. When and how did plate tectonics begin? Theoretical and empirical considerations. *Chin. Sci. Bull.* 52, 578–591.
- Stern, R.J., 2008. Modern-style plate tectonics began in Neoproterozoic time: an alternative interpretation of Earth's tectonic history. *Geol. Soc. Am. Spec. Pap.* 440, 265–280.
- Tokam, A.P.K., Tabod, C.T., Nyblade, A.A., Julià, J., Wiens, D.A., Pasyanos, M.E., 2010. Structure of the crust beneath Cameroon, West Africa, from the joint inversion of Rayleigh wave group velocities and receiver functions. *Geophys. J. Int.* 183, 1061–1076.
- Tong, H., Koyi, H., Huang, S., Zhao, H., 2014. The effect of multiple pre-existing weaknesses on formation and evolution of faults in extended sandbox models. *Tectonophysics* 626, 197–212.
- Tranos, M.D., 2012. Slip preference on pre-existing faults: a guide tool for the separation of heterogeneous fault-slip data in extensional stress regimes. *Tectonophysics* 544–545, 60–74.
- Ueda, K., Gerya, T.V., Burg, J.P., 2012. Delamination in collisional orogens: thermo-mechanical modeling. *J. Geophys. Res.* 117, B08202, <http://dx.doi.org/10.1029/2012JB009144>
- Ueta, K., Tani, K., Kato, T., 2000. Computerized X-ray tomography analysis of three-dimensional fault geometries in basement-induced wrench faulting. *Eng. Geol.* 84, 233–246.
- Vidal, M., Delor, C., Pouclot, A., Simeon, Y., Alric, G., 1996. Evolution géodynamique de l'Afrique de l'Ouest entre 2.2 Ga et 2 Ga; le style archéen' des ceintures vertes et des ensembles sédimentaires birimiens du nord-est de la Côte-d'Ivoire. *Bull. Soc. Géol. Fr.* 167, 307–319.
- Vigneress, J.L., Tikoff, B., 1999. Strain partitioning during partial melting and crystallizing felsic magmas. *Tectonophysics* 312, 117–132.
- Vigneress, J.L., Clemens, J.D., 2000. Granitic magma ascent and emplacement: neither diapirism nor neutral buoyancy. *Geol. Soc. Lond. Spec. Publ.* 174, 1–19.

- Walsh, J.J., Childs, C., Imber, J., Manzocchi, T., Watterson, J., Nell, P.A.R., 2002. Strain localisation and population changes during fault system growth within the Inner Moray Firth, northern North Sea. *J. Struct. Geol.* 25, 307–315.
- Weinberg, R.F., Mark, G., Reichardt, H., 2006. Magma ponding in the Karakoram shear zone, Ladakh, NW India. *Geol. Soc. Am. Bull.* 121, 278–285.
- Wibberley, C.A.J., Yielding, G., Di Toro, G., 2008. Recent advances in the understanding of fault zone internal structure: a review. *Geol. Soc. Lond. Spec. Publ.* 299, 5–33.
- Xing, H.L., Makinouchi, A., Mora, P., 2007. Finite element modeling of interacting fault systems. *Phys. Earth Planet. Inter.* 163, 106–121.
- Zhang, Y., Gartrell, A., Underschultz, J.R., Dewhurst, D.N., 2009. Numerical modelling of strain localisation and fluid flow during extensional fault reactivation: implications for hydrocarbon preservation. *J. Struct. Geol.* 31, 315–327.
- Zlotnik, S., Jiménez-Munt, I., Fernández, M., 2013. Coupled mantle dripping and lateral dragging controlling the lithosphere structure of the NW-Moroccan margin and the Atlas Mountains: a numerical experiment. *Lithos* 189, 16–27.

3.2 Interacting fault systems in southern New Zealand

Introduction

In the last section, a system of two pre-existing faults was used to study the processes of localization of deformation. However, what can we observe if the system contains multiple tectonic inheritances acquired from past tectonic events? How would such inheritances develop and accumulate strain over time under simple shear boundary conditions? How does the orientation of the tectonic inheritances influence the process of strain localization?

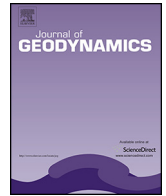
In order to answer these questions, the Alpine Fault zones seem like a godsend to explore. The reason is that the regional NE trending ridge segments and NW trending faults were widely distributed in the South Island of New Zealand during the Oligocene-Miocene times. These tectonic inheritances are thought to play a dominant role in the propagation of strike-slip faulting that matured to become the Australian-Pacific plate boundary fault in Southern New Zealand. In order to tackle this problem, a 3D numerical model has been constructed to explore the evolutionary process of deformation. This section has been published by *Journal of Geodynamics*, 2016, 100, 130-143.

3.2.1 Effect of strain-weakening on Oligocene-Miocene self-organization of the Australian-Pacific plate boundary fault in southern New Zealand: Insights from numerical modelling

Tectonic inheritance acquired from past geological events can control the formation of new plate boundaries. The aim of this paper is to explore the role of inherited NE and NW trending fabrics and their rheological influence on the propagation of Oligocene-Miocene strike-slip faulting that matured to become the Australian-Pacific plate boundary fault in southern New Zealand. Strain weakening plays a significant role in controlling the formation, growth and evolution of strain localization. In this study, three-dimensional thermo-mechanical models have been used to explore the effect of strain weakening on the Oligocene-Miocene self-organization of strain localization. Strain weakening is simulated through decreasing either the coefficient of friction of upper crust, its cohesion, or the rheological viscosity contrast between the inherited structures and their surrounding wall rocks. Viscosity contrast is obtained by varying the viscosity of inherited structures. Softening coefficient (α) is a measure of strain weakening. Our experiments robustly demonstrate that a primary boundary shear zone becomes mature quicker when softening coefficients are increased. Deformation is focused along narrow high-strain shear zones in the centre of the model when the softening coefficients are high, whereas the strain is more diffuse with many shear zones spread over the model and possibly some high-strain shear zones focused near one border at lower softening coefficients. Varying the viscosity contrast has less effect on the distribution of maximum finite strain.

3. Role of interacting fault systems on the localization of deformation in the upper crust

Under simple-shear boundary conditions, NW trending inherited structures make a major contribution to forming early zones of highly focused strain, up to a shear strain of about $\gamma = 3.7$. During this process, most NE-trending structures move and rotate passively, accommodate less strain, or even be abandoned through time.



Effect of strain-weakening on Oligocene–Miocene self-organization of the Australian–Pacific plate boundary fault in southern New Zealand: Insights from numerical modelling

Xiaojun Feng^{a,*}, Mark Walter Jessell^{a,b}, Prince Ofori Amponsah^{a,c}, Roland Martin^a, Jérôme Ganne^a, Daqing Liu^d, Geoffrey E. Batt^b

^a Geosciences Environnement Toulouse, Observatoire Midi Pyrénées, 14 av. E. Belin, 31400 Toulouse, France

^b Centre for Exploration Targeting, The University of Western Australia, 35 Stirling Highway, Crawley, Perth, WA 6009, Australia

^c Azumah Resources Ghana Limited, PMB CT452, Cantonments, Accra, Ghana

^d MOX (Laboratory of Modelling and Scientific Computing), Department of Mathematics, Politecnico di Milano, Piazza Leonardo da Vinci 32, 20133 Milano, Italy

ARTICLE INFO

Article history:

Received 2 September 2015

Received in revised form 23 February 2016

Accepted 4 March 2016

Available online 9 March 2016

Keywords:

Strain-weakening

Fault

Alpine Fault

Numerical modelling

ABSTRACT

Tectonic inheritance acquired from past geological events can control the formation of new plate boundaries. The aim of this paper is to explore the role of inherited NE and NW trending fabrics and their rheological influence on the propagation of Oligocene–Miocene strike-slip faulting that matured to become the Australian–Pacific plate boundary fault in southern New Zealand. Strain weakening plays a significant role in controlling the formation, growth and evolution of strain localization. In this study, three-dimensional thermo-mechanical models have been used to explore the effect of strain weakening on the Oligocene–Miocene self-organization of strain localization. Strain weakening is simulated through decreasing either the coefficient of friction of upper crust, its cohesion, or the rheological viscosity contrast between the inherited structures and their surrounding wall rocks. Viscosity contrast is obtained by varying the viscosity of inherited structures. Softening coefficient (α) is a measure of strain weakening. Our experiments robustly demonstrate that a primary boundary shear zone becomes mature quicker when softening coefficients are increased. Deformation is focused along narrow high-strain shear zones in the centre of the model when the softening coefficients are high, whereas the strain is more diffuse with many shear zones spread over the model and possibly some high-strain shear zones focused near one border at lower softening coefficients. Varying the viscosity contrast has less effect on the distribution of maximum finite strain.

Under simple-shear boundary conditions, NW trending inherited structures make a major contribution to forming early zones of highly focused strain, up to a shear strain of about $\gamma = 3.7$. During this process, most NE-trending structures move and rotate passively, accommodate less strain, or even be abandoned through time.

© 2016 Elsevier Ltd. All rights reserved.

1. Introduction

Continental deformation originates from the local concentration of strain resulting from heterogeneous stress fields and the persistent evolution of discrete weaknesses (Sutherland et al., 2000; Ariyoshi et al., 2009). Most discontinuities are deformed into linked networks of faults and shear zones through geological time (Tavarnelli and Pasqui, 2000; Aktug et al., 2013; Jessell

et al., 2005, 2009, 2012; Chousianitis et al., 2013). These shear zones have a lower resistance than that of their surrounding wall rocks (Rutter et al., 2001). The sliding stability of a shear zone is controlled by frictional properties (Scholz, 1998; Carpenter et al., 2012) and accommodation of net shear strain (Beeler et al., 1996; Marone, 1998; Ikari et al., 2011).

The formation and growth of faults are mainly influenced by heterogeneous stress fields (Chester et al., 1993), characterized by systematic increase in displacement and length relating to earthquake slip events on a regional scale or by relative motion of plates on a larger scale (Walsh and Watterson, 1987, 1988; Scholz and Cowie, 1990; Dawers et al., 1993; Kokkalas and Doutsos, 2001;

* Corresponding author.

E-mail address: fxjuncumt@gmail.com (X. Feng).

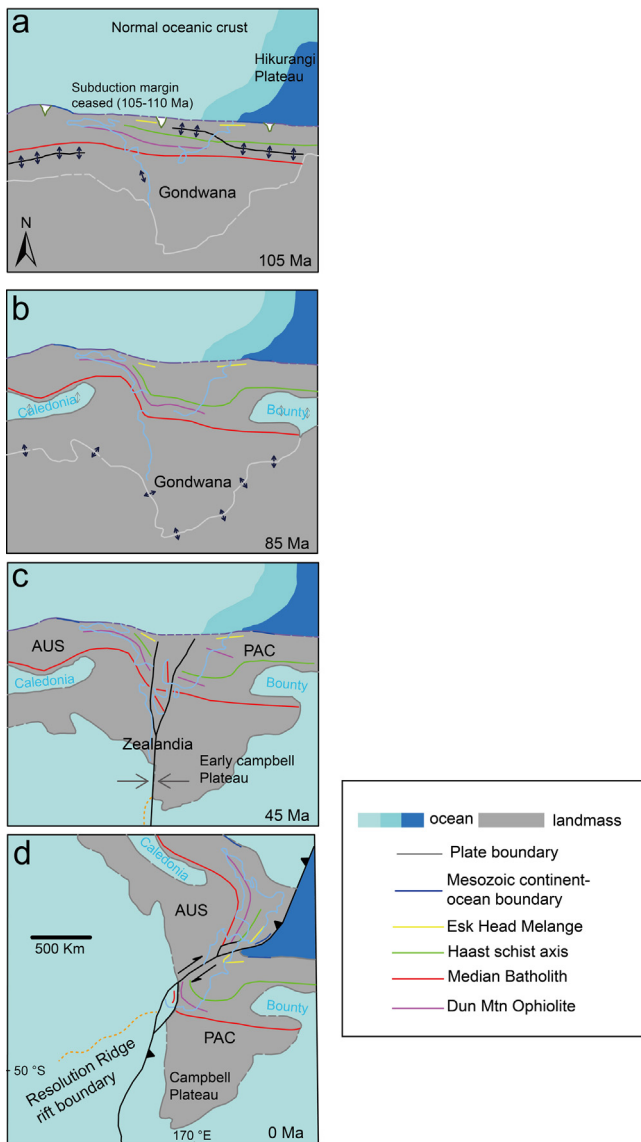


Fig. 1. Schematic diagram, showing the evolution of the Australian-New Zealand plates from Cretaceous to recent time (modified after Mortimer, 2014).

Walsh et al., 2003; Kim and Sanderson, 2005; Xu et al., 2010). With regards to global tectonics, plate boundary faults (such as the Alpine Fault and the San Andreas Fault) play a dominant role in the formation of lineaments observed at the present day (Woodcock and Daly, 1986), as well as the accommodation of plate motion (Dokka and Travis, 1990). Rheological heterogeneity and mechanical anisotropy in the lithosphere resulting from past tectonic events commonly provide preferential zones for strain concentration, which are thought to play a dominant role in controlling the formation of new plate boundaries (Vauchez et al., 1998; Thomas, 2006; Audet and Bürgmann, 2011). For example, during the Pangaea breakup, tectonic inheritance of large scale structures coincides with the distribution of large transform offsets of the continental margins (cf. Bahamas transform margin in Thomas (2006) and Whalen et al. (2015)).

Inherited structures within the crust can play a significant role in initializing the distribution and controlling the evolution of deformation and relief (Dooley and Schreurs, 2012; Tong et al., 2014; Feng et al., 2016). Such inherited structures can offer favoured sites for strain accumulation because of their function as a stress concentrator with respect to the host rock (Jessell and Lister, 1991; Jessell

et al., 2008). This is manifested by the operation of narrow and foliated high strain zones through geological time (Tchalenko, 1970). Within a shear zone, strain can either focus in intensity towards the central part of the shear zone, or as a localized simple shear component within the broader high strain zone (Fossen and Tikoff, 1998; Dooley and Schreurs, 2012; Gueydan et al., 2014).

In southern New Zealand, continental regions inherited intricate fabrics resulting from the accretion, localized uplift, and subsidence of the landmass through geological history (Little and Mortimer, 2001; Claypool et al., 2002; Upton et al., 2014). The early deformation history can be observed in the modern South Island. Its structural expression is consistent with the regional NE trending ridge segments and NW trending faults (Lamarche et al., 1997; Deckert et al., 2002; Gray and Foster, 2004). These inherited fabrics are thought to play an important role in controlling the evolution of strain localization during the Oligocene–Miocene early development of modern dextral strike-slip boundary conditions across the Alpine Fault. However, the details of the occurrence of this self-organization of strain localization as well as the modern coherent plate boundary development from the inherited fabrics in the study area is not completely understood (Barnes, 1994; Lamarche et al., 1997; Sutherland et al., 2000; Upton et al., 2014). Also the manner by which these mechanical and rheological parameters (i.e. viscosity, cohesion and friction coefficient; Gueydan et al., 2014; Upton et al., 2014) influence the process of strain localization and accumulation at a crustal scale in the study area is unclear.

In this paper, we use three-dimensional thermo-mechanical models to explore the Oligocene–Miocene self-organization of the Australian-Pacific (AUS-PAC) plate boundary fault in southern New Zealand. In our study we simulate strain weakening through decreasing either the coefficient of friction of upper crust, its cohesion, or the rheological contrast in viscosity between the inherited structures and their surrounding wall rocks. The aim of this paper is not to reproduce the exact evolutionary history of the Alpine Fault, but rather to broadly use this system as a geological basis for exploring and quantifying the effect of strain weakening on crustal deformation. This work will also shed light on the self-organization process of crustal deformation in southern New Zealand during the Oligocene–Miocene times, as well as quantifying the effect of strain weakening on the process of strain localization at a crustal scale.

2. Geological context

The continental portions of the Australian–New Zealand landmass started to split from the southern part of Gondwana during the late Cretaceous (Fig. 1). Separation of the Zealandia plate from Australia and Antarctica was initiated around 85 Ma, with rifting from south to north to form the new Tasman Sea (Gaina et al., 1998; Sutherland, 1999). At about ~45 Ma, the Resolution Ridge rift boundary (Fig. 1) is believed to have formed as a consequence of a spreading ridge propagating through southern New Zealand along the line of the Emerald fracture zone (Sutherland, 1999; Sutherland et al., 2000). From Oligocene to Early Miocene times, the plate boundary developed transform characteristics as the Australian–New Zealand spreading direction became progressively more oblique with respect to the nascent Challenger rift zone, with strike-slip motion dominant through much of the central South Island by around 21 Ma (King, 2000). Strike slip deformation subsequently dominated strain localization through on land continental New Zealand until a step-change in the Australian–New Zealand pole of rotation to the west at around 7–8 Ma introduced substantial oblique transpression across the system (Walcott, 1998; King, 2000; Batt, 2001), leading to rapid uplift of the Southern Alps.

Basement geology of the South Island of New Zealand is divided into Eastern and Western Province domains by the Median Tec-

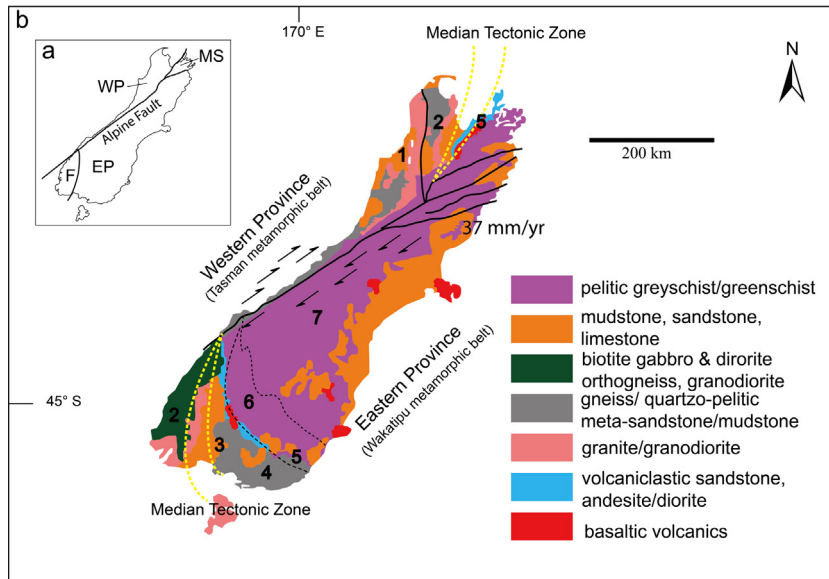


Fig. 2. (a) Simplified geological map of New Zealand, showing the major structural features related to the Australian-New Zealand plate boundary through the study area (South Island). MS, WP, EP and F represents Marlborough Sounds, Western Province, Eastern Province and Fiordland, respectively. (b) Simplified litho-structural map of the South Island of New Zealand (Modified after Barth et al., 2013; GNS Science, 2010; Sutherland, 1999). 1 = Buller Terrane, 2 = Takaka Terrane, 3 = Brook street Terrane, 4 = Murihiku Terrane, 5 = Maitai Terrane, 6 = Caples Terrane and 7 = Torlesse Terrane.

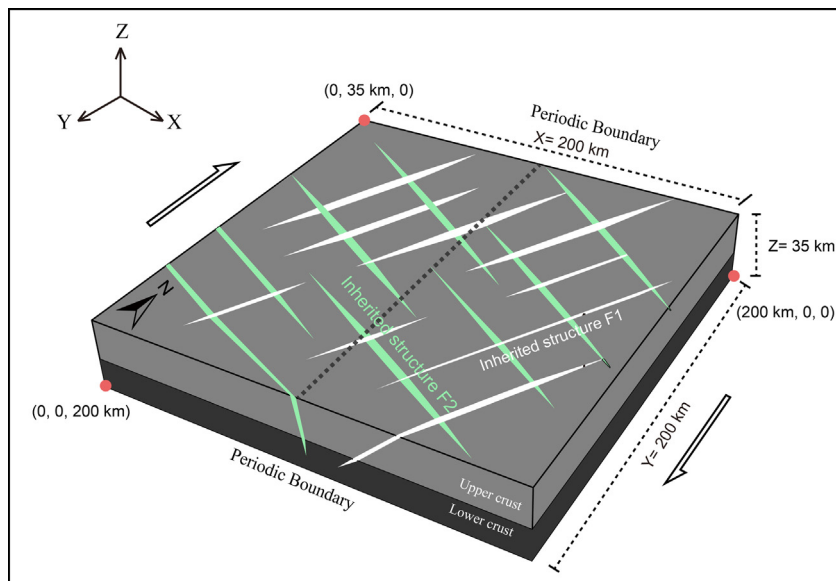


Fig. 3. Schematic diagram showing the geometry and boundary conditions used. The domain is 200 km long (Y direction), 200 km wide (X direction) and 35 km thick (Z direction). The crustal domain randomly contains two sets of inherited structures with different orientations (NE-trending faults F1 and NW-trending faults F2). F1 and F2 are defined by strike (α , represents the azimuth of the fault planes) and dip (α_{dip} , is counted clockwise around the azimuth direction of the fault expressed between $N0-180^\circ$) angles in the box. F1 is set to 30° for strike angle and 30° for dip angle, F2 is set to 120° for strike angle and 120° for dip angle. Boundary conditions are represented in black arrows. The bottom and surface of the model are set to free-slip boundary conditions.

tonic Zone (Fig. 2) (Landis and Coombs, 1967; Bradshaw et al., 1980; Bishop et al., 1985). The Western Province is comprised of fragments of the early-middle Palaeozoic continental margin of Gondwana cut by series of Upper Devonian to Lower Carboniferous granitoids (Park, 1921; Grindley, 1961; Suggate, 1965; Ireland and Gibson, 1998; Muir et al., 1998) and gneisses (Mortimer, 2004). The Eastern Province is mostly composed of metagreywacke together with higher-grade (pumpellyite-actinolite to amphibolite facies) equivalents in the Haast Schist group (Mortimer, 2004), resulting from convergent margin processes and corresponding metamorphism from Permian to Cretaceous times (Aronson, 1965). The Western Province is both older (Landis and Coombs, 1967) and for

the most part mechanically stronger (Gerbaulet et al., 2002) than the Eastern. The Western and Eastern Province domains also express contrasting metamorphic histories, with the Eastern Province dominated by the low temperature-high pressure Wakatipu Metamorphic Belt, and the Western Province the high temperature-low pressure Tasman Metamorphic Belt (Turner 1938; Miyashiro, 1961; Landis and Coombs, 1967; Coombs, 1985).

The South Island of New Zealand is made up of a network of faults and shear zones with the most dominant structure being the Alpine Fault (Fig. 2). The Alpine Fault operates as the effective tectonic boundary between the Australian and Pacific plates, and transects the western South Island as a variably southeast dip-

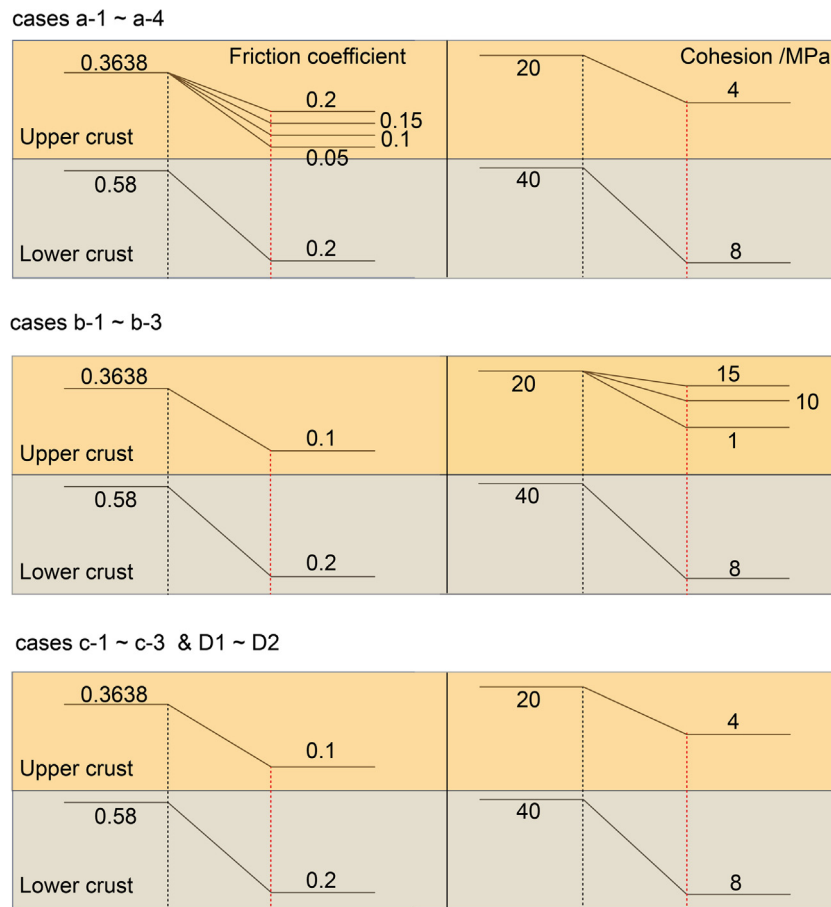


Fig. 4. Friction coefficient (left column), cohesion (right column, Mpa) in the upper (light orange area) and lower (light grey area) crusts. The black and red dotted lines represent the initial (0) and final (1) conditions of strain softening, respectively. Different values of fully reduced cohesion and coefficient of internal friction are defined for the upper crust (light yellow area). For the lower crust in all cases (light grey area), the initial cohesion and coefficient of internal friction are fixed to 40 Mpa and 0.58, the softened cohesion and coefficient of internal friction are fixed to 8 Mpa and 0.2, respectively. The initial cohesion and friction coefficients are reduced based on a linear relationship with the relative accumulated strain (Moresi et al., 2007b). (For interpretation of the references to colour in this figure legend, the reader is referred to the web version of this article.)

ping structure accommodating dextral strike-slip motion of about 3 cm/year (Norris et al., 1990; Berryman et al., 1992; Davey et al., 1995; Walcott, 1998). This structure accommodates about 70% of the current plate boundary motion, and has accounted for more than 50% of the plate displacement at a crustal scale since 45 Ma (Beavan et al., 1999; Sutherland et al., 2000).

3. Method and model setup

The modelling code Underworld Version 1.7 (Moresi et al., 2003, 2007a) is employed in this study. The defined model domain consists of an upper 20 km thick Newtonian rheological layer which represents the upper crust and is underlain by a 15 km thick lower crust dominated by creep processes. These crustal thicknesses are chosen to roughly correspond to the three-dimensional tomographic inversion of the South Island produced by Kohler and Eberhart-Phillips (2002), isovelocity surface corresponding to 7.8 km/s.

The model domain is also populated with two sets of inherited structures in different orientations (Fig. 3). These structures are represented as visco-plastic material with approximately incompressible rheology (Moresi et al., 2003) in a three-dimensional geometry. There is a rheological contrast in viscosity between the upper crust and the inherited structures (this is taken to be a factor of 1000; Malservisi et al., 2003). This version of Underworld code cannot model elastic behaviour. The effect of elasticity

does not significantly change results when modelling large-scale and long-term deformation, since materials rapidly reach their yield strength (Ellis et al., 2004; Buitner and Torsvik, 2007; Duretz et al., 2011; Nilfouroushan et al., 2012; Jaquet et al., 2014; Sun et al., 2014; Feng et al., 2016), which is evident from sensitivity tests (Abaqus, 2001).

The model domain is fixed to 200 km long (Y direction), 200 km wide (X direction) and 35 km thick (Z direction), and is modelled at a resolution of 2 km × 2 km × 1 km. In order to avoid the length effect in N-S direction on the localization of deformation, a N-S-directed periodic boundary is applied to the model (Fig. 3). A random initial particle layout with 30 particles in each cell is used, with their position and other properties at each computing step recorded. Mechanical boundary conditions are governed by simple shear with periodic boundary conditions, with the bottom and surface of the model set to free slip (Fig. 3). The shear rate is imposed as a fixed velocity of 3.7 cm/year at each side of the model (7.4 cm/year in total), which is similar to the estimated magnitude of offset experienced in southern New Zealand.

The governing equations of momentum, mass and energy conservation are introduced in detailed in Moresi et al. (2003, 2007a). The Underworld code uses a Lagrangian particle-in-cell finite element scheme and has been extensively used in geological modelling (e.g. Stegman et al., 2006; Schellart et al., 2007, 2010; OzBench et al., 2008; Capitanio et al., 2010; Moresi et al., 2014).

Table 1
Parameters for each model. The initial cohesion and friction coefficients are reduced based on a linear relationship with the relative accumulated strain (Moresi et al., 2007b). Regarding viscosity contrast, we modify the viscosity of inherited zones (η_{fault}), rather than modifying the initial viscosity of the upper crust, and the choice of modifying the viscosity of upper crust (Malservisi et al., 2003) could significantly alter the results, but are not studied here. F1 and F2 represent different inherited structures in the upper crust, as shown in Fig. 3. The bold and underlined values highlight variables according to different experiments.

Exp#	Initial friction coefficient in upper crust	Softened friction coefficient in upper crust	Initial cohesion in upper crust/MPa	Softened cohesion in upper crust/MPa	Viscosity contrast $\eta_{\text{crust}}/\eta_{\text{fault}}$	Inherited Structures
a-1	0.3638	0.2	20	4	1000	F1 & F2
a-2	0.3638	0.15	20	4	1000	F1 & F2
a-3	0.3638	0.1	20	4	1000	F1 & F2
a-4	0.3638	0.05	20	4	1000	F1 & F2
b-1	0.3638	0.1	20	15	1000	F1 & F2
b-2	0.3638	0.1	20	10	1000	F1 & F2
b-3	0.3638	0.1	20	1	1000	F1 & F2
c-1	0.3638	0.1	20	4	100	F1 & F2
c-2	0.3638	0.1	20	4	200	F1 & F2
c-3	0.3638	0.1	20	4	500	F1 & F2
D-1	0.3638	0.1	20	4	1000	F1
D-2	0.3638	0.1	20	4	1000	F2

A pressure-dependent Drucker–Prager yield criterion is applied to model the solid yield behaviour of the crust across the whole model domain. The yield stress equation is:

$$\tau_{\text{yield}} = P \times \varphi_p + \sigma_p \quad (1)$$

where P is the dynamic pressure, φ_p is the effective friction coefficient and σ_p is the effective cohesion, which are expressed as:

$$\sigma_p = 6 \times \sigma_{\text{eff}} \times \frac{\cos \varphi_{\text{eff}}}{(\sqrt{3} \times (3 - \sin \varphi_{\text{eff}}))} \quad (2)$$

$$\varphi_p = 6 \times \frac{\sin \varphi_{\text{eff}}}{(\sqrt{3} \times (3 - \sin \varphi_{\text{eff}}))} \quad (3)$$

Strain localization as well as rock strength reduction can be simulated by using a strain weakening principle (Sibson, 1977; Sibson and Xie, 1998; Ben-Zion and Sammis, 2003). In our study, the strain weakening principle is defined via effective friction and cohesion coefficients (Eqs. (4) and (5)).

$$\sigma_{\text{eff}} = \delta \times (1 - \lambda) + \delta_{\text{soften}} \times \lambda \quad (4)$$

$$\varphi_{\text{eff}} = \varphi \times (1 - \lambda) + \varphi_{\text{soften}} \times \lambda \quad (5)$$

where δ and δ_{soften} are the initial and fully reduced cohesion. Angle φ and φ_{soften} are the initial and fully reduced angle of friction, respectively. λ is the degree of strain weakening, ranging between 0 and 1. In all cases, the inherited shear zones (Fig. 3), have initial cohesion and coefficient of internal friction fixed to 1 Mpa and 0.0875, respectively. The fully reduced cohesion and coefficient of internal friction are set to 0. Since we mainly focus on exploring the re-organization of strain localization in the upper crust, different values of fully reduced cohesion and coefficient of internal friction are defined for the upper crust (Table 1; Fig. 4). Regarding materials pertaining to the models of the lower crust, the initial cohesion and coefficient of internal friction are fixed to 40 Mpa and 0.58. The softened cohesion and coefficient of internal friction are set to 8 Mpa and 0.2, respectively. The initial cohesion and friction coefficients are reduced based on a linear relationship (Table 1, Fig. 4) with the relative accumulated strain (Moresi et al., 2007b). The softening coefficient (α) is a measure of strain weakening, which is expressed as follows (Gueydan et al., 2014):

$$\alpha = 1 - \frac{\delta_{\text{soften}}}{\delta} \quad (6)$$

or

$$\alpha = 1 - \frac{\varphi'_{\text{soften}}}{\varphi'} \quad (7)$$

where φ' and φ'_{soften} are the initial and fully reduced friction coefficient (Table 1).

The strain-rate and stress tensor are given by:

$$e_{ij} = \frac{1}{2} \left[\left(\frac{\partial u_i}{\partial x_j} \right) + \left(\frac{\partial u_j}{\partial x_i} \right) \right] \quad (8)$$

$$\tau_{ij} = \eta_{\text{eff}} \left[\left(\frac{\partial u_i}{\partial x_j} \right) + \left(\frac{\partial u_j}{\partial x_i} \right) \right] \quad (9)$$

where e_{ij} is the strain-rate tensor and η_{eff} is the effective viscosity. More details on the method description can be found in Moresi et al. (2003, 2007a).

Elementary stresses increase with progressive loading. We note $\tau = \sqrt{\frac{1}{2} \tau_{ij} \tau_{ij}}$ the square root of the second invariant of the stress tensor. When τ is less than the yield stress τ_{yield} , the viscosity remains equal to the material viscosity $\eta = \eta_m$. However, when τ equals the yield stress τ_{yield} , the viscosity is modified such that:

$$\eta = \frac{\tau_{\text{yield}}}{2\epsilon} \text{ for } \tau = \tau_{\text{yield}} \quad (10)$$

The rheological parameters for the non-Newtonian power-law and other mechanical parameters are given in Table 2.

Underworld can accommodate thermal boundary conditions as either a fixed heat flow through the basal boundary or a fixed temperature gradient. In our model, we define a regular geotherm by applying fixed temperatures of 20 °C at the surface and 720 °C at the base of the model (in essence assuming a reference gradient of 20 °C/km corresponding to the Miocene thermal gradient resolved for Torlesse basement rocks east of the Alpine Fault by Kamp (1997)). A constant thermal diffusivity $10^{-6} \text{ m}^2/\text{s}$ is applied to the whole modelling domain (Vlaar et al., 1994).

4. Results

A total of 12 numerical models have been used to explore the effect of altering the coefficients of friction and cohesion, as well as viscosity contrast (by varying the viscosity of inherited shear structures), on strain localization at a crustal scale (Figs. 5–7). All the governing parameters are listed in Table 1 and Fig. 4. γ represents the shear strain gamma (captions in Figs. 5–7). All simulations were run at the same resolution using 200 processors in parallel computing on cluster machine EOS (2.8 Ghz, 20 cores per node) located at CALMIP in Toulouse.

4.1. Cumulative effect of the strain rate

Deformation in the crust results from the integration of instantaneous strain through geological time under external boundary

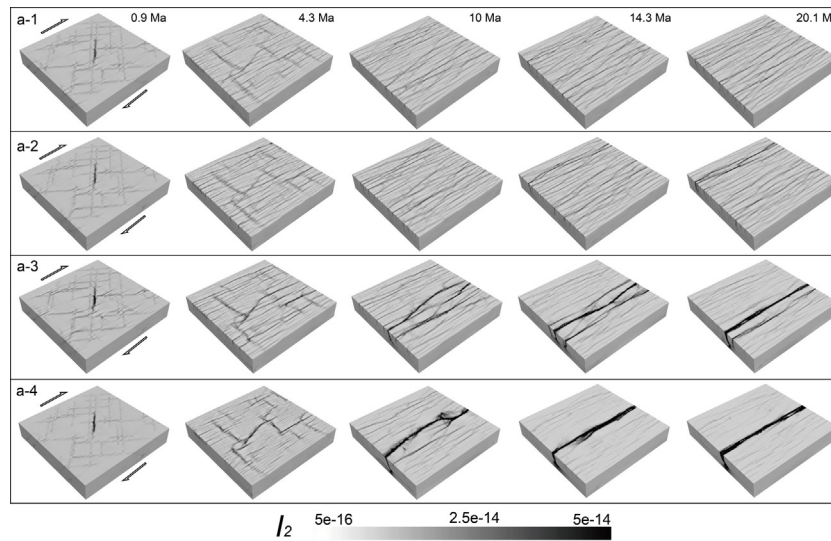


Fig. 5. Self-organization process of crustal deformation influenced by the softening degree of friction coefficients. The second invariant of the strain rate tensor is shown at 0.9 Ma ($\gamma=0.33$), 4.3 Ma ($\gamma=1.60$), 10 Ma ($\gamma=3.70$), 14.3 Ma ($\gamma=5.29$) and 20.1 Ma ($\gamma=7.44$) in the five columns. The name of each row in the left-top corner corresponds to the Exp# column in Table 1. Other mechanical and rheological parameters are given in Table 2 and Fig. 4.

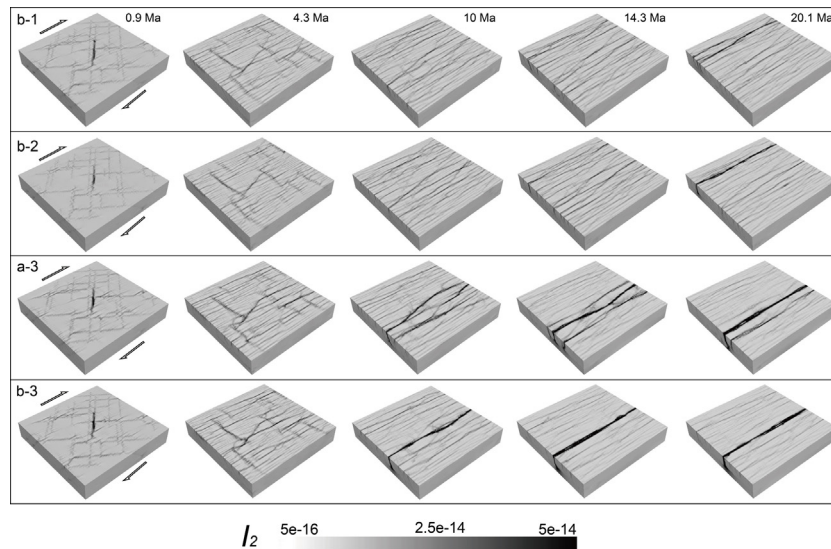


Fig. 6. Self-organization process of crustal deformation influenced by the softening degree of cohesion of upper crustal rocks. The second invariant of the strain rate tensor is shown at 0.9 Ma ($\gamma=0.33$), 4.3 Ma ($\gamma=1.60$), 10 Ma ($\gamma=3.70$), 14.3 Ma ($\gamma=5.29$) and 20.1 Ma ($\gamma=7.44$) in the five columns. The name of each row in the left-top corner corresponds to the Exp# column in Table 1. Other mechanical and rheological parameters are given in Table 2 and Fig. 4.

conditions (Braun et al., 2010). The accumulation of the second invariant of the strain rate tensor, is used to highlight shearing domains. The total accumulation of the second invariant of the strain rate tensor (see Supplementary material, Fig. S1 in the online version at DOI: [10.1016/j.jog.2016.03.002](https://doi.org/10.1016/j.jog.2016.03.002)), is of course influenced by the geometry and size of the computing domain, as it linearly increases with time step. For the softened friction coefficient, $f=0.2$ (case a-1) and $f=0.15$ (case a-2) arrive at a similar value of about $3.93e7$, while $f=0.05$ (case a-4) and $f=0.1$ (case a-3) yield a value of about $3.7e7$. Softened cohesion and contrast in viscosity indicate a less important role in accommodating total finite strain than the softened friction coefficient in these model.

The path of the maximum accumulation of the second invariant of the strain rate tensor among all particles (Fig. 8a–c), is more sensitive to changes in the parameters specified in Table 1 and Fig. 4. For cases with greater softened friction coefficient and cohesion (low softening coefficient), as well as greater viscosity contrast, do

have a slower strain rate and more vigorous resistance to deformation (Fig. 5–7). The scenario in Fig. 8 does not show significant differences in accommodating maximum strain over the first 7 Ma, which indicates that the major process of localization of deformation in the models takes place later. This mainly results from the slow strain rate and less localization prior to fully softening stage (controlled by strain weakening degree and path in Fig. 4). With respect to the softened friction coefficients (Fig. 8a), the maximum accumulation of the second invariant of the strain rate tensor arrive at about 19–20 over about 21.5 Ma when $f=0.2$ (case a-1) and $f=0.15$ (case a-2). With decreasing softened friction coefficient (yielding material is less competent and the system has a high mechanical anisotropy), a higher maximum accumulation of about 55 and 87 is observed when $f=0.1$ (case a-3) and $f=0.05$ (case a-4) respectively.

Increasing softened cohesion reflects a decreasing mechanical anisotropy in the system. The maximum accumulation of the sec-

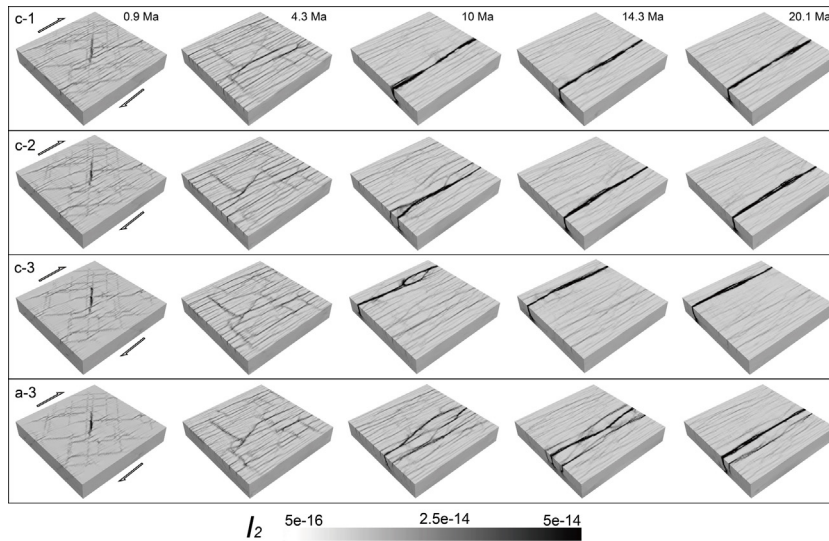


Fig. 7. Self-organization process of crustal deformation influenced by viscosity contrast between the inherited structures and surrounding rocks. The second invariant of the strain rate tensor is shown at 0.9 Ma ($\gamma = 0.33$), 4.3 Ma ($\gamma = 1.60$), 10 Ma ($\gamma = 3.70$), 14.3 Ma ($\gamma = 5.29$) and 20.1 Ma ($\gamma = 7.44$) in the five columns. The name of each row in the left-top corner corresponds to the Exp# column in Table 1. Other mechanical and rheological parameters are given in Table 2 and Fig. 4.

Table 2

Thermo-mechanical physical parameters of the model. A temperature-dependent non-Newtonian power law for the lower crust is set to $\eta = 0.25 \times (A)^{(-1/n)} \times \varepsilon^{((1/n)-1)} \times \exp(E/nRT)$ (Ranalli, 1995). Symbols with "*" indicate variables according to different cases.

Parameter	Symbol	Value-units
Thickness	H^{upper}	20 km
	H^{lower}	15 km
Density	ρ^{upper}	2800 kg/m ³
	ρ^{lower}	3000 kg/m ³
	ρ^{fault}	2500 kg/m ³
Dislocation creep power law pre-exponential factor ^a	A	$6.3 \times 10^{-21} \text{ Pa}^{-n}/\text{s}$
Dislocation creep power law exponent ^a	n	3.2
Power law creep activation energy ^a	E	244 kJ/mol
Viscosity	η^{crust}	10^{22} Pa s
	η^{fault}	10^{19} Pa s
Heat capacity	C	1000 J/kg K
Gas constant	R	$8.314 \text{ J mol}^{-1} \text{ K}^{-1}$
Gravitational acceleration	g	9.81 m/s ²
Friction angle (upper crust)	ϕ^{uf}	3–20°
Friction angle (lower crust)	ϕ^{lf}	11.5–30°
Cohesion (upper crust)	σ_c	1–20 Mpa
Cohesion (lower crust)	σ_c	8–40 Mpa

^a Plagioclase dominated rheology, after Ranalli (1995), Gerbault et al. (2009) and Ueda et al. (2012).

ond invariant of the strain rate tensor (Fig. 8b) yield about 85, 55, 44 and 29 for $\sigma_c = 1$ MPa (case b-3), $\sigma_c = 4$ MPa (case a-3), $\sigma_c = 10$ MPa (case b-2) and 15 MPa (case b-1) respectively over about 21.5 Ma, which indicates a large gap between $\sigma_c = 1$ MPa (case b-3) and $\sigma_c = 4$ Ma (case a-3).

For the rheological contrast in viscosity between the inherited structures and upper crustal rocks (Fig. 8c), the maximum accumulation of the second invariant of strain rate yields a highest point of 103 when the factor is taken to be 100 (case c-1), and from 85 to 95 for the cases c-2 and c-3 respectively. High viscosity contrast (2–3 orders of magnitude) between the shear zones and the surrounding rocks do help in concentrating the strain in the shear zone, as pointed out by Malservisi et al. (2003). According to the result, the viscosity contrast (by varying the viscosity of inherited shear zones) has less effect on accommodating finite strain under shear velocity field comparing with the softening degree of friction coefficient and cohesion in these models.

4.2. Onset of strain localization

Firstly, we test the effect of softening on the development of primacy of strain accommodation, by varying the coefficients of friction (Figs. 5 and 9a) and cohesion (Figs. 6 and 9b). The effect of viscosity contrast between the inherited structures and upper crustal rocks (Figs. 7 and 9c) is also examined. The dotted ellipse highlights the decreasing effect on capturing high strain localization in our models (Table 1 and Fig. 4). With respect to the softening effect of friction coefficient (Figs. 5 and 9a), cases a-3 and a-4 yield a similar age of about 10–14 Ma for focusing a developed fault zone under simple shear boundary conditions. With increasing softened friction coefficient from 0.1, the cases have a lower mechanical anisotropy and higher resistance to deformation. They respectively yield an increasing age of about 21.5 Ma and 28.8 Ma when softened friction coefficients are set to 0.15 and 0.2, this indicates an anticlockwise path with increasing softened friction coefficient. In terms of softening degree of cohesion, cases b-1 and b-2 locate in a same dotted ellipse, yields a similar age ranging between 19 and 21 Ma (Figs. 6 and 9b). Cases b-3 and a-3 concentrate developed primary structures at the age of about 10 Ma and 13 Ma. The ages for focusing such single structures increase with increasing softened cohesion (an increasing resistance to deformation), and exhibits a clockwise path. Viscosity contrast only achieved when the viscosity of the inherited structures change (Figs. 7 and 9c), the choice of modifying the viscosity of the upper crust is not studied here. For the cases c-1 and c-2, the onset of strain localization occurs at about 7 Ma and 11 Ma respectively. They yield a steep ascent path between the factor of 100 and 200 in viscosity, and then undergo a roughly flat path with increasing viscosity contrast. This generally flat path indicates that the role of viscosity of inherited shear zone does not significantly influence the timing of strain localization in this model due to its relatively lower volume ratio with respect to the whole computing domain.

4.3. Position of strain localization

In Fig. 10, the resulting models indicate that the spatial distribution of strain localization is controlled by different softening parameters (see details in Fig. 4. and Table 1). In all these experiments, the absolute distance to the NS-trending centre line (grey

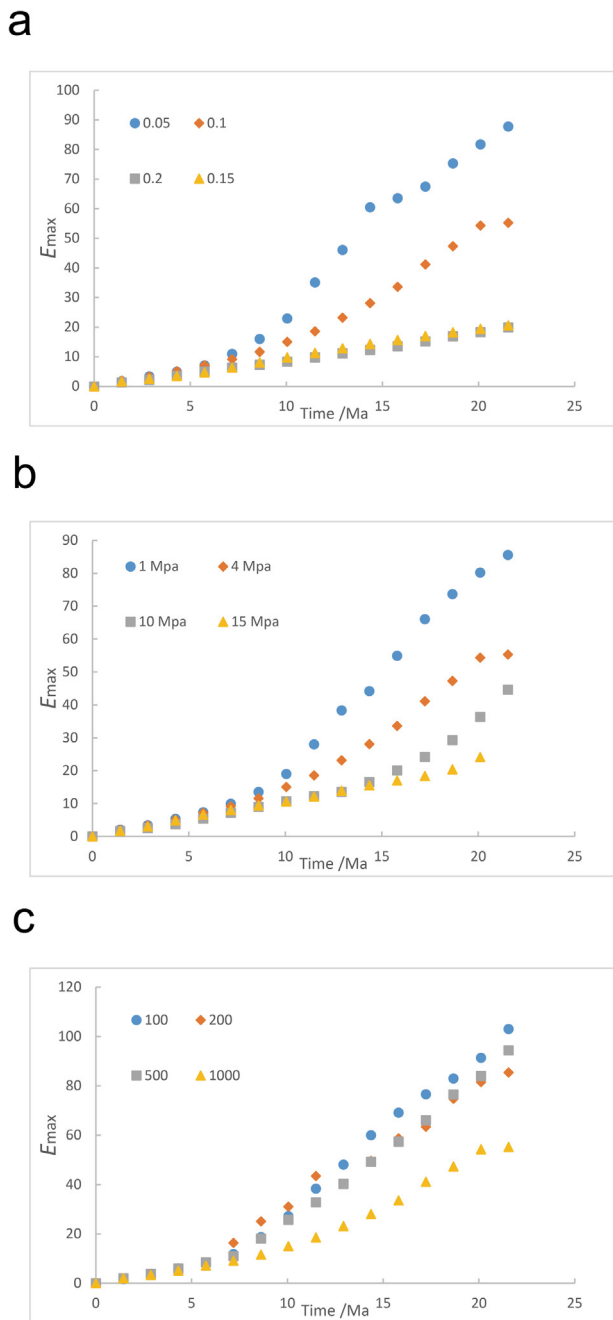


Fig. 8. Cumulative effect of the second invariant of the strain rate tensor influenced by the softening degree of friction coefficient (a) and cohesion (b) in upper crustal rocks, as well as viscosity contrast (c) between the inherited structures and surrounding wall rocks. The diagrams show the maximum accumulation of the second invariant of the strain rate tensor among all particles, calculated by $E_{max} = \max_{0 \leq i, m} E_i$. The legends in each figure represent the variables, corresponding to the terms in Table 1. Other mechanical and rheological parameters are given in Table 2 and Fig. 4.

dotted line in Fig. 3) generally decreases with the decreasing parameters (indicated by the grey arrow). The smaller difference between the inherited structures and softened surrounding rocks (indicated by the rectangle domain in light yellow), can be akin to the weak homogenous model to some extent. The strain localization in the model favours focusing near the middle line of model domain. The shortest distance (about 14 km) between the high strain zones and the NS-trending centre line is observed in experiment a-4 (Fig. 5). When the parameters are increased, experiments a-1, a-2, b-1, b-2 and c-3 yield a similar distance to

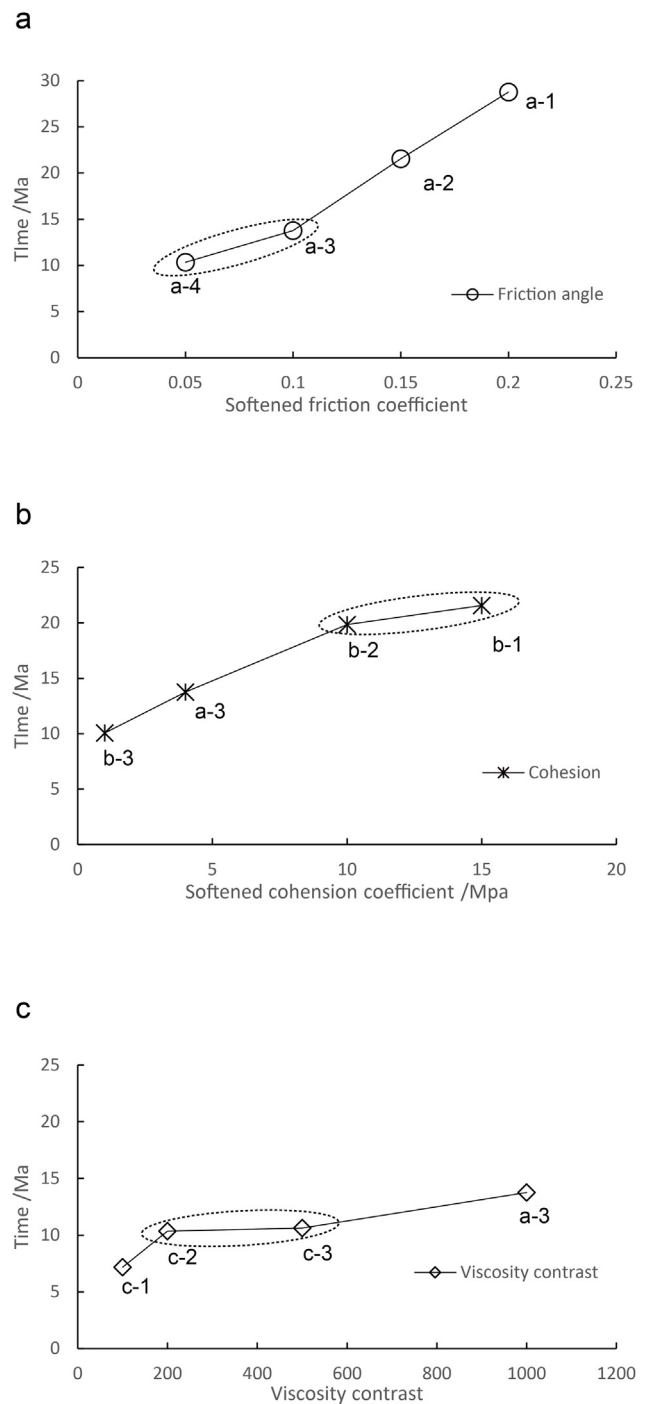


Fig. 9. Onset of shear strain localization influenced by the softening degree of friction (a) and cohesion (b) coefficients of upper crustal rock, as well as viscosity contrast (c) between the inherited structures and surrounding rocks. The dotted ellipses in these figures highlight the decreasingly promoting effect on capturing shear strain localization influenced by the strain weakening principle in these models. The names below the markers in each figure, corresponding to the Exp# column in Table 1. Other mechanical and rheological parameters are given in Table 2 and Fig. 4.

the NS-trending line (indicated by the rectangle domain in light purple). The phenomenon of focusing strain localization near the border mainly results from the difference in mechanical properties between inherited structures and surrounding rocks resulting in heterogeneously accumulating strain. The longest absolute distance (65 km) is observed in experiment a-1.

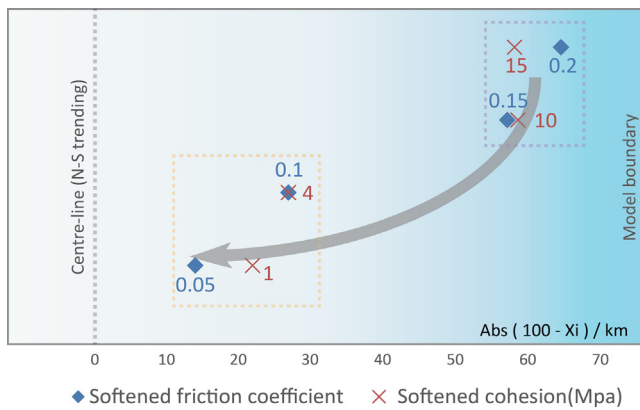


Fig. 10. Spatial position of strain localization in the model influenced by different softening coefficients, the colours of data labels (see details in Fig. 4. and Table 1) correspond to the legend. The blue marker represents the cases with different softened friction coefficient (corresponding to the parameters in the third column of Table 1), the red marker represents the cases with different softened cohesion (corresponding to the parameters in the fifth column of Table 1). The horizontal axis represents the absolute distance to the NS-trending centre line of model (indicated by the grey dotted line in Fig. 3), calculated by $Abs(100 - X_i)$, X_i represents the X coordinate (see details in Fig. 3) of presence of strain localization. (For interpretation of the references to colour in this figure legend, the reader is referred to the web version of this article.)

4.4. Influence of structure orientation

The initial model contains two sets of randomly inherited structures (NE-trending faults F1 and NW-trending faults F2), with different orientations (Fig. 3). In order to investigate the role of the numerous fabric orientations in strain localization, we tested the model only when it contains any one set of structure (Fig. 11), F1 (case D-1) or F2 (case D-2). The newly produced primary structure focuses near the border of the model in case D-1, while it is located near the centre line of the model in case D-2. The result also indicates that case D-1 undergoes a faster and more effective process for strain accumulation than case D-2. The difference in strain localization is dominantly influenced by the different orientations between inherited structures and the shear velocity fields. At about 5 Ma, a large amount of localized deformation tends to occur parallel to the external shear velocity field due to the fact that the NW trending structures are rotated to EW orientations and become non-favourable sites for strain accommodation (Feng et al., 2016). In addition, with respect to maximum accumulation of the second invariant of the strain rate tensor, they arrive at about 108 in case D-1 and 90 in case D-2 (Fig. 12).

5. Discussion

5.1. Strain weakening and orientations

Strain softening has a dominant role in affecting the strength of the upper crust, with evidence widely distributed in fault zones and in crustal rock on Earth (Wojtal and Mitra, 1986; Huisman and Beaumont, 2003, 2007; Bürgmann and Dresen, 2008; Qu et al., 2014). Strain weakening is used to produce the behaviour of strain softening in our models, which plays a significant role in controlling the formation, growth and evolution of strain localization (White et al., 1980; Hobbs et al., 1990; Jessell and Lister, 1991; Gerbault et al., 1999; Burlini and Bruhn, 2005), as rock strength averagely decreases with an increase in strain weakening (Warren et al., 2008; Niemeijer et al., 2010; Sharples et al., 2015).

In our models, strain localization influenced by different parameters of strain weakening shows a similar behaviour (Fig. 8a–c) before the system starts to experience strain softening (pre-

softening stage). When it accommodates enough deformation to strain softening (post-softening stage), thanks to the strain weakening mechanism, strain localization will progressively develop and grow under external boundary conditions (Frederiksen and Braun, 2001; Giger et al., 2008).

The degree of strain weakening plays a key role in influencing asymmetry of deformation (Sharples et al., 2015). When the inherited structures are re-activated under renewed boundary conditions, the spatial-temporal patterns of fault zones are strongly influenced by the strain weakening mechanism (Figs. 9 and 10). These models show a more homogeneous character when the softening coefficients are higher (see parameters and definition in Table 1). The greater occurrences of fault zones appear close to the centre line of the model (indicated by the light yellow dotted box, in Fig. 10). On the contrary, the model represents a more heterogeneous behaviour with decreasing softening coefficients during the post-softening stage (Table 1), fault zones mainly focus near the border of the model (indicated by the light purple dotted box in Fig. 10).

Inherited weaknesses in the crust play an important role in the initiation and evolving self-organization of strain localization re-activated by external boundary conditions, ex: influenced by changes or rotations of far field stresses (Tong et al., 2014; Feng et al., 2016). Inherited structures will be concentrated into narrow belts parallel to the imposed shearing direction through geological time. Oriented structures (NW trending fabrics F2s in Fig. 3) according to external shearing conditions would progressively accommodate strain, while most mis-oriented structures (NE trending fabrics F1s in Fig. 3) would be abandoned or passively rotated due to their non-favoured sites for strain accumulation from the eastern and western sides. This phenomena is reproduced quite well by a large number of analogue (e.g. Naylor et al., 1986; Richard et al., 1991, 1995; see review by Dooley and Schreurs (2012), and reference therein; Leever et al., 2011), numerical (Feng et al., 2016) and analytical (Sanderson and Marchini, 1984; Fossen and Tikoff, 1998) models. These models show that the orientation and shape of finite strain ellipsoids tend to change continuously as a result of the increase in simple shear component compared to the coaxial components of deformation. Furthermore, heterogeneous deformation can arise as a result of non-steady-state strain partition during the process of strain accommodation. At the end of continuously concentrating strain accumulation onto the higher net-strain portions, a single primary fault could be observed in the models (Figs. 5–7), which can play a significant role in accommodating long-term tectonic deformation and facilitating constituting visible complex tectonic structures through geological time (Ben-Zion and Sammis, 2003).

For models only containing one set of inherited structure (Fig. 11), Faults F2s have a more preferred orientation than faults F1s according to the external boundary conditions. The NE-trending faults F1s would be passively rotated to 90° from 30° (α , strike angle) to the shearing direction over about 4–5 Ma, accompanying with decreasing capacity in accommodating strain from the eastern and western walls. At the moment of arriving at 90° to the border (turning point), these pre-existing weaknesses have a smallest capacity to accommodate strain from the imposed boundary conditions (Feng et al., 2016). Therefore, a large amount of localized deformation in the surrounding rock would tend to occur parallel to the shear velocity field. For case D-2, the NW-trending faults F2s have an increasing capacity in accumulating strain over time, which tend to rotate to parallel to the shearing direction without undergoing a turning point in the process of strain accumulation. Therefore, the primacy fault in case D-2 occurs later and the position is closer to the centre line of the model than that in case D-1.

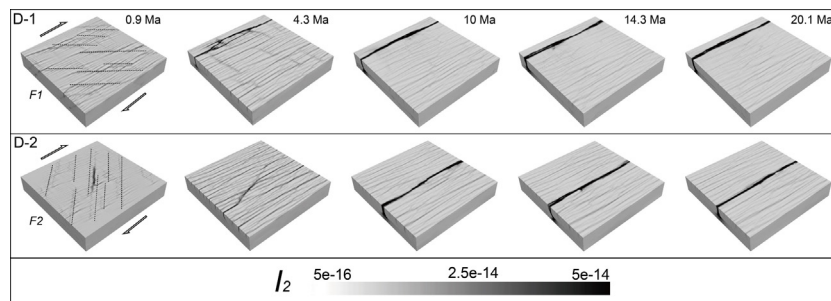


Fig. 11. Self-organization process of crustal deformation influenced by different orientations of inherited structures. The second invariant of the strain rate tensor is shown at 0.9 Ma ($\gamma=0.33$), 4.3 Ma ($\gamma=1.60$), 10 Ma ($\gamma=3.70$), 14.3 Ma ($\gamma=5.29$) and 20.1 Ma ($\gamma=7.44$) in the five columns. The name of each row in the left-top corner corresponds to the Exp# column in Table 1. Other mechanical and rheological parameters are given in Table 2 and Fig. 4.

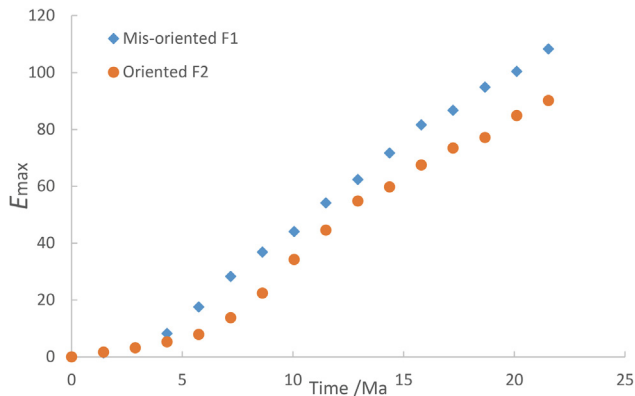


Fig. 12. Cases D-1 and D-2 arrive at maximum accumulation of the second invariant of the strain rate tensor of about 108 and 90 over 21.5 Ma respectively under the imposed shearing boundary conditions (solid arrows in Fig. 11).

5.2. Reconstruction: model application to the Alpine Fault

Strain weakening is widely suggested as an original trigger for strain localization in the lithosphere (e.g. Montési and Zuber, 2002; Regenauer-Lieb and Yuen, 2004; Montési, 2013; Gueydan et al., 2014). On a continental scale, the progressive interaction between strain weakening and strain localization leads to the progressive growth and maturation of new plate boundaries under external boundary conditions, while plate interiors may still remain intact (Jordan, 1978; Gueydan et al., 2014).

Most original NE and NW trending fabrics in southern New Zealand region were resulted from the extensional deformation phase associated with the breakup between portions of the Gondwana Australian-New Zealand plates and the rest of Gondwana, mostly located along the margins of the Otago block (Deckert et al., 2002; Gray and Foster, 2004). These fabrics subsequently grew and were re-activated by the interaction and spreading of continental plates, with strike-slip, transpressional and transtensional deformation.

During the Oligocene–Miocene times, the progressive propagation of the strike-slip deformation led to the maturation of the Australian–New Zealand plate boundary fault through the southern New Zealand (King, 2000; Upton et al., 2014). We suggest that our modelled inherited structures grew and developed during this stage. Under this, dominated dextral strike-slip boundary conditions, the distributed network of the initially inherited structures would influence the distribution and evolution of strain localization (Cooper et al., 1987; White, 2002; Batt et al., 2004). Most mis-oriented NE-trending structures would move and rotate passively, accommodate less strain or even be abandoned through geological time, as particular inherited NW-trending structures which have more optimally oriented geometries would grow and accommo-

date strain more progressively (Figs. 5–7). The self-organization of strain localization in the present study (Fig. 13c) is in general agreement with analytical results (Fig. 13a and b) in Lamarche et al. (1997) and Sutherland et al. (2000), their results show that pre-existing structures have been well oriented to accommodate plate motion since 20 Ma (Fig. 13). The NW trending shear zones (deep pink solid line in Fig. 13a and b) act as preferential loci for strain accommodation and have subsequently resulted in strain localization and led to maturation of the Australian–Pacific plate boundary fault (the Alpine Fault).

The NE-trending structures (F1s, Figs. 3 and 11) were preferably and passively rotated to vertical to the shearing direction at a shear strain of about $\gamma=1.6$, while the NW-trending structures (F2s, Figs. 3 and 11) were rotated to parallel to the NS direction under the extremal boundary conditions. Subsequently, these models with a greater softening coefficients would quickly transfer to the stage of forming a primary shear zone near the NS-directed centre-line of model (ex: experiments a-3, a-4, b-3 c-1 and c-2, in Figs. 9 and 10). These models with a smaller softening coefficients would undergo a longer time to form a primary fault (Figs. 9 and 10) due to a high resistance to deformation. The materials of the NW-trending structures (F2s, Fig. 3) synchronously migrate with the external shearing field, which can be thought to play a major role in contributing to forming relatively early potential high strain zones, while the NE-trending structures (F1s, Fig. 3) continuously and passively rotated under the far field boundary conditions.

When we arrived at a shear strain of about $\gamma=3.7$, the materials of the NE-trending structures (F1s, Fig. 3) were rotated to parallel to NS shearing direction and subsequently started to completely accumulate strain from the eastern-western sides. Combining with some materials of the NW-trending structures (F2s, Fig. 3), strain would be progressively accommodated on those merged and previously optimally oriented sites. A primary shear zone would be seen at the end of this evolutionary process with progressive maturation of the plate boundary fault, and this might be able to shed light on explaining the modern dominance and evolutionary history of the Alpine Fault (Oligocene–Miocene times) prior to the onset (approximately 7–8 Ma) of oblique convergence and the resulting Kaikoura Orogeny (thickening crustal pile) in southern New Zealand.

5.3. Limitations and perspectives

The repeated localization of deformation along pre-existing faults and shear zones is mainly controlled by their geometric (Feng et al., 2016) and internal rheological evolution (Upton et al., 2014) on either short or large time scales (Rutter et al., 2001). However, with respect to the natural case (the study area), the numerical model presented here contains two sets of faults, which have identical orientations (the NE and NW trending fabrics, indicated by Lamarche et al. (1997), Deckert et al. (2002) and Gray and Fos-

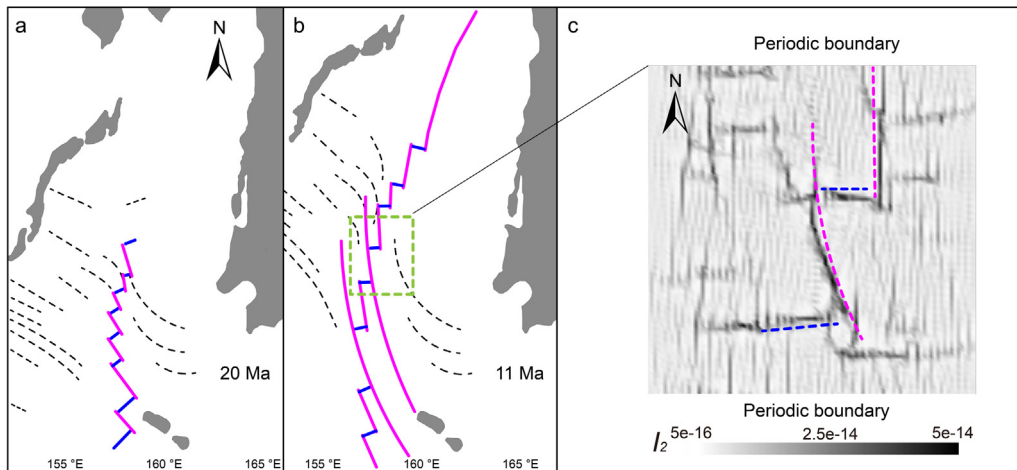


Fig. 13. Geometry of a two stage Australian-Pacific boundary (a, b, modified after Lamarche et al., 1997). Black dashed line = fracture zones; dark solid blue line = inherited NE trending fabrics (spreading ridges); deep pink solid line = inherited NW trending fabrics. (c) Numerical result in this study, case a-4. Dark blue dashed line = inherited structure F1s (NE trending, Fig. 3); dark pink dashed line = inherited structure F2s (NW trending, Fig. 3). The high strain zones indicated by dark pink dashed line will form a primary shear zone with increasing time steps (Fig. 5, a-4). (For interpretation of the references to colour in this figure legend, the reader is referred to the web version of this article.)

ter (2004)). The width of the inherited structures in the model is also fixed. To an extent, the geometric simplifications may result in reducing the complexities of the interaction of inherited structures and strain localization compared to the natural case. We are aiming to improve the geometric constrains of inherited structures in future numerical models.

The nature of deformation in the upper mantle and the structure of the fault beneath the Moho are open to great uncertainty (Norris and Toy, 2014). We therefore did not take into account the structural expressions in upper mantle (Norris and Toy, 2014) and the distribution of Moho depths in the South Island of New Zealand. This limitation can be improved in future models by using seismic images from the study area (Savage, 1999; Savage et al., 2004).

In terms of the boundary conditions, in our model we employed a fixed shear rate (Upton et al., 2014) without taking into account the changing position of the pole of rotation of the Pacific plate with respect to the Australian plate. This limitation may slightly alter the process of localization of deformation. Future models can be improved by considering the finite rotations (Lebrun et al., 2003) according to the kinematic reconstruction of the southern Australian-Pacific plate boundary (King, 2000).

We deliberately only focused on exploring the role of strength characteristic of the upper crust plays in controlling the behaviour of strain localization without involving any fluid behaviour. It would be delicate but interesting to couple with the dynamic fluid in the future, as it is important to mineral and hydrocarbon reserves (Rutter et al., 2001; Byerlee, 1993). In addition, we only focused on the self-organization of deformation at a crustal scale using a viscoplastic material, in the near future, in order to better constrain and improve the model, the effect of upper mantle and brittle shell (including elastic behaviour for upper continental crust) of Earth should be taken into consideration.

6. Conclusion

In this paper, three-dimensional thermo-mechanical models have been used to explore the effect of strain weakening on Oligocene–Miocene self-organization of the Australian-Pacific plate boundary in southern New Zealand under simple shear boundary conditions. The effect of the rheological contrast in viscosity was also studied.

The softening coefficients of the upper crust play a dominant role in the spatial and temporal patterns of strain localization in these models. The resulting model indicates the age of maturation of a primary shear zone decreases with increasing softening coefficients. The greater occurrences of faults appear close to the centre line of the model when the softening coefficients are greater. On the contrary, faults mainly focus near the border of the model with decreasing softening coefficients. The viscosity contrast has less effect on accommodating maximum finite strain comparing with the effect of softening degree of friction and cohesion coefficients in the model.

We reconstructed the process of Oligocene–Miocene self-organization of the Australian-Pacific plate boundary fault in southern New Zealand, the resulting model indicates that the materials of the NW-trending structures make a major contribution to forming relatively early potential high strain zones under the external shearing field before we arrived at a shear strain of about $\gamma = 3.7$. During this process, most NE trending structures would move and rotate passively, and accommodate less strain or even be abandoned through geological time. High rate of strain accumulation would contribute to initializing and facilitating the Australian-Pacific plate boundary fault. This model is suggested by the authors as a most likely process to interpret the evolution of structures and deformation at a crustal scale in southern New Zealand during the Oligocene–Miocene times.

Acknowledgments

This project was granted access to the High-Performance Computing (HPC) resources of both the French supercomputing centre, CCRT of the French Nuclear Agency, under allocation #2014-046351 awarded by GENCI (Grand Equipement National de Calcul Intensif), and the regional computing centre, CALMIP in Toulouse, France, under allocation #P1403. We also thank the development teams at the Victorian Partnership for Advanced Computing (VPAC) and Monash University for technical assistance with the software Underworld. We gratefully acknowledge John Mansour for comments and modifications on the previous code. Figures are plotted using open source package Visit developed by the Lawrence Livermore National Laboratory. X.F thanks the Chinese Scholarship Council (CSC) for his PhD scholarship. Two anonymous reviewers,

Guest editor Vincent Strak and Editor-in-Chief Wouter Schellart are gratefully acknowledged for their constructive comments.

References

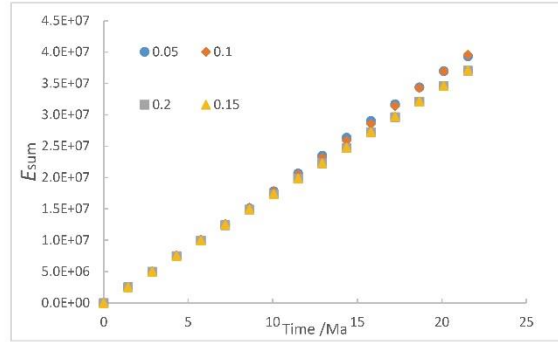
- Abaqus, 2001. *Standard, User's Manual*, vols. 1 and 2, version 6.2. Abaqus Inc., Pawtucket, RI, USA.
- Aktug, B., Dikmen, U., Dogru, A., Ozener, H., 2013. Seismicity and strain accumulation around Karliova triple junction (Turkey). *J. Geodyn.* 67, 21–29.
- Ariyoshi, K., Matsuzawa, T., Yabe, Y., Kato, N., Hino, R., Hasegawa, A., Kaneda, Y., 2009. Character of slip and stress due to interaction between fault segments along the dip direction of a subduction zone. *J. Geodyn.* 48 (2), 55–67.
- Aronson, J.L., 1965. Reconnaissance rubidium-strontium geochronology of New Zealand plutonic and metamorphic rocks. *N. Z. J. Geol. Geophys.* 8 (3), 401–423.
- Audet, P., Bürgmann, R., 2011. Dominant role of tectonic inheritance in supercontinent cycles. *Nat. Geosci.* 4 (3), 184–187.
- Bürgmann, R., Dresen, G., 2008. Rheology of the lower crust and upper mantle: evidence from rock mechanics, geodesy, and field observations. *Annu. Rev. Earth Planet. Sci.* 36 (1), 531.
- Barnes, P.M., 1994. Inherited structural control from repeated Cretaceous to Recent extension in the North Mernoo fault zone, western Chatham Rise, New Zealand. *Tectonophysics* 237 (1), 27–46.
- Barth, N.C., Boulton, C., Carpenter, B.M., Batt, G.E., Toy, V.G., 2013. Slip localization on the southern Alpine Fault, New Zealand. *Tectonics* 32 (3), 620–640.
- Batt, G.E., Baldwin, S.L., Cottam, M., Fitzgerald, P., Brandon, M.T., 2004. Cenozoic plate boundary evolution in the South Island of New Zealand: new thermochronological constraints. *Tectonics* 23, TC4001, <http://dx.doi.org/10.1029/2003TC001527>.
- Batt, G.E., 2001. The approach to steady state thermochronological distribution following orogenic development in the Southern Alps of New Zealand. *Am. J. Sci.* 301, 374–384.
- Beavan, J., Moore, M., Pearson, C., Henderson, M., Parsons, B., Bourne, S., England, P., Walcott, D., Blick, G., Darby, D., Hodgkinson, K., 1999. Crustal deformation during 1994–1998 due to oblique continental collision in the central Southern Alps, New Zealand, and implications for seismic potential of the Alpine fault. *J. Geophys. Res.: Solid Earth* (1978–2012) 104 (B11), 25233–25255.
- Beeler, N.M., Tullis, T.E., Blanpied, M.L., Weeks, J.D., 1996. Frictional behavior of large displacement experimental faults. *J. Geophys. Res.: Solid Earth* (1978–2012) 101 (B4), 8697–8715.
- Ben-Zion, Y., Sammis, C.G., 2003. Characterization of fault zones. *Pure Appl. Geophys.* 160 (3–4), 677–715.
- Berryman, K.R., Beanland, S., Cooper, A.F., Cutten, H.N., Norris, R.J., Wood, P.R., 1992. The Alpine Fault New Zealand: variation in quaternary structural style and geomorphic expression. *Ann. Tectonica* VI, 126–163.
- Bishop, D.G., Bradshaw, J.D., Landis, C.A., 1985. Provisional terrane map of South Island, New Zealand. In: Howell, G. (Ed.), *Tectonostratigraphic Terranes of the Circum-Pacific Region*, Earth Science Series, vol. 1. AAPG Circum-Pacific Council for Energy and Mineral Resources, Houston, Texas, pp. 515–521.
- Bradshaw, J.D., Andrews, P.B., Adams, C.J., 1980. Carboniferous to Cretaceous on the Pacific margin of Gondwana: The Rangitata phase of New Zealand. *Proceedings Fifth International Gondwana Symposium*.
- Braun, J., Herman, F., Batt, G., 2010. Kinematic strain localization. *Earth Planet. Sci. Lett.* 300 (3), 197–204.
- Buiter, Susanne J.H., Torsvik, T.H., 2007. Horizontal movements in the eastern Barents Sea constrained by numerical models and plate reconstructions. *Geophys. J. Int.* 171, 1376–1389.
- Burlini, L., Bruhn, D., 2005. High-strain zones: laboratory perspectives on strain softening during ductile deformation. *Geol. Soc. Lond., Special Publ.* 245 (1), 1–24.
- Byerlee, J., 1993. Model for episodic flow of high-pressure water in fault zones before earthquakes. *Geology* 21 (4), 303–306.
- Capitanio, F.A., Stegman, D.R., Moresi, L.N., Sharples, W., 2010. Upper plate controls on deep subduction, trench migrations and deformations at convergent margins. *Tectonophysics* 483 (1), 80–92.
- Carpenter, B.M., Saffer, D.M., Marone, C., 2012. Frictional properties and sliding stability of the San Andreas fault from deep drill core. *Geology* 40 (8), 759–762.
- Chester, F.M., Evans, J.P., Biegel, R.L., 1993. Internal structure and weakening mechanisms of the San Andreas Fault. *J. Geophys. Res.* 98 (B1), 771–786.
- Chousianitis, K., Ganas, A., Giannou, M., 2013. Kinematic interpretation of present-day crustal deformation in central Greece from continuous GPS measurements. *J. Geodyn.* 71, 1–13.
- Claypool, A.L., Klepeis, K.A., Dockrill, B., Clarke, G.L., Zwingmann, H., Tulloch, A., 2002. Structure and kinematics of oblique continental convergence in northern Fiordland, New Zealand. *Tectonophysics* 359 (3), 329–358.
- Coombs, D.S., 1985. New Zealand terranes. Third Circum-Pacific Terrane Conference. Geological Society of Australia. Extended abstracts.
- Cooper, A.F., Barreiro, B.A., Kimbrough, D.L., Mattinson, J.M., 1987. Lamprophyre dike intrusion and the age of the Alpine fault New Zealand. *Geology* 15 (10), 941–944.
- Davey, F.J., Henyey, T., Kleffman, S., Melhuish, A., Okaya, D., Stern, T.A., Woodward, D.J., 1995. Crustal reflections from the Alpine Fault Zone, South Island, New Zealand. *N. Z. J. Geol. Geophys.* 38, 601–604.
- Dawers, N.H., Anders, M.H., Scholz, C.H., 1993. Growth of normal faults: Displacement-length scaling. *Geology* 21 (12), 1107–1110.
- Deckert, H., Ring, U., Mortimer, N., 2002. Tectonic significance of Cretaceous bivergent extensional shear zones in the Torlesse accretionary wedge, central Otago Schist, New Zealand. *N. Z. J. Geol. Geophys.* 45 (4), 537–547.
- Dokka, R.K., Travis, C.J., 1990. Role of the eastern California shear zone in accommodating Pacific-North American plate motion. *Geophys. Res. Lett.* 17 (9), 1323–1326.
- Dooley, T.P., Schreurs, G., 2012. Analogue modelling of intraplate strike-slip tectonics: a review and new experimental results. *Tectonophysics* 574, 1–71.
- Duret, T., Gerya, T.V., May, D.A., 2011. Numerical modelling of spontaneous slab breakoff and subsequent topographic response. *Tectonophysics* 502 (1), 244–256.
- Ellis, S., Schreurs, G., Panien, M., 2004. Comparisons between analogue and numerical models of thrust wedge development. *J. Struct. Geol.* 26 (9), 1659–1675.
- Feng, X., Amponsah, P.O., Martin, R., Ganne, J., Jessell, M.W., 2016. 3-D numerical modelling of the influence of pre-existing faults and boundary conditions on the distribution of deformation: example of North-Western Ghana. *Precambrian Res.* 274, 161–179.
- Fossen, H., Tikoff, B., 1998. Extended models of transpression and transtension, and application to tectonic settings. *Geol. Soc. Lond., Special Publ.* 135 (1), 15–33.
- Frederiksen, S., Braun, J., 2001. Numerical modelling of strain localisation during extension of the continental lithosphere. *Earth Planet. Sci. Lett.* 188 (1), 241–251.
- GNS Science, 2010. 1:1 000 000 Geological Map of New Zealand, Institute of Geological and Nuclear Sciences, Lower Hutt, New Zealand, <http://portal.onegeology.org/>.
- Gaina, C., Müller, R.D., Royer, J.Y., Stock, J., Hardebeck, J., Symonds, P., 1998. The tectonic history of the Tasman Sea: a puzzle with 13 pieces. *J. Geophys. Res.* B 103 (B6), 12413–12433.
- Gerbault, M., Burov, E.E., Poliakov, A.A., Marc, D., 1999. Do faults trigger folding in the lithosphere? *Geophys. Res. Lett.* 26 (2), 271–274.
- Gerbault, M., Davey, F., Henrys, S., 2002. Three-dimensional lateral crustal thickening in continental oblique collision: an example from the Southern Alps, New Zealand. *Geophys. J. Int.* 150 (3), 770–779.
- Gerbault, M., Cembrano, J., Mpodozis, C., Farias, M., Pardo, M., 2009. Continental margin deformation along the Andean subduction zone: thermo-mechanical models. *Phys. Earth Planet. Inter.* 177 (3), 180–205.
- Giger, S.B., Cox, S.F., Tenthorey, E., 2008. Slip localization and fault weakening as a consequence of fault gouge strengthening—insights from laboratory experiments. *Earth Planet. Sci. Lett.* 276 (1), 73–84.
- Gray, D.R., Foster, D.A., 2004. ⁴⁰Ar/³⁹Ar thermochronologic constraints on deformation, metamorphism and cooling/exhumation of a Mesozoic accretionary wedge, Otago Schist, New Zealand. *Tectonophysics* 385, 181–210.
- Grindley, G.W., 1961. Geological Map of New Zealand, 1:250,000. New Zealand, Dept. Sci. Ind. Res. Sheet 13, Golden Bay.
- Gueydan, F., Précigout, J., Montési, L.G.J., 2014. Strain weakening enables continental plate tectonics. *Tectonophysics* 631, 189–196.
- Hobbs, B.E., Mühlhaus, H.B., Ord, A., 1990. Instability, softening and localization of deformation. *Geol. Soc. Lond., Special Publ.* 54 (1), 143–165.
- Huismans, R.S., Beaumont, C., 2003. Symmetric and asymmetric lithospheric extension: relative effects of frictional-plastic and viscous strain softening. *J. Geophys. Res.: Solid Earth* (1978–2012) 108 (B10), <http://dx.doi.org/10.1029/2002JB002026>.
- Huismans, R.S., Beaumont, C., 2007. Roles of lithospheric strain softening and heterogeneity in determining the geometry of rifts and continental margins. *Geol. Soc. Lond., Special Publ.* 282 (1), 111–138.
- Ikari, M.J., Marone, C., Saffer, D.M., 2011. On the relation between fault strength and frictional stability. *Geology* 39 (1), 83–86.
- Ireland, T., Gibson, G.M., 1998. SHRIMP monazite and zircon geochronology of high-grade metamorphism in New Zealand. *J. Metamorph. Geol.* 16 (2), 149–167.
- Jaquet, Y., Arthur, B., Stefan, S.M., 2014. Viscous overthrusting versus folding: 2-D quantitative modeling and its application to the Helvetic and Jura fold and thrust belts. *J. Struct. Geol.* 62, 25–37.
- Jessell, M.W., Lister, G.S., 1991. Strain localization behaviour in experimental shear zones. *Pure Appl. Geophys.* 137 (4), 421–438.
- Jessell, M.W., Siebert, E., Bons, P.D., Evans, L., Piazzolo, S., 2005. A new type of numerical experiment on the spatial and temporal patterns of localization of deformation in a material with a coupling of grain size and rheology. *Earth Planet. Sci. Lett.* 239 (3), 309–326.
- Jessell, M.W., Siebert, E., Bons, P., Evans, L., Piazzolo, S., 2008. Localisation of deformation. *Microdyn. Simul.*, 225–230.
- Jessell, M.W., Bons, P.D., Griera, A., Evans, L.A., Wilson, C.J., 2009. A tale of two viscosities. *J. Struct. Geol.* 31 (7), 719–736.
- Jessell, M.W., Amponsah, P.O., Baratoux, L., Asiedu, D.K., Loh, G.K., Ganne, J., 2012. Crustal-scale transcurrent shearing in the Paleoproterozoic Sefwi-Sunyani-Comoé region, West Africa. *Precambrian Res.* 212–213, 155–168.
- Jordan, T.H., 1978. Composition and development of the continental tectosphere. *Nature* 274 (5671), 544–548.
- Kamp, P.J.J., 1997. Paleogeothermal gradient and deformation style Pacific front of the Southern Alps orogen: constraints from fission track thermochronology. *Tectonophysics* 271, 37–58.
- Kim, Y.S., Sanderson, D.J., 2005. The relationship between displacement and length of faults: a review. *Earth-Sci. Rev.* 68 (3), 317–334.

- King, P.R., 2000. Tectonic reconstructions of New Zealand: 40 Ma to the present. *N. Z. J. Geol. Geophys.* 43 (4), 611–638.
- Kohler, M.D., Eberhart-Phillips, D., 2002. Three-dimensional lithospheric structure below the New Zealand Southern Alps. *J. Geophys. Res.: Solid Earth* (1978–2012) 107 (B10), <http://dx.doi.org/10.1029/2001JB000182>.
- Kokkalas, S., Doutsos, T., 2001. Strain-dependent stress field and plate motions in the south-east Aegean region. *J. Geodyn.* 32 (3), 311–332.
- Lamarche, G., Collot, J.-Y., Wood, R.A., Sossion, M., Sutherland, R., Delteil, J., 1997. The Oligocene–Miocene Pacific–Australia plate boundary, south of New Zealand: evolution from oceanic spreading to strike-slip faulting. *Earth Planet. Sci. Lett.* 148 (1), 129–139.
- Landis, C.A., Coombs, D.S., 1967. Metamorphic belts and orogenesis in southern New Zealand. *Tectonophysics* 4 (4), 501–518.
- Lebrun, J.F., Lamarche, G., Collot, J.Y., 2003. Subduction initiation at a strike-slip plate boundary: the Cenozoic Pacific–Australian plate boundary, south of New Zealand. *J. Geophys. Res.: Solid Earth* 108 (B9).
- Leever, K.A., Gabrielsen, R.H., Sokoutis, D., Willingshofer, E., 2011. The effect of convergence angle on the kinematic evolution of strain partitioning in transpressional brittle wedges: insight from analog modeling and high-resolution digital image analysis. *Tectonics* 30, TC2013, <http://dx.doi.org/10.1029/2010TC002823>.
- Little, T.A., Mortimer, N., 2001. Rotation of ductile fabrics across the Alpine Fault and Cenozoic bending of the New Zealand orocline. *J. Geol. Soc.* 158 (5), 745–756.
- Malservisi, R., Gans, C., Furlong, K., 2003. Numerical modeling of strike-slip creeping faults and implications for the Hayward fault, California. *Tectonophysics* 361, 121–137.
- Marone, C., 1998. Laboratory-derived friction laws and their application to seismic faulting. *Annu. Rev. Earth Planet. Sci.* 26 (1), 643–696.
- Miyashiro, A., 1961. Evolution of metamorphic belts. *J. Petrol.* 2 (3), 277–311.
- Montési, L.G., Zuber, M.T., 2002. A unified description of localization for application to large-scale tectonics. *J. Geophys. Res.: Solid Earth* (1978–2012) 107 (B3), <http://dx.doi.org/10.1029/2001JB000465>.
- Montési, L.G., 2013. Fabric development as the key for forming ductile shear zones and enabling plate tectonics. *J. Struct. Geol.* 50, 254–266.
- Moresi, L., Dufour, F., Mühlhaus, H.B., 2003. A Lagrangian integration point finite element method for large deformation modeling of viscoelastic geomaterials. *J. Comput. Phys.* 184 (2), 476–497.
- Moresi, L., Quenette, S., Lemiale, V., Meriaux, C., Appelbe, B., Mühlhaus, H., 2007a. Computational approaches to studying non-linear dynamics of the crust and mantle. *Phys. Earth Planet. Inter.* 163 (1), 69–82.
- Moresi, L., Mühlhaus, H.B., Lemiale, V., May, D., 2007b. Incompressible viscous formulations for deformation and yielding of the lithosphere. *Geol. Soc. Lond., Special Publ.* 282 (1), 457–472.
- Moresi, L., Betts, P.G., Miller, M.S., Cayley, R.A., 2014. Dynamics of continental accretion. *Nature* 508 (7495), 245–248.
- Mortimer, N., 2004. New Zealand's geological foundations. *Gondwana Res.* 7 (1), 261–272.
- Mortimer, N., 2014. The orocline bend in the South Island, New Zealand. *J. Struct. Geol.* 64, 32–38.
- Muir, R.J., Ireland, T.R., Weaver, S.D., Bradshaw, J.D., Evans, J.A., Eby, G.N., Shelley, D., 1998. Geochronology and geochemistry of a Mesozoic magmatic arc system, Fiordland, New Zealand. *J. Geol. Soc.* 155 (6), 1037–1053.
- Naylor, M.A., Mandl, G.T., Supestejin, C.H.K., 1986. Fault geometries in basement-induced wrench faulting under different initial stress states. *J. Struct. Geol.* 8 (7), 737–752.
- Niemeijer, André, Marone, Chris, Elsworth, Derek, 2010. Frictional strength and strain weakening in simulated fault gouge: competition between geometrical weakening and chemical strengthening. *J. Geophys. Res.: Solid Earth* (1978–2012) 115, B10207, <http://dx.doi.org/10.1029/2009JB000838>.
- Nilfouroushan, F., Pysklywec, R., Cruden, A., 2012. Sensitivity analysis of numerical scaled models of fold-and-thrust belts to granular material cohesion variation and comparison with analog experiments. *Tectonophysics* 526, 196–206.
- Norris, R.J., Toy, V.G., 2014. Continental transforms: a view from the Alpine Fault. *J. Struct. Geol.* 64, 3–31.
- Norris, R.J., Koons, P.O., Cooper, A.F., 1990. The obliquely-convergent plate boundary in the South Island of New Zealand: implications for ancient collision zones. *J. Struct. Geol.* 12 (5), 715–725.
- OzBench, M., Regenauer-Lieb, K., Stegman, D.R., Morra, G., Farrington, R., Hale, A., May, D.A., Freeman, J., Bourgoin, L., Mühlhaus, H., Moresi, L., 2008. A model comparison study of large-scale mantle–lithosphere dynamics driven by subduction. *Phys. Earth Planet. Inter.* 171 (1), 224–234.
- Park, J., 1921. Geology and mineral resources of western Southland. *N. Z. Geol. Surv. Bull.* 23, 1–88.
- Qu, W., Lu, Z., Zhang, Q., Li, Z., Peng, J., Wang, Q., Drummond, J., Zhang, M., 2014. Kinematic model of crustal deformation of Fenwei basin, China based on GPS observations. *J. Geodyn.* 75, 1–8.
- Ranalli, G., 1995. *Rheology of the Earth*. Springer Science & Business Media, pp. 413.
- Regenauer-Lieb, K., Yuen, D., 2004. Positive feedback of interacting ductile faults from coupling of equation of state, rheology and thermal-mechanics. *Phys. Earth Planet. Inter.* 142 (1), 113–135.
- Richard, P., Mocquet, B., Cobbold, P.R., 1991. Experiments on simultaneous faulting and folding above a basement wrench fault. *Tectonophysics* 188 (1), 133–141.
- Richard, P.D., Naylor, M.A., Koopman, A., 1995. Experimental models of strike-slip tectonics. *Pet. Geosci.* 1 (1), 71–80.
- Rutter, E.H., Holdsworth, R.E., Knipe, R.J., 2001. The nature and tectonic significance of fault-zone weakening: an introduction. *Geol. Soc. Lond., Special Publ.* 186 (1), 1–11.
- Sanderson, D.J., Marchini, W.R.D., 1984. Transpression. *J. Struct. Geol.* 6 (5), 449–458.
- Savage, M.K., Fischer, K.M., Hall, C.E., 2004. Strain modelling, seismic anisotropy and coupling at strike-slip boundaries: applications in New Zealand and the San Andreas Fault. *Geol. Soc. Lond., Special Publ.* 227 (1), 9–39.
- Savage, M.K., 1999. Seismic anisotropy and mantle deformation: what have we learned from shear wave splitting? *Rev. Geophys.* 37 (1), 65–106.
- Schellart, W.P., Freeman, J., Stegman, D.R., Moresi, L., May, D., 2007. Evolution and diversity of subduction zones controlled by slab width. *Nature* 446 (7133), 308–311.
- Schellart, W.P., Stegman, D.R., Farrington, R.J., Freeman, J., Moresi, L., 2010. Cenozoic tectonics of western North America controlled by evolving width of Farallon slab. *Science* 329 (5989), 316–319.
- Scholz, C.H., Cowie, P.A., 1990. Determination of total strain from faulting using slip measurements. *Nature* 346 (6287), 837–839.
- Scholz, C.H., 1998. Earthquakes and friction laws. *Nature* 391 (6662), 37–42.
- Sharples, W., Moresi, L.N., Jadamec, M.A., Revote, J., 2015. Styles of rifting and fault spacing in numerical models of crustal extension. *J. Geophys. Res.: Solid Earth* 120, <http://dx.doi.org/10.1002/2014JB011813>.
- Sibson, R.H., Xie, G., 1998. Dip range for intracontinental reverse fault ruptures: truth not stranger than fiction? *Bull. Seismol. Soc. Am.* 88 (4), 1014–1022.
- Sibson, R.H., 1977. Fault rocks and fault mechanisms. *J. Geol. Soc.* 133 (3), 191–213.
- Stegman, D.R., Freeman, J., Schellart, W.P., Moresi, L., May, D., 2006. Influence of trench width on subduction hinge retreat rates in 3D models of slab rollback. *Geochim. Geophys. Geosyst.* 7, Q03012, <http://dx.doi.org/10.1029/2005GC001056>.
- Suggate, R.P., 1965. The tempo of events in New Zealand geological history. *N. Z. J. Geol. Geophys.* 8 (6), 1139–1148.
- Sun, Y., Dong, S., Zhang, H., Shi, Y., 2014. Numerical investigation of the geodynamic mechanism for the late Jurassic deformation of the Ordos block and surrounding orogenic belts. *J. Asian Earth Sci.* 114, 623–633.
- Sutherland, R., Davey, F., Beavan, J., 2000. Plate boundary deformation in South Island, New Zealand, is related to inherited lithospheric structure. *Earth Planet. Sci. Lett.* 177 (3), 141–151.
- Sutherland, R., 1999. Basement geology and tectonic development of the greater New Zealand region: an interpretation from regional magnetic data. *Tectonophysics* 308 (3), 341–362.
- Tavarnelli, E., Pasqui, V., 2000. Fault growth by segment linkage in seismically active settings: examples from the Southern Apennines, Italy, and the Coast Ranges, California. *J. Geodyn.* 29 (3), 501–516.
- Tchalenko, J.S., 1970. Similarities between shear zones of different magnitudes. *Geol. Soc. Am. Bull.* 81 (6), 1625–1640.
- Thomas, W.A., 2006. Tectonic inheritance at a continental margin. *GSA Today* 16 (2), 4–11.
- Tong, H., Koyi, H., Huang, S., Zhao, H., 2014. The effect of multiple pre-existing weaknesses on formation and evolution of faults in extended sandbox models. *Tectonophysics* 626, 197–212.
- Turner, F.J., 1938. Progressive regional metamorphism in southern New Zealand. *Geol. Mag.* 75, 160–174.
- Ueda, K., Gerya, T.V., Burg, J.P., 2012. Delamination in collisional orogens: thermomechanical modeling. *J. Geophys. Res. Solid Earth* 117, B8.
- Upton, P., Craw, D., Walcott, R., 2014. Far-field deformation resulting from rheologic differences interacting with tectonic stresses: an example from the Pacific/Australian plate boundary in southern New Zealand. *Geosciences* 4 (3), 93–113.
- Vauchez, A., Tommasi, A., Barruol, G., 1998. Rheological heterogeneity, mechanical anisotropy and deformation of the continental lithosphere. *Tectonophysics* 296 (1), 61–86.
- Vlaar, N.J., Van Keken, P.E., Van den Berg, A.P., 1994. Cooling of the Earth in the Archean: consequences of pressure-release melting in a hotter mantle. *Earth Planet. Sci. Lett.* 121 (1), 1–18.
- Walcott, R.I., 1998. Modes of oblique compression: late Cenozoic tectonics of the South Island of New Zealand. *Rev. Geophys.* 36, 1–26.
- Walsh, J.J., Watterson, J., 1987. Distributions of cumulative displacement and seismic slip on a single normal fault surface. *J. Struct. Geol.* 9 (8), 1039–1046.
- Walsh, J.J., Watterson, J., 1988. Analysis of the relationship between displacements and dimensions of faults. *J. Struct. Geol.* 10 (3), 239–247.
- Walsh, J.J., Childs, C., Imber, J., Manzocchi, T., Watterson, J., Nell, P.A.R., 2003. Strain localisation and population changes during fault system growth within the Inner Moray Firth, Northern North Sea. *J. Struct. Geol.* 25 (2), 307–315.
- Warren, C.J., Beaumont, C., Jamieson, R.A., 2008. Deep subduction and rapid exhumation: role of crustal strength and strain weakening in continental subduction and ultrahigh-pressure rock exhumation. *Tectonics* 27, TC6002, <http://dx.doi.org/10.1029/2008TC002292>.
- Whalen, L., Gazel, E., Vidito, C., Puffer, J., Bizimis, M., Henika, W., Caddick, M.J., 2015. Supercontinental inheritance and its influence on supercontinental breakup: the Central Atlantic Magmatic Province and the breakup of Pangea. *Geochim. Geophys. Geosyst.* 16 (10), 3532–3554.
- White, S.H., Burrows, S.E., Carreras, J., Shaw, N.D., Humphreys, F.J., 1980. On mylonites in ductile shear zones. *J. Struct. Geol.* 2 (1), 175–187.

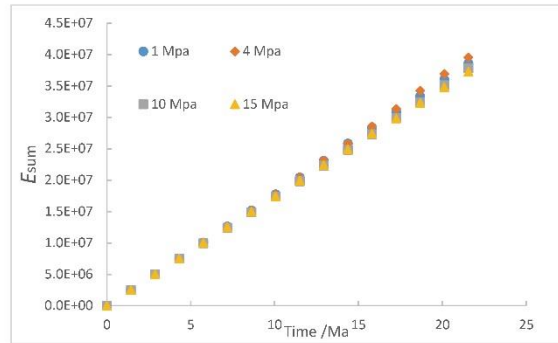
- White, S.R., 2002. The Siberia Fault Zone, northwest Otago, and kinematics of mid-Cenozoic plate boundary deformation in southern New Zealand. *N. Z. J. Geol. Geophys.* 45 (2), 271–287.
- Wojtal, S., Mitra, G., 1986. Strain hardening and strain softening in fault zones from foreland thrusts. *Geol. Soc. Am. Bull.* 97 (6), 674–687.
- Woodcock, N.H., Daly, M.C., 1986. The role of strike-slip fault systems at plate boundaries [and discussion]. *Philos. Trans. R. Soc. Lond. A: Math. Phys. Eng. Sci.* 317 (1539), 13–29.
- Xu, S., Nieto-Samaniego, A.F., Alaniz-Álvarez, S.A., Velasquillo-Martínez, L.G., Grajales-Nishimura, J.M., García-Hernández, J., Murillo-Muñetón, G., 2010. Changes in fault length distributions due to fault linkage. *J. Geodyn.* 49 (1), 24–30.

3.2.2 Appendix

a



b



c

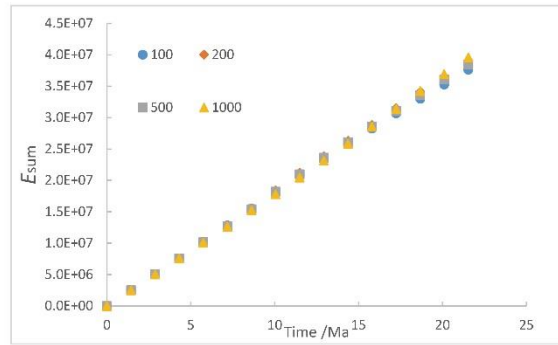


Figure S1: Cumulative effect of the second invariant of the strain rate tensor influenced by the softening degree of friction (figure. a) and cohesion (figure. b) coefficients in upper crustal rocks, as well as viscosity contrast (figure. c) between the inherited structures and surrounding wall rocks. They show the total accumulation of the second invariant of the strain rate tensor in the whole computing domain, calculated by $E_{sum} = \sum_{i=1}^n E_i$, i represents particles, in which $E_i = \sum_{j=0}^t I_2 \cdot \Delta t$, and $I_2 = \dot{\epsilon}_{xx} \cdot \dot{\epsilon}_{yy} + \dot{\epsilon}_{xx} \cdot \dot{\epsilon}_{zz} + \dot{\epsilon}_{yy} \cdot \dot{\epsilon}_{zz} - \dot{\epsilon}_{xy}^2 - \dot{\epsilon}_{xz}^2 - \dot{\epsilon}_{yz}^2$.

Chapter 4

The role of interacting fault systems on the exhumation of the lower crust

Introduction

In chapter 3, the influence of pre-existing faults on the processes of localization of deformation has been explored under both simple shear and pure shear boundary conditions. However, in these cases, partial melting is not taken into account, even though the process of partial melting can significantly change the rheology and density of the system. This chapter includes two main sections aiming to explore the exhumation of lower crust during extension and transtension.

In section 4.1, 2D and 3D thermo-mechanical models presented here aim to explore exhumation during extensional, using as a constraint the geology of NW Ghana during the Eburnean Orogeny (Block et al., 2015). More specifically, the modelling examines the role pre-existing faults play in influencing the spatial-temporal distribution of the lower crust exhumation in an extensional tectonic regime. This section was submitted for publication to *Tectonophysics* on 23/02/2016.

In Section 4.2, 3D thermo-mechanical models are employed to explore the processes of fault growth and the lower crust exhumation driven by transtension boundary conditions. The modelling results can be used to better understand the loci of the lower crust exhumation and evolution of deformation in the Sefwi terrane, SW Ghana. This section is planned to be submitted to *Journal of Structural Geology* for publication in December, 2016

4.1 Influence of pre-existing faults on the distribution of lower crust exhumation under extension: Numerical modelling and Implications for NW Ghana

Highlights

1. 2D and 3D thermo-mechanical models have been constructed to explore the influence of the orientation of pre-existing faults on the exhumation of partially molten lower crustal rocks during extension.
2. The Bole-Bulenga Terrane was stretched on the order of cm/year during the D2 N-S extension.
3. High-strain corridors are used to explain the loci of lower crust exhumation in NW Ghana (ca. 2.15-2.05 Ga).

Abstract

2D and 3D thermo-mechanical models have been constructed to explore the influence of pre-existing faults on the temporal-spatial distribution of exhumation of the lower crust during extension. The different dip angles of a pre-existing fault are studied in 2D models, and a system of three pre-existing faults is further explored in 3D models. The 2D models show that time length required for lower crust exhumation beneath a flat fault is longer compared to a steep fault. The fastest exhumation from 12 kbar to 6 kbar is achieved within 1 Ma when stretched on the order of 2 cm/year. The 3D models show that the exhumation of lower crust occurs at a relatively low rate prior to Stretching Factor (SF) = 4.2%. The partially molten lower crust rocks tend to move towards the center of the model (up to 20 km) and focus exhumation near the intersection-zones of pre-existing faults.

The high-strain corridors observed in 3D models are used to better understand the loci of exhumation in the Bole-Bulenga domain of NW Ghana. In the eastern and western parts of the high grade rock corridors in NW Ghana, partially molten rocks exhumed from the lower into middle-upper crustal levels are interpreted to have been dominantly facilitated by the km-scale high-strain corridors. In the central part of the Bole-Bulenga domain, the high grade rocks are interpreted to have been exhumed as a result of a coupling between two mechanisms:

- (1) The concentration of partially molten rocks between the Jirapa and Bole-Nangodi faults increases due to the reduction in space from north to south.
- (2) The concentration of lower partially molten rocks in the central part, as a result of inherited orthogonal (E-W) structures.

Keywords: Extension, Partial melting, Thermo-mechanical model, Pre-existing fault, Eburnean Orogeny

4.1.1 Introduction

Pre-existing discontinuities in the crust generally provide sites for strain concentration (Jessell and Lister, 1991; Morley et al., 2004; Willingshofer et al., 2005; Bellahsen and Daniel, 2005). The role of the orientation of such discontinuities on growth and re-activation of fault systems has been widely explored in numerical (D'Agostino et al., 1998; Feng et al., 2016b) and analogue (Imber et al., 2004; Dooley et al., 2012) models, as well as field investigations (Thatcher and Hill, 1991; Hand and Sandiford, 1999).

The formation process of metamorphic core complexes (MCCs) is generally related to extensional tectonics at a continental scale. This is characterized by the exhumation of partially molten lower crustal materials up to the upper crustal levels (Lister and Davis, 1989). Although numerous 2D-numerical (Burg et al., 2009; Rey et al., 2009a, 2009b, 2011; Choi et al., 2013) and analogue (Brun et al., 1994; Tirel et al., 2006; Sokoutis et al., 2007) models have been used to study the formation processes of MCCs in extensional tectonic settings, the use of 3D numerical modelling (Le Pourhiet et al., 2012) including pre-existing faults remains largely unexplored.

The emplacement of partially molten rocks into the upper crust is usually assisted by pre-existing shear zones (Vigneresse and Tikoff, 1999; Neves et al., 1996). In the high grade Bole-Bulenga Terrane (BBT) of NW Ghana, three high-strain zones separate high grade rocks (amphibolite-migmatite facies) from adjacent low grade greenstone belts (Block et al., 2015a, 2015b, 2016). These high-strain (shear zones) zones are known as the Bole-Nangodi shear zones, the Jirapa shear zone and the Bulenga shear zone (Figure 4.1.1). The BBT is mainly influenced by two deformation phases (D1 and D2). The initial deformation stage (D1) is characterized by crustal thickening. The second deformation stage (D2) is defined by N-S extension (Block et al., 2015a).

According to Block et al. (2015a) and Block, (2015b), the EW Bulenga shear zone is a consequence of the initial deformation phase (D1). The preliminary form of the NE-SW Bole-Nangodi shear zones resulted from the processes of bringing low- and high- grade rocks in contact during the D1 phase. Some inherited structures of the NS Jirapa shear zone also appeared in the D1 stage. During the D2 N-S extension stage, a large amount of amphibolite-migmatites were exhumed along these fault zones between 2137 ± 8 Ma and 2127 ± 7 Ma (Block et al., 2015a). Partially molten rocks with pressures up to about 6-7 kbar (corresponding to an approximate burial of 20 km), were exhumed during the D2 extension.

In order to understand how pre-existing shear zones contribute and influence the exhumation processes under extension, a series of 2D and 3D thermo-mechanical numerical models were constructed and analyzed. The models were constrained by the metamorphic rock record observed in

the structures within the study area by Block et al. (2015a). Firstly, we employ the use of five 2D models to test the role of a single normal fault with different dip angles have on the processes of exhumation in general (same parameters with 3D models). Subsequently, ten 3D models (with differently oriented faults) related to the high grade BBT geometry have been constructed to explore the evolutionary history of partially molten crustal materials exhumed during extension. This study may shed light on the effect of orientation of pre-existing faults on the formation and development processes of lower crust exhumation during extension.

4.1.2 Geological setting

4.1.2.1 The West African Craton (WAC)

The WAC consists of three major Archaean and Paleoproterozoic blocks (Figure 4.1.1a); these blocks are the Réguibat Shield to the north, the Leo-Man Shield (Figure 4.1.1b) to the south and the smaller Kenieba and Kayes Inliers which lies in between the Reguibat Shield and the Leo-Man Shield (Bessoles, 1977; Sylvester and Attoh, 1992; Figure 4.1.1a). The volcano-sedimentary and plutonic belts in the Leo-Man Shield form roughly parallel bands, while this is not observed in the Réguibat Shield, perhaps suggesting a different geodynamic setting. In the 2.20-2.00 Ga Birimian terrane of the Leo-Man Shield, the geodynamic setting has been suggested to be associated with either an immature volcanic arc (Dioh et al., 2006) or an oceanic plateau (Boher et al., 1992).

4.1.2.2 The Leo-Man Shield

The Leo-Man shield (Figure 4.1.1b) is bounded to the east and west by Pan-African and Hercynian orogenic belts. It consists of the Archaean age Kénema-Man domain to the west and the Proterozoic Baoulé-Mossi domain to the east. The contact between the Archaean and Proterozoic domains is marked by the Sassandra Fault (SF).

The Baoulé-Mossi domain (also known as the Birimian domain) is located to the north and east of the Kénema-Man domain (Figure 4.1.1b), and is characterized by extensively distributed N-S to NE-SW trending greenstone belts intruded and separated by several generations of granitoids, and/or by sedimentary basins. The earliest granitoids intrusions were emplaced at 2195-2172 Ma (Hirdes et al., 1992; Sakyi et al., 2014), roughly contemporaneous with the Birimian mafic volcanic activities (Baratoux et al., 2011). The main magmatic pulses intruded the whole volcanic complexes between ~2153 Ma and 2068 Ma (U-Pb and Pb-Pb zircon ages, Hirdes et al., 1996; Gasquet et al., 2003).

The Eburnean orogenic event in the Leo-Man Shield operated from ~2130 Ma (or 2160 Ma, Baratoux et al., 2011) to 1980 Ma (Davis et al., 1994; Feybesse et al., 2006) and is characterized by two main deformation phases. The first phase (D1), is characterized by a major crustal thickening event (Allibone et al., 2002; Vidal et al., 2009) between 2160 Ma and 2110 Ma (Baratoux et al., 2011). The second

phase (D2) continued up to 1980 Ma, where the initial E-W compressional regime in the D1 is switched to a dominant strike-slip transpression.

4.1.2.3 Summary of the Bole-Bulenga Terrane (BBT)

The Paleoproterozoic BBT is located in the eastern portion of the Baoulé-Mossi domain (Figure 4.1.1c). The BBT consists of the NE-SW Bole-Nangodi shear zones, the N-S trending Wa-Lawra belt, the NNW trending Jirapa and the adjacent Jang shear zones, the E-W trending Julie belt, the northern Koudougou-Tumu granitoid domain, the central Bole-Bulenga domain, the southern Abulembire domain and the southeastern Maluwe basin (Figure 4.1.1c, Block et al., 2015a).

The E-W-oriented Julie belt separates the Koudougou-Tumu granitoid domain from the Bole-Bulenga domain, and mostly consists of basalt, volcano-sedimentary rocks and granitoids (Amponsah et al., 2015). The foliation planes in the volcano-sedimentary rocks within the belt exhibit stretching lineation diving down-dip (Block et al., 2015). To the west of the Julie belt, the NNW trending Jirapa and its adjacent Jang shear zones separate the Koudougou-Tumu granitoid domain from the Wa-Lawra belt. The Jirapa shear zone merged with the southern portion of the Bole-Nangodi shear zones during extension (Block et al., 2015).

The Bole-Nangodi shear zones extend into the southern portion of Burkina Faso for over 300 km in NE-SW direction (Naba et al., 2004). The shear zones contain volcanic rocks, greywackes, shales, gabbros and deformed to undeformed granitoids with crystallization ages ranging from 2195 Ma to 2119 Ma. These rocks have been metamorphosed up to greenschist to amphibolite facies metamorphic grade (De Kock et al., 2011). The Maluwe basin lies to the south of the Bole-Nangodi shear zones. It mainly contains volcanic and volcani-clastic rocks, intruded by several pulses of granitoids with crystallization ages between 2137 Ma and 2118 Ma (De Kock et al., 20011).

4. Role of interacting fault systems on the exhumation of the lower crust

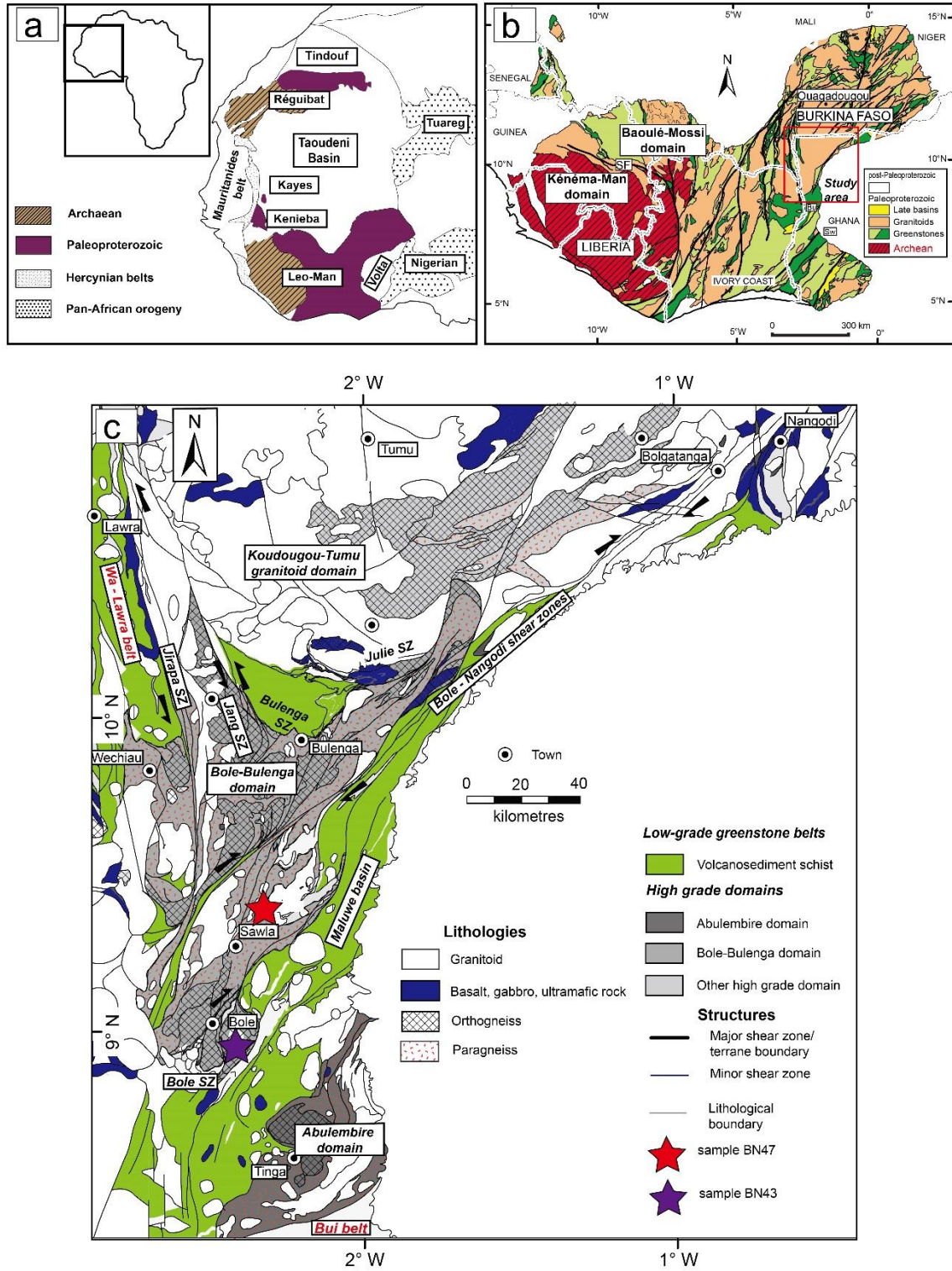


Figure 4.1.1: (a) Sketch map of the WAC, modified after Peucat et al. (2005) (b) Main geological units in the Leo-Man Shield, modified after the BRGM SIGAfrique map (Milési et al., 2004). (c) The high grade BBT, several dominant shear zones separate low grade greenstone belt (volcano-sediment) from high grade tectono-metaphoric terranes (after Block et al., 2015a). Purple and red stars are used to show PT-paths in Figure 4.1.2.

PT-paths (Block et al., 2015a) show a near-isothermal decompression (Figure 4.1.2) during the D2 stage, which took place between 2137±8 Ma and 2127±7 Ma (U-Pb dating). This indicates a localized extension on a magnitude order of cm/year (Rey et al., 2009b). The maximum pressures calculated from paragneiss samples (Figure 4.1.2) at the beginning of the D2 decompression range between 11 kbar and 13 kbar (corresponding to a depth of about 45 km).

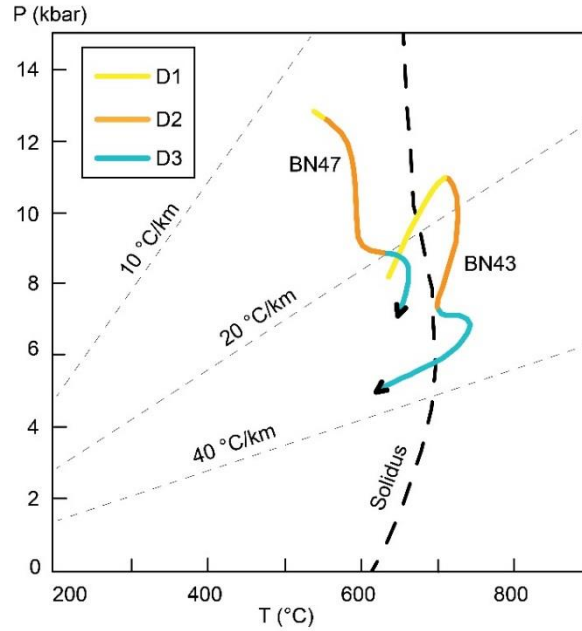


Figure 4.1.2: PT-paths after Block et al. (2015a), the information of latitude/longitude of samples is given in figure. 1. BN43 is a migmatitic paragneiss from the southern Bole-Nangodi shear zones. BN47 is a sample of paragneiss from the Bole-Bulenga domain.

4.1.3 Numerical method and assumptions for the model

The numerical code *Underworld* is used to model the exhumation of partially molten lower crustal materials during extension (corresponding to the D2 extension stage in the study area during the Eburnean Orogeny in the WAC, Figure 4.1.2). The code uses a Lagrangian Particle in Cell (PIC) finite element scheme (Moresi et al., 2003, 2007). The governing equations of momentum, mass (approximately incompressible material) and energy are expressed as follows (De Smet et al., 1998; Moresi et al., 2003, 2007);

$$\frac{\partial \sigma_{ij}}{\partial x_j} = \rho_{eff} \cdot g_i \quad (4.1.1)$$

$$\nabla \cdot u = 0 \quad (4.1.2)$$

$$\frac{\partial T}{\partial t} + u \cdot (\nabla T) = k \nabla^2 T + \frac{H}{C_p} - \frac{lh}{C_p} \cdot \frac{\partial M}{\partial t} \quad (4.1.3)$$

where ρ_{eff} is the effective density, k is the thermal diffusion, H is the radiogenic heat production per mass unit, C_p is the heat capacity, lh is the latent heat and M is the melt fraction.

The 2D model, is 400 km long and 70 km thick, modelled with a resolution of 2 km x 1 km (Figure 4.1.3). The 3D model is 310 km long, 240 km wide and 60 km thick, with a resolution of 3 km x 2 km x 1 km (Figure 4.1.4). We use a random initial particle layout with 30 particles in each cell and modeled as a visco-plastic rheology (Rey et al., 2009a, 2009b, 2011). The use of elastic properties is not possible in this version of the UNDERWORLD code, but the effect of deformation does not significantly influence the results for long time scale since materials yield rapidly (Ellis et al., 2004; Buitter et al., 2006; Nilfouroushan et al., 2012).

The 2D and 3D models domains consist of an upper 35 km thick Non-Newtonian rheological layer (Figures 4.1.3 and 4.1.4, represent mafic crust). A 10 km thick Non-Newtonian lower crust is defined below the upper crust. Beneath the lower crust, a 15 km thick Non-Newtonian upper mantle defines the base of the model. In the lower crust (Figures 4.1.3 and 4.1.4), two groups of passive particles (100 particles for the 2D model, 420 particles for the 3D model) are placed at depths $Z = -35$ km and $Z = -40$ km respectively in order to track displacements.

For the 2D model, we employ a sticky air layer overlying the upper crust, with a low density of 1 kg/m^3 . Variations in the thickness and the viscosity of the sticky 'air' layer could influence the evolution of topography (Crameri et al., 2012). Since the study of topography is not the main task in this work, a low viscosity of 10^{18} Pa s and a medium thickness of 10 km are defined for the sticky air layer (similar values of viscosity and thickness were used in Ueda et al., 2012; Ruh et al., 2013; Marques et al., 2013; Liao et al., 2013). Given the chosen layer thickness, viscosity and density, this layer could approximate a freely evolving surface at least for long time-scales.

The displacement boundary condition is set for extension with a rate of 2 cm/year for each side, 4 cm/year in total (indicated by red arrows in Figures 4.1.3 and 4.1.4). At the base of the model, the upper mantle is allowed to flow in, with a normal velocity (free slip in horizontal direction), balancing the volume reduction per time step due to extension (Liao and Gerya, 2014). For the thermal conditions, we model the extension of a "hot" lithosphere, with a 45 km crust (including 35 km mafic upper crust and 10 km lower crust) and a Moho temperature of about 900 °C (Tirel et al., 2008; Wang et al., 2015), assuming a temperature gradient of 20 °C/km. The temperatures at the surface ($Z=0$) and bottom ($Z=-60$ km) are fixed to 20 °C and 1220 °C, respectively (at bottom $Z = -60$ km, temperature conditions are similar to those defined by Tirel et al., 2008; Ganne et al., 2014; Wang et al., 2015). Other physical and thermal properties are given in Tables 3.

4. Role of interacting fault systems on the exhumation of the lower crust

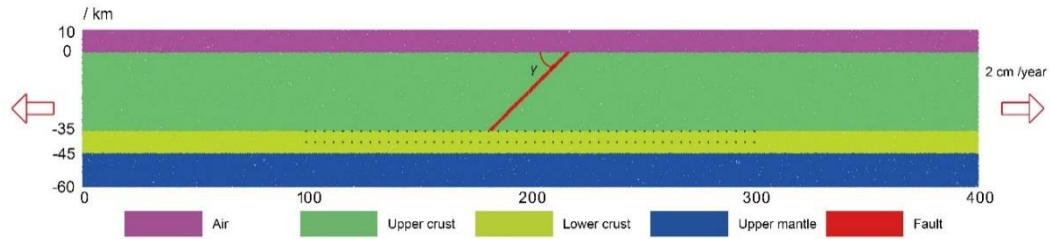


Figure 4.1.3: 2D thermo-mechanical model under extensional boundary conditions. In the upper crust, we define a crustal-scale fault with variable angles of dip (γ) whose thickness is set to about 2 km (Le Pourhiet et al., 2004). Two rows of passive particles located in the lower crust are employed to track the evolution of lower crust exhumation.

Table 4.1.2: 2D Experiments with different dip angles.

Angle of dip (γ) /($^{\circ}$)	90	75	60	45	35
Experiment 2D [#]	D90	D75	D60	D45	D35

A depth dependent Drucker-Prager yield criterion is employed to model the solid-deformation behavior, which is expressed as follows (Moresi et al., 2007; Sharples et al., 2015):

$$\tau_{II} = \delta_c + P \cdot \tan\varphi \quad (4.1.4)$$

In which τ_{II} is the second invariant of the deviatoric stress tensor, P is the local pressure, φ is the internal friction angle. We employ an initial cohesion of 15 MPa and an initial coefficient of friction angle of 0.44 for the crust and mantle domains, the pre-existing faults are set to 10% of the initial values (Rey et al., 2009b). For the crust and mantle domains, a strain-weakening principle (OzBench et al., 2008; Gueydan et al., 2014; Feng et al., 2016b) is applied to model the effective cohesion and coefficient of friction angle (drop to a maximum of 20%, Rey et al., 2009b; Collettini et al., 2009; Faulkner et al., 2010).

Table 4.1.2: 3D Experiments with different orientations (all initial models are plotted in Figure. 4. 1. S1).

Experiment 3D#	γ_A /($^{\circ}$)	γ_C /($^{\circ}$)	γ_B /($^{\circ}$)	Stretching Factor (SF)
3D-a	90	60	90	5.8%
3D-b	90	120	90	5.5%
3D-c	120	60	60	5.3%
3D-d	120	120	60	5.6%
3D-e	120	30	60	5.4%
3D-f	120	150	60	5.2%
3D-g	120	120	120	5.1%
3D-h	60	120	120	5.2%
3D-i	90	No fault	90	7.0%
3D-j	120	No fault	60	6.4%

4. Role of interacting fault systems on the exhumation of the lower crust

With respect to the partially molten process for the crust layers; the upper mafic crust rock has a very low rate of melt productivity and starts to melt at a relative high solidus temperature of $T_{sol} = 836 \text{ }^\circ\text{C}$ (Ganne et al., 2014). This corresponds to a buried depth of about 40 km at the given temperature gradient of $20 \text{ }^\circ\text{C}$. In this study, the thickness of upper crust is set to 35 km, with an extensional boundary condition. Based on this model setup and thermodynamic assumptions, we do not allow the upper crust to melt but the lower crust can melt. The volumetric melt fraction for the lower crust is calculated according to the procedures outlined by Gerya and Yuen, (2003). The volumetric melting coefficient (X_M) for calculating melt fraction (M) is expressed as equations (4.1.5) and (4.1.6):

$$\begin{aligned}
 X_M &= 0 && \text{at } T \leq T_{sol} \\
 X_M &= \frac{T - T_{sol}}{T_{liq} - T_{sol}} && \text{at } T_{sol} < T < T_{liq} \\
 X_M &= 1 && \text{at } T \geq T_{liq}
 \end{aligned}
 \tag{4.1.5}$$

where T_{sol} and T_{liq} are the wet solidus and dry liquidus temperatures of the lower crust, respectively. We assume that the T_{sol} and T_{liq} temperatures do not change with pressure (Gerya et al., 2008; Ganne, et al., 2014).

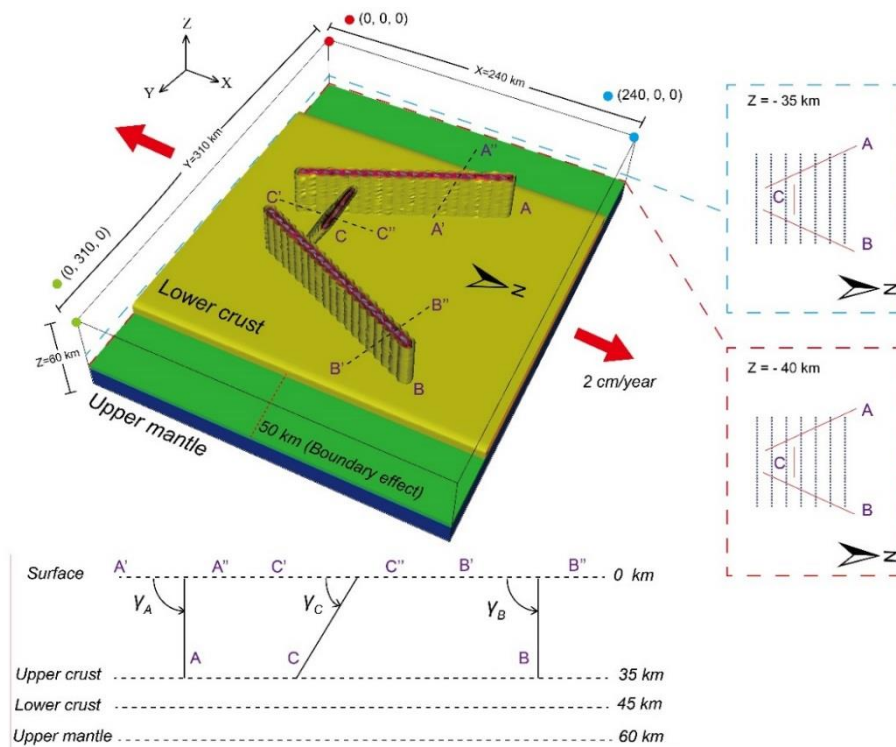


Figure 4.1.4: 3D thermo-mechanical model consists of three pre-existing faults (faults A, B and C) in the upper crustal domain (35 km thick). The azimuth of faults A, B and C are fixed to 335° , 25° and 90° , respectively. To the east and west of faults, a 50 km wide distance is employed to reduce the boundary effect. The angles

4. Role of interacting fault systems on the exhumation of the lower crust

γ_A, γ_B and γ_C are counted counterclockwise from surface to faults A, B and C, indicated by the cross-sections A'-A'', B'-B'' and C'-C''. 420 passive particles in total are placed in the horizontal planes of $Z = -35$ km and $Z = -40$ km.

We also assume that the volumetric melt fraction (M) linearly increases with the temperature, when the temperature is above the wet solidus temperature and below the dry liquidus temperature (Gerya et al., 2008; Ganne et al., 2014).

$$M = X_M \cdot M_{max} \quad (4.1.6)$$

When the temperature reaches the melting point of the lower crust (T_{sol}), a reduced effect (equation (4.1.7)) is applied to model effective viscosity (Pinkerton and Stevenson, 1992), which is function of melt fraction M and is expressed as follows:

$$\eta_{eff} = 5 \times 10^{16} \cdot \exp\left(2.5 + (1 - M) \left(\frac{1-M}{M}\right)^{0.48}\right) \quad (4.1.7)$$

Table 4.1.3: Thermo-mechanical model parameters, symbol and value-units.

Parameter	Symbol	Value-units
Thickness	H_{upper}	35 km
	H_{lower}	10 km
	H_{mantle}	15 km
Density	ρ_{upper}	3050 kg/m ³
	ρ_{lower}	2700 kg/m ³
	ρ_{mantle}	3250 kg/m ³
	ρ_{fault}	2800 kg/m ³
Melting point of lower crust (Ganne et al., 2014)	T	$T_{sol} = 636$ °C (1%) $T_{liq} = 1200$ °C (80%)
Heat capacity	Cp	1000 J/kg·K
Thermal diffusivity	k	10 ⁻⁶ m ² /s
thermal expansion coefficient	α	3x10 ⁻⁵ K ⁻¹
Latent heat	lh	300 KJ kg ⁻¹ K ⁻¹
Gas constant	R	8.314 J mol ⁻¹ K ⁻¹
Gravitational acceleration	g	9.81 m/s ²
Friction angle for Drucker-Prager criterion	φ/f	3-25°
Cohesion for Drucker-Prager criterion	δ_c	3-15 MPa

Table 4.1.4: Rheological parameters for different layers (from Ranalli, 1995 and references therein). The effective viscosity is calculated with a non-Newtonian power law using the equation: $\eta_0 = 0.25 \cdot (0.75A)^{(-1/n)} \cdot \dot{\epsilon}^{((1/n)-1)} \cdot \exp(Q/nRT)$.

Layer	Rock type	A (MPa ⁻ⁿ /s)	n	Q (kJ/mol)
Upper crust	Diabase	2.0 x 10 ⁻⁴	3.4	260
Lower crust	Quartzodiorite	1.3 x 10 ⁻³	2.4	219
Uppermost mantle	Dry olivine	7 x 10 ⁴	3.3	520
Fault			10 ²⁰ Pa s	

The effective density in the computational domain is calculated according to the temperature and the thermal expansion coefficient (α) of $3 \cdot 10^{-5} \text{ K}^{-1}$. A constant thermal diffusivity of $10^{-6} \text{ m}^2/\text{s}$ is applied. To relate density to temperature, a linear relationship for the non-melttable layers (upper crust, upper mantle and fault domains) is expressed as:

$$\rho_{eff} = \rho[1 - \alpha(T - T_0)] \quad (4.1.8)$$

For the lower crust, we follow the UNDERWORLD module (LinearDensityMelt) to calculate the effective density, which is a function of temperature, melt fraction and pressure and expressed as (similarly prescribed in Rey et al., 2009b):

$$\rho_{eff} = \rho[1 - \alpha(T - T_0) - mc \cdot M + \beta(P - P_0)] \quad (4.1.9)$$

where ρ_{eff} is the effective density, ρ is the original density, α is the thermal expansion coefficient, T is the local temperature, T_0 is the reference temperature at surface (20 °C), mc is the coefficient of expansion related to phase change, β is the compressibility coefficient (10^{-11} Pa^{-1} , similar to Ganne et al., 2014), P is the local pressure and P_0 is the reference pressure.

4.1.4 Results

Five 2D and ten 3D models tested the influence of orientation of pre-existing faults on the distribution of lower crust exhumation (decompression from 11-13 kbar to 6-7 kbar). All models were run on the EOS cluster in Toulouse (CALMIP center, 2.8 Ghz, 20 cores per node). The 2D and 3D models were run on a parallel 20 and 200 cores, respectively. In this section, we employ the accumulation of the second invariant (ϵ_{II}) of the strain rate (E_{II} shearing strain, calculated by $E_{II} = \sum_0^t \epsilon_{II} \cdot \Delta t$) and N-S-directed (ϵ_{xx}) strain rate over time (E_{xx} extensional strain, calculated by $E_{xx} = \sum_0^t \epsilon_{xx} \cdot \Delta t$) to show the potential/preferential channels for further emplacement.

4.1.4.1 2D models

4.1.4.1.1 Influence of fault dip angle.

Initially, we tested the role of the dip angle of fault playing in exhumation of partially molten lower crustal materials using 2D models. From experiments D90 and D75, topography remains symmetric, with the highest relief near both the left and right boundaries of basin (Figure 4.1.5). Experiments D60, D45 and D35 display an asymmetric relief that reaches its highest height at the right margin of basin, where the footwall of the pre-existing fault is located (Figure 4.1.5).

In experiments D90, D75 and D60, two high-strain shear bands form during extension (Figure 4.1.5). The intersection angle of shear bands increases with time resulting from upward flow of partially molten rocks. Experiments D45 and D35, only produce a single major shear band with dip angles ranging between 30° and 40°. The dip angles on the single shear band do not change significantly as extension continues. This indicates that the pre-existing fault in experiments D90, D75 and D60 plays a passive role in the process of strain concentration as most of the deformation is focused on the shear band. In experiments D60, D45 and D35, the pre-existing fault concentrates more strain.

These experiments show that the upper particles in the lower crust move slowly towards the footwall of pre-existing fault compared to the deeper ones. The partially molten rocks beneath a flat fault is less sensitive to exhumation compared to a steep fault. The distance between neighboring particles located in the deeper level of the lower crust becomes shorter with time. When the dip angle of fault increases from 35° to 90°, lower crust exhumation shows an increasing impact on the evolutionary deformation of pre-existing fault.

4. Role of interacting fault systems on the exhumation of the lower crust

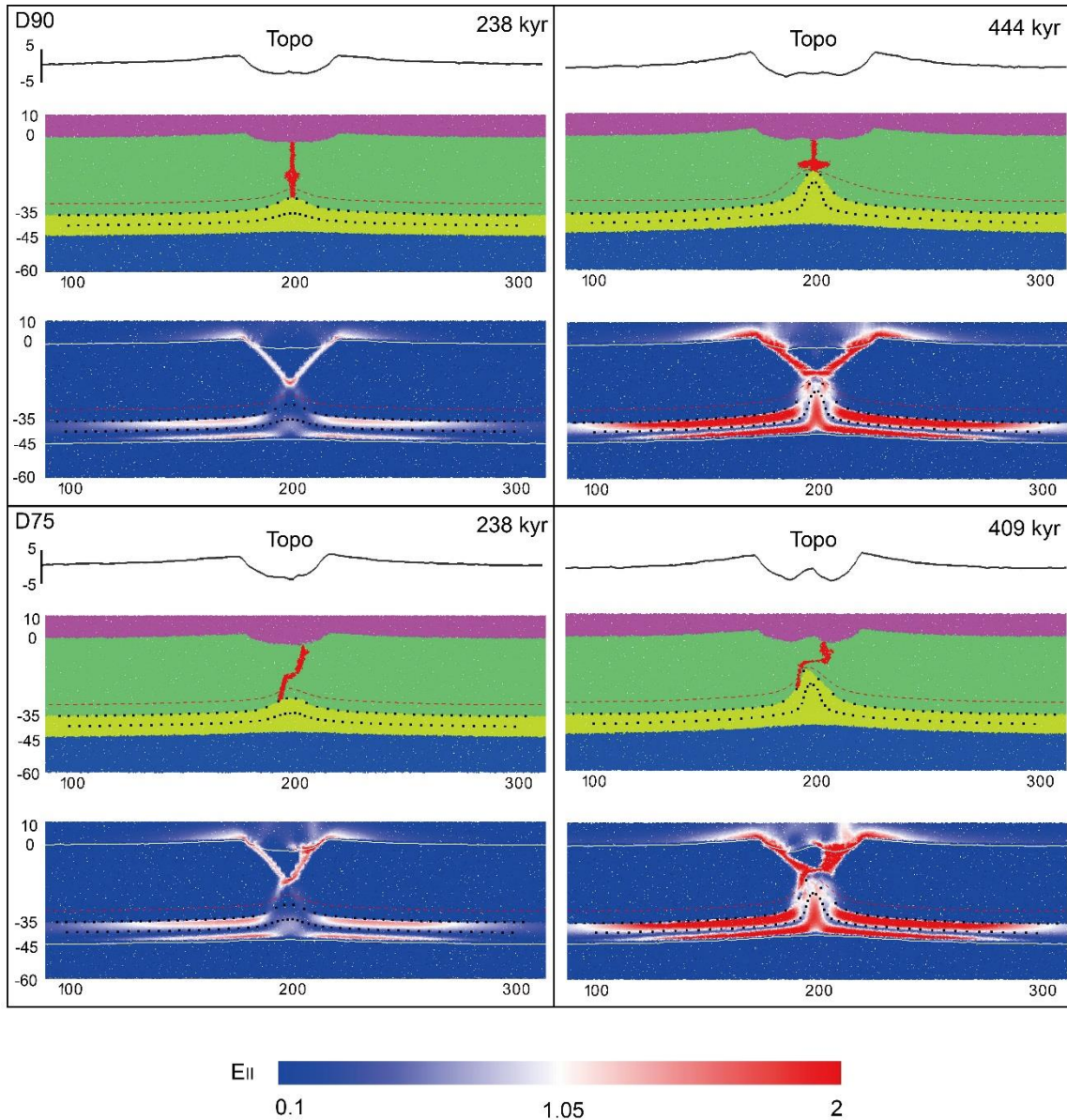


Figure 4.1.5. Evolution of lower crust exhumation and topography in an extensional tectonic regime (stretched at a total rate of 4 cm/year). The dip angles of fault are set to 90° (D90), 75° (D75), 60° (D60), 45° (D45), 35° (D35), respectively. E_{II} represents the accumulation of the second invariant (ϵ_{II}) of the strain rate, calculated by $E_{II} = \sum_0^t \epsilon_{II} \cdot \Delta t$. Horizontal and vertical axis values are in km.

4. Role of interacting fault systems on the exhumation of the lower crust

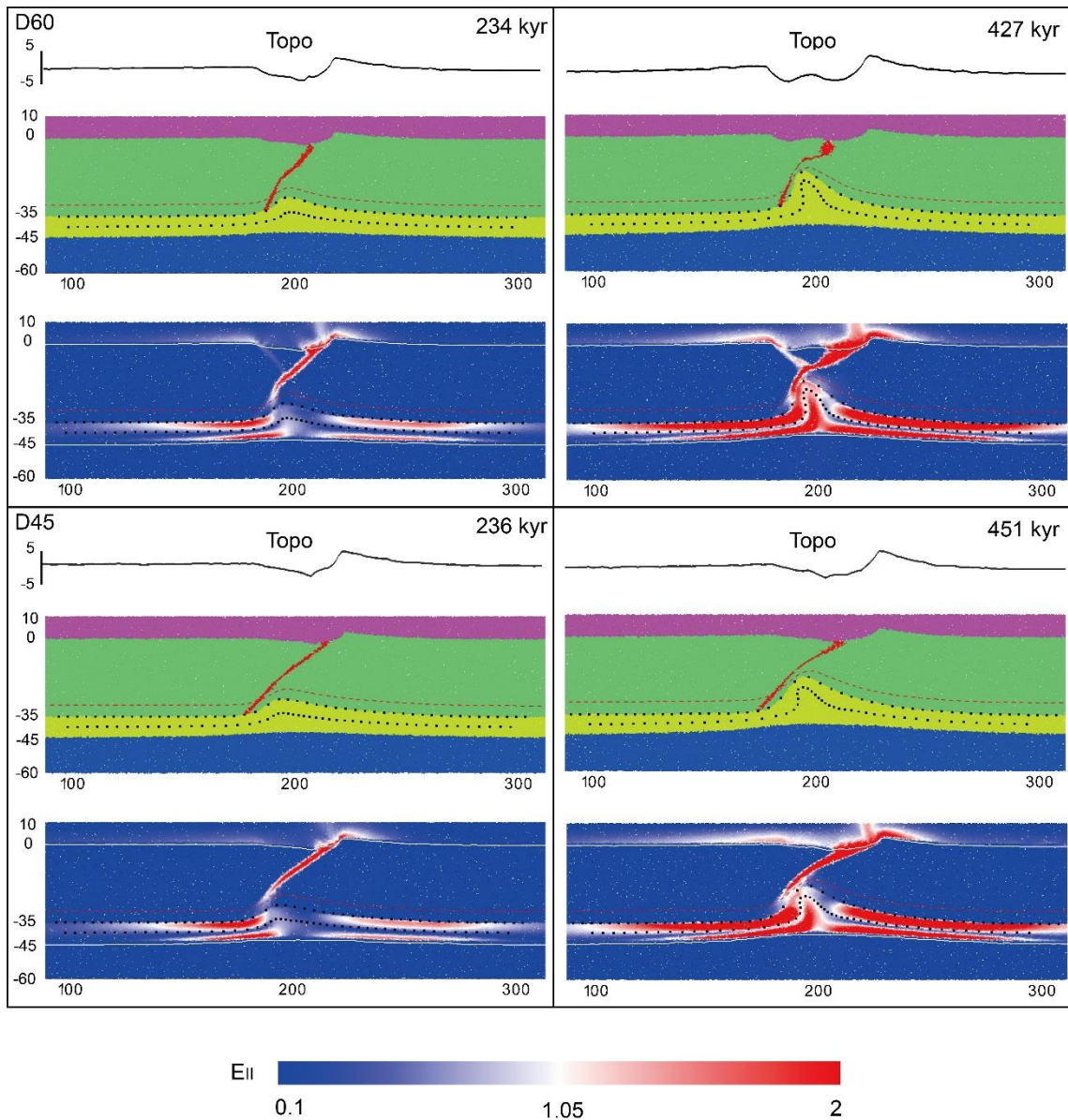


Figure 4.1.5. (Continued)

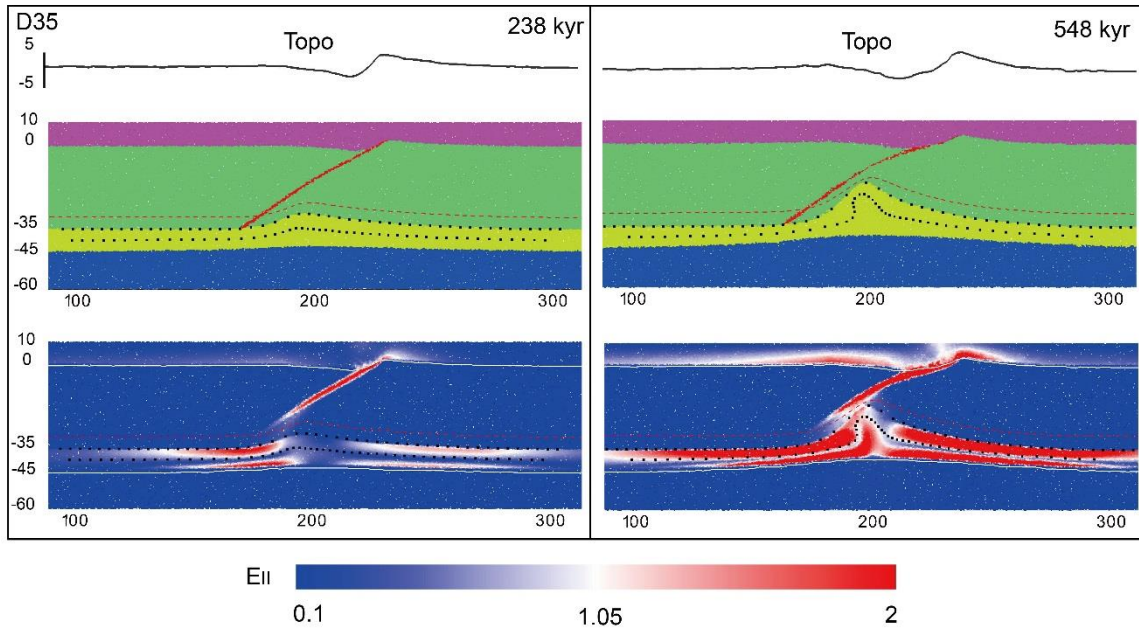


Figure. 4.1.5 (Continued)

4.1.4.1.2 Exhumation rate

Figure 4.1.6 shows that different dip angles of the pre-existing fault yield similar P-T paths when the pressure is between 12 kbar and 6 kbar. The fastest exhumation is achieved within 1 Ma. The time required for the lower crust to exhume beneath a flat fault is longer than a steep fault. For experiments D45 and D35, time for exhumation increases from about 450 to 550 kyr when the dip angle of fault decreases from 45° (D45) to 35° (D35). However, for a relatively steep fault (experiments D90, D75 and D60), these cases yield a similar time length of about 425 kyr for exhumation.

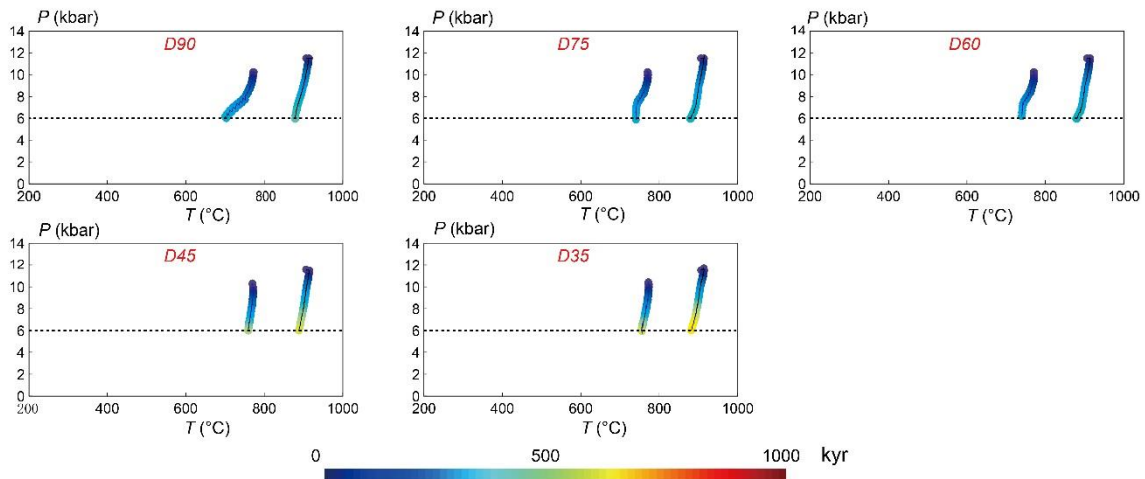


Figure 4.1.6. Exhumation rate (PT-t) influenced by different dip angles (γ) of fault. Red font in each figure corresponds to the item (Experiment #) in Table 4.1.2. The color scale bar represents the time length.

4.1.4.2 Exhumation of lower crust in the 3D models

A series of 3D models were employed to explore the role of pre-existing faults (Figure 4.1.4) in the spatial distribution of partially molten rocks during extension (Figures 4.1.7.3D-a ~ 4.1.7.3D-h and Figure 4.1.S1). For experiments 3D-a and 3D-b (Figures 4.1.7. 3D-a and 3D-b), faults A and B were both set to vertical ($\gamma_A = \gamma_B = 90^\circ$), and the dip of fault C was set to $\gamma_C = 60^\circ/120^\circ$, respectively. The results show that partially molten lower crustal rocks generally move towards and concentrate along the pre-existing faults A, B and C. The two experiments show that the main difference between models with different fault dips is in the distribution of molten rocks focused in the southern part of the two models, with high concentration of molten rocks along the footwall of fault C (Figure 4.1.7. 3D-a and 3D-b). Partially molten rocks upwell with increasing stretching factor as extension continues. Such rocks can break through fault C and emplace at a shallower depth in the hanging wall.

When faults A and B were set to be symmetrically inclined ($\gamma_A = 120^\circ$, $\gamma_B = 60^\circ$) and the dip of fault C was set to $\gamma_C = 60^\circ / 120^\circ$ for cases 3D-c and 3D-d (Figures 4.1.7. 3D-c and 3D-d) and $30^\circ / 150^\circ$ for cases 3D-e and 3D-f (Figure 4.1.7. 3D-e and 3D-f), partially molten rocks tend to focus along the footwalls of faults A, B and C during extension. The concentration of partially molten lower crustal materials is greater when the dip of fault C was fixed to $\gamma_C = 60^\circ / 120^\circ$ than that when the dip of fault C was fixed to $30^\circ / 150^\circ$.

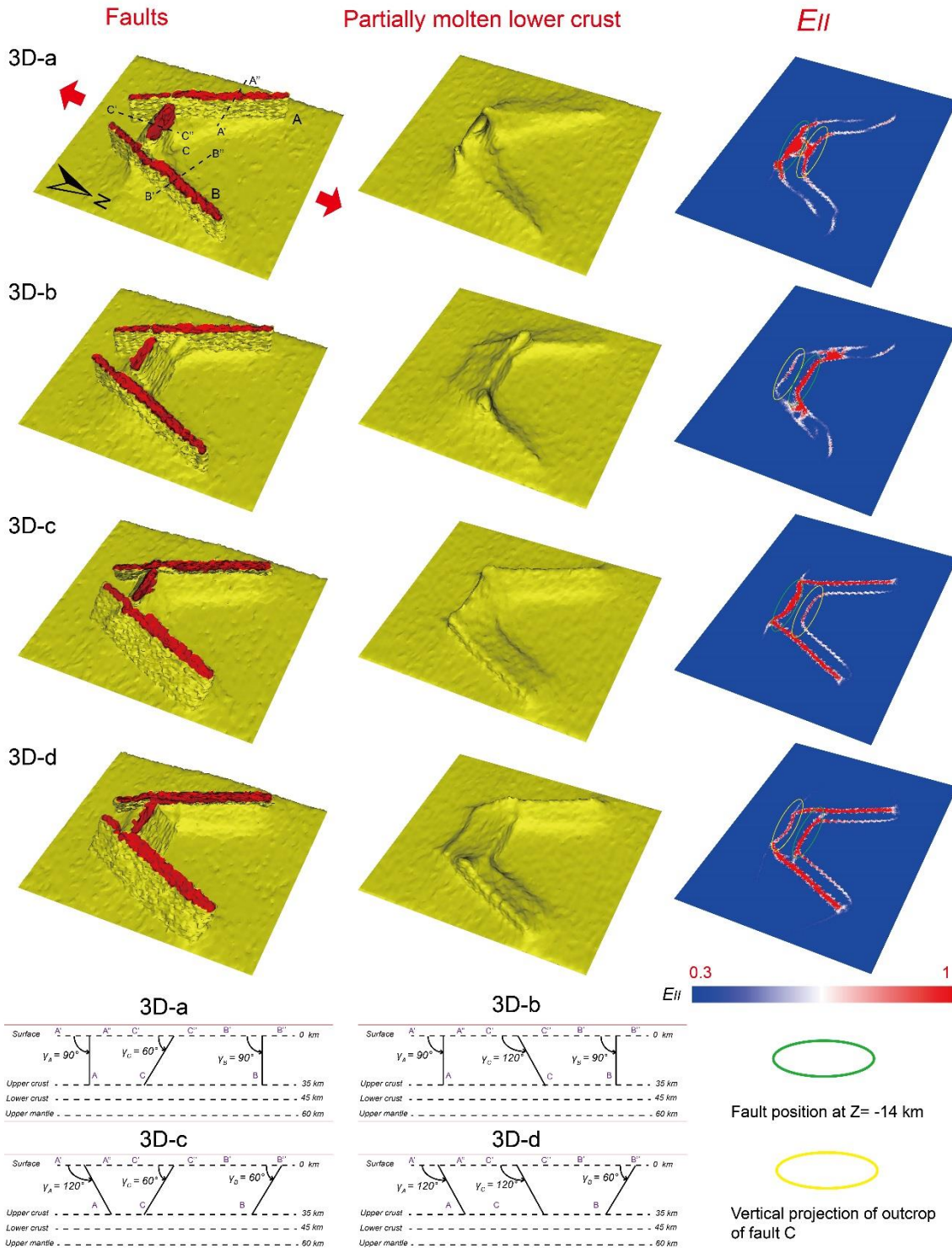
In order to test the role the dips of faults A, B and C played in concentrating partially molten rocks in a fault system during extension, for experiments 3D-e and 3D-f, the dips of fault A and B were fixed to $60^\circ/120^\circ$ which is relatively steeper than the dip of fault C ($\gamma_C = 30^\circ / 150^\circ$, Figure 4.1.7. 3D-e and 3D-f). The results show that the exhumation of lower crust is more significant along the footwalls of faults A and B than that along the footwall of fault C. This indicates that, in a fault system, dip angles of faults and their relative positions jointly control the concentration and distribution of partially molten lower crustal materials during extension.

The cross sections of finite strain at $Z = -14$ km show the accumulations of shearing (Figure 4.1.7) and tensile (Figure 4.1.S2) strains. Tensile areas mainly focus at the fault C (Figure 4.1.S2). In Figure 4.1.7, double bounded finite strain belts are observed in experiments 3D-a ~ 3D-f (Figure 4.17): one belt is evolved from pre-existing faults, the other one is newly formed during exhumation along the boundaries of pre-existing faults.

Experiment 3D-h (faults A and B are symmetrically inclined: $\gamma_A = 60^\circ$, $\gamma_B = 120^\circ$) only shows one high-strain belt whose two tips reach the eastern and western borders of the model. For the asymmetric system (Figure 4.1.7. 3D-g), one tip of high-strain belt reaches the eastern border of the model. This is due to the fact that partially molten rocks in experiments 3D-h and 3D-g concentrate preferentially

4. Role of interacting fault systems on the exhumation of the lower crust

along the external boundaries of faults A and B (along the footwalls of faults A and B), the distance from partially molten crustal materials to the eastern and western borders of the model is decreased so that the boundary effect is probably amplified.



Continued

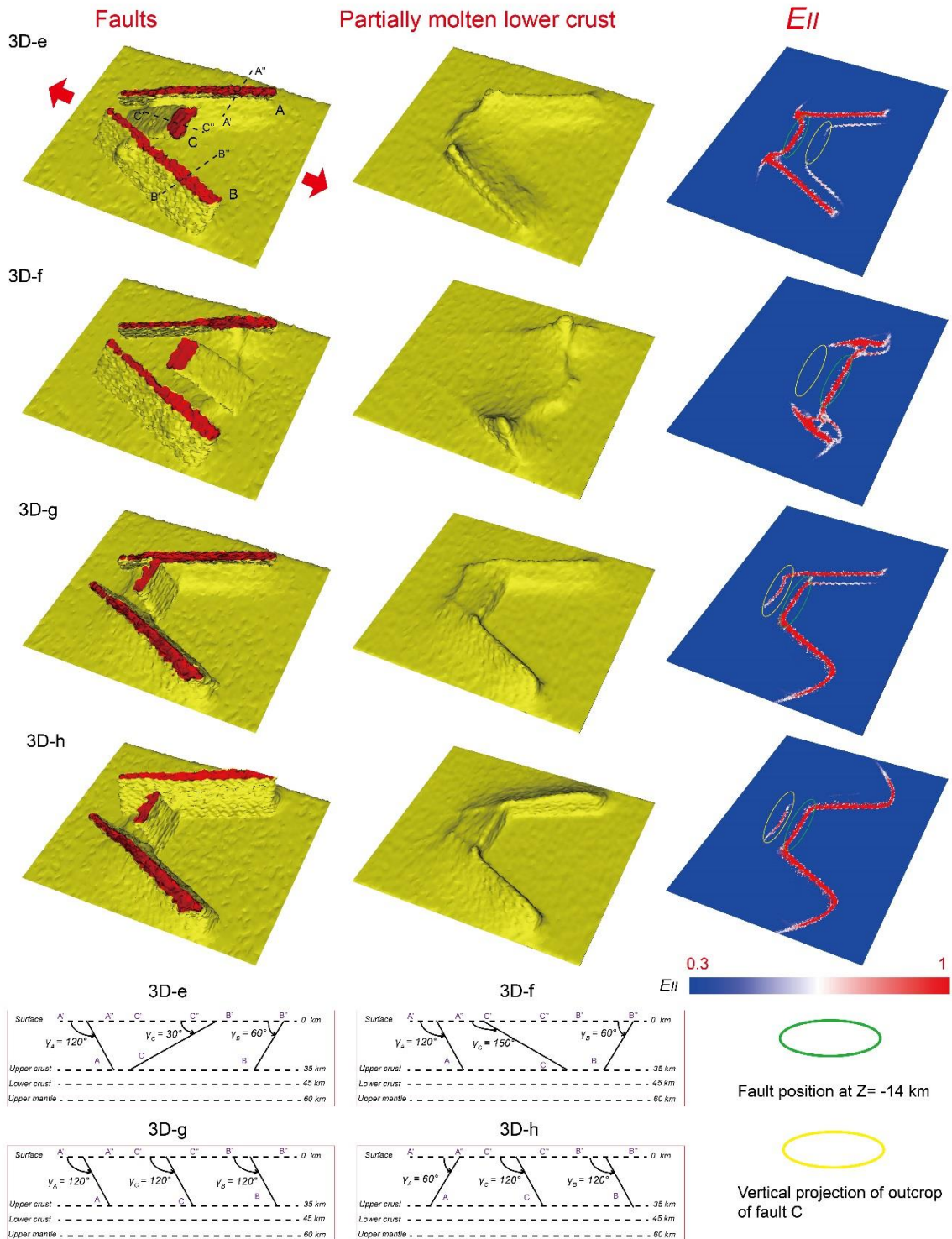


Figure 4.1.7: Influence of the orientation of faults on exhumation of the partially molten lower crust. The faults and the upper surface of the partially molten lower crust are plotted in the first column in yellow as in Figure 4.1.S1, the upper surface (outcrops) of the faults are indicated in red (see details of different models in Figure

4.1.S1). The relief of the upper surface of the partially molten lower crust alone is plotted in the second column. In the third column E_{II} is shown (sections in column three at a depth of $Z = -14$ km), which is the accumulation of the second invariant of the strain rate (ε_{II}) over time (calculated by $E_{II} = \sum_0^t \varepsilon_{II} \cdot \Delta t$).

4.1.5 Discussion

4.1.5.1 Distribution of lower crust

The orientation of pre-existing faults (Figures 4.1.5 and 4.1.7), geothermal gradient and thickness of the lithosphere (Wang et al., 2015) all play an important role in influencing the evolution and distribution of lower crust exhumation during extension. For an over-thickened continental crust, Rey et al. (2009b) numerically modeled a normal fault with a specific dip angle (45°) in the homogeneous upper crust. In their models, the domes always remain at the footwall of the normal fault for different rates of extension (Rey et al., 2009a, 2009b, 2011). In the analogue models of Brun et al. (1994) and Sokoutis et al. (2007), the role of location and orientation of weak heterogeneities in the extension of sandbox models were tested and correlated well with the wide rifting mode of extension found in numerical modelling (Rey et al., 2009a, 2009b, 2011). Wang et al. (2015) explored the conditions of MCCs formation in a non-over-thickened continent crust (35 km thick), and they demonstrated that a high local geothermal gradient in the lithosphere, a weak ductile lower crust and a slow extension rate can also result in the formation of MCCs.

In order to quantify the effect of buoyancy in the upward flow of partially molten lower crustal materials, we plot the paths of two groups of passive particles at different stretching factors (Figure 4.1.8) for the reference model 3D-a (Figure 4.1.S1). This figure shows that exhumation of lower crust occurs at a relatively low rate prior to $SF = 4.2\%$, and the major exhumation takes place later as extension continues. The reason for the lag is probably due to the resistance to deformation and the effect of strain weakening (Wang et al., 2015; Feng et al., 2016b). This also can be explained by the findings of Huisman and Beaumont, (2002): their results show that the lithospheric extension commonly has a two-phase spatial-temporal development over a wide range of extension rates (from 0.3 cm/year to 30 cm/year). Phase one is mainly controlled by frictional behavior and phase two is controlled by ductile rheology.

In the upper and middle planes of lower crust, density and viscosity contrasts resulting from increasing temperature, viscosity and melting fraction (Ganne et al., 2014) and the role of extension rate (Rey et al., 2011) significantly influence the path of particle flow. The shallower passive particles (top panel, Figure 4.1.8) are less sensitive to extension as they are mechanically constrained by the competent upper crust and relatively lower ambient temperature. The deeper passive particles (bottom panel, Figure 4.1.8) tend to move towards the center of the model (up to 20 km, indicated by the blue arrows

in Figure 4.1.8), which is associated with significant exhumation between the nearly-intersecting-zones of the pre-existing faults.

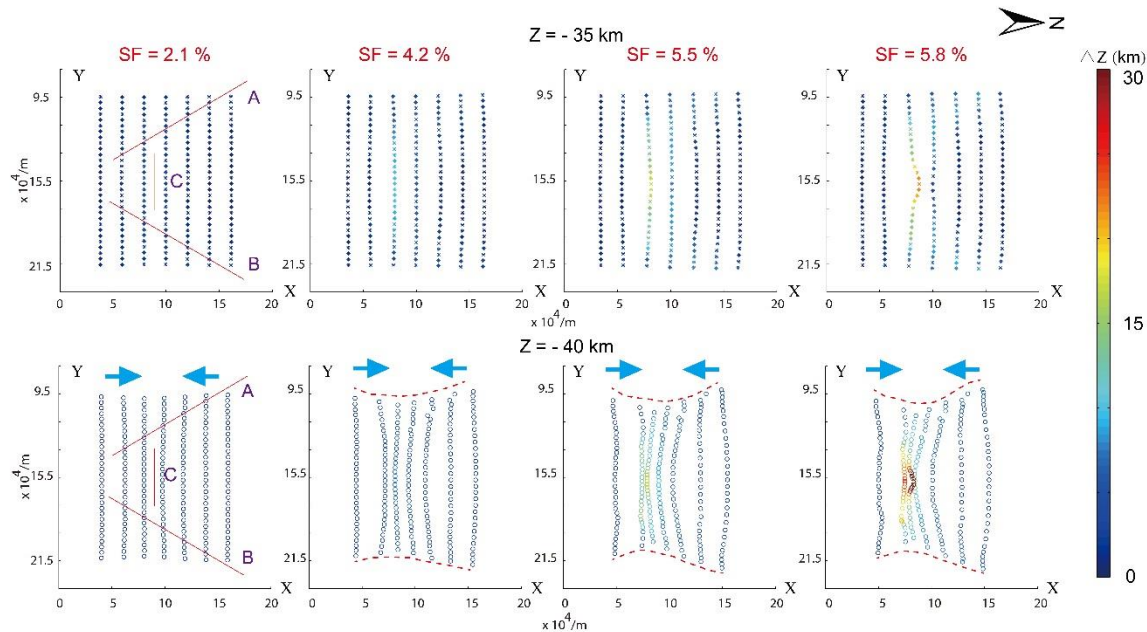


Figure 4.1.8. Experiment 3D-a, the tracks and exhumation of passive particles, which are placed in the lower crust (displayed in figure.4, plane of $Z = -35$ km at top, plane of $Z = -40$ km at bottom). The coordinate system is consistent with the global setting in Figure 4.1.4. SF represents the N-S-directed Stretching Factor (Table 4.1.2). The color bar represents the uplifted height (ΔZ) of passive particles during extension.

4.1.5.2 Distribution of finite strain

High-strain zones are commonly thought to play an important role in the emplacement of partially molten rocks (Neves et al., 2000; Weinberg et al., 2006). In order to further explore the influence of pre-existing faults on the evolution and formation of high-strain zones, we simplified the 3D models by removing fault C (Figure 4.1.9, Figure 4.1.S1). Double finite strain belts are observed in Figure 4.1.9, which is similar to experiments 3D-a ~ 3D-f in Figure 4.1.7. Pre-existing faults generally involve a lateral velocity discontinuity and act as a localization factor for deformation (Le Pouhiet et al., 2004). During extension, pre-existing faults are easily re-activated and tend to concentrate high strain due to their rheological heterogeneity and mechanical anisotropy compared to their surrounding rocks. The processes of concentrating strain into the pre-existing faults lead to the formation one of the two finite strain belts (the zone not bounded by a yellow solid line in Figure 4.1.9).

Along the internal boundaries of the high-strain belt which re-activated pre-existing faults, a new high-strain belt is formed in the models (bounded by yellow solid lines in Figure 4.1.9). During extension, the partially molten lower crustal rocks always favor to concentrate along the footwalls of pre-existing faults (Figures 4.1.7 and 4.1.9). The upward flow of partially molten rocks results in weakening and

reducing the rheology and strength of the overlying rocks due to an increasing ambient temperature gradient (see the power law rheology equation in Table 4.1.3). Therefore, we suggest that the mechanisms of forming such a high-strain belt (bounded by yellow lines in Figure 4.1.9) probably result from a combination of mechanical deformation of pre-existing faults and concentration of upwelling partially molten rocks along the footwalls of pre-existing faults during extension.

Comparing the newly formed belts in experiments 3D-i ($\gamma_A = \gamma_B = 90^\circ$) and 3D-j ($\gamma_A = 60^\circ, \gamma_B = 120^\circ$), the results show that the width of the belts segment located in the intersection of faults is wider in experiment 3D-i (Figure 4.1.9. 3D-i). This indicates that the dips of fault play a significant role in influencing the relative position of forming such high-strain belts. By observing the spatial relationship and distribution of partially molten lower crustal materials and high-strain belts (Figures 4.1.7 and 4.1.9), we can see that the exhumation of partially molten rocks are almost bounded by the two high-strain belts, resulting in the formation of high grade rocks corridors in the models (trapezoid-shape, Figure 4.1.9).

When the fault system does not include fault C (Figure 4.1.8), the concentration of partially molten lower crust at the southern nearly-intersecting region of the pre-existing faults is still observed (indicated by red ellipses). This is due to the increasing concentration of partially molten lower crust along pre-existing faults as the space between faults A and B narrows from north to south.

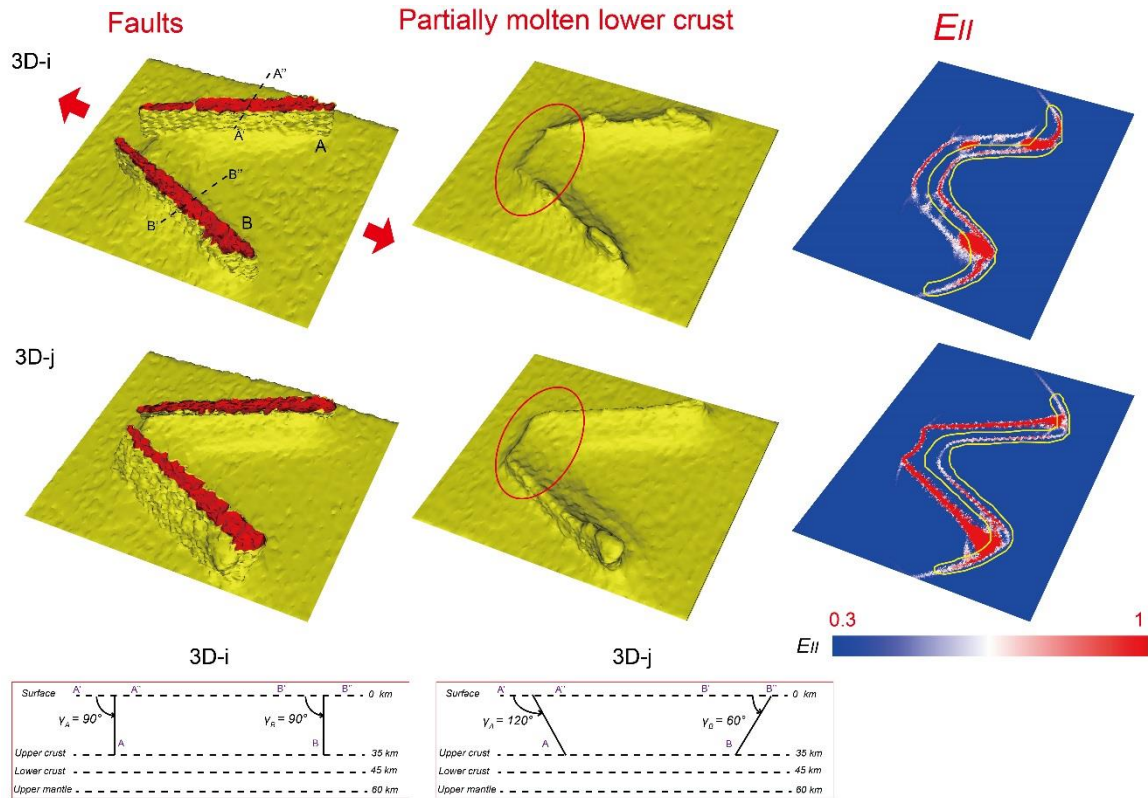


Figure 4.1.9: Model domain consists of two pre-existing faults (faults A and B). Red ellipse is used to locate the highly concentrated zones of partially molten rocks due to the narrowing between faults A and B from north to south. The faults and the upper surface of the lower crust are plotted in the first column in yellow as in Figure 4.1.S1, the upper surface (outcrops) of the faults are indicated in red (see details of different models in Figure 4.1.S1). The relief of the upper surface of the partially molten lower crust alone is plotted in the second column. Yellow lines (third column) are used to indicate the newly produced high-strain belt during N-S-directed extension (at a depth of $Z = -14$ km).

4.1.5.3 Model implications for the BBT

Identifying and exploring the spatial distribution and relationship of structures plays helps to constrain our models of the evolution of deformation and exhumation of lower crust during the Eburnean orogeny. Figure 4.1.10a shows a sketch of the evolutionary history of main structures based on our numerical modelling (Figures 4.1.7 and 4.1.9). During the D2 N-S extension, newly-formed high-strain belt bounded by faults A and B overlap with the inherited fault C (Figure 4.1.10a). The mechanisms for the formation of this new high-strain belt probably result from a combined contribution of short-wavelength mechanical deformation of pre-existing faults and emplacement of upwelling partially molten lower crust rocks along faults (section 4.1.5.2).

The high-strain corridors (black ellipses in Figure 4.1.10a) defined and located by the inherited and newly formed structures would channelize partially molten rocks, this can be supported and evidenced by both of the high concentration of partial molten rocks along pre-existing faults (Figures 4.1.7 and 9)

4. Role of interacting fault systems on the exhumation of the lower crust

and mechanisms of high-strain zones favoring the exhumation of partially molten rocks from low source into upper crust (Neves et al., 1996, 2000; Vigneresse and Tikoff, 1999; Weinberg et al., 2006).

In NW Ghana, high-strain zones (red and blue lines in Figure 4.1.10b) separate high-grade rocks (up to amphibolite to migmatite facies) from adjacent lower grade greenstone belts. In the eastern and western parts of the high grade rock corridors (indicated by black ellipses in Figure 4.1.10b), the high grade rocks exhumed from the lower into middle crustal levels (and possibly to the upper crust) would be facilitated by these km-scale high-strain corridors (indicated by black ellipses in Figure 4.1.10a). In the central part of the Bole-Bulenga domain (indicated by black box in Figure 4.1.10b), the high grade rocks are exhumed under a coupling assistance according to the main structures. Therefore:

- (1) Increasing concentration (Figure 4.1.9) of partially molten rocks with the narrowing space from north to south between the Jirapa and Bole-Nangodi faults (faults A and B in Figure 4.1.10a)
- (2) Inherited orthogonal (E-W) structures (fault C in Figure 4.1.10a) would significantly increase the concentration of lower partially molten rocks in the central part (Figure 4.1.7), otherwise partially molten rocks would have been difficultly exhumed and have hardly formed such high concentration (Figure 4.1.10) in the study area in the center of the Bole-Bulenga domain.

Extensional processes predating D3 events significantly contributed to this exhumation of deep partially molten rocks. The numerical results indicate that the processes of exhumation involve fast movements (kyr) under the assistance of pre-existing shear zones, that is three magnitude orders lower compared to the Myr-scale encompassing the Eburnean events (~2.15 to 2.1 Gyr).

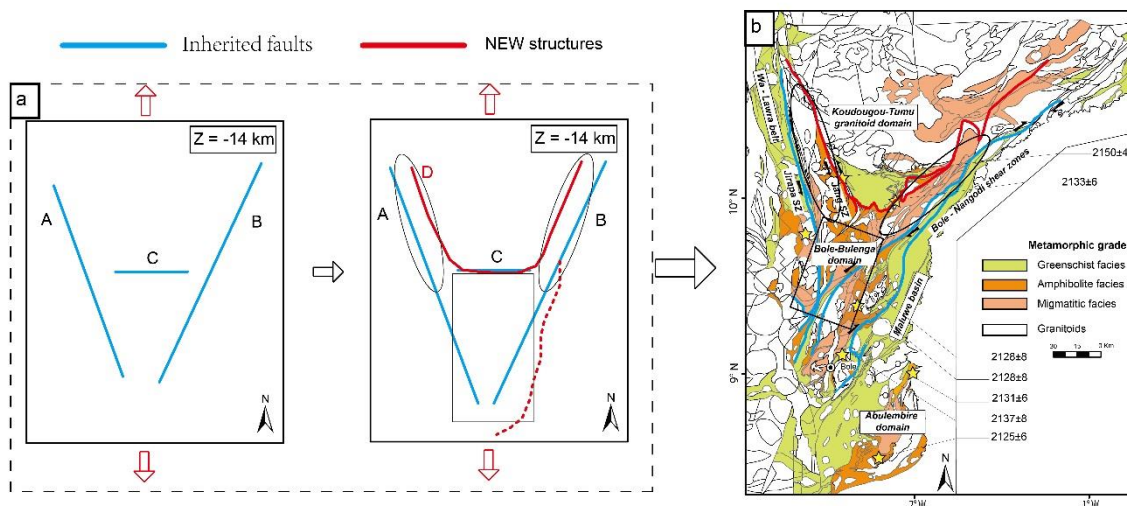


Figure 4.1.10: (a) Sketch showing the evolution of main structures (at $Z = -14$ km, pressure is about 4~5 kbar, corresponding to the pressure at the end of D3 stage in Figure 4.1.2) according to numerical modelling results (Figures 4.1.7 and 4.1.9). Faults A, B and C are thought to be inherited structures. During the N-S-directed

extension, a new high-strain belt (red solid line in figure a) will be produced and bounded by pre-existing faults A and B (as shown in Figure 4.1.9). This new high-strain belt results from the effect of upward flow of partially molten rocks on weakening and reducing the rheology and strength of the overlying rocks due to increasing ambient temperature gradient. Fault C provides initial weak sites for concentrating strain, and as a result, the newly formed high-strain belt would overlap with fault C. (b) Metamorphic map in the study area and radiometric ages of rocks, modified after Block et al. (2015a). We highlight the main structures in blue and red lines, we suggest that the high-strain belt highlighted in red probably results from a re-activation and development of inherited Fault C (as shown in Figure a) during the D2 N-S extension.

4.1.5.4 Limitations and perspectives

Although we have stated that the elastic deformation does not significantly influence the results, since the materials yield at small strains (Ellis et al, 2004; Buitter et al., 2006; Nilfouroushan et al., 2012), it would be useful to include this part of deformation when the elastic module of the numerical code *Underworld* becomes available. In order to better study the influence of orientation of pre-existing faults on regional exhumation of lower crust, processes of fluid transfer in the pre-existing faults were not taken into considerations. In future work, these processes could be coupled by using a two-phase solid-fluid mechanism (Keller et al., 2013). Although we have employed a 50 km wide distance to reduce the boundary effect on the exhumation of lower crust, a bigger box with a higher resolution is still required to further reduce the boundary effect. In addition, since we focus here on discussing the influence of orientation of faults in exhumation of the lower crust, only the upper part of the lithosphere is modelled (60 km), the whole lithospheric scale modelling is not thought to substantially influence the result, but could be included in the future.

In order to optimize the setup of the model, further geophysical and geochemical constraints (Moho depth, geochronological and petrological data, viscosity of partially molten rocks, stretching rate et al.) could be included. In this study, we only model an episodic N-S-directed extensional process (D2 stage) by assuming the thickened thickness of crust at the end of the D1 stage. It will be interesting and significant to model a continuous deformation process by including crustal thickening during the D1 (Feng et al., 2016a) and the subsequent D2 extension.

4.1.6 Conclusions

We have built 2D and 3D thermo-mechanical models to explore the influence of pre-existing faults on the lower crust exhumation under an extensional tectonic regime. The 2D models show that the fastest process of lower crust exhumation (decompression from 12 kbar to about 6 kbar) can be achieved within a time scale of about 1000 kyr when stretched on the order of 2 cm/year. The time required for lower crust exhumation generally increases with decreasing dip angles. The 3D models show that the exhumation of lower crust occurs at a relatively low rate prior to SF = 4.2%, and the major exhumation

takes place later. The partially molten lower crust rocks tend to move towards the center of the model (up to 20 km) and focus exhumation around the near-intersection-zones of pre-existing faults.

The high-strain corridors observed in the numerical models can be used to explain the loci of exhumation of the lower crust in NW Ghana during the D2 N-S extension. In the eastern and western parts of the corridors in NW Ghana, high grade rocks exhumed from the lower to middle crustal level (and possibly to the upper crust) would be dominantly facilitated by these km-scale high-strain corridors. In the central part of the Bole-Bulenga domain, the high grade rocks are exhumed resulting from a coupling between:

(1) The concentration of partially molten rocks between the faults Jirapa and Bole-Nangodi would increase due to the reduction in space from north to south.

(2) Inherited orthogonal (E-W) structures would significantly increase the quantity of partially molten rocks, as otherwise partially molten rocks would have been hard to exhume in the center of the Bole-Bulenga domain.

4.1.7 Acknowledgements

This project was granted access to the high-performance computing (HPC) resources of the regional computing centre, CALMIP in Toulouse, France, under allocation #P1403. We also acknowledge the development teams at the Victorian Partnership for Advanced Computing (VPAC) and Monash University for technical assistance with the software *Underworld*. Figures are plotted using open source package Visit developed by the Lawrence Livermore National Laboratory, they also provided some helpful suggestions on plotting figures. X.F thanks the Chinese Scholarship Council (CSC) for his PhD scholarship. Laetitia Le Pourhiet is warmly thanked for constructive comments on the earlier version of this paper.

4.1.8 Appendix

4. Role of interacting fault systems on the exhumation of the lower crust

Figure 4.1.S1. Initial setup of the 3D numerical models, the orientations of the pre-existing faults correspond to definitions in the Table 4.1.2.

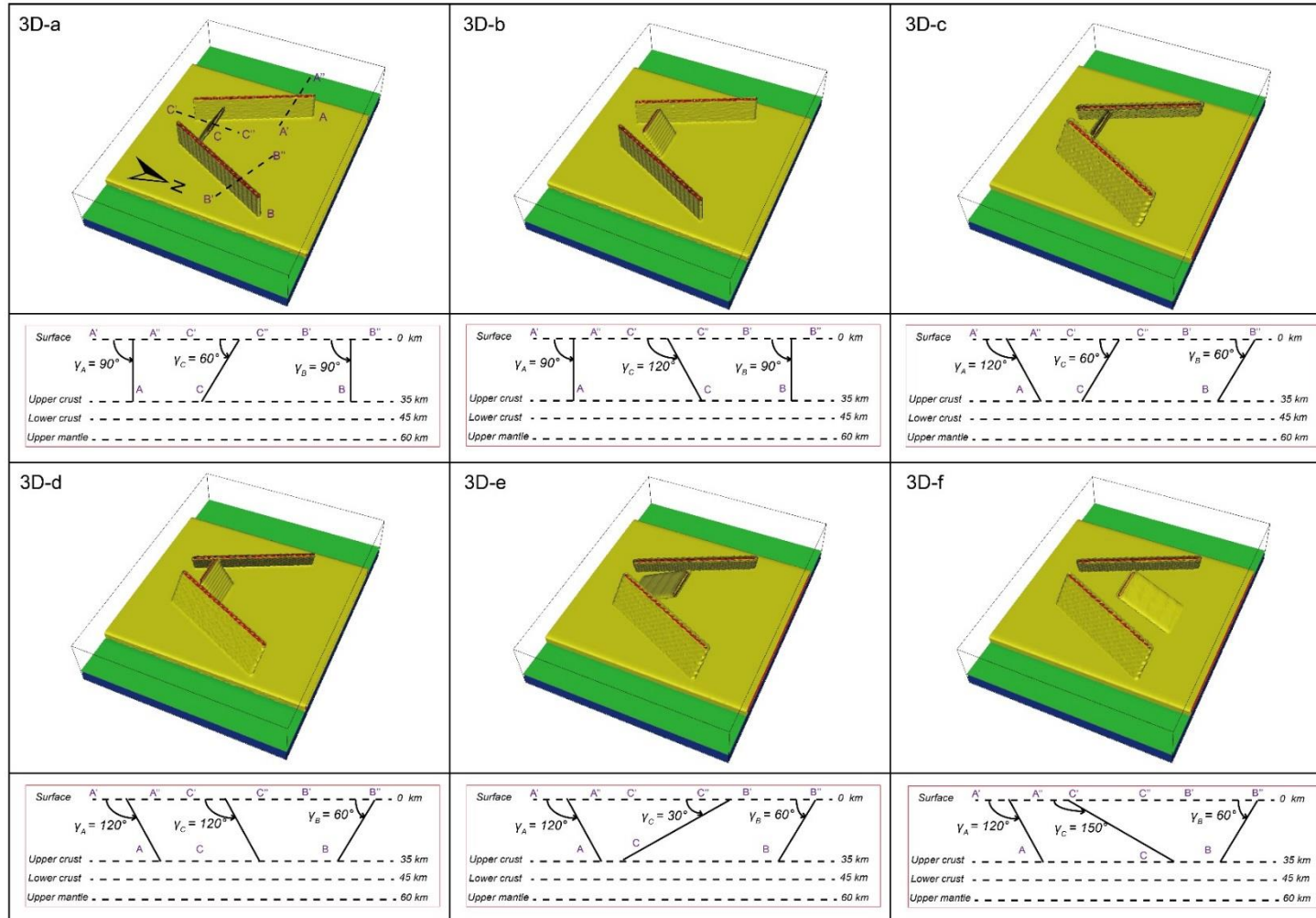
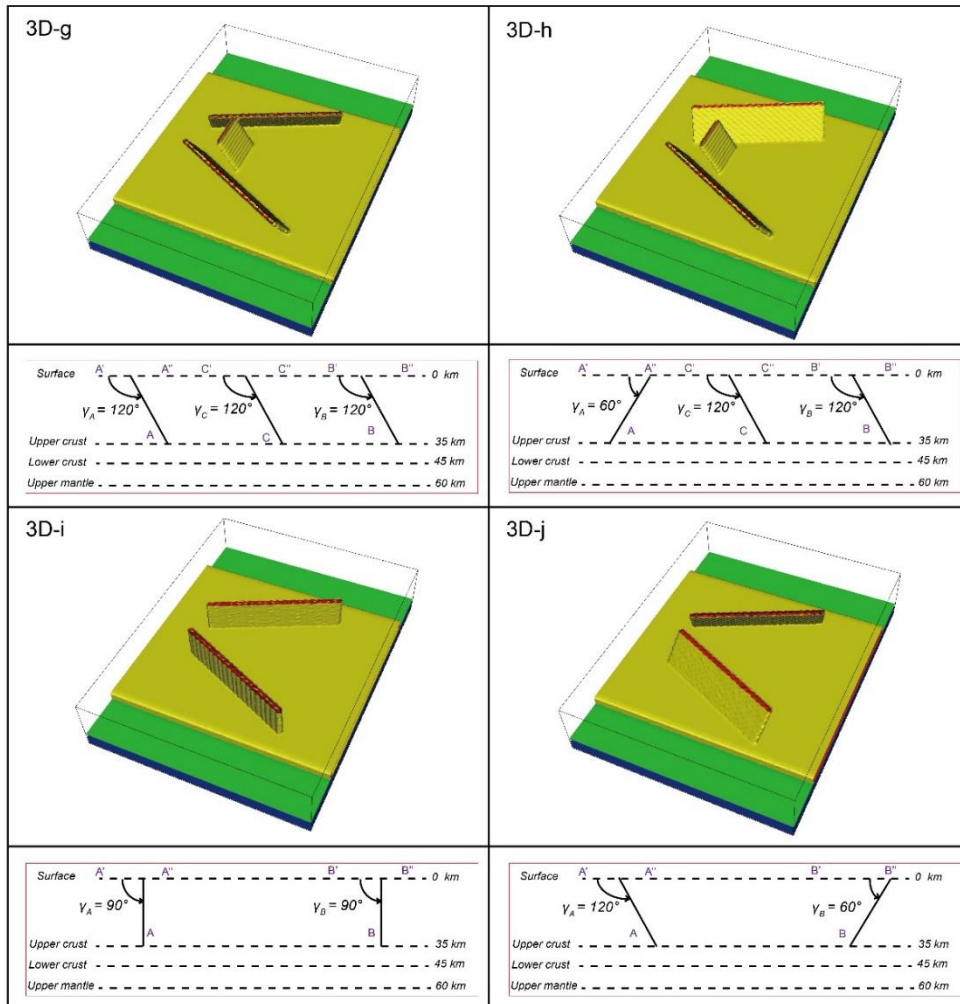


Figure 4.1.S1-Continued

4. Role of interacting fault systems on the exhumation of the lower crust



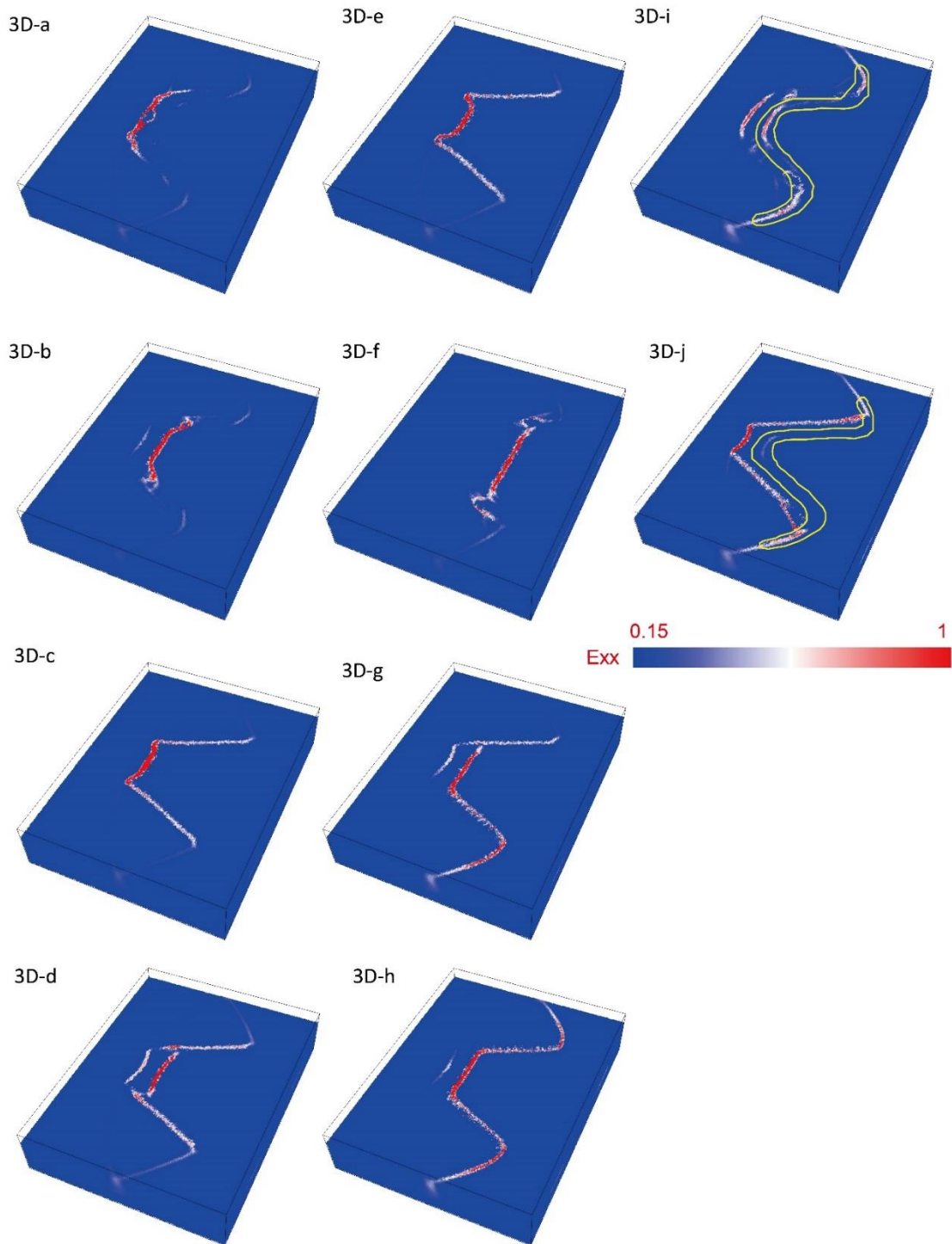


Figure 4.1.S2. Finite strains are calculated (sections are at $Z = -14$ km). Exx is the accumulation of extensional strain rate in N-S (XX) direction (Figure 4.1.4b), corresponding to a process of N-S directed extension.

4.1.9 References

- Agyei Duodu, J., Loh, G.K., Boamah, K.O., 2009. Geological map of Ghana 1:1 000 000. Geological Survey Department of Ghana (GSD).
- Allibone, A., Teasdale, J., Cameron, G., Etheridge, M., Uttley, P., Soboh, A., Lamb, E., 2002. Timing and structural controls on gold mineralization at the Bogoso gold mine, Ghana, West Africa. *Economic Geology*, 97, 949-969.
- Amponsah, P. O., Salvi, S., Béziat, D., Siebenaller, L., Baratoux, L., Jessell, M. W., 2015. Geology and geochemistry of the shear-hosted Julie gold deposit, NW Ghana. *Journal of African Earth Sciences* 112, (B), 505-523.
- Baratoux, L., Metelka, V., Naba, S., Jessell, M. W., Grégoire, M., Ganne, J., 2011. Juvenile Paleoproterozoic crust evolution during the Eburnean orogeny (~2.2-2.0Ga), western Burkina Faso. *Precambrian Research*, 191, 18-45.
- Bellahsen, N., Daniel, J. M., 2005. Fault reactivation control on normal fault growth: an experimental study. *Journal of Structural Geology*, 27, 769-780.
- Bessoles, B., 1977. *Géologie de l'Afrique: le craton ouest africain* (No. 88-89). BRGM.
- Block, S., Ganne, J., Baratoux, L., Zeh, A., Parra-Avila, L. a., Jessell, M., Aillères, L., Siebenaller, L., 2015a. Petrological and geochronological constraints on lower crust exhumation during Paleoproterozoic (Eburnean) orogeny, NW Ghana, West African Craton. *Journal of Metamorphic Geology*, 33 (5), 463-494.
- Block, S., 2015b. *Evolution géodynamique du craton Ouest Africain au nord du Ghana* (Doctoral dissertation, Université de Toulouse, Université Toulouse III-Paul Sabatier).
- Block, S., Jessell, M., Aillères, L., Baratoux, L., Bruguier, O., Zeh, A., Bosch, D., Cabby, R. and Mensah, E., 2016. Lower crust exhumation during Paleoproterozoic (Eburnean) orogeny, NW Ghana, West African Craton: Interplay of coeval contractional deformation and extensional gravitational collapse. *Precambrian Research*, 274, 82-109.
- Boher, M., Abouchami, W., Michard, A., Albarede, F., Arndt, N. T., 1992. Crustal growth in West Africa at 2.1 Ga. *Journal of Geophysical Research: Solid Earth* (1978-2012), 97, 345-369.
- Brun, J. P., Sokoutis, D., Van Den Driessche, J., 1994. Analogue modeling of detachment fault systems and core complexes. *Geology*, 22, 319-322.
- Buiter, Susanne JH, Trond H. Torsvik., 2007. Horizontal movements in the eastern Barents Sea constrained by numerical models and plate reconstructions. *Geophysical Journal International*,

171, 1376-1389.

- Burg, J. P., Bodinier, J. L., Gerya, T., Bedini, R. M., Boudier, F., Dautria, J. M., Balanec, J. L., 2009. Translithospheric mantle diapirism: geological evidence and numerical modelling of the Kondyor zoned ultramafic complex (Russian Far-East). *Journal of Petrology*, 50, 289-321.
- Choi, E., Buck, W. R., Lavier, L. L., Petersen, K. D., 2013. Using core complex geometry to constrain fault strength. *Geophysical Research Letters*, 40, 3863-3867.
- Cramer, F., H. Schmeling, G. J. Golabek, T. Duretz, R. Orendt, S. J. H. Buitter, D. A. May, B. J. P. Kaus, T. V. Gerya, and P. J. Tackley., 2012 A comparison of numerical surface topography calculations in geodynamic modelling: an evaluation of the 'sticky air' method. *Geophysical Journal International*, 189, 38-54.
- Collettini, C., Niemeijer, A., Viti, C., Marone, C., 2009. Fault zone fabric and fault weakness. *Nature*, 462, 907-910.
- D'Agostino, N., Chamot-Rooke, N., Funicello, R., Jolivet, L., Speranza, F., 1998. The role of pre-existing thrust faults and topography on the styles of extension in the Gran Sasso range (central Italy). *Tectonophysics*, 292, 229-254.
- Davis, D. W., Hirdes, W., Schaltegger, U., Nunoo, E. A., 1994. U-Pb age constraints on deposition and provenance of Birimian and gold-bearing Tarkwaian sediments in Ghana, West Africa. *Precambrian Research*, 67, 89-107.
- De Kock, G. S., Armstrong, R. A., Siegfried, H. P., Thomas, E., 2011. Geochronology of the Birim Supergroup of the West African craton in the Wa-Bolé region of west-central Ghana: Implications for the stratigraphic framework. *Journal of African Earth Sciences*, 59, 1-40.
- De Smet, J. H., Van Den Berg, A. P., Vlaar, N. J., 1998. Stability and growth of continental shields in mantle convection models including recurrent melt production. *Tectonophysics*, 296, 15-29.
- Dioh, E., Béziat, D., Debat, P., Grégoire, M., Ngom, P.M., 2006. Diversity of the Palaeoproterozoic granitoids of the Kédougou inlier (eastern Sénégal): Petrographical and geochemical constraints. *Journal of African Earth Science*, 44, 351-371.
- Dooley, T. P., Schreurs, G., 2012. Analogue modelling of intraplate strike-slip tectonics: A review and new experimental results. *Tectonophysics*, 574-575, 1-71.
- Ellis, S., Schreurs, G., Panien, M., 2004. Comparisons between analogue and numerical models of thrust wedge development. *Journal of Structural Geology*, 26, 1659-1675.
- Faulkner, D. R., Jackson, C. A. L., Lunn, R. J., Schlische, R. W., Shipton, Z. K., Wibberley, C. A. J., Withjack,

- M. O., 2010. A review of recent developments concerning the structure, mechanics and fluid flow properties of fault zones. *Journal of Structural Geology*, 32, 1557-1575.
- Feng, X., Amponsah, P. O., Martin, R., Ganne, J., Jessell, M. W., 2016a. 3-D numerical modelling of the influence of pre-existing faults and boundary conditions on the distribution of deformation: example of North-Western Ghana. *Precambrian Research*, 274, 161-179.
- Feng, X., Jessell, M. W., Amponsah, P. O., Martin, R., Ganne, J., Liu, D., Batt, G. 2016b. Effect of strain-weakening on Oligocene-Miocene self-organization of the Australian - Pacific plate boundary fault in southern New Zealand: insight from numerical modelling. *Journal of Geodynamics*. doi:10.1016/j.jog.2016.03.002
- Feybesse, J. L., Billa, M., Guerrot, C., Duguey, E., Lescuyer, J. L., Milesi, J. P., Bouchot, V., 2006. The paleoproterozoic Ghanaian province: geodynamic model and ore controls, including regional stress modeling. *Precambrian Research*, 149, 149-196.
- Gasquet, D., Barbey, P., M Adou, B., Paquette, J., 2003. Structure, Sr-Nd isotope geochemistry and zircon U-Pb geochronology of the granitoids of the Dabakala area (Côte d'Ivoire): evidence for a 2.3 Ga crustal growth event in the Palaeoproterozoic of West Africa? *Precambrian Research*, 127, 329-354.
- Ganne, J., De Andrade, V., Weinberg, R.F., Vidal, O., Dubacq, B., Kagambega, N., Naba, S., Baratoux, L., Jessell, M., Allibon, J., 2012. Modern-style plate subduction preserved in the Palaeoproterozoic West African craton. *Nature Geoscience*, 5, 60-65.
- Ganne, J., Gerbault, M., Block, S., 2014. Thermo-mechanical modeling of lower crust exhumation-Constraints from the metamorphic record of the Palaeoproterozoic Eburnean orogeny, West African Craton. *Precambrian Research*, 243, 88-109.
- Gerya, T. V., Yuen, D. A., 2003. Rayleigh-Taylor instabilities from hydration and melting propel 'cold plumes' at subduction zones. *Earth and Planetary Science Letters*, 212, 47-62.
- Gerya, T. V., Perchuk, L. L., Burg, J. P., 2008. Transient hot channels: Perpetrating and regurgitating ultrahigh-pressure, high-temperature crust-mantle associations in collision belts. *Lithos*, 103, 236-256.
- Gueydan, F., Précigout, J., Montesi, L. G., 2014. Strain weakening enables continental plate tectonics. *Tectonophysics*, 631, 189-196.
- Hand, M., Sandiford, M., 1999. Intraplate deformation in central Australia, the link between subsidence and fault reactivation. *Tectonophysics*, 305, 121-140.

- Hirdes, W., Davis, D.W., Eisenlohr, B.N., 1992. Reassessment of Proterozoic granitoid ages in Ghana on the basis of U/Pb zircon and monazite dating. *Precambrian Research*, 56, 89-96.
- Hirdes, W., Davis, D.W., Lüdtke, G., Konan, G., 1996. Two generations of Birimian (Paleoproterozoic) volcanic belts in northeastern Côte d'Ivoire (West Africa): consequences for the "Birimian controversy." *Precambrian Research*, 80, 173-191.
- Huisman, R. S., Beaumont, C., 2002. Asymmetric lithospheric extension: The role of frictional plastic strain softening inferred from numerical experiments. *Geology*, 30, 211-214.
- Imber, J., Tuckwell, G. W., Childs, C., Walsh, J. J., Manzocchi, T., Heath, A. E., Bonson, C. G., Strand, J., 2004. Three-dimensional distinct element modelling of relay growth and breaching along normal faults. *Journal of Structural Geology*, 26, 1897-1911.
- Jessell, M. W., Lister, G. S., 1991. Strain localization behaviour in experimental shear zones. *Pure and applied geophysics* 137, 421-438.
- Keller, T., May, D. A., Kaus, B. J., 2013. Numerical modelling of magma dynamics coupled to tectonic deformation of lithosphere and crust. *Geophysical Journal International*, 195, 1406-1442.
- Lavier, L. L., Buck, W. R., Poliakov, A. N., 1999. Self-consistent rolling-hinge model for the evolution of large-offset low-angle normal faults. *Geology*, 27, 1127-1130.
- Le Pourhiet, L., Burov, E., Moretti, I., 2004. Rifting through a stack of inhomogeneous thrusts (the dipping pie concept). *Tectonics*, 23(4).
- Le Pourhiet, L., Huet, B., May, D. A., Labrousse, L., Jolivet, L., 2012. Kinematic interpretation of the 3D shapes of metamorphic core complexes. *Geochemistry, Geophysics, Geosystems*, 13 (9).
- Liao, J., Gerya, T., 2014. Influence of lithospheric mantle stratification on craton extension: Insight from two-dimensional thermo-mechanical modeling. *Tectonophysics*, 631, 50-64.
- Lister, G. S., Davis, G. A., 1989. The origin of metamorphic core complexes and detachment faults formed during Tertiary continental extension in the northern Colorado River region, USA. *Journal of Structural Geology*, 11, 65-94.
- Marques, F. O., Nikolaeva, K., Assumpção, M., Gerya, T. V., Bezerra, F. H., do Nascimento, A. F., Ferreira, J. M., 2013. Testing the influence of far-field topographic forcing on subduction initiation at a passive margin. *Tectonophysics*, 608, 517-524.
- Moresi, L., Dufour, F., Mühlhaus, H. B., 2003. A Lagrangian integration point finite element method for large deformation modeling of viscoelastic geomaterials. *Journal of Computational Physics*, 184, 476-497.

- Moresi, L., Quenette, S., Lemiale, V., Meriaux, C., Appelbe, B., Muhlhaus, H., 2007. Computational approaches to studying non-linear dynamics of the crust and mantle. *Physics of the Earth and Planetary Interior*, 163, 69-82.
- Morley, C. K., Haranya, C., Phoosongsee, W., Pongwapee, S., Kornsawan, A., Wonganan, N., 2004. Activation of rift oblique and rift parallel pre-existing fabrics during extension and their effect on deformation style: examples from the rifts of Thailand. *Journal of Structural Geology*, 26(10), 1803-1829.
- Milési, J.P., Feybesse, J.L., Ledru, P., Dommanget, A., Ouedraogo, M.F., Marcoux, E., Prost, A., Vinchon, C., Sylvain, J.P., Johan, V., Tegye, M., Calvez, J.Y., Lagny, P., 1989. Minéralisations aurifères de l'Afrique de l'ouest, leurs relations avec l'évolution litho-structurale au Protérozoïque inférieur. Carte géologique au 1/2.000.000. *Chronique de la recherche minière* 497, 3–98
- Naba, S., Lompo, M., Debat, P., Bouchez, J. L., Béziat, D., 2004. Structure and emplacement model for late-orogenic Paleoproterozoic granitoids: the Tenkodogo-Yamba elongate pluton (Eastern Burkina Faso). *Journal of African Earth Sciences*, 38, 41-57.
- Neves, S. P., Vauchez, A., Archanjo, C. J., 1996. Shear zone-controlled magma emplacement or magma-assisted nucleation of shear zones? Insights from northeast Brazil. *Tectonophysics*, 262, 349-364.
- Neves, S. P., Vauchez, A., Feraud, G., 2000. Tectono-thermal evolution, magma emplacement, and shear zone development in the Caruaru area (Borborema Province, NE Brazil). *Precambrian Research*, 99, 1-32.
- Nilfouroushan, F., Pysklywec, R., Cruden, A., 2012. Sensitivity analysis of numerical scaled models of fold-and-thrust belts to granular material cohesion variation and comparison with analog experiments. *Tectonophysics*, 526, 196-206.
- OzBench, M., Regenauer-Lieb, K., Stegman, D.R., Morra, G., Farrington, R., Hale, A., May, D.A., Freeman, J., Bourgouin, L., Mühlhaus, H. and Moresi, L., 2008. A model comparison study of large-scale mantle–lithosphere dynamics driven by subduction. *Physics of the Earth and Planetary Interiors*, 171, 224-234.
- Ranalli, G., 1995. *Rheology of the Earth*. Springer Science & Business Media. pp. 413.
- Rey, P.F., Teyssier, C., Whitney, D.L., 2009a. Extension rates, crustal melting, and core complex dynamics. *Geology*, 37, 391-394.
- Rey, P.F., Teyssier, C., Whitney, D.L., 2009b. The role of partial melting and extensional strain rates in the development of metamorphic core complexes. *Tectonophysics*, 477, 135-144.

- Rey, P.F., Teyssier, C., Kruckenberg, S.C., Whitney, D.L., 2011. Viscous collision in channel explains double domes in metamorphic core complexes. *Geology*, 39, 387-390.
- Ruh, J. B., Gerya, T., Burg, J. P., 2013. High-resolution 3D numerical modeling of thrust wedges: Influence of décollement strength on transfer zones. *Geochemistry, Geophysics, Geosystems*, 14, 1131-1155.
- Sakyi, P. A., Su, B. X., Anum, S., Kwayisi, D., Dampare, S. B., Anani, C. Y., Nude, P. M., 2014. New zircon U-Pb ages for erratic emplacement of 2213-2130Ma Paleoproterozoic calc-alkaline I-type granitoid rocks in the Lawra Volcanic Belt of Northwestern Ghana, West Africa. *Precambrian Research*, 254, 149-168.
- Sharples, W., Moresi, L. N., Jadamec, M. A., Revote, J., 2015. Styles of rifting and fault spacing in numerical models of crustal extension. *Journal of Geophysical Research: Solid Earth*, 120, 4379-4404.
- Sokoutis, D., Corti, G., Bonini, M., Pierre Brun, J., Cloetingh, S., Mauduit, T., Manetti, P., 2007. Modelling the extension of heterogeneous hot lithosphere. *Tectonophysics* 444, 63-79.
- Sylvester, P. J., Attoh, K., 1992. Lithostratigraphy and composition of 2.1 Ga greenstone belts of the West African Craton and their bearing on crustal evolution and the Archaean-Proterozoic boundary. *The Journal of Geology*, 377-393.
- Thatcher, W., Hill, D. P., 1991. Fault orientations in extensional and conjugate strike-slip environments and their implications. *Geology*, 19, 1116-1120.
- Tirel, C., Brun, J. P., Sokoutis, D., 2006. Extension of thickened and hot lithospheres: Inferences from laboratory modeling. *Tectonics* 25, n/a–n/a. doi: 10.1029/2005TC001804
- Tirel, C., Brun, J. P., Burov, E., 2008. Dynamics and structural development of metamorphic core complexes. *Journal of Geophysical Research: Solid Earth*, 113(B4).
- Peucat, J. J., Capdevila, R., Drareni, A., Mahdjoub, Y., Kahoui, M., 2005. The Eglab massif in the West African Craton (Algeria), an original segment of the Eburnean orogenic belt: petrology, geochemistry and geochronology. *Precambrian Research*, 136, 309-352.
- Pinkerton, H., Stevenson, R. J., 1992. Methods of determining the rheological properties of magmas at sub-liquidus temperatures. *Journal of Volcanology and Geothermal Research*, 53, 47-66.
- Ueda, K., Gerya, T. V., Burg, J. P., 2012. Delamination in collisional orogens: Thermomechanical modeling. *Journal of Geophysical Research: Solid Earth* 117, B08202, doi: 10.1029/2012JB009144

- Vidal, M., Gumiaux, C., Cagnard, F., Pouclet, A., Ouattara, G., Pichon, M., 2009. Evolution of a Paleoproterozoic “weak type” orogeny in the West African Craton (Ivory Coast). *Tectonophysics*, 477, 145-159.
- Vignerresse, J.L., Tikoff, B., 1999. Strain partitioning during partial melting and crystallizing felsic magmas. *Tectonophysics*, 312, 117–132.
- Villeneuve, M., 2005. Paleozoic basins in West Africa and the Mauritanide thrust belt. *Journal of African Earth Sciences*, 43, 166-195.
- Viruete, J. E., 1999. One- and two-dimensional thermal modelling of orogenic crustal extension in the Tormes Gneissic Dome, NW Iberian Massif, Spain. *International Journal of Earth Sciences*, 88, 444-457.
- Wang, K., Burov, E., Gumiaux, C., Chen, Y., Lu, G., Mezri, L., Zhao, L., 2015. Formation of metamorphic core complexes in non-over-thickened continental crust: A case study of Liaodong Peninsula (East Asia). *Lithos*, 238, 86-100.
- Weinberg, R.F., Mark, G., Reichardt, H., 2006. Magma ponding in the Karakoram shear zone, Ladakh, NW India. *Geol. Soc. Am. Bull.* doi:10.1130/B26358.1
- Willingshofer, E., Sokoutis, D., Burg, J. P., 2005. Lithospheric-scale analogue modelling of collision zones with a pre-existing weak zone. *Geological Society, London, Special Publications*, 243, 277-294.

4.2 3D numerical modelling of the re-distribution of partially molten lower crust rocks in relay zones between faults during transtension: Implications for the Sefwi terrane, SW Ghana

Abstract

High-grade tectono-metamorphic domains in the Sefwi terrane of Ghana are separated from adjacent low-grade greenstone belts by two main shear zones. The high grade rocks are thought to have been exhumed along sinistral shear zones during the D2 ENE-WSW transtension. In order to better understand the role boundary conditions and the spatial relationship of faults play in the redistribution of partially molten lower crust, ten 3D thermo-mechanical models have been constructed. The results show that the normal component of velocity boundary conditions mainly controls the exhumation of the lower crust occurred along pre-existing faults, while the exhumation in the relay zones between faults is dominated by the ratio of extension rate to shear rate applied at the boundaries. The strike of the exhumation belt made of partially molten lower crust rocks in the relay zone is sub-orthogonal to the transtension direction. The isostatic compensation from low-density upper mantle to overlying crust (thinning) is higher under transtension than that under extension.

The lower crust exhumation influenced by inherited shear zones can be used to better understand the loci of the high grade rocks in the Sefwi terrane. We suggest that the Kukuom-Juaboso domain composed of up to amphibolite-migmatite facies probably resulted from the concentration of partially molten rocks in the relay zone between the Ketesso and Kenyase shear zones during the D2 ENE-WSW transtension. The two shear zones probably underwent two main stages for growth and maturation from the D1 to D2 deformation phases. The regional exhumation of the high grade rocks in the Sefwi terrane probably occurred within a duration of less than 5 Ma.

Keywords: Thermo-mechanical modelling, Exhumation, Transtension, Partial melting, West African Craton

Highlights

1. We have used 3D thermo-mechanical models to explore the re-distribution of partially molten lower crust in relay zones between two faults.
2. Boundary conditions control the concentration of partially molten lower crust in fault system.
3. We have reconstructed the evolution of deformation in the Sefwi terrane, Ghana.

4.2.1 Introduction

Pre-existing faults commonly act as preferentially re-activated sites when external boundary conditions change (Chester et al., 1991; Beekman et al., 1996), and play a dominant role in concentrating high strain (Morley et al., 2004) through geological time. A regional scale fault commonly results from the process changes of a network of local pre-existing discontinuities (Feng et al., 2016b), through which fracture propagation of their surrounding rocks will be inhibited (Teufel and Clark, 1984; Morley, 1999). With respect to an interacting strike-slip fault system, both soft and hard linkages are commonly involved. During the growth and propagation of faults, a soft linkage can mature to a hard linkage via fracture propagation at the tips of faults and repeated interaction between faults (Gupta and Scholz, 2000; Pachell and Evans, 2002; Kim et al., 2005).

The emplacement of partially molten rocks is dominantly driven by the contrasts in density and viscosity compared to surrounding solid rocks (Brown, 1994; Petford et al., 2000). Pre-existing faults are thought to play an important role in influencing and promoting the processes of the emplacement (Neves et al., 1996; Koyi and Skelton, 2001; Weinberg et al., 2006; Tirel et al., 2008). For extension-dominated regional exhumation of lower crust, Feng et al. (2016c) demonstrated that the orientation of pre-existing faults largely controls the rate and distribution of lower crust exhumation using 2D and 3D thermo-mechanical models. The influence of pre-existing faults on the formation process of metamorphic core complexes (MCCs) during extension was also explored in analogue models (Brun et al., 1994, Koyi and Skelton, 2001): the structural evolution coincides well with numerical results (Tirel et al., 2008; Rey et al., 2009a, 2009b, 2011; Feng et al., 2016c).

The growth of a fault system under transtension boundary conditions has been widely studied (Luyendyk, 1991; Dewey et al., 1998; Fossen and Tikoff, 1998; Lin et al., 1998; Dooley and Schreurs, 2012). Furthermore, the exhumation of high grade rocks simulated by numerical and analogue models has been also largely explored under compressional (Lin et al., 2000; Burov et al., 2001; Seyferth and Henk, 2004; Ganne et al., 2014) and extensional (Brun et al., 1994; Rey et al., 2009a, 2009b, 2011; Le Pourhiet et al., 2012; Feng et al., 2016c) boundary conditions. However, 3D numerical models including the processes of fault growth and lower crust exhumation driven by transtension boundary conditions have still not been completely explored. The Sefwi terrane of SW Ghana is mainly composed of the North-Western Sunyani basin, the South-Eastern Kumasi basin and the central high grade Kukuom-Juaboso domain (KJD). The KJD domain is bounded by two main shear zones: the Kenyase shear zones to the Northwest and the Ketesso shear zones to the Southeast. In order to better understand how the two shear zones influence the regional exhumation of the partially molten lower crustal rocks during the D2 transtensional deformation stage, ten 3D thermo-mechanical models have been constructed. The models are constrained by the metamorphic rock records within the study area and structural

interpretation performed by McFarlane et al. (2016a, 2016b) and Jessell et al. (2012). This study may shed light on the role high strain zones play in re-distribution of partially molten lower crust rocks in general under transtension boundary conditions, as well as on the evolution of structures and deformation in the Sefwi terrane during the Eburnean Orogeny (ca. 2.20 - 2.00 Ga).

4.2.2 Geological setting

The Leo-Man Craton (Figure 4.2.1) is the southernmost segment of the West African Craton (WAC). It is composed of the Eastern Paleoproterozoic Baoulé-Mossi (BM) domain and the South-Western Archaean Kénéma-Man (KM) domain. The two domains are separated by the Sassandra Fault (SF). The KM domain consists of the oldest rock (gneisses) in the WAC, ranging between 3600 and 3500 Ma (Rollinson, 2016). The ages of major rocks range between 3026 and 2850 Ma. This domain was mainly intruded by two episodic magmatic pulses, one between 3260 and 3050 Ma and the other between 2960 and 2850 Ma (Rollinson, 2016). The BM domain consists of extensively distributed N-S trending greenstone-granitoid belts (Figure 4.2.1b). The intruded granitoids in the BM domain locally yield ages between 2195 and 2172 Ma (Hirdes et al., 1992; Baratoux et al., 2011; Sakyi et al., 2014). Several generations of main magmatic pulses took place later, ranging between 2153 and 2068 Ma (Hirdes et al., 1996; Egal et al., 2002; Gasquet et al., 2003; Baratoux et al., 2011; Block et al., 2015).

The Sefwi-Sunyani-Comoé region (Figure 4.2.1b, outlined by red box) is located in South-Western Ghana and the Ivory Coast, consists of several sub-parallel NE-SW trending greenstone belts. The Sunyani and Kumasi basins (Figure 4.2.2) is mainly comprised of volcanoclastics, wackes and argillites (Leube et al., 1990). The two basins was intruded by numerous granitoids with crystallization ages of 2088 ± 1 Ma for the Sunyani basin and 2116 ± 2 Ma for the Kumasi basin, respectively (U/Pb zircon dating, Hirdes et al., 1992). The Sefwi greenstone belt is composed of metamorphosed tholeiitic lavas, volcanoclastic and granitoids (Agyei duodu et al., 2009). The intruded granitoids within the belt yield ages of about 2180-2170 Ma (Hirdes et al., 1992).

The KJD high grade tectono-metamorphic domain of up to amphibolite-migmatite facies is bounded by the Kenyase and Ketesso shear zones (Figure 4.2.2). The NE-trending Kenyase shear zones mark the boundary between the KJD high grade domain and the Sunyani basin. The NE-trending Ketesso shear zones cross through the Sefwi terrane. They separate lower grade domains of greenschist to non-metamorphosed facies in the Kumasi Basin from high grade domains in the Sefwi belt (Feybesse et al., 2006). According to the metamorphic results and structural interpretation performed for the Sefwi terrane by McFarlane et al. (2016a), the D1 tectono-metamorphic event contributing to crustal thickening buried crustal rocks up to 10-12 kbar (corresponding to a buried depth of about 30-40 km) and 700-800 °C. The D2 deformation phase was a decompressional stage that took place at about 2073

4. Role of interacting fault systems on the exhumation of the lower crust

Ma (McFarlane et al., 2016a), through which P-T values decreased to 7-8 kbar (corresponding to a buried depth of about 20-25 km) and 650-700 °C, respectively.

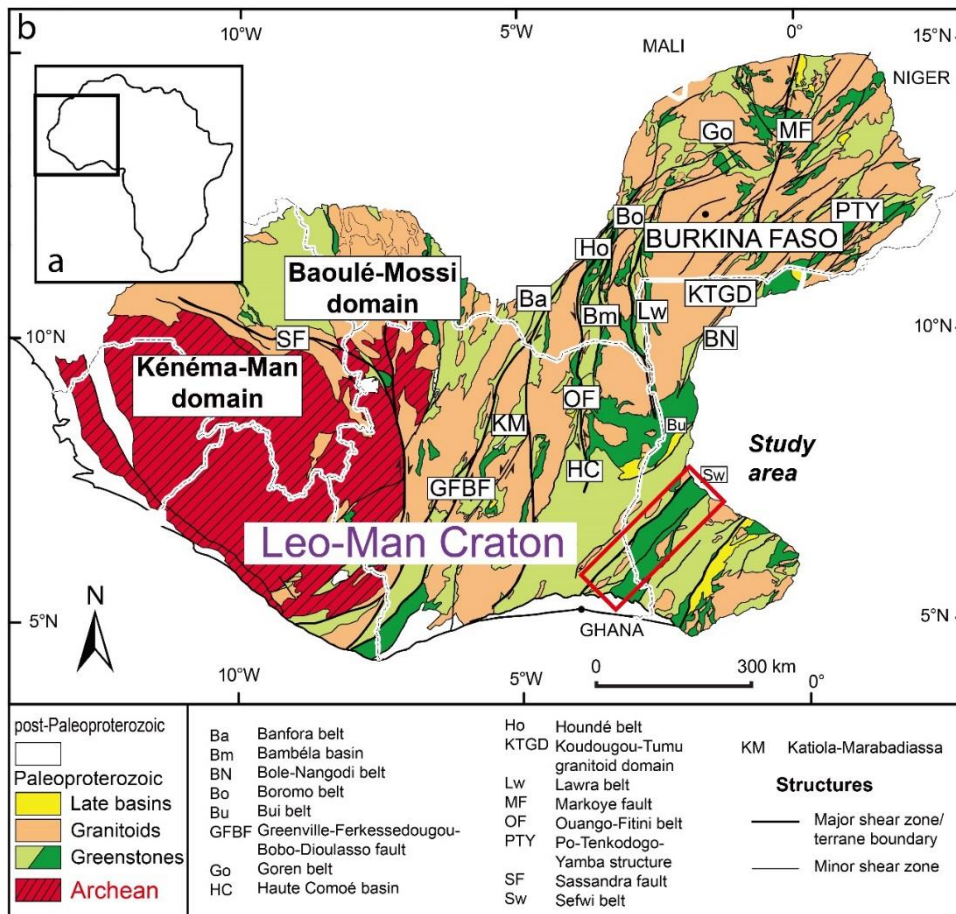


Figure 4.2.1: Geological map of the Leo-Man Craton of the WAC. This map is modified after Milési et al. (2004). It shows major shear zones and Paleoproterozoic-Archaean blocks. The Ghanaian Sefwi domain is indicated by a red box, and a detailed metamorphic and structural map can be found in Figure 4.2.2.

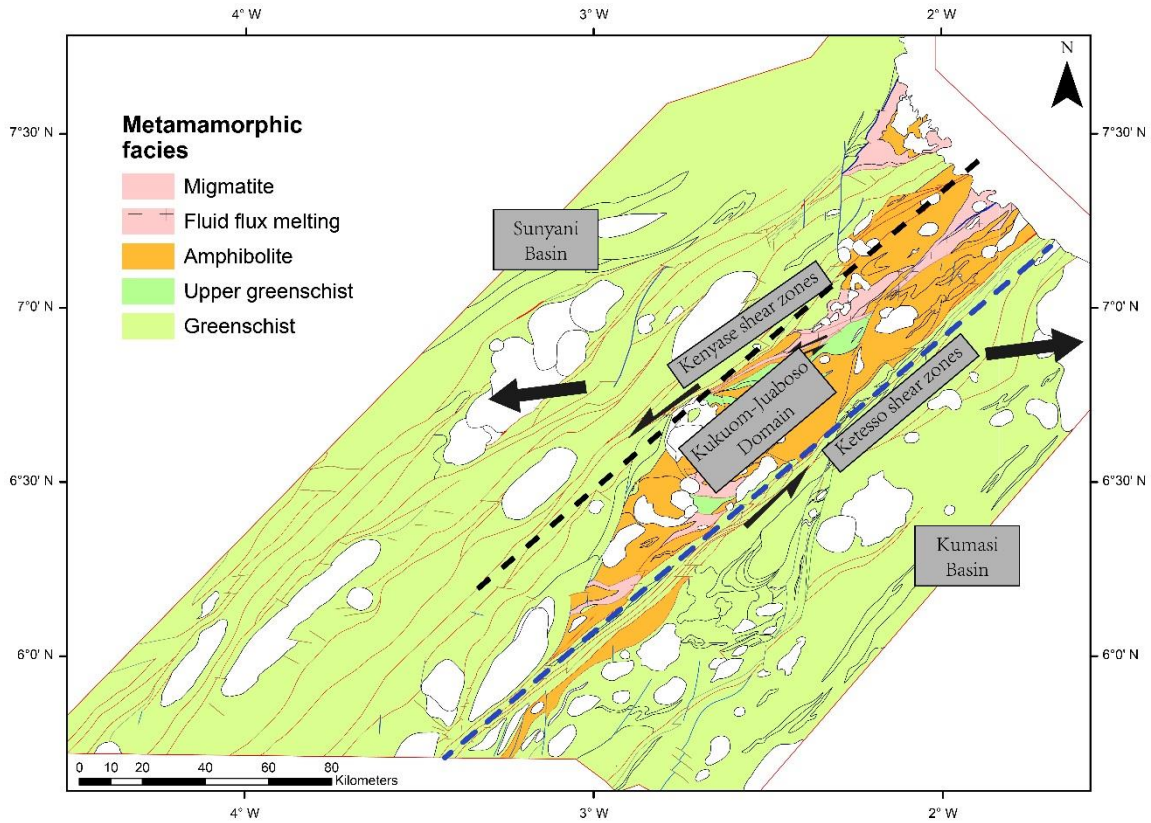


Figure 4.2.2: Metamorphic map of the Sefwi terrane of SW Ghana (modified after McFarlane et al., 2016b). The D2 deformation stage was dominated by the D2 ENE-WSW transtension (indicated by black arrows). The KJD high grade domain is bounded by two shear zones: the Kenyase shear zones and the Ketesso shear zones (indicated by black and blue dotted lines).

4.2.3 Method and model setup

The exhumation of lower crust is simulated in a 3D Cartesian geometry using a visco-plastic rheology with the numerical code *Underworld* (Moresi et al., 2003, 2007). The code uses a Lagrangian *PIC* finite element scheme. The governing mass, momentum and energy conservation equations are solved under the *Underworld* standard modelling framework, which is expressed as follows (Moresi et al., 2003, 2007):

$$\frac{\partial \sigma_{ij}}{\partial x_j} = \rho_{eff} \cdot g_i \quad (4.2.1)$$

$$\nabla \cdot u = 0 \quad (4.2.2)$$

$$\frac{\partial T}{\partial t} + u \cdot (\nabla T) = k \nabla^2 T + \frac{H}{C_p} - \frac{lh}{C_p} \cdot \frac{\partial M}{\partial t} \quad (4.2.3)$$

4. Role of interacting fault systems on the exhumation of the lower crust

where σ_{ij} is the Cauchy stress tensor, g_i is the gravitational acceleration, ρ_{eff} is the effective density, u is the velocity, k is the thermal diffusivity, H is the radiogenic heat production per mass unit, C_p is the heat capacity, lh is the latent heat of fusion and M is the melt fraction.

The 3D model domain is 300 km long (x direction), 140 km wide (y direction) and 60 km thick (z direction), and modelled with a resolution of 2 km x 2 km x 1 km (Figure 4.2.3). The model is comprised of 16 km thick upper volcano-sediment, 16 km thick middle crust (mafic), 10 km thick lower crust and 18 km thick upper mantle (from top to bottom, Figure 4.2.3). In the sedimentary and middle crustal domains, two vertical faults are placed in parallel. In order to explore the role that spatial relationship of pre-existing faults plays in the exhumation of the lower crust, two different patterns of fault system (with or without an overlapping zone between faults, corresponding to Model A and Model B shown in Figure 4.2.3) are tested in this study. According to the ratio of extension rate to shear rate applied on the boundaries, ten 3D thermo-mechanical models are designed for test cases (detailed parameters about the boundary conditions are listed in Tables 4.2.1 and 2).

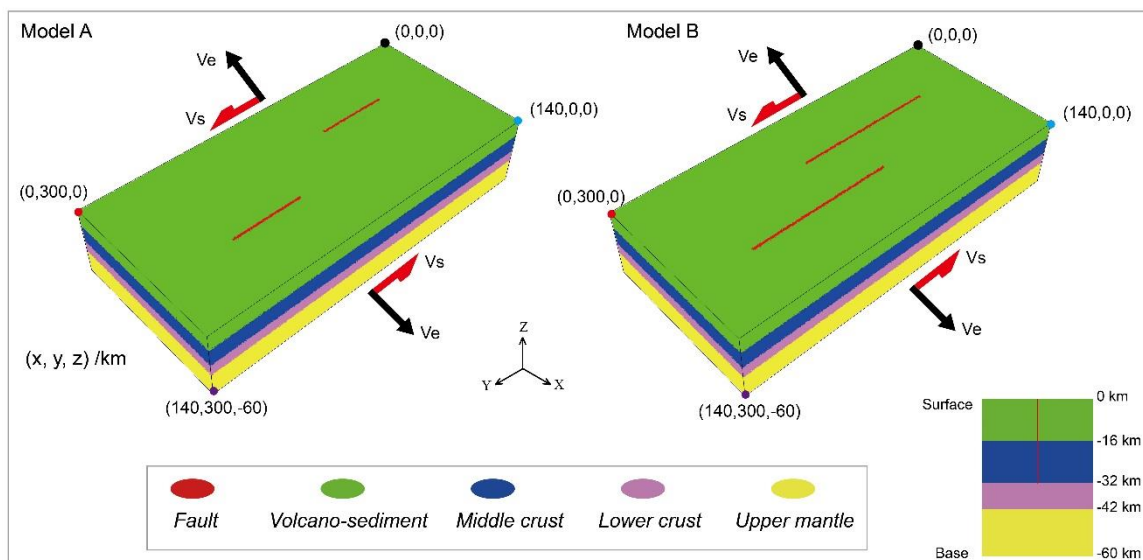


Figure 4.2.3: 3D numerical models are built with the numerical code *Underworld* (Moresi et al., 2003, 2007). The mechanical boundary conditions are indicated by black and red arrows. Two interacting vertical faults with a thickness of 2 km (Le Pourhiet et al., 2004) are initialized in Model A and Model B (red colour). The difference between Model A and Model B is in the spatial relationship between faults (with or without an overlapping zone between two parallel faults). 450 passive particles divided into two groups are placed in the upper surfaces of the lower crust ($z = -32$ km) and the upper mantle ($z = -42$ km), respectively.

Under the PIC finite element frame of the code *Underworld*, 30 particles are initialized in each cell. In order to show the exhumation of the lower crust and the compensation from the upper mantle to the overlying crust (crustal thinning during extension), we therefore employ 450 passive particles to trace the changes of position and vertical velocity during transtension (extension). The particles are divided

4. Role of interacting fault systems on the exhumation of the lower crust

into two groups: one placed in the upper surface of the lower crust ($z = -32$ km) and the other one placed in the upper surface of the upper mantle ($z = -42$ km).

Table 4.2.1: Experiments with different parameters on boundary conditions.

Pattern	Exp#	Extension rate (V_e , cm/year)	Shear rate (V_s , cm/year)	V_e/V_s	Von Mises strain* (ϵ_{eq})	Normalized /year (10^6)
Model A	A1	2	0	∞	0.09	0.10
	A2	2	1	2	0.10	0.13
	A3	2	2	1	0.16	0.19
	A4	1	2	0.5	0.28	0.17
	A5	1	4	0.25	0.51	0.33
Model B	B1	2	0	∞	0.08	0.10
	B2	2	1	2	0.11	0.13
	B3	2	2	1	0.16	0.19
	B4	1	2	0.5	0.29	0.17
	B5	1	4	0.25	0.41	0.33

* The Von Mises equivalent strain is calculated by: $\epsilon_{eq} = \frac{2}{3} \sqrt{\frac{3(e_{xx}^2 + e_{yy}^2 + e_{zz}^2)}{2} + \frac{3(\gamma_{xy}^2 + \gamma_{yz}^2 + \gamma_{zx}^2)}{4}}$.

The mechanical boundaries are constrained by transtension (or extension) with yy -directed periodic boundary conditions (Figure 4.2.3). The bottom of the model is modelled with a free-slip boundary. The surface of the model is a free surface and its boundary thus directly corresponds to the topography (Moresi et al., 2003; Feng et al., 2016a). In order to balance the volume reduction due to applied extension rate, the upper mantle is allowed to flow in with a normal velocity during extension/transtension (Liao and Gerya, 2014; Ganne et al., 2014). With respect to the constraints on thermal boundary conditions, we here model the extension and transtension of a “hot” lithosphere, with a Moho temperature of 840 °C. We use fixed temperatures of 0 °C for the model surface and 1200 °C for the base of the model, assuming a fixed temperature gradient of 20 °C/km. The solid-deformation behaviour is modelled with a depth-dependent yielding criterion (Drucker and Prager, 2013), which is expressed as follows (Moresi et al., 2007; Sharples et al., 2015):

$$\tau_{II} = \delta_c + P \cdot \tan\varphi \quad (4.2.4)$$

where τ_{II} is the second invariant of the deviatoric stress tensor, δ_c is the effective cohesion of rocks, P is the local pressure, $\tan\varphi$ is the effective friction coefficient of rocks. In the crustal domain, an initial cohesion value of 15 MPa and an initial coefficient of internal friction angle of 0.3 are defined. The effective cohesion and coefficient of internal friction angle (drop to a maximum of 20%, Rey et al., 2009b; Faulkner et al., 2010) is modelled by coupling with a strain weakening principle (Gueydan et al.,

4. Role of interacting fault systems on the exhumation of the lower crust

2014; Feng et al., 2016b). The cohesion and coefficient of internal friction angle of pre-existing faults are set to 10% of the initial values of the crust (Rey et al., 2009b).

Table 4.2.2: Thermo-mechanical model parameters, symbol and value-units.

	Parameter	Symbol	Value-units
Thickness	Volcano-Sediment	H_{sed}	16 km
	Middle crust	H_{mid}	16 km
	Lower crust	H_{low}	10 km
	Upper mantle	H_{mantle}	18 km
Density	Volcano-Sediment	ρ_{sed}	2800 kg/m ³
	Middle crust	ρ_{mid}	3050 kg/m ³
	Lower crust	ρ_{low}	2700 kg/m ³
	Upper mantle	ρ_{mantle}	3250 kg/m ³
	Pre-existing faults	ρ_{fault}	2750 kg/m ³
	Melting point of the lower crust	T	$T_{sol} = 636 \text{ }^{\circ}\text{C}$ (1%) $T_{liq} = 1200 \text{ }^{\circ}\text{C}$ (80%)
	Heat capacity	Cp	1000 J/kg·K
	Thermal diffusivity	k	10 ⁻⁶ m ² /s
	Latent heat of fusion	lh	250 KJ·kg ⁻¹ ·K ⁻¹
	Dislocation creep power law pre-exponential factor	A	MPa ⁻ⁿ /s
	Dislocation creep power law exponent	n	-
	Creep power law activation energy	Q	KJ/mol
	Gas constant	R	8.314 J·mol ⁻¹ ·K ⁻¹
	Gravitational acceleration	g	9.81 m/s ²

4. Role of interacting fault systems on the exhumation of the lower crust

Friction angle for Drucker-Prager criterion	φ/f	3-25°
Cohesion for Drucker-Prager criterion	δ_c	3-15 MPa

Table 4.2.3: Rheological parameters employed for modelling different lithospheric layers are collected from Ranalli, (1995). The effective viscosity is calculated with a non-Newtonian power law using the equation: $\eta_0 = 0.25 \cdot (0.75A)^{(-1/n)} \cdot \dot{\epsilon}^{((1/n)-1)} \cdot \exp(Q/nRT)$.

Layer	Rock type	A (MPa ⁻ⁿ / s)	n	Q (KJ/mol)
Volcano-Sediment	Wet quartzite	3.2×10^{-4}	2.3	154
Middle crust	Diabase	2.0×10^{-4}	3.4	260
Lower crust	Quartzodiorite	1.3×10^{-3}	2.4	219
Upper mantle	Dry olivine	7×10^4	3.3	520
Pre-existing fault			Initial viscosity (10^{20} Pa s)	

According to the metamorphic modelling results calculated by Ganne et al. (2014), the mafic crust rocks start to melt (from 1% to 30 %) at a solidus temperature of about 836 °C (corresponding to a buried depth of about 42 km at the given temperature gradient of 20 °C /km). In this study, the middle crust layer is placed between $z = -16$ km and $z = -32$ km (Figure 4.2.3, Table 4.2.3). Under extension (transtension) boundary conditions, the upper crust is hardly to get melted. We therefore only allow the lower crust to undergo partial melting process. We assume that the T_{sol} and T_{liq} temperatures of the lower crust do not change with pressure/depth (Gerya et al., 2008; Ganne, et al., 2014). In order to calculate the volumetric melt fraction (M), the volumetric melting coefficient (X_M) for calculating melt fraction (M) is introduced as follows (Gerya and Yuen, 2003; Gerya and Burg, 2007; Gerya et al., 2008):

$$\begin{aligned}
 X_M &= 0 && \text{at } T \leq T_{sol} \\
 X_M &= \frac{T - T_{sol}}{T_{liq} - T_{sol}} && \text{at } T_{sol} < T < T_{liq} \\
 X_M &= 1 && \text{at } T \geq T_{liq}
 \end{aligned} \tag{4.2.5}$$

where T_{sol} and T_{liq} represent the wet solidus and dry liquidus temperatures of the lower crust, respectively.

We assume that the volumetric melt fraction (M) increases linearly, when the temperature is above the wet solidus temperature and below the dry liquidus temperature (Gerya et al., 2008; Ganne et al., 2014).

$$M = X_M \cdot M_{max} \tag{4.2.6}$$

In natural cases, the effective viscosity of partially molten rocks is usually $10^3 \sim 10^{10}$ times lower than their surrounding solid rocks (Vanderhaeghe, 2001). In our models, when the local temperature reaches the melting point of the lower crust (T_{sol}), we model the effective viscosity by using a function of melt fraction (M) (Pinkerton and Stevenson, 1992):

$$\eta_{eff} = 5 \times 10^{16} \cdot \exp\left(2.5 + (1 - M) \left(\frac{1-M}{M}\right)^{0.48}\right) \quad (4.2.7)$$

The effective density in the model domain is calculated according to the local temperature, the thermal expansion coefficient (α) of $3 \cdot 10^{-5} \text{ K}^{-1}$ and the melt fraction (M). For non-melt-able rocks, a linear relationship used for calculating effective density is expressed as equation (4.2.8). For the lower crust layer, the effective density is calculated by equation (4.2.9), which is similar to the equations employed in Rey et al. (2009b):

$$\rho_{eff} = \rho[1 - \alpha \cdot (T - T_0)] \quad (4.2.8)$$

$$\rho_{eff} = \rho[1 - \alpha \cdot (T - T_0) - \beta \cdot M] \quad (4.2.9)$$

where ρ_{eff} is the effective density, β is the coefficient of thermal expansion, T is the local temperature, T_0 is the reference temperature at surface (0 °C), β is the coefficient of expansion related to phase change (Rey et al., 2009b).

4.2.4 Results

We have constructed ten 3D thermo-mechanical models (including five Model A and five Model B, detailed parameters about the boundary conditions can be found in Table 4.2.1 and Figure 4.2.3) to explore the influence of pre-existing faults on re-distribution of partially molten lower crust during extension and transtension. All simulations were run in parallel on the EOS cluster machine in Toulouse, France (<https://www.calmip.univ-toulouse.fr/>).

4.2.4.1 The upper surface of the partially molten lower crust

Initially, we applied a fixed extension rate of 2 cm/year on the boundaries for experiments A1 and B1 (Figures 4.2.4A1 and 4B1). The results show that the partially molten lower crust rocks concentrate preferentially along pre-existing faults during extension. In the relay zone between faults, the concentration of the partially molten lower crustal materials is much lower than that along the faults. Comparing cases A1 with B1, the focus of exhumation in relay zones between faults in case A1 is higher than that in case B1.

In experiments A2 and B2, a tangential component of velocity boundary conditions was additionally introduced into the fault system. The ratio of extension rate to shear rate applied on the boundaries was set to 2, which means that this fault system is still dominated by the applied normal component of velocity boundary conditions. For case A2 (Figure 4.2.4A2), the partially molten lower crust rocks

move towards the faults and their overlapping zone, leading to the formation of a rising belt (red in Figure 4.2.4A2, reaching about 10 km of uplift) made of partially molten rocks. While case B2 (Figure 4.2.4B2) only shows a high concentration of the partially molten lower crust rocks along the faults. At about 0.88 Ma, the upper surface of the partially molten lower crust in case B2 reaches about 10 km of uplift along the faults and only 5-7 km of uplift in their relay zone.

In experiments A3 and B3, we further increased the shear rate in the fault system, making it equal to extension rate applied on boundaries. Case A3 (Figure 4.2.4A3) shows that a high concentration of the lower crust exhumation is observed both along the faults and in the relay zone between faults. Compared to case A2, the relay zone in case A3 concentrates much more partially molten rocks. Regarding the exhumation along the faults in case B3 (Figure 4.2.4B3), which shows a very similar distribution of the lower crust with cases B1 and B2. While the exhumation occurred around the relay zone in case B3, it is largely increased compared to cases B1 and B2. The difference in the distribution of the lower crust exhumation indicates that increasing the shear rate to the value of extension rate applied can enhance the concentration of the partially molten lower crust in the relay zone between faults during transtension.

Further increasing the shear rate in experiments A4 and B4 (making the ratio of extension rate to shear rate equal to 0.5) results in the tangential component of velocity boundary conditions becomes dominant in the fault system. Case A4 shows that the branch of the red exhumation belt located into the relay zone is wider than its other red branches along the faults (Figure 4.2.4A4). Regarding case B4 (Figure 4.2.4B4), it shows that the distribution of the lower crust exhumation is similar to case B3. Highly concentrated partially molten rocks in the relay zone link the uplifted partially molten rocks along the faults.

In experiments A5 and B5, the ratio of extension rate to shear rate applied on boundaries was decreased to 0.25, and the tangential component of velocity boundary conditions dominates compared to other experiments (A1-A4, B1-B4). The results show that the distribution of the exhumation in cases A5 and B5 is characterized by a relatively high concentration of partially molten lower crust rocks along two parallel high strain zones and a relatively low concentration of the exhumation in the relay zone. The two parallel high strain zones originated from the two pre-existing faults become well developed and matured during transtension (white dotted lines in Figures 4.2.4A5 and 4B5).

Comparing all the experiments, the results show that the normal component of velocity boundary conditions generally controls the exhumation of the partially molten rocks occurred along faults, while the exhumation of the lower crust in the relay zone between faults is pre-dominated by the ratio of

4. Role of interacting fault systems on the exhumation of the lower crust

extension rate to shear rate applied on boundaries. With respect to the exhumation of the lower crust occurred in the relay zone between faults, its concentration generally increases with the decreasing ratio of extension rate to shear rate to an extent (experiments A1-A4 and B1-B4).

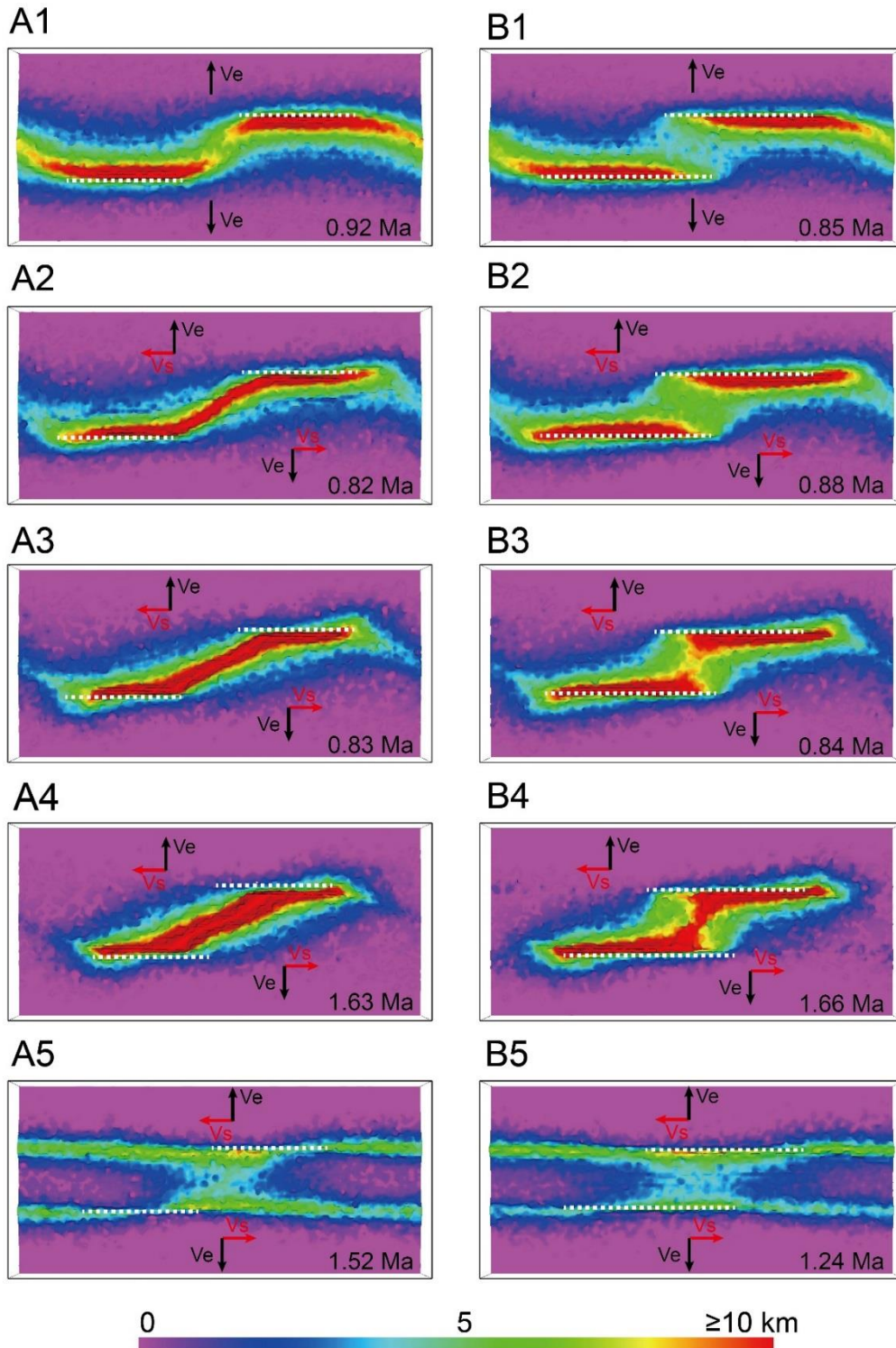


Figure 4.2.4: The relief of the upper surface of the partially molten lower crust in extension (experiments A1 and B1) and transtension (experiments A2-A5 and B2-B5). The first and second columns correspond to the different

standard models: Model A and Model B (Figure 4.2.3), respectively. Pre-existing faults are indicated in white dotted lines. Boundary conditions are indicated by black and red arrows. The colour bar represents the exhumation of the partially molten lower crust during extension and transtension.

4.2.4.2 Surface relief

At a crustal scale, the processes of faulting and lower crust exhumation both play an important role in shaping surface relief (D'Agostino et al., 1998; Feng et al., 2016a). In an extensional setting (Figures 4.2.5A1 and 5B1), the relay zone between faults in case A1 shows a subsidence of about 1-1.5 km, while in case B1 it shows about 2 km of uplift at 0.85 Ma.

In transtension, experiments A2-A4 show a generally similar distribution of relief with each other (Figure 4.2.5A2, 5A3 and 5A4). Subsidence (green colour) mainly focus along faults and in the relay zone between faults, resulting in forming a continuous subsidence belt. The width of the subsidence belt in the relay zone increases with the decreasing ratio of extension rate to shear rate applied (the ratio decreases by the order: A1-A2-A3-A4). Regarding the distribution of uplift, cases A1 and A2 show a highly concentrated uplift along the South-Eastern and North-Western edges of the subsidence region. The uplifted region observed in experiments A3 and A4 also focus along the edges of the subsidence belts, but it distributes in a generally even fashion compared to experiments A1 and A2. For experiments B1-B4, the subsidence region in the relay zone between faults widens with the decreasing ratio of extension rate to shear rate (from experiments B1 to B4), while the distribution of the uplifted region is similar with each other.

Experiments A5 and B5 were designed to have a ratio of 0.25 (extension rate to shear rate). This indicates that the fault system is dominated by the tangential component of velocity boundary conditions. Two subsidence belts are observed along the strike of pre-existing faults, yielding a subsidence of about 1.5-2 km at 1.5 Ma. The uplifted regions are observed mainly between the two subsidence belts, as well as slightly along the external boundaries of the subsidence belts. In experiment A5, the uplifted region between the two subsidence belts shows a step form (Figure 4.2.5A5), while in Experiment B5 it displays a linear distribution (Figure 4.2.5B5). The two experiments yield a similar uplift of about 2 km.

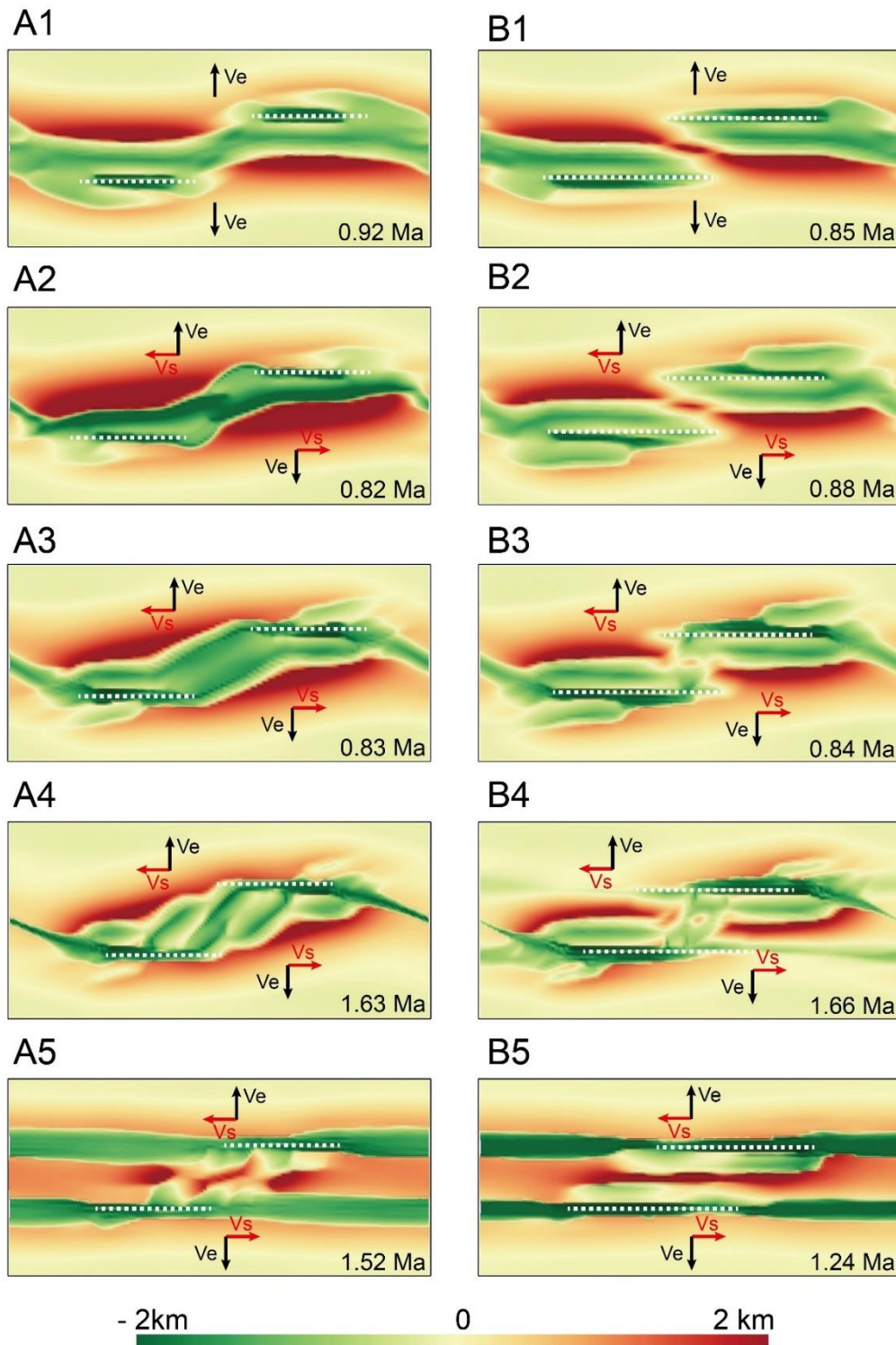


Figure 4.2.5: The surface relief influenced by different ratios of extension rate to shear rate applied and the spatial relationship of faults. The first and second columns correspond to the standard models: Model A and Model B (Figure 4.2.3), respectively. Pre-existing faults are indicated in white dotted lines. Boundary conditions are indicated by black and red arrows.

4.2.4.3 Particles motion: extension versus transtension

Here, in order to compare and quantify the effect of boundary conditions on the lower crust exhumation and the compensation from the upper mantle to the overlying crust (crustal thinning during extension), two groups of passive particles are initialized (Figures 4.2.6 and 7) in the upper surfaces of the lower crust and the upper mantle, respectively.

In extension (experiment B1, Table 4.2.1), no significant exhumation (Figure 4.2.6) is observed prior to 0.25 Ma, and the compensation from the upper mantle to the overlying crust is not remarkable, either. At about 0.85 Ma, a maximum uplift of about 10 km (dark red in Figure 4.2.6) is recorded by the particles placed along faults, while the particles initialized in the relay zone between faults only show about 6 km of uplift (yellow to light orange colour in Figure 4.2.6). With respect to the deeper particles placed in the upper surface of the upper mantle, they yield a maximum uplift of about 6-7 km, showing a similar distribution with the uplifted regions observed in the upper particles.

In transtension (experiment B3), all the particles integrally move and rotate with the applied tangential component of velocity boundary conditions (Figure 4.2.7). The distribution of uplift does not show significant difference compared to experiment B1 (extension) prior to about 0.47 Ma. As transtension continues (at about 0.63 Ma), the upper particles located in the relay zone between faults significantly exhume, yielding a height of about 7 km. At about 0.84 Ma, the upper particles record a maximum uplift of about 10 km. With respect to the particles placed in the upper surface of the upper mantle, they show a relatively even distribution of uplift, yielding a height of about 8-9 km at 0.84 Ma.

4. Role of interacting fault systems on the exhumation of the lower crust

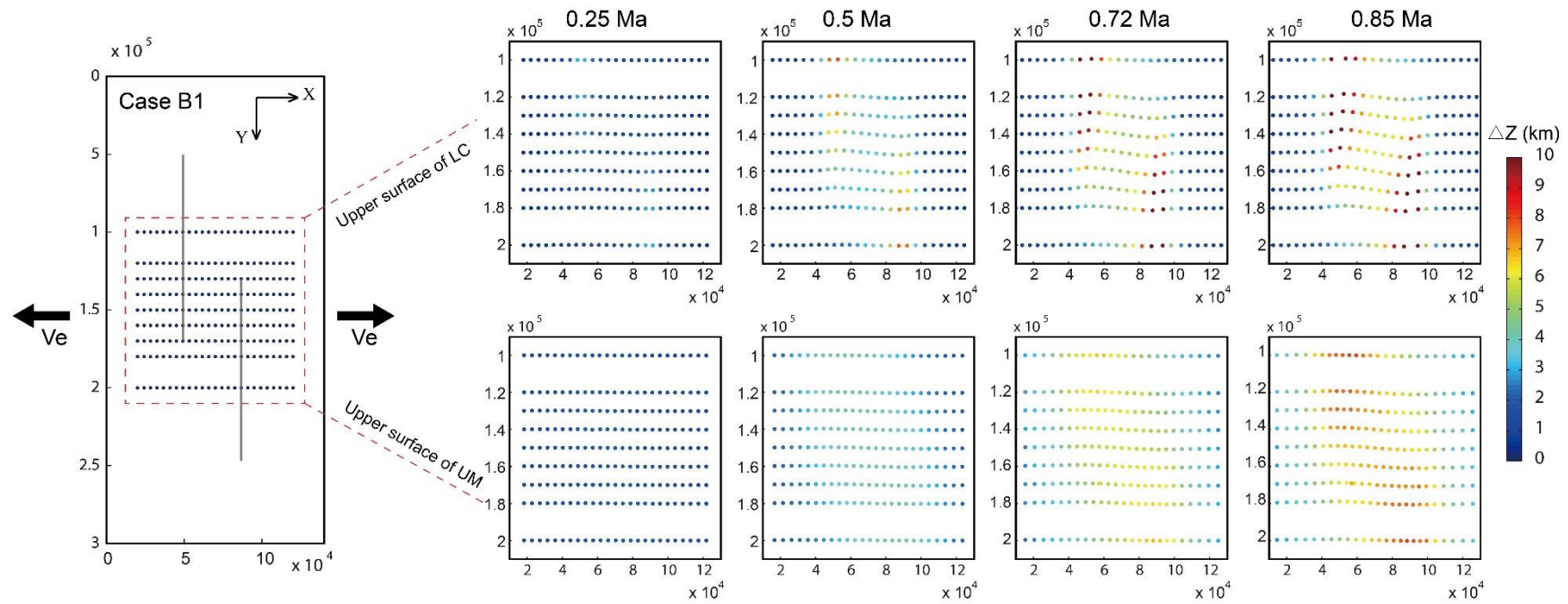


Figure 4.2.6: Model B1: evolution of migration of passive particles during extension. In left panel, the coordinate system is identical to Figure 4.2.3. The upper surfaces of the lower crust (LC, upper panel) and the upper mantle (UM, lower panel) contain 450 passive particles in total. The exhumation of passive particles is shown by the colour bar. Two pre-existing faults are indicated in black lines in left panel. Extension boundary conditions are indicated in black arrows.

4. Role of interacting fault systems on the exhumation of the lower crust

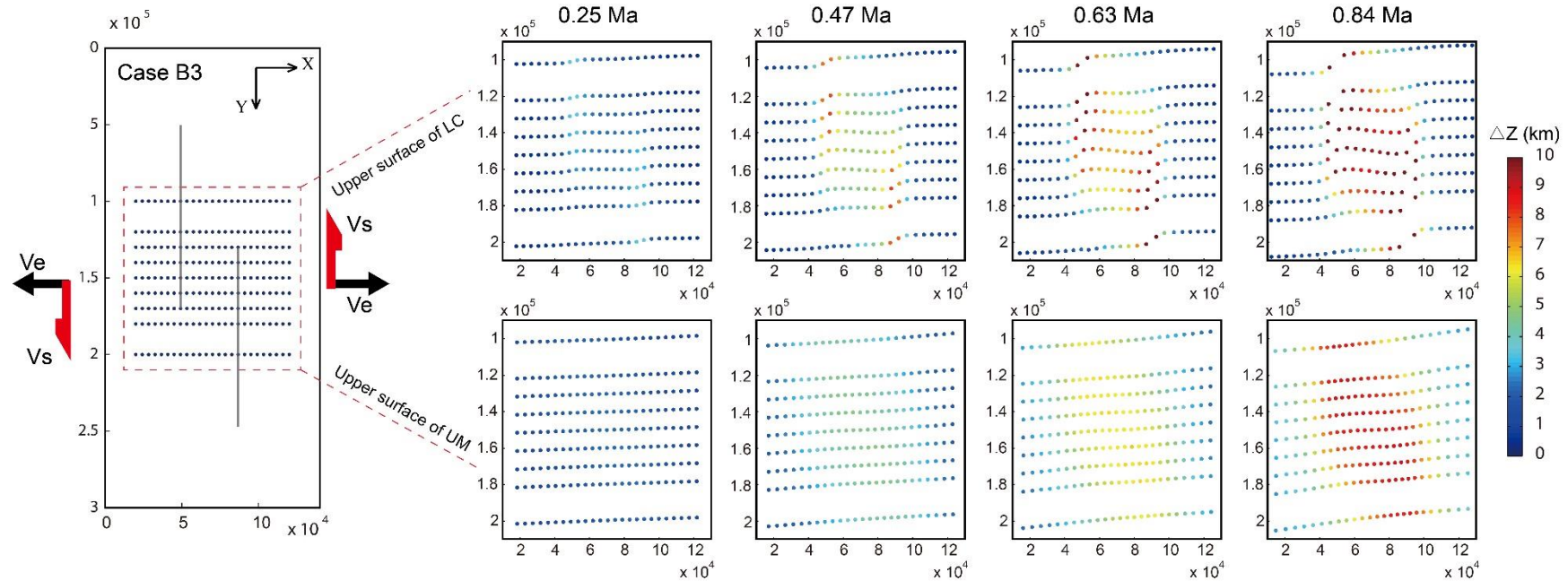


Figure 4.2.7: Model B3, migration of passive particles during transtension. In total of 450 particles divided into two groups are placed in the upper surfaces of the lower crust (LC) and the upper mantle (UM), respectively. The colour of passive particles represents the exhumation of the lower crust and the compensation from the upper mantle to the overlying crust during transtension. Two vertical faults are placed (black lines in left panel). Boundary conditions are shown by red and black arrows. V_s and V_e with red and black arrows represent the rates and directions of shear and extension (see detailed parameters in Table 4.2.1), respectively.

4.2.5 Discussion

4.2.5.1 Migration of particles: extension versus transtension

In a system comprised of pre-existing faults and partially molten lower crustal rocks, the orientation of faults and boundary conditions are both thought to play an important role in influencing the distribution of lower crust exhumation (Rey et al., 2009b; Feng et al., 2016c). Feng et al. (2016c) traced the upper and middle planes of lower crust using passive particles in extension. Their results show that the passive particles in the middle plane integrally move towards the intersection zones of pre-existing faults and largely contribute to regional exhumation.

The uplift observed on the deeper particles can be explained by the isostatical compensation from the lower density mantle to the thinning part of overlying crust during transtension (Abers et al., 2002; Huet et al., 2011). The difference in uplift between the two planes of particles (the upper surfaces of the lower crust and the upper mantle) is about 3-4 km under extension (case B1) and about 1-2 km under transtension (case B3), respectively (Figure 4.2.6 and 7). The reason for forming such gap of uplift between the upper and lower planes of particles is probably due to (1) the partially molten rocks in the middle level of the lower crust significantly move towards the relay zone between faults, and make a significant contribution to regional exhumation (Feng et al., 2016c), (2) the upper mantle rocks are mechanically vigorous compared to the lower crust rocks (partially molten rocks) and they must show more resistance to deformation compared to the overlying partially molten lower crust (Feng et al., 2016c) and display some lag to flow upward to compensate the thinning part of the overlying crust (Abers et al., 2002; Rey et al., 2011; Piccardo, 2016). This also indicates that, for experiment B1 controlled by extension, the partially molten lower crustal rocks in the middle level make a higher contribution to exhumation in the relay zone between faults than that under transtension (experiment B3). In other words, the low-density upper mantle compensate much more the overlying crust in experiment B3 (transtension) compared to experiment B1 (extension). This inference is supported by the curves of the exhumation rate over time in Figures 4.2.8a and 9a (detailed discussions will be presented in following section 4.2.5.2).

According to the distribution of upwelling partially molten rocks observed in experiments B1 and B3, the regional exhumation of the lower crust along the faults does not show significant difference between the cases in extension and transtension. In the relay zone between faults, the tangential component of velocity boundary conditions plays an important role in allowing the concentration of partially molten lower crust rocks. The reason for focusing such high concentration of the partially molten rocks in the relay zone is probably due to the fact that the tangential component of velocity boundary conditions can help produce linking damage/weak zones (Kim et al., 2004) around a strike-

slip fault zone. The linking damage/weak zones evolve and become matured through the interaction between the tips of adjacent faults (Kim et al., 2001), undergoing a process from a soft linkage to a hard linkage. These damage/weak zones (in the relay zone between faults) could make a direct contribution to concentrating partially molten rocks during transtension (extension), this process could be also indirectly assisted and enhanced by the removal of overburden in the relay zone (subsidence regions shown in Figure 4.2.5).

4.2.5.2 Exhumation rate

The exhumation rate of partially molten rocks in metamorphic core complexes (MCCs) can provide some stretching history (Rey et al., 2009b). Here, we discuss the influence of the spatial relationship of faults and ratio of extension rate to shear rate applied on boundaries on exhumation rate of the partially molten lower crust rocks.

Figures 4.2.8a and 9a show the vertical velocity of a selected particle ((x, y z) / (70, 150, -32) /km, see Figure 4.2.3) pertaining to the upper surface of the lower crust, which can be used to indicate the exhumation rate of the partially molten lower crustal materials during transtension (extension). During extension/transtension, rocks can be transferred from the underlying low-density mantle to the overlying crust (crustal thinning) due to isostatic unbalance, this is referred to a compensation process (Banks et al., 1977; Banks and Swain, 1978). Figures 4.2.8b and 9b present the vertical velocity of a passive particle ((x, y z) / (70, 150, -42) /km, see Figure 4.2.3) initialized in the upper surface of the upper mantle, which can be employed to quantify the compensated process occurred in the relay zone between faults.

For Model A and Model B (including ten experiments according to the ratio of extension rate to shear rate applied on boundaries), the compensation rate from the upper mantle to the overlying crust generally shows a similar trend with the exhumation rate of the lower crust (Figures 4.2.8 and 9). At the ratio of 1 (extension rate equals to shear rate), the maximum rate of the lower crust exhumation is observed in the relay zone between faults, as well as the maximum compensation rate from the upper mantle to the overlying crust. When the ratio of extension rate to shear rate was set to 0.25, indicating a predominantly simple shear fault system, the lowest rates of the exhumation and the compensation are recorded in the relay zone.

In terms of the influence of spatial relationship of pre-existing faults on the lower crust exhumation and the compensation from the upper mantle to the overlying crust (Model A with Model B, Figure 4.2.8 and 9), Model A (experiments A1-A4) generally shows a high exhumation rate compared to Model B (experiments B1-B4). This indicates that the relay zone between faults in Model A prefers to concentrate the partially molten lower rocks compared to Model B (Figure 4.2.3). Experiments A5 and

B5 having a ratio of 0.25 (extension rate to shear rate) do not show significant difference in the captured vertical velocity (Figures 4.2.8 and 9). In addition, the curves in Model A show a generally linear increase over time prior to arriving about 10 km of uplift (Figure 4.2.8). For Model B, some early peaks of vertical velocity are observed at about 0.3 Ma (Figure 4.2.9).

The difference in the paths of capturing vertical velocity between Model A and Model B probably suggests a different process of developing high strain zones and exhuming the partially molten lower crust exhumation took place in the relay zone between faults during extension and transtension. Since the pure extensional cases (experiments A1 and B1) do not show significant exhumation in the relay zone between faults (Figures 4.2.4A1 and 4B1), we thereby only focus on discussing the developmental process of the lower crust exhumation under transtension (experiments A2-A5 and B2-B5).

We here suggest a conceptual model (Figure 4.2.10) to explain the possible mechanisms that result in appearing early vertical velocity peaks in Figure 4.2.9. At a fault tip, it commonly has a maximum stress concentration (e.g. Cowie and Scholz, 1992; Vermilye and Scholz, 1999; Gupta and Scholz, 2000). The interaction between the tips of faults leads to the growth, propagation and maturation of faults (Kim et al., 2001).

In Model A (Figure 4.2.10), nodes n and p (tips of faults) must intensely interact with a high stress concentration (e.g., Soliva et al., 2008) resulting in linking each other through fractures (Kim et al., 2001, 2004) when they are initially re-activated. After the re-activation, we can ideally mark the linked fractures as the blue line (Figure 4.2.10) according to the analogue (Peacock and Parfitt, 2002; Bellahsen and Deniel, 2005), numerical modelling (Soliva et al., 2008) and field investigations (Acocella et al., 2000; Hus et al., 2006; Giba et al., 2012). The linked high strain zones are generally sub-orthogonal to the equivalent direction of transtension (red arrows in Figure 4.2.10). In other words, these high strain zones would be fully stretched over time by the equivalent transtensional boundary. This indicates that the partially molten lower crust rocks beneath the relay zone between faults would sub-linearly (as shown in Figure 4.2.8) exhume to the middle-upper crust along the blue line and its surrounding areas (indicated by inclined black lines, Figure 4.2.10). This conclusion can be evidenced by both the spatial distribution (Figure 4.2.4) and the sub-linear exhumation rate (Figure 4.2.8) of the partially molten lower crust.

In terms of Model B, nodes n and p would undergo the same processes (concentrating high stress; e.g. Cowie and Scholz, 1992; Vermilye and Scholz, 1999; Gupta and Scholz, 2000) with Model A when they are initially re-activated. The strike of the linked high strain zones (blue line in Model B, Figure 4.2.10) would be sub-parallel to the equivalent direction of transtension. This indicates that the linked high strain zones are not predominant sites (blue line of Model B) to concentrate strain over time in

4. Role of interacting fault systems on the exhumation of the lower crust

transension. We propose that the linked high strain zones resulted from the initial re-activation (blue line in Model B, Figure 4.2.10) would be reprinted and overlapped during transension (Kim et al., 2001). This probably can help explain the early peaks of vertical velocity observed in Model B (Figure 4.2.9). In addition, this conceptual model also indicates that the newly produced high strain zones (indicated by inclined lines, Figure 4.2.10) would be generally sub-orthogonal to the equivalent direction of transension. Partially molten lower crust rocks would exhume along the strike of the newly produced high strain zones. This feature coincides well with our numerical results (Figure 4.2.4), showing that the strike of the exhumation belt (red) made of the partially molten lower crust in the relay zone between faults is sub-orthogonal to the equivalent direction of transension.

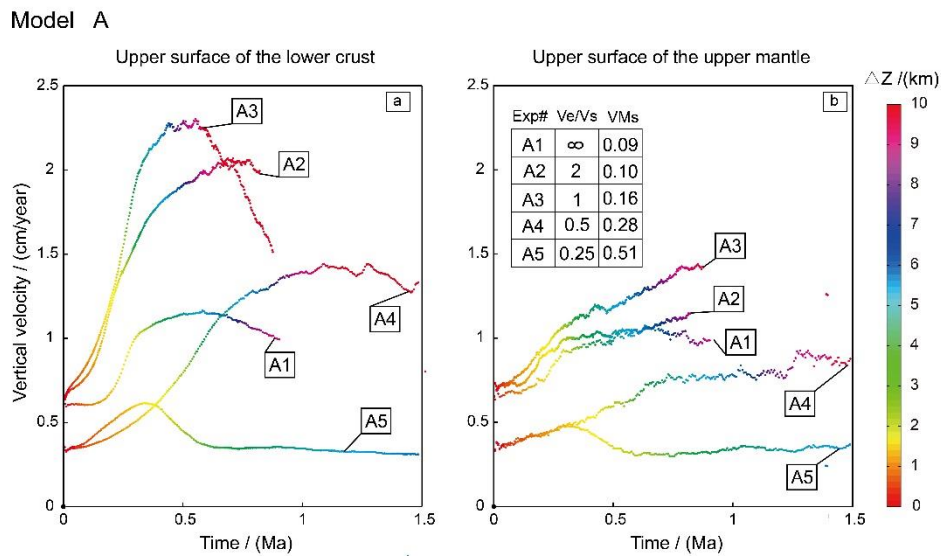


Figure 4.2.8: Model A. (a) Exhumation rate of the lower crust, (b) the isostatic compensation from the upper mantle to the overlying crust. The passive particles employed for plotting the left and right figures are located at (70, 150, -32) and (70, 150, -42) (x, y, z /km), respectively. The colour bar represents the accumulative height of exhumation over time. Exp# is the name of experiment. V_e/V_s is the ratio of extension rate to shear rate applied on the boundaries. VMs represents the Von Mises equivalent strain.

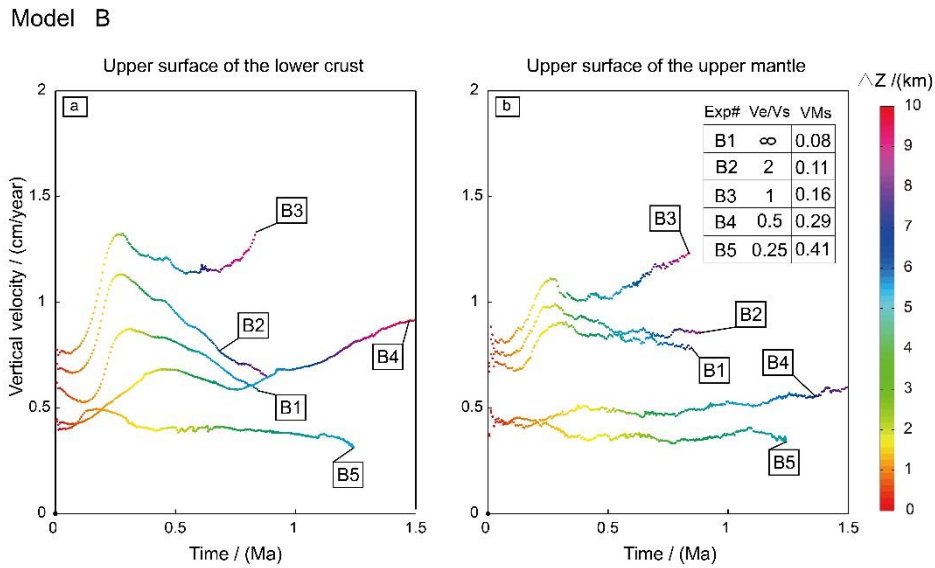


Figure 4.2.9: Model B. (a) Exhumation rate of the lower crust, (b) the isostatic compensation from the upper mantle to overlying crust. The passive particles employed for plotting (a) and (b) are located at (70, 150, -32) and (70, 150, -42) (/km), pertaining to the upper surfaces of the lower crust and the upper mantle, respectively.

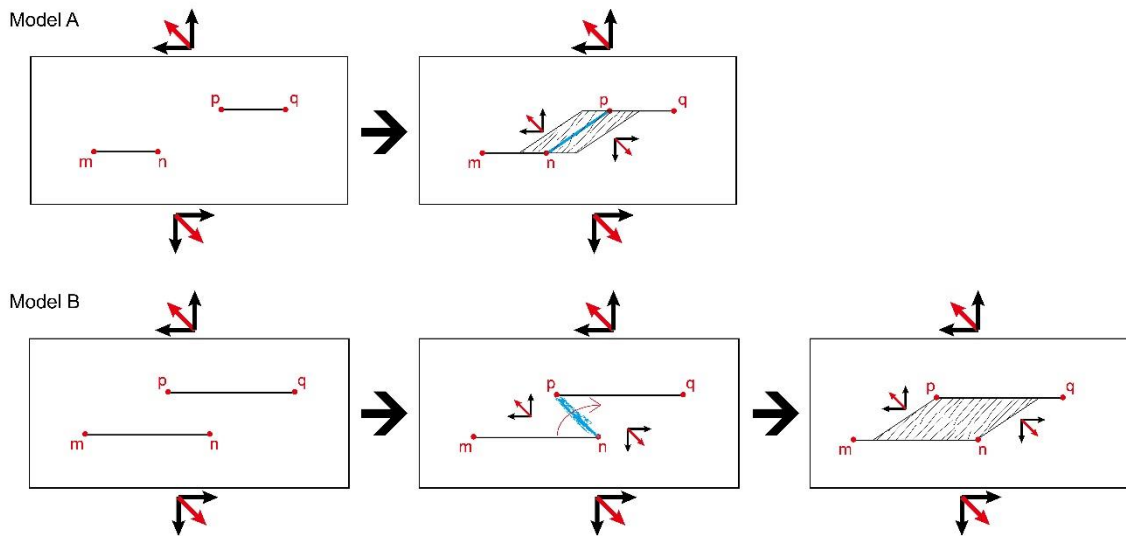


Figure 4.2.10: Conceptual models are constructed to explain the process of faults-related exhumation in the overlapping zone. The first column shows the initial geometry of pre-existing faults according to the numerical model setup (Model A and Model B, from Figure 4.2.3), m, n, p and q are used to mark the tips of faults. Black arrows represent the applied extension and shear rates, red arrows represent the equivalent direction of transtension. The middle and right columns represent the different stages of producing linking high strain zones driven by the external boundary conditions.

4.2.5.3 Model implications for the Ghanaian Sefwi terrane

Craton-scale shear zones in NW (Block et al., 2015; 2016) and SW (McFarlane et al., 2016a) Ghana commonly mark the boundaries between low-grade greenstone belts and high-grade metamorphic

rocks of up to amphibolite-migmatite facies. Identifying the role the shear zones play in the exhumation of the lower crust in Birimian province can allow to better understand the evolution of deformation during the Eburnean Orogeny (ca. 2.20 - 2.00 Ga).

In the Sefwi terrane, the KJD high grade tectono-metamorphic domain is bounded by two main shear zones: the Ketesso and Kenyase shear zones. Based on the fault-induced exhumation of the lower crust shown by the numerical results (Figure 4.2.11a), the western boundary (red dotted line, Figure 4.2.11a) bounding the lower crustal materials is sub-parallel to the exhumation belt (red belt) in the relay zone between faults, and is sub-orthogonal to the equivalent direction of transtension (red arrows in Figure 4.2.11a). This feature coincides well with the metamorphic map in the Sefwi terrane (McFarlane et al., 2016b), the western boundary (purple dotted line in Figure 4.2.11b) of the KJD domain is sub-parallel to the distribution of migmatite (indicated by ellipse) and sub-orthogonal to the ENE-WSW transtension direction.

The concentration of the partially molten lower crust rocks increases along the direction from the relay zone to fault tips (Figure 4.2.11a). This can be used to explain the distribution of the migmatite-amphibolite bounded by an ellipse in the KJD domain, with a high concentration of migmatite around the heads of the ellipse (red and light blue areas, Figure 4.2.11b) and of amphibolite in the central part of the ellipse.

Regarding the evolution of structures, we suggest that the Ketesso and Kenyase shear zones probably underwent two stages for growth and maturation from the D1 to D2 deformation phases. During the D1 compression stage, the preliminary structures of the two shear zones were initialized in parallel. The Ketesso shear zones did not cross through the Sefwi terrane during the D1 stage, and they were located only in the southern part of the Sefwi terrane (dark blue dotted line, Figure 4.2.11b). At the same time, the preliminary forms of the Kenyase shear zones were located only in the northern part of the Sefwi terrane (dark blue dotted line, Figure 4.2.11b). This distribution of the two shear zones probably resulted from a significantly oblique component of the D1 compression stage. These preliminary structures of the Ketesso and Kenyase shear zones provided preferential sites for subsequent re-activation. During the subsequent D2 transtension, the two shear zones developed along their initial strikes (pink dotted lines) and became matured.

With respect to the high grade rocks observed in the North-Eastern part of the Sefwi terrane (indicated by black dotted box, Figure 4.2.11b), if we accept this model, this could be explained by regional exhumation controlled and promoted by the newly matured part (pink dotted part, Figure 4.2.11b) of the Ketesso shear zones during the D2 transtension. Second-order faults between the two main shear

4. Role of interacting fault systems on the exhumation of the lower crust

zones (the Ketesso and Kenyase shear zones) could also have made a significant contribution to the exhumation of the high grade rocks.

Regarding the time length required for the regional exhumation of the partially molten lower crust (about 10 km of uplift equalling to a drop in pressure of 4 kbar during the D2 transtension stage suggested by McFarlane et al., 2016a), according to our numerical experiments, all the modelling results yield a similar time length of less than 2 Ma when using rates of 1-2 cm/year for extension and 0-4 cm/year for shear. Taking into account the variations in velocities (V_s and V_e) applied on boundaries, we suggest that the main regional exhumation of the lower crust in the Sefwi terrane probably occurred within a short duration of less than 5 Ma.

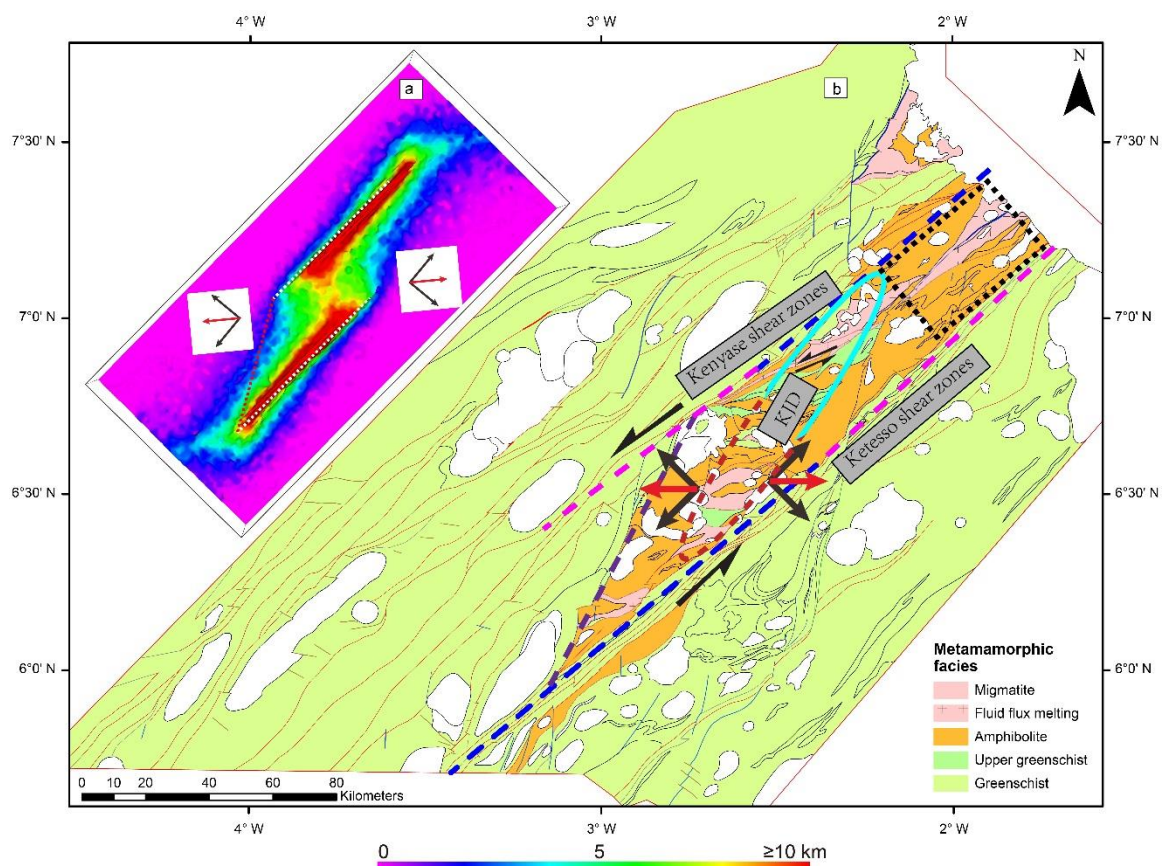


Figure 4.2.11: (a) The numerical results (case B3, Figure 4.2.4-B4) show the uplift of the upper surface of the partially molten lower crust (0-10 km scale colour bar). (b) Metamorphic map in the Sefwi terrane modified after McFarlane et al. (2016b). Transtension boundary conditions are indicated by red arrows.

4.2.5.4 Limitations and perspectives

Although we have tested ten 3D thermo-mechanical models under extension and transtension boundary conditions, the ratio of extension rate to shear rate applied on boundaries should be more extensively tested in further models. In our study, we focused our attentions on exploring the regional

re-distribution of the lower crust exhumation influenced by the spatial relationship of pre-existing faults and boundary conditions, and the process of fluid transfer in fractures/faults was thus deliberately not included, but we aim to couple this process in future studies by employing solid-fluid mechanisms developed by Keller et al. (2013). Regarding the effective viscosity of partially molten rocks, it's still overestimated in this study compared to the experimental results (between 10^6 - 10^{18} Pa s; Vanderhaeghe, 2001). This is due to the high consumption in computing huge viscosity variations (Moresi and Solomatov, 1995).

We aim to improve the setup of the initial model (e.g., more realistic spatial-relationship of pre-existing faults, dating the timing of main structures in the study area) under the assistance of more field works in the future. In addition, we only concerned here the D2 deformation stage occurred in the Sefwi terrane of SW Ghana. We installed the initial model according to the geological data estimated at the end of the D1 deformation stage (P, T and crustal thickness based on the metamorphic estimates performed by Block et al. (2015) and McFarlane et al. (2016a)). In particular, the variation in the distribution of the Moho depth (Jessell et al., 2016) resulting from the D1 compression stage was not taken into considerations for modelling. That could be interesting if we can perform a continuous process for the Sefwi terrane by including the D1 crustal thickening (Feng et al., 2016a) and the D2 transtension triggering the regional exhumation. In addition, we aim to involve more geophysical and geochemical constrains (Ganne et al., 2016) to improve the model setup (e.g., geochronological data; more P-T paths; distribution of Moho depth; thickness of the lithosphere and the mantle potential temperature during the Eburnean Orogeny etc.).

4.2.6 Conclusions

In this study, we constructed ten 3D thermo-mechanical model to test the role pre-existing faults and boundary conditions play in the re-distribution of the exhumation of the lower crust. Different patterns of faults and boundary conditions were tested.

The 3D models show that the normal component of boundary conditions in the fault system controls the exhumation of the lower crust along faults, while the exhumation in the relay zone between faults is dominated by the ratio of extension rate to shear rate applied on boundaries. The strike of the exhumation belt made of partially molten lower crustal materials in the relay zone between faults is sub-orthogonal to the transtension direction. The spatial relationship of faults control the distribution of surface relief in general. The maximum subsidence and uplift yield relief values of about -2 km and 2 km, respectively. The isostatic compensation from the low-density upper mantle to the overlying crust (crustal thinning) is higher under transtension than that under extension.

4. Role of interacting fault systems on the exhumation of the lower crust

The re-distribution of the partially molten lower crust rocks controlled by high strain zones can be used to better understand the loci of the high grade rocks in the Sefwi terrane. The Kukuom-Juaboso domain (KJD) comprised of up to amphibolite-migmatite facies probably resulted from the concentration of the partially molten rocks in the relay zone between the Ketesso and Kenyase shear zones during the D2 ENE-WSW transtension (a drop in pressure of about 4 kbar). These two shear zones could undergo two phases for development and growth from the D1 to D2 deformation stages. The mainly regional exhumation in the Sefwi terrane probably occurred within a duration of less than 5 Ma.

4.2.7 Acknowledgements

Helen McFarlane is greatly thanked for fruitful discussions on this paper and providing us the metamorphic maps of SW Ghana. This study was granted access to the high-performance computing (HPC) resources of the regional computing centre, CALMIP in Toulouse, France, under allocations #P1403 and #P1503. We also thank the development team at the Victorian Partnership for Advanced Computing (VPAC) and Monash University for patient assistance with the numerical code *Underworld* over years. Figures are plotted using open source package Visit developed by the Lawrence Livermore National Laboratory, they are thanked for providing some helpful suggestions on producing figures. X.F thanks the Chinese Scholarship Council (CSC) for his PhD scholarship.

4.2.8 References

- Abers, G. A., Ferris, A., Craig, M., Davies, H., Lerner-Lam, A. L., Mutter, J. C., Taylor, B., 2002. Mantle compensation of active metamorphic core complexes at Woodlark rift in Papua New Guinea. *Nature*, 418, 862-865.
- Acocella, V., Gudmundsson, A., Funiciello, R., 2000. Interaction and linkage of extension fractures and normal faults: examples from the rift zone of Iceland. *Journal of Structural Geology*, 22, 1233-1246.
- Agyei Duodu, J., Loh, G.K., Boamah, K.O., 2009. Geological map of Ghana 1:1 000 000. Geological Survey Department of Ghana (GSD).
- Baratoux, L., Metelka, V., Naba, S., Jessell, M. W., Grégoire, M., Ganne, J., 2011. Juvenile Paleoproterozoic crust evolution during the Eburnean orogeny (~2.2-2.0Ga), western Burkina Faso. *Precambrian Research*, 191, 18-45.
- Banks, R. J., Parker, R. L., Huestis, S. P., 1977. Isostatic compensation on a continental scale: local versus regional mechanisms. *Geophysical Journal International*, 51, 431-452.
- Banks, R.J. Swain, C.J., 1978. The isostatic compensation of East Africa. In *Proceedings of the Royal Society of London: Mathematical, Physical and Engineering Sciences* (Vol. 364, No. 1718, pp. 331-352). The Royal Society.
- Beekman, F., Bull, J. M., Cloetingh, S. A. P. L., Scrutton, R. A., 1996. Crustal fault reactivation facilitating lithospheric folding/buckling in the central Indian Ocean. Geological Society, London, Special Publications, 99, 251-263.
- Bellahsen, N., Daniel, J. M., 2005. Fault reactivation control on normal fault growth: an experimental study. *Journal of Structural Geology*, 27, 769-780.
- Block, S., Ganne, J., Baratoux, L., Zeh, A., Parra-Avila, L. A., Jessell, M., Aillères, L., Siebenaller, L., 2015. Petrological and geochronological constraints on lower crust exhumation during Paleoproterozoic (Eburnean) orogeny, NW Ghana, West African Craton. *Journal of Metamorphic Geology*, 33, 463-494.
- Block, S., Jessell, M., Aillères, L., Baratoux, L., Bruguier, O., Zeh, A., Bosch, D., Caby, R. and Mensah, E., 2016. Lower crust exhumation during Paleoproterozoic (Eburnean) orogeny, NW Ghana, West African Craton: interplay of coeval contractional deformation and extensional gravitational collapse. *Precambrian Research*, 274, 82-109.
- Brun, J. P., Sokoutis, D., Van Den Driessche, J., 1994. Analogue modeling of detachment fault systems and core complexes. *Geology*, 22, 319-322.

- Burov, E., Jolivet, L., Le Pourhiet, L., Poliakov, A., 2001. A thermomechanical model of exhumation of high pressure (HP) and ultra-high pressure (UHP) metamorphic rocks in Alpine-type collision belts. *Tectonophysics*, 342, 113-136.
- Chester, J. S., Logan, J. M., Spang, J. H., 1991. Influence of layering and boundary conditions on fault-bend and fault-propagation folding. *Geological Society of America Bulletin* 103, 1059-1072.
- Cowie, P. A., Scholz, C. H., 1992. Physical explanation for the displacement-length relationship of faults using a post-yield fracture mechanics model. *Journal of Structural Geology*, 14(10), 1133-1148.
- D'Agostino, N., Chamot-Rooke, N., Funicello, R., Jolivet, L., Speranza, F., 1998. The role of pre-existing thrust faults and topography on the styles of extension in the Gran Sasso range (central Italy). *Tectonophysics*, 292, 229-254.
- Dewey, J. F., Holdsworth, R. E., Strachan, R. A., 1998. Transpression and transtension zones. *Geological Society, London, Special Publications* 135, 1-14.
- Drucker, D. C., Prager, W., 2013. Soil mechanics and plastic analysis or limit design. *Quarterly of applied mathematics*, 10.
- Dooley, T. P., Schreurs, G., 2012. Analogue modelling of intraplate strike-slip tectonics: A review and new experimental results. *Tectonophysics*, 574, 1-71.
- Egal, E., Thiéblemont, D., Lahondere, D., Guerrot, C., Costea, C.A., Iliescu, D., Delor, C., Goujou, J.C., Lafon, J.M., Tegye, M. and Diaby, S., 2002. Late Eburnean granitization and tectonics along the western and northwestern margin of the Archaean Kénéma–Man domain (Guinea, West African Craton). *Precambrian Research*, 117, 57-84.
- Faulkner, D. R., Jackson, C. A. L., Lunn, R. J., Schlische, R. W., Shipton, Z. K., Wibberley, C. A. J., Withjack, M. O., 2010. A review of recent developments concerning the structure, mechanics and fluid flow properties of fault zones. *Journal of Structural Geology*, 32, 1557-1575.
- Feng, X., Amponsah, P. O., Martin, R., Ganne, J., Jessell, M. W., 2016a. 3-D numerical modelling of the influence of pre-existing faults and boundary conditions on the distribution of deformation: example of North-Western Ghana. *Precambrian Research*, 274, 161-179.
- Feng, X., Jessell, M. W., Amponsah, P. O., Martin, R., Ganne, J., Liu, D., Batt, E. G., 2016b. Effect of strain-weakening on Oligocene-Miocene self-organization of the Australian-Pacific plate boundary fault in southern New Zealand: Insights from numerical modelling. *Journal of Geodynamics*, doi: 10.1016/j.jog.2016.03.002.

- Feng, X., Ganne, J., Amponsah, P. O. Martin, R., Jessell, M. W., Guo, C., 2016c. Numerical modelling of the influence of pre-existing faults on the temporal-spatial distribution of lower crust exhumation in an extensional tectonic regime: application to North-Western Ghana. (To be submitted)
- Feybesse, J. L., Billa, M., Guerrot, C., Duguey, E., Lescuyer, J. L., Milesi, J. P., Bouchot, V., 2006. The paleoproterozoic Ghanaian province: geodynamic model and ore controls, including regional stress modeling. *Precambrian Research*, 149, 149-196.
- Fossen, H., Tikoff, B., 1998. Extended models of transpression and transtension, and application to tectonic settings. Geological Society, London, Special Publications, 135, 15-33.
- Ganne, J., De Andrade, V., Weinberg, R.F., Vidal, O., Dubacq, B., Kagambega, N., Naba, S., Baratoux, L., Jessell, M., Allibon, J., 2012. Modern-style plate subduction preserved in the Palaeoproterozoic West African craton. *Nature Geoscience*, 5, 60-65.
- Ganne, J., Gerbault, M., Block, S., 2014. Thermo-mechanical modeling of lower crust exhumation— Constraints from the metamorphic record of the Palaeoproterozoic Eburnean orogeny, West African Craton. *Precambrian Research*, 243, 88-109.
- Ganne, J., Feng, X., Rey, P., Andrade, V. D., 2016. Statistical Petrology Reveals a Link Between Supercontinents Cycle and Mantle Global Climate. *American Mineralogist*. Doi.org/10.2138/am-2016-5868.
- Gerya, T. V., Yuen, D. A., 2003. Rayleigh–Taylor instabilities from hydration and melting propel ‘cold plumes’ at subduction zones. *Earth and Planetary Science Letters*, 212, 47-62.
- Gerya, T. V., Burg, J. P., 2007. Intrusion of ultramafic magmatic bodies into the continental crust: numerical simulation. *Physics of the Earth and Planetary Interiors*, 160, 124-142.
- Gerya, T. V., Perchuk, L. L., Burg, J. P., 2008. Transient hot channels: perpetrating and regurgitating ultrahigh-pressure, high-temperature crust–mantle associations in collision belts. *Lithos*, 103, 236-256.
- Giba, M., Walsh, J. J., Nicol, A., 2012. Segmentation and growth of an obliquely reactivated normal fault. *Journal of Structural Geology*, 39, 253-267.
- Gueydan, F., Précigout, J., Montesi, L. G., 2014. Strain weakening enables continental plate tectonics. *Tectonophysics*, 631, 189-196.
- Gupta, A., Scholz, C. H., 2000. A model of normal fault interaction based on observations and theory. *Journal of Structural Geology*, 22, 865-879.

- Rollinson, H., 2016. Archaean Crustal evolution in West Africa: A new synthesis of the Archaean geology in Sierra Leone, Liberia, Guinea and Ivory Coast, *Precambrian Research*, doi: <http://dx.doi.org/10.1016/j.precamres.2016.05.005>
- Hirdes, W., Davis, D.W., Eisenlohr, B.N., 1992. Reassessment of Proterozoic granitoid ages in Ghana on the basis of U/Pb zircon and monazite dating. *Precambrian Research*, 56, 89–96.
- Hirdes, W., Davis, D.W., Lüdtke, G., Konan, G., 1996. Two generations of Birimian (Paleoproterozoic) volcanic belts in northeastern Côte d'Ivoire (West Africa): consequences for the "Birimian controversy." *Precambrian Research*, 80, 173-191.
- Huet, B., Le Pourhiet, L., Labrousse, L., Burov, E., Jolivet, L., 2011. Post-orogenic extension and metamorphic core complexes in a heterogeneous crust: the role of crustal layering inherited from collision. Application to the Cyclades (Aegean domain). *Geophysical Journal International*, 184, 611-625.
- Hus, R., De Batist, M., Klerkx, J., Matton, C., 2006. Fault linkage in continental rifts: structure and evolution of a large relay ramp in Zavarotny; Lake Baikal (Russia). *Journal of structural geology*, 28, 1338-1351.
- Jessell, M. W., Siebert, E., Bons, P. D., Evans, L., Piazzolo, S., 2005. A new type of numerical experiment on the spatial and temporal patterns of localization of deformation in a material with a coupling of grain size and rheology. *Earth and Planetary Science Letters*, 239, 309-326.
- Jessell, M. W., Bons, P. D., Griera, A., Evans, L. A., Wilson, C. J., 2009. A tale of two viscosities. *Journal of Structural Geology*, 31, 719-736.
- Jessell, M. W., Amponsah, P. O., Baratoux, L., Asiedu, D. K., Loh, G. K., Ganne, J., 2012. Crustal-scale transcurrent shearing in the Paleoproterozoic Sefwi-Sunyani-Comoé region, West Africa. *Precambrian Research*, 212-213, 155-168.
- Jessell, M. W., Begg, G. C., Miller, M. S., 2016. The geophysical signatures of the West African Craton. *Precambrian Research*, 274, 3-24.
- Keller, T., May, D. A., Kaus, B. J., 2013. Numerical modelling of magma dynamics coupled to tectonic deformation of lithosphere and crust. *Geophysical Journal International*, 195, 1406-1442.
- Kim, Y. S., Andrews, J. R., Sanderson, D. J., 2001. Reactivated strike-slip faults: examples from north Cornwall, UK. *Tectonophysics*, 340, 173-194.
- Kim, Y. S., Peacock, D. C., Sanderson, D. J., 2004. Fault damage zones. *Journal of structural geology*, 26, 503-517.

- Kim, Y. S., Sanderson, D. J., 2005. The relationship between displacement and length of faults: a review. *Earth-Science Reviews*, 68, 317-334.
- Koyi, H. A., Skelton, A., 2001. Centrifuge modelling of the evolution of low-angle detachment faults from high-angle normal faults. *Journal of structural Geology*, 23, 1179-1185.
- Le Pourhiet, L., Burov, E., Moretti, I., 2004. Rifting through a stack of inhomogeneous thrusts (the dipping pie concept). *Tectonics*, 23(4).
- Le Pourhiet, L., Huet, B., May, D. A., Labrousse, L., Jolivet, L., 2012. Kinematic interpretation of the 3D shapes of metamorphic core complexes. *Geochemistry, Geophysics, Geosystems*, 13(9).
- Liao, J., Gerya, T., 2014. Influence of lithospheric mantle stratification on craton extension: Insight from two-dimensional thermo-mechanical modeling. *Tectonophysics*, 631, 50-64.
- Lin, C. H., 2000. Thermal modeling of continental subduction and exhumation constrained by heat flow and seismicity in Taiwan. *Tectonophysics*, 324, 189-201.
- Lin, S., Jiang, D., Williams, P. F., 1998. Transpression (or transtension) zones of triclinic symmetry: natural example and theoretical modelling. Geological Society, London, Special Publications, 135, 41-57.
- Luyendyk, B. P., 1991. A model for Neogene crustal rotations, transtension, and transpression in southern California. *Geological Society of America Bulletin*, 103, 1528-1536.
- McFarlane, H. B., Block, S., Ailleres, L., Betts, P., Ganne, J., Baratoux, L., Jessell, M., 2016a. Lower and middle crust exhumation during Palaeoproterozoic accretionary tectonics: Key new evidence from the Sefwi Greenstone Belt, SW Ghana. 35th International Geological Congress (IGC), 27 AUGUST-4 SEPTEMBER 2016, Cape Town, South Africa, abstract.
- McFarlane, H. B., Block, S., Ailleres, L., Betts, P., Ganne, J., Baratoux, L., Jessell, M., 2016b. Lower and middle crust exhumation during Palaeoproterozoic accretionary tectonics: Key new evidence from the Sefwi Greenstone Belt. *Journal of Metamorphic geology* (in preparation).
- Milési, J.P., Feybesse, J.L. Pinna, P. et al., 2004. Geological map of Africa 1:10,000,000, SIGAfrique project. In: 20th Conference of African Geology. BRGM, Orleans, France, 2-7 June. Available at: <http://www.sigafrique.net>.
- Moresi, L., Solomatov, S., 1995. Numerical investigation of 2D convection with extremely large viscosity variations. *Physics of Fluids* (1994-present) 7, 2154-2162.

- Moresi, L., Dufour, F., Mühlhaus, H. B., 2003. A Lagrangian integration point finite element method for large deformation modeling of viscoelastic geomaterials. *Journal of Computational Physics*, 184, 476-497.
- Moresi, L., Quenette, S., Lemiale, V., Meriaux, C., Appelbe, B., Mühlhaus, H., 2007. Computational approaches to studying non-linear dynamics of the crust and mantle. *Physics of the Earth and Planetary Interior*, 163, 69-82.
- Morley, C. K., 1999. How successful are analogue models in addressing the influence of pre-existing fabrics on rift structure? *Journal of Structural Geology*, 21, 1267-1274.
- Morley, C. K., Haranya, C., Phoosongsee, W., Pongwapee, S., Kornsawan, A., Wonganan, N., 2004. Activation of rift oblique and rift parallel pre-existing fabrics during extension and their effect on deformation style: examples from the rifts of Thailand. *Journal of Structural Geology*, 26, 1803-1829.
- Neves, S. P., Vauchez, A., Feraud, G., 2000. Tectono-thermal evolution, magma emplacement, and shear zone development in the Caruaru area (Borborema Province, NE Brazil). *Precambrian Research*, 99, 1-32.
- Pachell, M. A., Evans, J. P., 2002. Growth, linkage, and termination processes of a 10-km-long strike-slip fault in jointed granite: the Gemini fault zone, Sierra Nevada, California. *Journal of structural geology*, 24, 1903-1924.
- Peacock, D. C. P., Parfitt, E. A., 2002. Active relay ramps and normal fault propagation on Kilauea Volcano, Hawaii. *Journal of structural geology*, 24, 729-742.
- Piccardo, G. B., 2016. Evolution of the lithospheric mantle during passive rifting: Inferences from the Alpine–Apennine orogenic peridotites. *Gondwana Research*.
- Ranalli, G., 1995. *Rheology of the Earth*. Springer Science & Business Media. pp. 413.
- Rey, P.F., Teyssier, C., Whitney, D.L., 2009a. Extension rates, crustal melting, and core complex dynamics. *Geology*, 37, 391–394.
- Rey, P.F., Teyssier, C., Whitney, D.L., 2009b. The role of partial melting and extensional strain rates in the development of metamorphic core complexes. *Tectonophysics*, 477, 135–144.
- Rey, P.F., Teyssier, C., Kruckenberg, S.C., Whitney, D.L., 2011. Viscous collision in channel explains double domes in metamorphic core complexes. *Geology*, 39, 387–390.
- Sakyi, P. A., Su, B. X., Anum, S., Kwayisi, D., Dampare, S. B., Anani, C. Y., Nude, P. M., 2014. New zircon U-Pb ages for erratic emplacement of 2213-2130Ma Paleoproterozoic calc-alkaline I-type

- granitoid rocks in the Lawra Volcanic Belt of Northwestern Ghana, West Africa. *Precambrian Research*, 254, 149-168.
- Seyferth, M., Henk, A., 2004. Syn-convergent exhumation and lateral extrusion in continental collision zones-Insights from three-dimensional numerical models. *Tectonophysics*, 382, 1-29.
- Sharples, W., Moresi, L. N., Jadamec, M. A., Revote, J., 2015. Styles of rifting and fault spacing in numerical models of crustal extension. *Journal of Geophysical Research: Solid Earth*, 120, 4379-4404.
- Soliva, R., Benedicto, A., Schultz, R. A., Maerten, L., Micarelli, L., 2008. Displacement and interaction of normal fault segments branched at depth: Implications for fault growth and potential earthquake rupture size. *Journal of Structural Geology*, 30, 1288-1299.
- Teufel, L. W., Clark, J. A., 1984. Hydraulic fracture propagation in layered rock: experimental studies of fracture containment. *Society of Petroleum Engineers Journal*, 24, 19-32.
- Tirel, C., Brun, J. P., Burov, E., 2008. Dynamics and structural development of metamorphic core complexes. *Journal of Geophysical Research: Solid Earth*, 113(B4).
- Vanderhaeghe, O., 2001. Melt segregation, pervasive melt migration and magma mobility in the continental crust: the structural record from pores to orogens. *Physics and Chemistry of the Earth, Part A: Solid Earth and Geodesy*, 26, 213-223.
- Vermilye, J. M., Scholz, C. H., 1999. Fault propagation and segmentation: insight from the microstructural examination of a small fault. *Journal of Structural Geology*, 21, 1623-1636.
- Weinberg, R. F., Mark, G., Reichardt, H., 2006. Magma ponding in the Karakoram shear zone, Ladakh, NW India. *Geological Society of America Bulletin*, 121, 278-285.

Chapter 5 A
numerical study of exhumation modes in the
WAC during regional compression

Introduction

In section 3.1 and chapter 4, in order to explore the possible tectonic evolution of greenstone-granitoid belts during the Eburnean Orogeny, two and three dimensional numerical models were used to explore the regional evolution of deformation in NW and SW Ghana. However, the structural deformation in the lower crust on a large scale remains unclear, at the same time, the origin of granitoids, tectonic and geodynamic regimes in the WAC are also still under strong debate. This chapter aims to shed new light on the evolution of granitoid-greenstone belts from a numerical study. We aims to submit this work in November 2016.

5 Role of volcano-sedimentary basin on spatial-temporal evolution of lower crust exhumation in the West African Craton (ca. 2.20-2.00 Ga): A numerical model

Highlights

1. The mantle potential temperature (T_p) yields 1500-1600 °C in the West African Craton during the Eburnean Orogeny (ca. 2.20-2.00 Ga).
2. The width of sedimentary basin plays an important role in the formation of N-S-oriented greenstone-granitoid belts.
3. A new tectonic model is suggested to account for the evolution of greenstone-granitoid belts.
4. High grade partially molten rocks may be widely capped by a resistant upper crust at a depth of about 10-15 km in the Leo-Man Shield.

Abstract

Greenstone belts in the West African Craton (WAC) are separated by several generations of granitoids intruded around ca. 2.18-1.98 Ga. Simultaneous folding and exhumation are thought to play an important role in the formation of greenstone-granitoid belts during the Eburnean Orogeny. However, the overall tectonic regime and origin of granitoids remain controversial. In this study, we present the estimates of the mantle potential temperature (T_p) for the WAC, which yields values of about 1500-1600 °C. The pressures of initial (P_i) and final (P_f) melting yield values of about 3.7-5.2 GPa and 1-1.3 GPa, respectively. Melt fraction for accumulated fractional melting ranges between 0.29-0.34. Subsequently, 2D thermo-mechanical models have been constructed to explore the effect of volcano-sedimentary basin on spatial-temporal evolution of diapirs that emplaced in the lower-middle crust during compression. The models show that the lower crust beneath sedimentary sequences is deformed into a buckle fold during the first compressional stage, through which relief uplifts slowly. Subsequently, the buckle fold is further deformed into several individual folds. Diapirs made of lower crust rocks ascend and emplace in the middle-upper crust, and relief uplifts in a high rate.

This study presents a new tectonic model to account for the deformation of greenstone-granitoid belts in the WAC during the Eburnean Orogeny (ca. 2.20-2.00 Ga). This model suggests that a series of sheet-like granitoids possibly derived from either subducted mélanges, lower crust and/or mantle melting accumulated at depths of the subcontinental mantle would channel along diapirs before feeding the upper crust. When the granitoids arrive at the solidified lids of the diapirs, they would favour migrating horizontally and intruding into the upper crust through weakening zones between the diapirs. This model also suggests an asymmetry of structures between the upper and middle-lower crust, with the dome-like granitoids overlying high-grade sedimentary synforms and high-grade diapirs underlying low-grade greenstone belts.

Keywords: Mantle potential temperature (T_p); Thermo-mechanical model; Exhumation; Eburnean Orogeny; Gravitational instabilities; West African Craton (WAC)

5.1 Introduction

Precambrian terranes generally display a homogeneous tectonic style over a 1000 km² range. In the West African Craton (WAC), Precambrian terranes show widespread greenstone belts separated by several generations of granitoids intruded around ca. 2.18-1.98 Ga (Baratoux et al., 2011). The maximum thickness of greenstone belts within the Paleoproterozoic domain of the WAC was reported by Condie et al. (1994, 2013) and Baratoux et al. (2011) to be between 10 and >20 km. However, only few studies have been reported on the geometrical constraint (width) of volcano-sedimentary basin. This is due to the ongoing debates and uncertainties surrounding the geodynamic evolution, tectonic regime and origin of granitoids during the Eburnean Orogeny. Ganne et al. (2014) explored the exhumation of lower crust under a convergent setting by employing a volcano-sedimentary basin of about 280-290 km in width (evidence from the Sigui basin which straddles upper Guinea-Southwest Mali). Their model produced two synchronous diapirs made of partially molten lower crustal rocks, 70 km apart. They concluded that, this distribution is compatible to the wavelength of the alternation between granitoids and greenstone belts across the Craton.

However, Glazner et al. (2004) suggested that, plutons generally grow in small increments as highlighted in many geological terranes. Regarding a diapir derived from lower crustal sources, it typically becomes solidified at a depth of 10-15 km due to its slow rise compared to the rate at which magma ascends along a dike (Bittner and Schmelting, 1995; Petford et al., 2000; Glazner et al., 2004). Therefore, the upper part of a diapir would undergo solid-state deformational behaviour. The authors argued that the difference in the rate of rise indicates that a diapir can hardly ascend or exhume through the upper crust under convergent tectonic regimes (Miller et al., 1988; Glazner et al., 2004; Ganne et al., 2014).

In addition, the current geochronological data that is currently available for West Africa (i.e., the Boromo, Houndé belts and neighbouring magmatic terranes), suggests small continuous magmatic episodes in anyone region rather than a single large pulse. The small pulses would have much smaller and more heterogeneous impact on the whole system than the single large pulse. This indicates that, the emplacement of diapirs resulting from compression might not have direct implications for the formation and deformation of greenstone-granitoid belts. Based on these new investigations enumerated above, it's necessary to further explore the role of diapirs in exhumation and plutonic activities in the WAC.

Moreover, the only extensional event in the Craton during the Eburnean Orogeny was reported in NW Ghana by Block et al. (2015). This means that structures in the lower crust remain uncertain compared to the well addressed deformation of the upper crust (Jessell et al., 2012). In this study, we do not aim

to exactly investigate the evolutionary history of deformation in the WAC (as it still remains open to discussions), but we rather explore the role of volcano-sedimentary sequences in geometric evolution of diapirs using 2D thermo-mechanical models. This paper could shed light on the Tp, geodynamic evolution and thickness of the lithosphere in the WAC during the Eburnean Orogeny (ca. 2.20-2.00 Ga). In addition, in terms of gravity instabilities that occurred in the middle crust, this work could also help reveal the structural evolution of greenstone-granitoid belts in the Leo-Man Shield.

5.2 Geological setting

5.2.1 Geological framework in the Leo-Man Shield

The Leo-Man Shield consists of the Paleoproterozoic Baoulé-Mossi domain to the east and the Archaean age Kénema-Man domain to the west (Figure 5.1). The Baoulé-Mossi domain consists of narrow (or large) volcano-sedimentary basins (greenstones *sensu lato*) and linear (or arcuate narrow) volcanic belts (greenstones *sensu stricto*) separated by extensive granitoids sequences. Radiometric dating shows that the early pulses of granitoids intrusions contemporaneous to the Birimian volcanisms were emplaced around ca. 2.20-2.17 Ga (Oberthür et al., 1998; De Kock et al., 2012). The main plutonic activities took place around ca. 2.15-1.98 Ga (Milési et al., 1992, Hirdes et al., 1996, Vidal et al., 1996, 2009; Dombia et al., 1998; Feybesse et al., 2006; Hein et al. 2010). The number of deformation phases characterizing the Eburnean orogeny is still under strong debates (Feybesse et al., 2006 and refs. therein). The existence of a S1 fabric developed at the early stages (D1) of the Eburnean orogenesis in the volcano-sedimentary belts is supported by some authors (Hein et al., 2010 and refs. therein) and contested by other ones (Vidal et al., 2009). Transition of D1 to the following D2 deformation phase is probably to have occurred at around 2.13 Ga in Ghana, following a major pulse in granitoids emplaced at around ca. ~ 2.15 Ga (Feybesse et al., 2006). The subsequent D2 deformation phase is responsible for most of the main structures observed in the Birimian Province, greenstones basins were deformed into linear to arcuate belts or transcurrent shear zones (Jessell et al., 2012) map-able on magnetic images.

5.2.2 Geological summary in South-Western Burkina Faso

The SW part of Burkina Faso consists of several sub-parallel N-S to NNE trending greenstone belts. From east to west is the Boromo-Lawra, Houndé-Ouango-Fitini and Banfora greenstone belts (Figure 5.1). The Boromo greenstone belt consists of flysch-like metasediments, tuffs and epiclastic volcano-sediments with occasional intercalations of andesites and rhyolites (Baratoux et al., 2011). This belt extends down to Ghana without major interruptions, where it is named as the Lawra belt (Leube et al., 1990). The eastern half of the Lawra belt is mainly composed of 2139±2 Ma metamorphosed sedimentary rocks and 2153±4 Ma granitoids (Agyei Duodu et al., 2009; Amponsah et al., 2015; Block

5. A numerical study of exhumation modes in the WAC during regional compression

et al., 2015). The western half is composed of 2187±3 Ma granitoids and high grade gneisses (Agyei Duodu et al., 2009), which have been metamorphosed up to amphibolite facies.

The Houndé-Ouango-Fitini (HOF, Figure 5.1) greenstone belt was intruded by granitoids between 2014±3 and 2152±2 Ma (Hirdes et al., 1996; Lüdtke et al., 1998). The eastern portion of the belt is composed of andesite pyroclastic flow and volcano-sediments in the centre (Baratoux et al., 2011), and some rhyolites at the base. The western part of the belt is composed of intermediate to acid calc-alkaline volcanic series including basaltic andesites and pyroclastic flows (Hirdes et al., 1996; Baratoux et al., 2011).

The eastern margin of the Banfora greenstone belt (Figure 5.1) consists of basalt, andesite pyroclastic flow and rhyolite, while the western margin is only composed of volcano-sedimentary rocks. In the KM area, the belt was intruded by main pulses of granitoids between 2123±3 and 2097±3 Ma (Dombia et al., 1998).

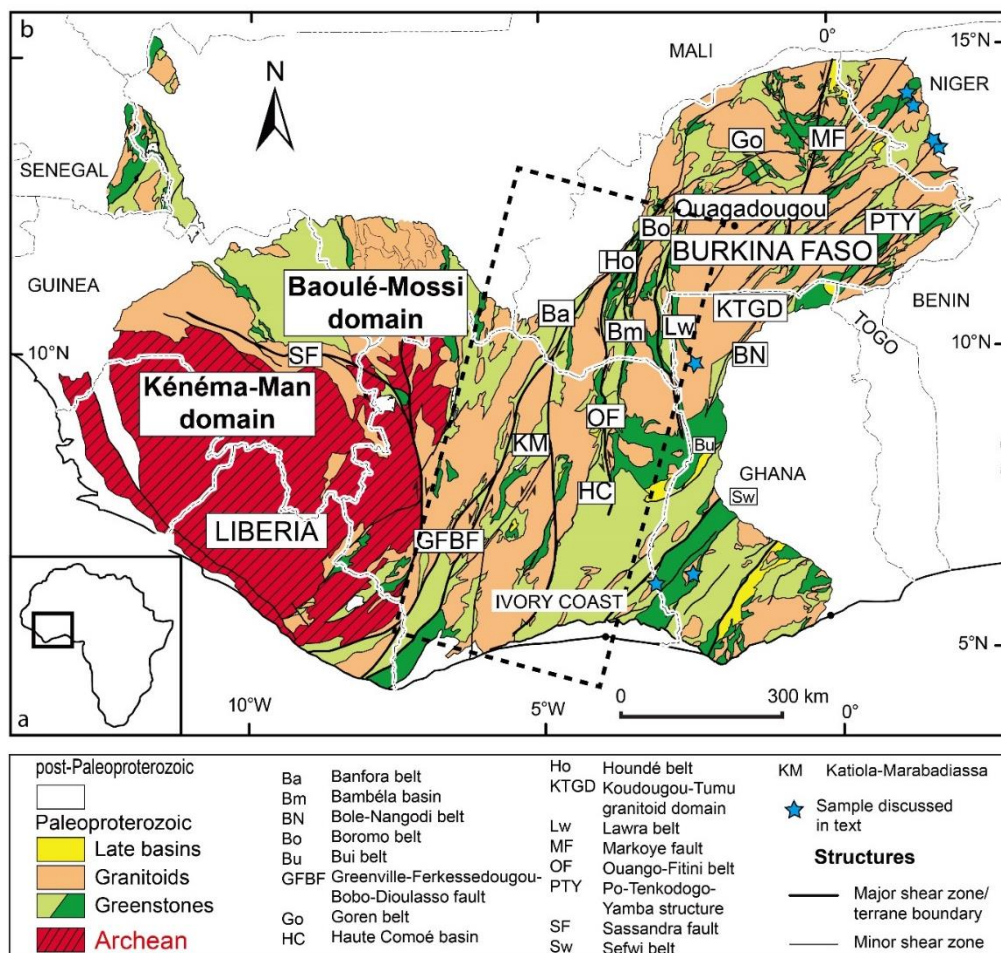


Figure 5. 1: Simplified geological map of the Leo-Man Shield, modified after Milési et al. (2004). The Archean basement is surrounded by greenstone-granitoids belts. The samples (blue stars) used to estimate the T_p are collected from Ama Salah et al. (1996), Soumaila, (2000), Galipp et al. (2003), Hirdes et al. (2007), Thomas et al. (2009). More detailed info on the samples are provided in Tables. 1 and S1.

5.2.3 Gravimetric responses

Gravity signals of characteristic wavelength stemmed from density anomalies at depth can help determine the structures in the lithosphere. In Figure 5.2, we show the signatures of Complete Bouguer gravity anomalies in the study area over six different profiles. These anomalies have been provided by the EGM2008 model of the BGI/Bureau Gravimétrique International. The negative values and amplitude of the Bouguer Anomaly (Figure 5.2b) can help to reveal the architecture and geometry of large-scale structures at depth, in this case the Leo-Man Shield (Figure 5.2a). Similar to the gravity model in Baratoux et al. (2011), the peaks and valleys of the gravity anomalies generally outline the greenstone and granitoid belts (orange and green in Figure 5.2a) respectively. Only the GFBF area (black dotted lines in Figure 5.2) is marked by weakly positive anomalies. The density anomalies in Figure 5.2b also reflect the position of craton-scale major shear zones in the area and their steeply dip angles to an extent. These shear zones transect the greenstone belts or/and define the boundaries with granitoid bodies.

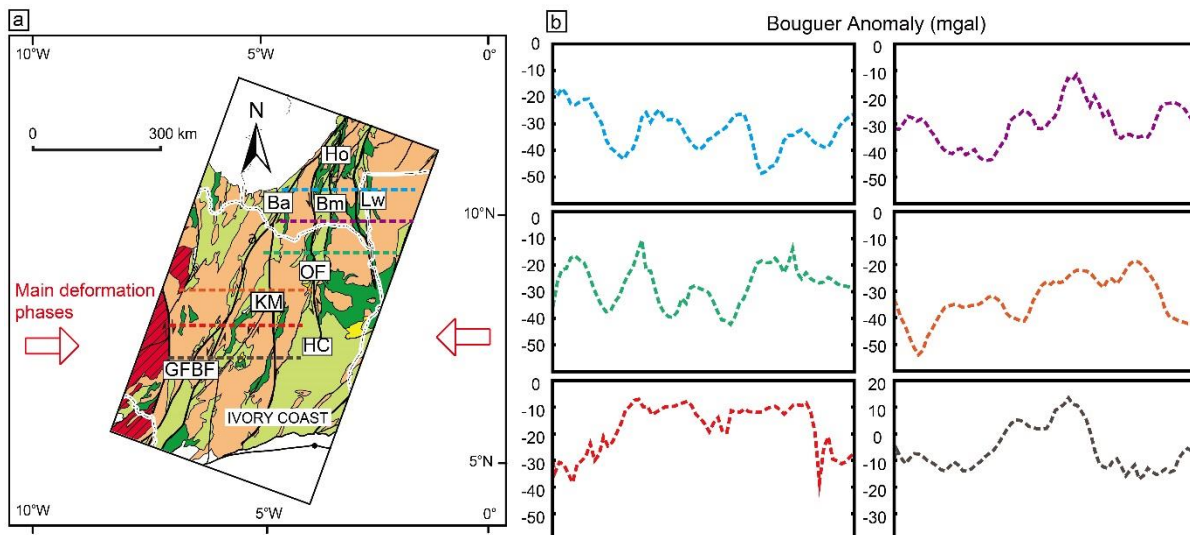


Figure 5. 2: (a) Six geological profiles lines in which the gravity data was acquired. (b) Graphical interpretation of gravity data corresponds to each profile line (different colour lines correspond to the geographic location shown in Figure a).

5.3 Tectonic models: the deformation of greenstone-granitoid belts

Precambrian volcano-sedimentary basins have some striking similarities and differences compared to modern Phanerozoic sedimentary basins (Eriksson et al., 1998; Catuneanu et al., 2005; Catuneanu and Eriksson, 2007; Bose et al., 2012). In SW Burkina Faso (Figures 5.1 and 5.2), Baratoux et al. (2011) proposed that the volcanic and meta-sedimentary rocks underwent long-wavelength amplitude buckling during the transition from an ocean crust to a thickened continental crust (~ 30 km, Figure 5.3a). The granitoids were possibly generated by oceanic slab melting in subduction zone and/or by re-

melting of lower crustal rocks (Baratoux et al., 2011 and ref therein). Regarding the process of subduction, two scenarios were proposed: (1) each belt (Boromo, Houndé and Banfora greenstone belts) corresponds to a volcanic arc and (2) only one volcanic arc existed (at least 400 km in width), which was shortened and folded into the present fashion of greenstone belts.

However, in Ivory Coast (Figure 5.1 and 5.2), Vidal et al. (2009) proposed a two stage scenario to explain the evolution of deformation on the basis of “dome and basin” fashion (Figure 5.3c). The D1 stage is characterized by the self-development of “dome and basin” only due to the contrast in density without the involvement of horizontal tectonic forces. This mechanism corresponds well with the fashion of diapirs emplaced in the Archaean orogenies (Gorman et al., 1978; Chardon et al., 1996, 2002). The D2 stage is characterized by coeval ascent of diapirs and shortening.

Compared to Vidal et al. (2009), an opposing model (crustal thickening by nappe stacking) was proposed by Feybesse et al. (2006) for the Sunyani-Comoé basin (Figure 5.1) on the basis of the geometric relationship between upwelling leucogranites and regional shear zones (Figure 5.3d). The D1 stage was responsible for thrusting and accretion. During the D2 stage, leucogranites emplaced in the crust by two steps: (1) initiating brittle deformation in the crust, (2) leucogranites emplaced through the brittle fractures under transcurrent regimes.

Regarding a numerical study (Figure 5.3b), Ganne et al. (2014) modelled the post-accretion Eburnean collisional-orogeny. A relatively homogeneous temperature profile was suggested, characterized by a moderate temperature gradient of 20 to 30 °C /km. They proposed that the exhumation of partially molten rocks, characterized by strong lateral metamorphic gradients, was mainly controlled by simultaneous folding/shortening and gravitational instabilities in the crust.

These different tectonic models suggest that the overall tectonic regime in the WAC during the Eburnean Orogeny is still a matter of debate, due to limited outcrop exposures (Baratoux et al., 2011; Jessell et al., 2012), uncertain geophysical signatures of the Moho depth and lithospheric thickness (Jessell et al., 2016) and vague thermal state of the mantle (T_p). For the geodynamic setting, it is thought to be related with immature arcs (Dioh et al., 2006) or oceanic plateaus (Boher et al., 1992; Lompo, 2009). All these uncertainties suggest that the origin of granitoids in the WAC remains incompletely understood.

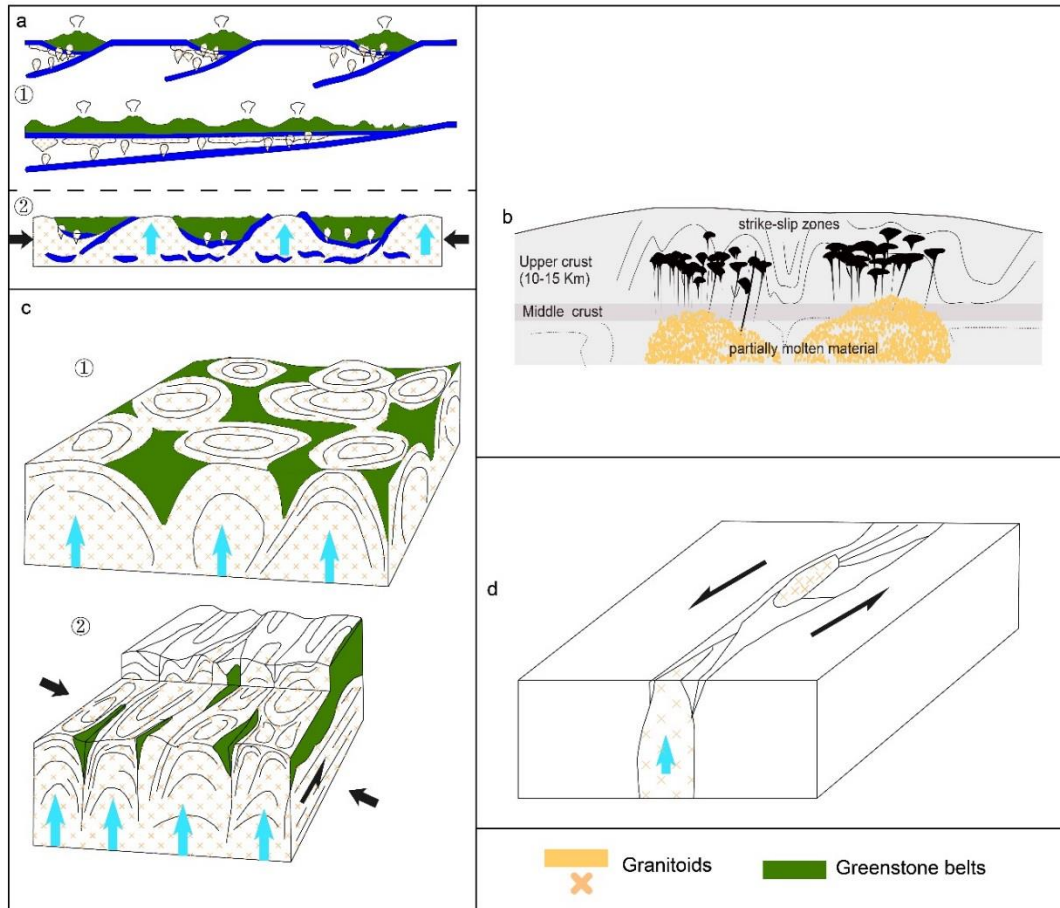


Figure 5. 3: Different tectonic models accounting for the evolution of greenstone-granitoid belts in the Leo-Man Shield were proposed by (a) Baratoux et al., 2011, (b) Ganne et al., 2014, (c) Vidal et al., 2009, (d) Feybesse et al., 2006, respectively. Boundary conditions are indicated in black arrows. The upward motion of granitoids is indicated by blue arrows.

5.4 Ambient mantle temperature (T_p)

The thermal state of the mantle depends on the balance between heat production by radiogenic elements and heat loss by mantle convection. Basalts are thought to be a thermal probe of the mantle, as their compositions significantly change with the T_p through geological time (Thompson and Gibson, 2000; Putirka et al., 2007; Herzberg et al., 2010; Herzberg, 2011). The T_p evolution calculated on a global scale shows a limited secular cooling of 200-150 °C since ca. 4.0 Ga (Herzberg et al., 2010).

In order to obtain the T_p info in the WAC during the Eburnean Orogeny, we have explored different magma databases (GEOROC database, <http://georoc.mpch-mainz.gwdg.de/georoc/>; WAXI database, the West African Exploration Initiative project). The mantle-derived primary magmas are analysed with the software PRIMELT3 (Herzberg and Asimow, 2015). All T_p solutions have been filtered according to the graphic procedures given in Herzberg and Asimow, (2008). Seven samples (their GPS coordinates are roughly indicated by blue stars) of volcanic rocks or lavas (less than 1% survived from the dataset

5. A numerical study of exhumation modes in the WAC during regional compression

of > 1000 data) yield successful solutions (Figure 5.4 and Table 5.1). The bulk compositions of samples are provided in Table 5.S1. All samples yield approximate ages of about ca. 2.20-2.10 Ga. Fe_2O_3 is calculated with $FeO/FeO_T = 0.9$ and $Fe_2O_3/TiO_2 = 0.5$. Melting is assumed to be accumulated fraction. All calculated primary magma compositions are aggregates of all melt increments that mix perfectly.

The T_p yields between 1500 and 1600 °C, approximately yielding a mean value of 1520 °C (Figure 5.4). The pressures of initial (P_i) and final (P_f) melting yield about 3.7-5.2 GPa (corresponding to a depth of about 120-170 km) and 1-1.3 GPa, respectively (Figure 5.5). Melt fraction ranges between about 0.29-0.34 (Table 5.1).

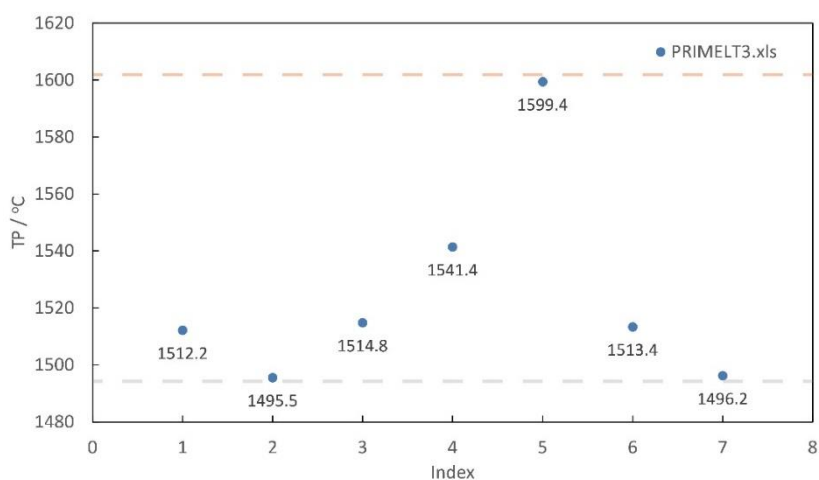


Figure 5. 4: The T_p is calculated with the software PRIMELT3 (Herzberg and Asimow, 2015). The grey and orange dotted lines indicate the approximately minimum (1500 °C) and maximum (1600 °C) values, respectively. The horizontal axis corresponds to the “index” row in Table 5.1.

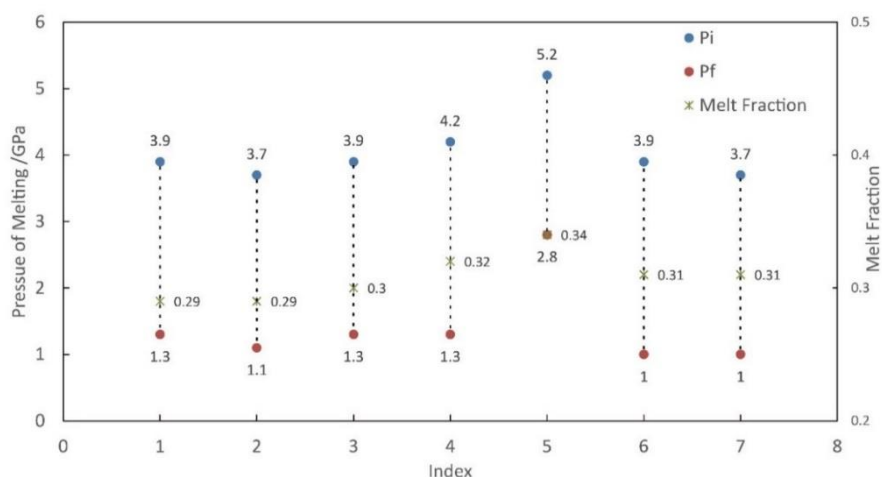


Figure 5. 5: The pressures of initial and final melting of samples are calculated with the PRIMELT3 software (Herzberg and Asimow, 2015). Melt fraction ranges between 0.29 and 0.34. The horizontal axis shows the sample information, corresponding to the “index” row in Table 5.1. P_i = Pressure of initial melting, P_f =Pressure of final melting.

5. A numerical study of exhumation modes in the WAC during regional compression

Table 5. 1: Primary Magma Solutions for volcanic rocks in the WAC (ca. 2.20-2.10 Ga)

Reference	Hirdes et al. (2007)	Ama Salah et al. (1996)	Thomas et al. (2009)	Galipp et al. (2003)	Ama Salah et al. (1996)	Soumaila. (2000)	Soumaila. (2000)
Sample	1074	AS-393	EC2036	KG 18	AS-5	755	810
Index	1	2	3	4	5	6	7
Location	Ghana Sefwi Belt	Niger Nigerian Liptako	Ghana Wa-Larwa Belt	Ghana Sefwi Belt	Niger Nigerian Liptako	Niger Nigerian Liptako (Zawa Tondi)	Niger Nigerian Liptako (Zawa Tondi)
Rock type	BASALT	BASALT	BASALT	BASALT	BASALT	BASALT	BASALT
lat	6	13.5	9.666	6.08	13.5	14	14
long	-2.8	1.5	-2.46	-2.95	1.5	1	1
SiO ₂ ^a	48.30	48.82	48.50	48.56	47.26	49.01	49.81
TiO ₂	0.27	0.25	0.35	0.47	0.20	0.44	0.43
Al ₂ O ₃	11.52	12.77	11.20	10.68	10.03	11.34	10.75
Cr ₂ O ₃	0.00	0.00	0.00	0.00	0.00	0.00	0.00
Fe ₂ O ₃	0.14	0.12	0.17	0.23	0.10	0.22	0.21
FeO	9.55	9.27	9.56	9.91	10.66	9.50	9.23
MnO	0.16	0.16	0.16	0.17	0.18	0.16	0.17
MgO	17.98	17.34	18.09	19.13	21.43	18.03	17.36
CaO	10.32	10.14	10.56	9.34	9.10	9.93	9.70
Na ₂ O	1.58	1.10	1.16	1.38	0.88	1.14	1.95
K ₂ O	0.15	0.01	0.22	0.07	0.06	0.10	0.26
NiO	0.00	0.00	0.00	0.00	0.00	0.00	0.00
P ₂ O ₅	0.03	0.03	0.02	0.05	0.10	0.13	0.12
La/Yb	-	2.0	1.3	-	1.7	0.8	1.5
T OL (°C) ^b	1394.79	1375.32	1391.87	1414.03	1450.21	1390.57	1389.12
T P (°C) ^c	1529.53	1515.18	1531.79	1553.91	1599.65	1530.55	1515.78
T P (°C) ^d	1512.18	1495.54	1514.83	1541.44	1599.42	1513.38	1496.23
OL Mg ^e	0.92	0.91	0.92	0.92	0.92	0.92	0.91

5. A numerical study of exhumation modes in the WAC during regional compression

F AFM ^f	0.29	0.29	0.30	0.32	0.34	0.31	0.31
Pi (GPa) ^g	3.9	3.7	3.9	4.2	5.2	3.9	3.7
Pf (GPa) ^h	1.3	1.1	1.3	1.3	2.8	1	1

- a. Lava sample in original source reference for which PRIMELT3.XLS has been applied.
- b. Olivine liquidus temperature at 1 atmosphere (°C).
- c. Mantle potential temperature (°C) (PRIMELT2.XLS).
- d. Mantle potential temperature (°C) (PRIMELT3.XLS).
- e. Mg number of olivine to crystallize from primary magma at 1 atmosphere.
- f. Melt fractions for peridotite KR-4003 for the case of accumulated fractional melting.
- g. Pressure of initial melting. h. Pressure of final melting.

5.5 Numerical method and model assumptions

In this study, six 2D thermo-mechanical models have been built according to our previous work (Ganne et al., 2014) with the code *Underworld* (Moresi et al., 2003, 2007). This code uses a Lagrangian Particle-in-Cell (PIC) finite element scheme. The governing equations for momentum, mass and energy conservation are solved according to *Underworld* framework (the method is not recalled here as more details on the method description can be found in De Smet et al., 1998; Moresi et al., 2003, 2007).

The model domain (Figure 5.6) is 600 km long (X direction) and 60 km thick (Y direction), with a resolution of 2 km × 1 km (X and Y direction) in a 2D geometry and a visco-plastic rheology. We use a random initial particle layout. 30 particles are initialised in each cell. The model is made of an upper mantle, a sedimentary basin, an upper crust and a lower crust. In the upper crust, we define a volcano-sedimentary basin with different widths. The schematic model is given in Figure 5.6. In this paper, we apply convergent boundary conditions at a rate of 2.5 mm/year for each side. The base of the model domain is fixed, a free re-meshing boundary condition is applied to the model surface to produce relief (Moresi et al., 2003; Feng et al., 2016a). For the thermal conditions of the model, we model the compression of a “hot” lithosphere. We apply fixed temperatures of 0 °C at the surface, and the temperature at the Moho depth is about 500-625 °C, that is consistent with the results of Mckenzie et al. (2005) and Wang et al. (2015). Other physical and thermal properties are given in Table 4.

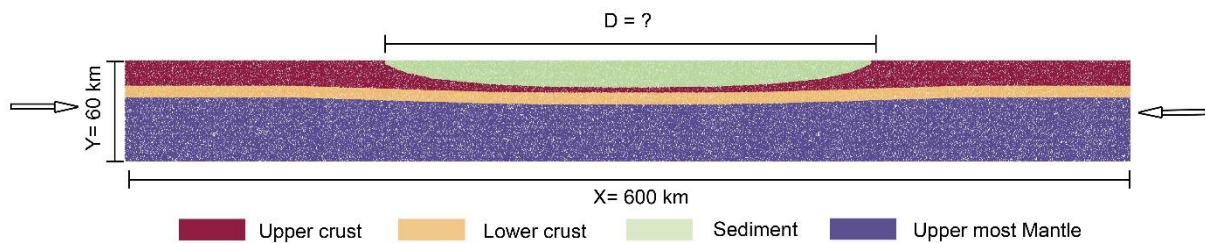


Figure 5. 6: 2D thermo-mechanical model. The convergent rate is set to 2.5 mm/year for each side. The model domain is 600 km long and 60 km thick. In the upper crust we define a 16 km thick volcano-sediment overlaying the 10 km thick crustal layers (including 3 km mafic crust and 7 km lower crust). The width of sediment (D) is variable according to different cases listed in Table 5.2.

Table 5. 2: Parameters for each model, Exp # represents the name of experiment.

Width of sediment (D=?)	200 km	250 km	290 km	350 km	400 km	450 km
Exp #	Model200	Model250	Model290	Model350	Model400	Model450

At depth, rock deformation is sensitive to temperature. Generally, this behaviour is described by a temperature-dependent non-Newtonian power law (Ranalli, 1995). Parameters used in equation (1) are given in Table 4.1.3. Viscosity (η) is given by:

5. A numerical study of exhumation modes in the WAC during regional compression

$$\eta = 0.25 \cdot (0.75A)^{(-1/n)} \cdot \dot{\epsilon}^{((1/n)-1)} \cdot \exp(Q/nRT) \quad (5.1)$$

where $\dot{\epsilon}$ is the second invariant of the strain rate, Q is the activation energy, R is the universal gas constant, A is a pre-exponential constant and n is a power law exponent.

Table 5. 3: Rheological properties of different lithospheric layers (Ranalli, 1995 and references therein).

Layer	A / MPa ⁻ⁿ / s	n	Q / KJ/mol
Upper crust	2.0 x 10 ⁻⁴	3.4	260
Lower crust	1.3 x 10 ⁻³	2.4	219
Sediment	3.2 x 10 ⁻⁴	2.3	154
Upper most mantle	7 x 10 ⁴	3.3	520

The effect of latent heating is introduced into the modelling, following the methodology of Gerya et al. (2008) and Ganne et al. (2014) to model the effective heat capacity of partially molten rocks ($M > 1\%$) and their expansion coefficient. The latent heat of melting is fixed to 300 kJ/kg for all crustal rocks (Bittner and Schmeling, 1995; Ganne., et al., 2014). The volumetric melt fraction is calculated following the methodologies of Gerya and Yuen. (2003); Gerya et al. (2008); Ganne et al. (2014). The volumetric melting coefficient (X_M) for calculating melt fraction (M) according to temperature is expressed as equations (5.2) and (5.3):

$$\begin{aligned}
 X_M &= 0 && \text{at } T \leq T_{solidus} \\
 X_M &= \frac{T - T_{solidus}}{T_{liquidus} - T_{solidus}} && \text{at } T_{solidus} < T < T_{liquidus} \\
 X_M &= 1 && \text{at } T \geq T_{liquidus}
 \end{aligned} \quad (5.2)$$

where $T_{solidus}$ and $T_{liquidus}$ are the wet solidus and dry liquidus temperatures of crust layers, respectively. We assume that the $T_{solidus}$ and $T_{liquidus}$ do not change with pressure (Gerya et al., 2008; Ganne, et al., 2014).

For the volumetric melt fraction (M), we assume that it increases linearly with the temperature, when temperature is above the wet solidus temperature and below the dry liquidus temperature (Gerya et al., 2008; Ganne et al., 2014). M is expressed as

$$M = X_M \cdot M_{max} \quad (5.3)$$

When the temperature reaches $T_{solidus}$, an effective viscosity is used to model partially molten rocks. Gerya et al. (2008) employed a constant viscosity of 10¹⁷ Pa s for partially molten rocks. Whereas Ganne et al. (2014) assigned an effective viscosity function (equation 4) with volumetric melt fraction (M), the effective viscosity is obtained ranging between 6x10¹⁷ Pa s ($M=1$) and 8x10¹⁸ Pa s ($M=0.1$) according to different melting conditions. We use equation (5.4) to model the effective viscosity when the

5. A numerical study of exhumation modes in the WAC during regional compression

volumetric melt fraction exceeds 1% (Pinkerton and Stevenson, 1992). Melting points of different layers are listed in Table 5.5.

$$\eta_{eff} = 5 \times 10^{16} \cdot \exp\left(2.5 + (1 - M) \left(\frac{1-M}{M}\right)^{0.48}\right) \quad (5.4)$$

Table 5. 4: Parameters used in experiments.

Parameter	Symbol	Value-units
Density	ρ_{upper}	3050 kg/m ³
	ρ_{lower}	2700 kg/m ³
	$\rho_{sediment}$	2800 kg/m ³
	ρ_{mantle}	3250 kg/m ³
Width of sediment	D	-
Dislocation creep power law pre-exponential factor	A	MPa ⁻ⁿ /s
Dislocation creep power law exponent	n	-
Power law creep activation energy	E	KJ/mol
Temperature	T	°C
Gas constant	R	8.314 J mol ⁻¹ K ⁻¹
Heat capacity	C	1000 J/kg·K
Latent heat	lh	kJ/kg
Gravitational acceleration	g	9.81 m/s ²
Friction angle for Drucker-Prager	φ	8-20°
Cohesion for Drucker-Prager	σ	5-10 Mpa
Viscosity limit	η	$10^{18} < \eta < 10^{23}$ Pa s

Table 5. 5: Melting points of different lithospheric layers (According to metamorphic modelling with Perple-x by Ganne et al., 2014).

Layer	Rock type	$T_{solidus}$ /°C	$T_{liquidus}$ /°C	M_{max}
Upper crust	Diabase	836	1200	0.3
Lower crust	Quartzodiorite	636	1200	0.8
Sediment	Wet quartzite	700	1200	0.8

The density is calculated based on the temperature and a thermal expansion coefficient of $3 \cdot 10^{-5}$ K⁻¹. A constant thermal diffusivity of 10^{-6} m²/s is applied to the whole modelling domain. For the uppermost mantle, a linear equation relating density to temperature is expressed as equation (5.5):

$$\rho_{eff} = \rho[1 - \alpha \cdot (T - T_0)] \quad (5.5)$$

For the layers involving partial melting, we employ a similar equation with De Smet et al. (1998); Gerya et al. (2008); Ganne et al. (2014). The effective density varying with temperature, melt fraction and pressure is calculated by equation (5.6):

$$\rho_{eff} = \rho[1 - \alpha \cdot (T - T_0) - mc \cdot M + \beta \cdot (P - P_0)] \quad (5.6)$$

where ρ_{eff} is the effective density, α is the thermal expansion coefficient, ρ is the original density, T is the local temperature, T_0 is the reference temperature (surface), mc is the coefficient of expansion related to phase change (Rey et al., 2009), β is the compressibility coefficient (10^{-11} Pa^{-1} , Gerya et al., 2008; Ganne et al., 2014), P is the local pressure and P_0 is the reference pressure.

5.6 Thermo-mechanical modelling results

Six 2D thermo-mechanical models are used to test the influence of volcano-sediment in the evolutionary geometry of diapirs made of lower crustal sources (listed in Table 5.2). All simulations were run in parallel on the cluster machine EOS located at CALMIP in Toulouse (2.8 Ghz, 20 cores per node).

5.6.1 Model200 and Model250

Model200 and Model250 show a similar single diapir resulting from the development of two and two to three crustal-scale folds (Figures 5.7 and 5.8), respectively. Within the first compressional stage (Model200, about 28 Ma; Model250, 31 Ma), the competent mafic crust beneath the weak sediment develops folds. The lower crustal rocks undergo partial melting with increasing buried depth. A narrow reservoir forms between the folds and begins to preserve early moderate-high pressure volcano-sedimentary rocks (about 30-35 km, corresponding to about 10 kbar). The mafic layer prevents a direct contact and interaction between the lower crust and sediment rocks (Figures 5.7a and 5.8a). As convergence continues, partially molten lower crustal rocks are buried to deeper depth. The gravity instabilities resulting from increasing temperature, pressure and melt fraction become significant. At about 43 Ma for Model200 (46 Ma for Model250), the less dense lower crust rocks completely break through the overlying mafic layer and ascend into the weak sediment. A diapir widely spreads and emplaces at a depth of 10-15 km. The width of the diapir is about 50 km for Model200 (70 km for Model250). High strain zones (shear) mostly focus within the centre of the diapir and lower crust layer on the left and right sides of the sediment (Figures 5.7c and 5.8c).

Regarding the relief, the results show the surface uplifts with time in general. For Model200, the uplift and subsidence reach about 2800 m and -1500 m at 28 Ma, about 3800 m and -3300 m at 43 Ma. For Model250, the maximum uplift and subsidence reach about 2700 m and -1600 m at about 31 Ma, about 3300 m and -3300 m at 46 Ma (Figures 5.7a and 5.8a).

5.6.2 Model290

When the width of the sediment is increased to 290 km, the mafic layer beneath the weak sediment is deformed into three crustal-scale folds by about 35 Ma. These folds have a similar width of about 50 km (Figure 5.9). High strain slowly concentrates in the middle fold (Figure 5.9c). With continuing convergences, lower crustal rocks start to ascend towards the weak sedimentary zone. The middle fold plays a significant role in recharging the other two folds via formed weaknesses between neighbouring folds. Two narrow zones form between the folds under compression, which exist as reservoirs to preserve high pressure volcano-sedimentary rocks. At about 50 Ma, two similar diapirs emplace at a depth of 10-15 km (corresponding to 3 kbar). The diapirs are about 50 km wide. The sedimentary rocks beneath the diapirs reach a high melt fraction of > 0.5 (Figure 5.9d).

Regarding the relief, the results show that, the head-positions of diapirs influence the distribution of uplift. The maximum uplift and subsidence reach about 2700 m and -2000 m at 35 Ma, about 2950 m and -3100 m at 50 Ma (Figure 5.9a).

5.6.3 Model350 and Model400

Model350 and Model400 show a similar process from folding to exhumation. A wide buckle fold is deformed into three crustal-scale folds during compression (Figures 5.10 and 5.11). The middle fold has a larger size than the ones on the left and right sides. Similar to other cases displayed in Figures 5.7, 5.8 and 5.9, two narrow reservoirs are observed. They persevere much more high pressure sedimentary rocks compared to the scenarios in Model200, Model250 and Model290. These persevered sedimentary and lower crustal rocks start to undergo partial melting with increasing burial depth. For Model350, the width of folds is about 50-70 km. For Model400, the width of the folds ranges between 30 and 100 km. At 36 Ma, the lower crustal rocks start to break completely through the overlying mafic layer due to fact that the gravity instabilities become more significant. At 53 Ma, three diapirs completely break through the mafic layer and emplace in the sediment. No interaction between two neighbouring diapirs occurs during the processes of folding-exhumation, which is different from what was observed in cases Model200, Model250 and Model290. The widths of diapirs are 30-50 km in Model350 and 30-80 km in Model400 (Figures 5.10 and 5.11).

For Model350, the maximum uplift and subsidence yield about 2800 m and -2000 m at 36 Ma, 3100 m and -3700 m at 53 Ma, respectively. For Model400, the maximum uplift and subsidence yield about 2800 m and -2300 m at 37 Ma, about 3000 m and -3800 m at 53 Ma (Figures 5.10a and 5.11a).

5.6.4 Mode450

When the width of sediment is set to 450 km, a large buckle fold is deformed into four crustal-scale folds by about 37 Ma during compression (Figure 5.12). Two wide folds are located in the middle of the model domain, which are about 70-80 km wide. Two smaller ones are about 30-40 km wide. Three reservoirs preserving high pressure volcano sedimentary rocks form between the neighbouring folds as convergence continues (the maximum burial depth of sedimentary rocks is up to about 35 km, melt fraction is about 0.3-0.4). High strain zones mainly focus in the smaller folds and the reservoirs. *E*ll ranges between 6 and 10 (Figure 5.12c).

At 58 Ma, two groups of diapirs (including four) distinguished by their sizes ascend into the overlying weak sediment and emplace at a depth of about 10-15 km. Neighbouring diapirs are separated by about 5 (between the two diapirs on the left or right sides) -10 km (between the two middle ones) wide sedimentary rocks. Mafic crustal layer bends and intrudes into the lower crust layer.

The maximum uplift and subsidence yield about 2500 m and -2500 m at 37 Ma. At 58 Ma, the maximum uplift and subsidence yield about 1200 m and -5400 m, respectively.

5. A numerical study of exhumation modes in the WAC during regional compression

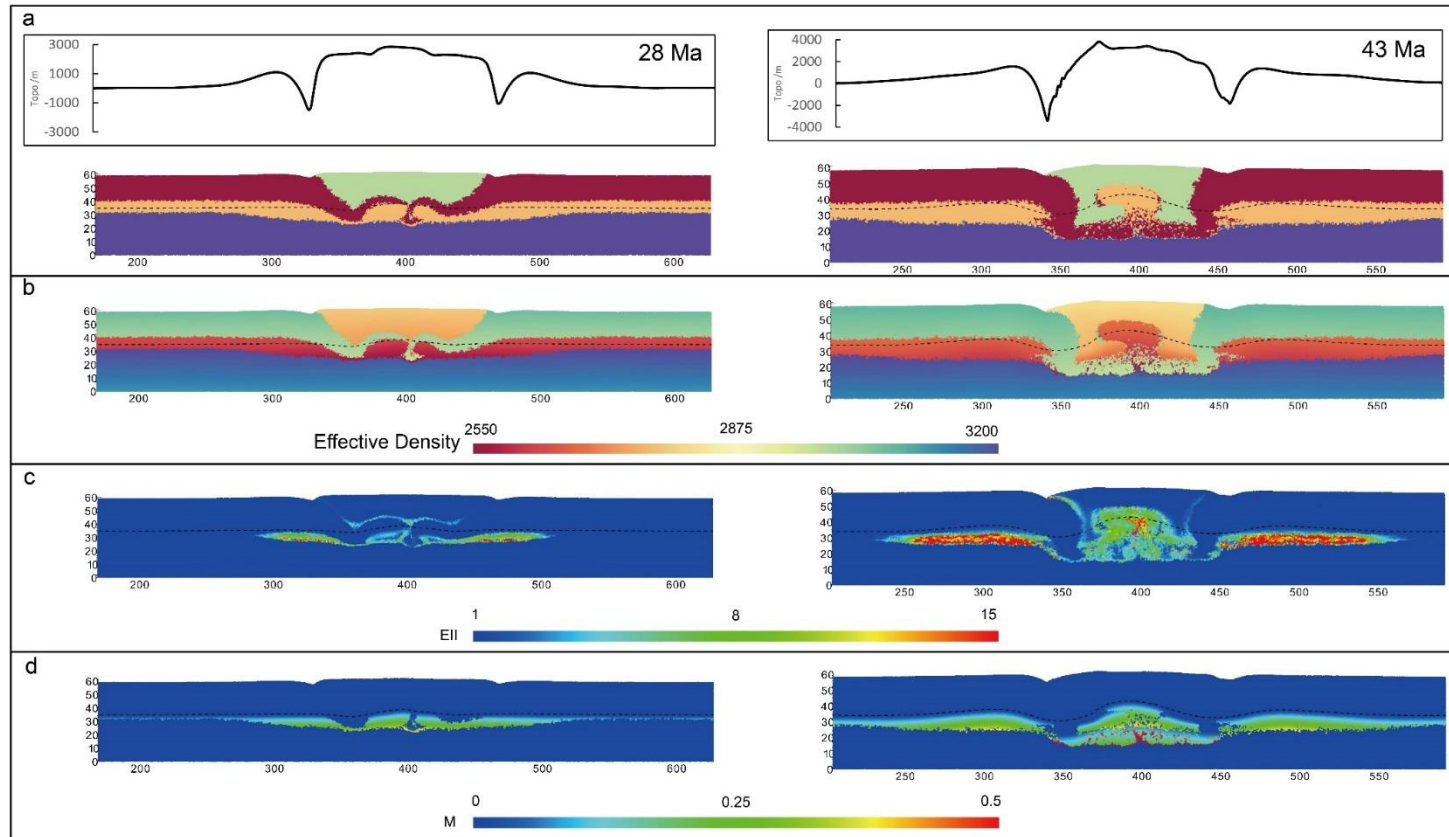


Figure 5. 7: Model M200 shows the evolution of folding-exhumation when the width of sediment is set to 200 km. The solidus temperature of the lower crust is shown in black dashed line. (a) At 28 Ma, buoyant lower crustal rocks start to form two crustal-scale folds and break through the mafic layer beneath the sediment (28 Ma). At about 43 Ma, partially molten lower crust rocks ascend into the sediment and form a diapir. Relief (Topo) is modelled using a free re-meshing surface boundary condition. The height of left side of the model is taken as 0 point to calculate uplift or subsidence. (b) Effective density is calculated by equations (5) and (6). (c) The accumulation (EII) of the second invariant of the strain rate (ε_{II} , s^{-1}) is employed to identify shear zones over time (calculated by $EII = \sum_0^t \varepsilon_{II} \cdot \Delta t$). (d) Melt fraction is obtained by equations (2) and (3).

5. A numerical study of exhumation modes in the WAC during regional compression

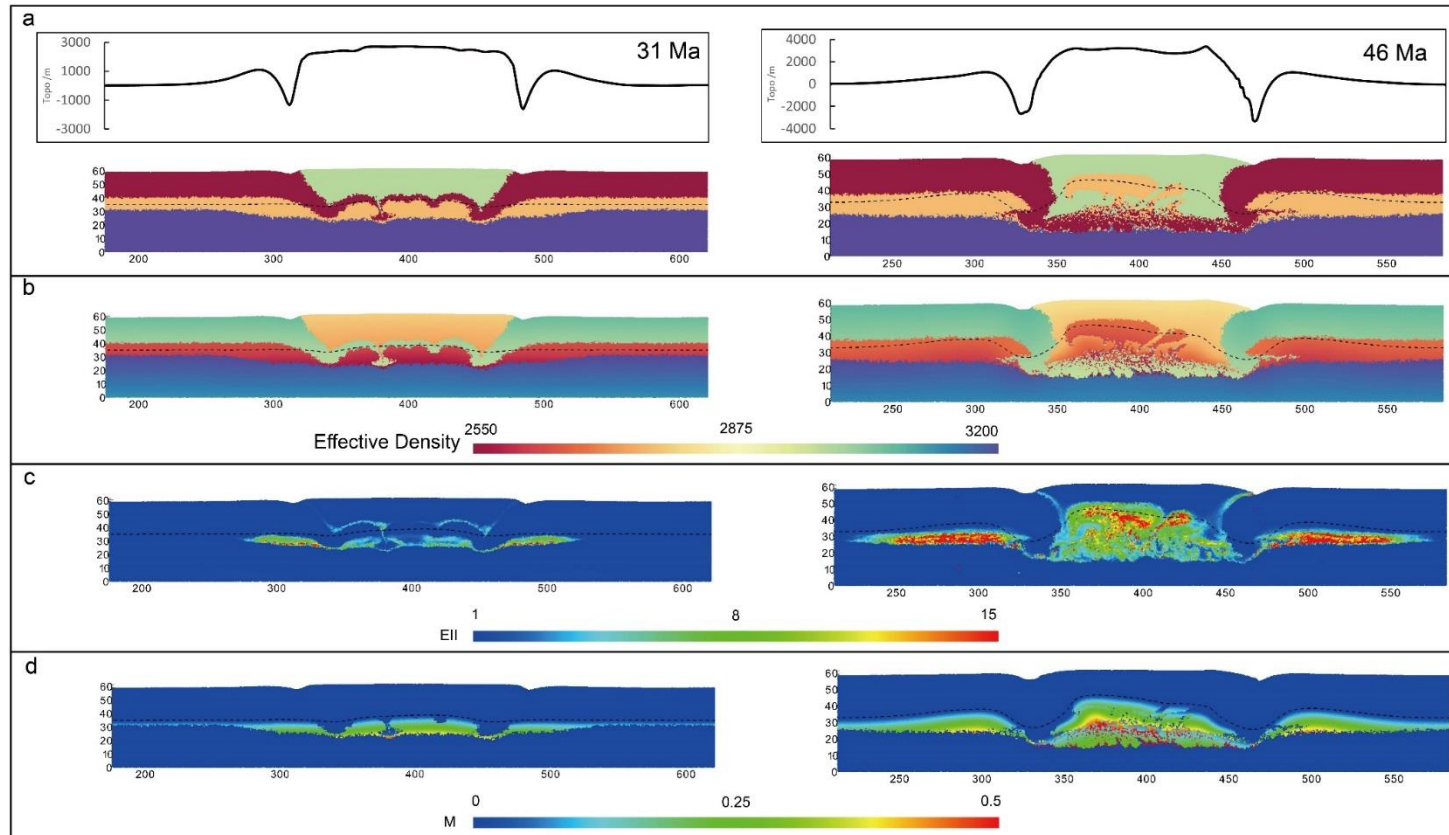


Figure 5. 8: Model M250, the width of sediment is set to 250 km. The solidus temperature of the lower crust is shown in dashed line. At about 31 Ma, lower crustal rocks start to break through the mafic layer beneath the weak sediment. At 46 Ma, partially molten rocks ascend towards the sediment and form a diapir, which is wider than the diapir observed in model M250.

5. A numerical study of exhumation modes in the WAC during regional compression

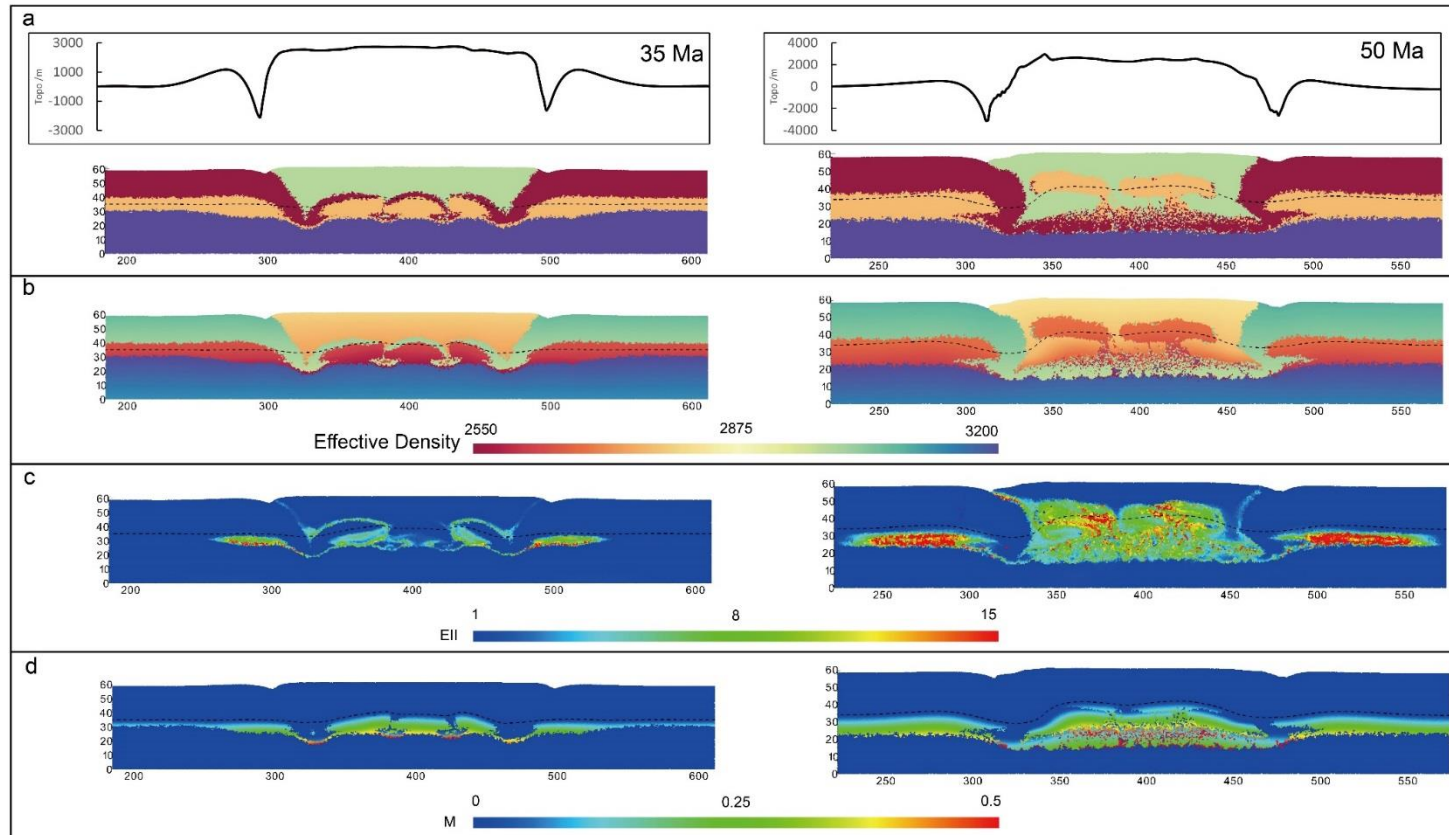


Figure 5. 9: Model M290, the width of sediment is set to 290 km. The solidus temperature of the lower crust is shown in dashed line. At 35 Ma, lower crustal rocks form three crustal-scale folds. Moderate-high pressure volcano-sedimentary rocks are preserved in two fold hinges. As convergence continues (50 Ma), partially molten lower crustal rocks ascend into the sedimentary basin and form two similar diapirs.

5. A numerical study of exhumation modes in the WAC during regional compression

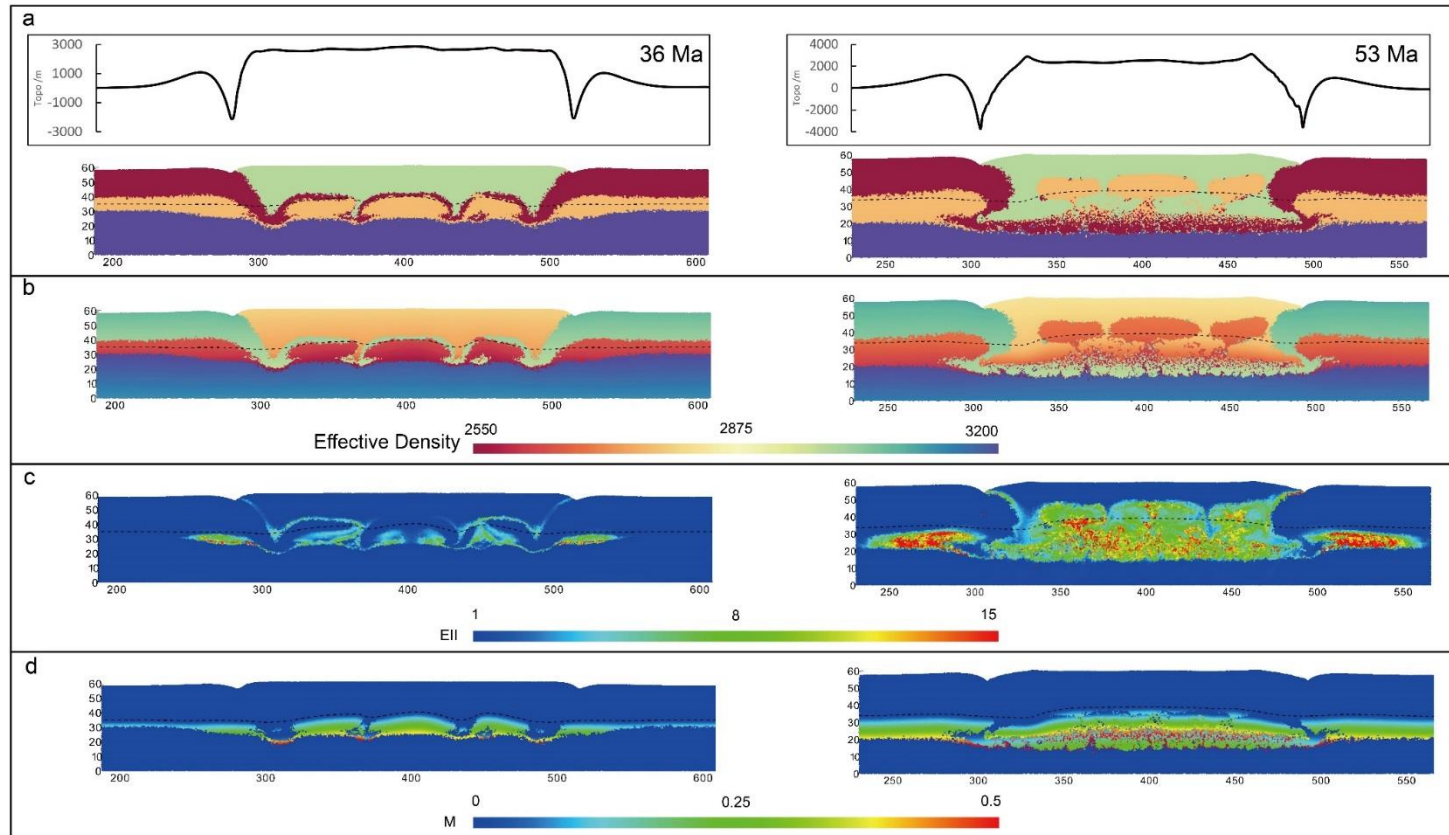


Figure 5. 10: Model M350, the width of sediment is set to 350 km. The solidus temperature of the lower crust is shown in dashed line. At 36 Ma, less dense lower crustal rocks start to form three crustal-scale folds. Two fold hinges are wider and preserve much more moderate-high pressure volcano-sedimentary rocks that that in case Model290. At 53 Ma, partially molten lower crustal rocks ascend into the sediment and form three diapires.

5. A numerical study of exhumation modes in the WAC during regional compression

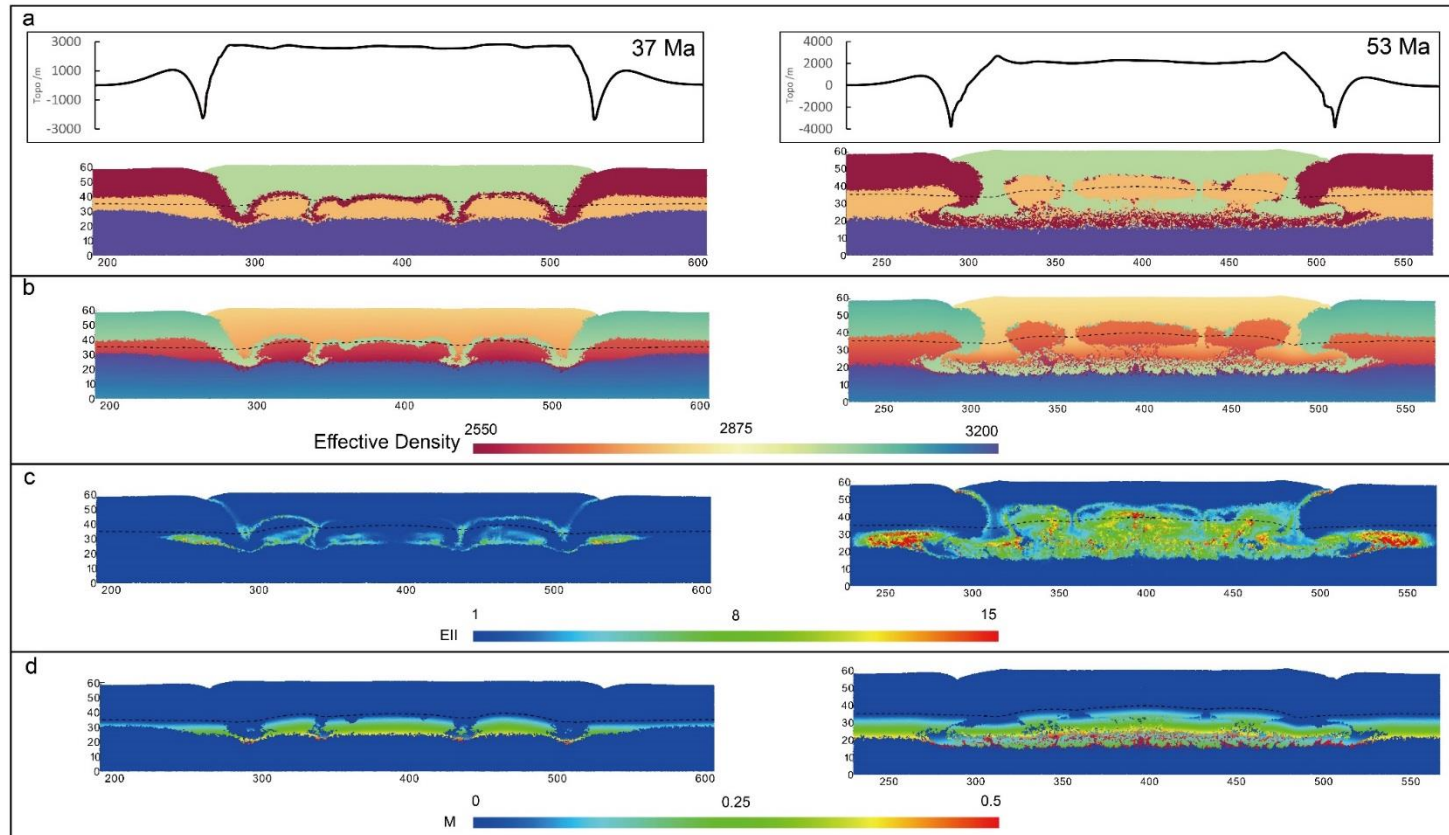


Figure 5. 11: Model M400, the width of sediment is set to 400 km. The solidus temperature of the lower crust is shown in dashed line. At 37 Ma, buoyant lower crustal rocks start to form three crustal-scale folds and break through the competent mafic layer beneath the sediment. Moderate-high pressure volcano-sedimentary rocks are preserved in two fold hinges. At 53 Ma, partially molten lower crustal rocks ascend into the sediment and form three diapirs.

5. A numerical study of exhumation modes in the WAC during regional compression

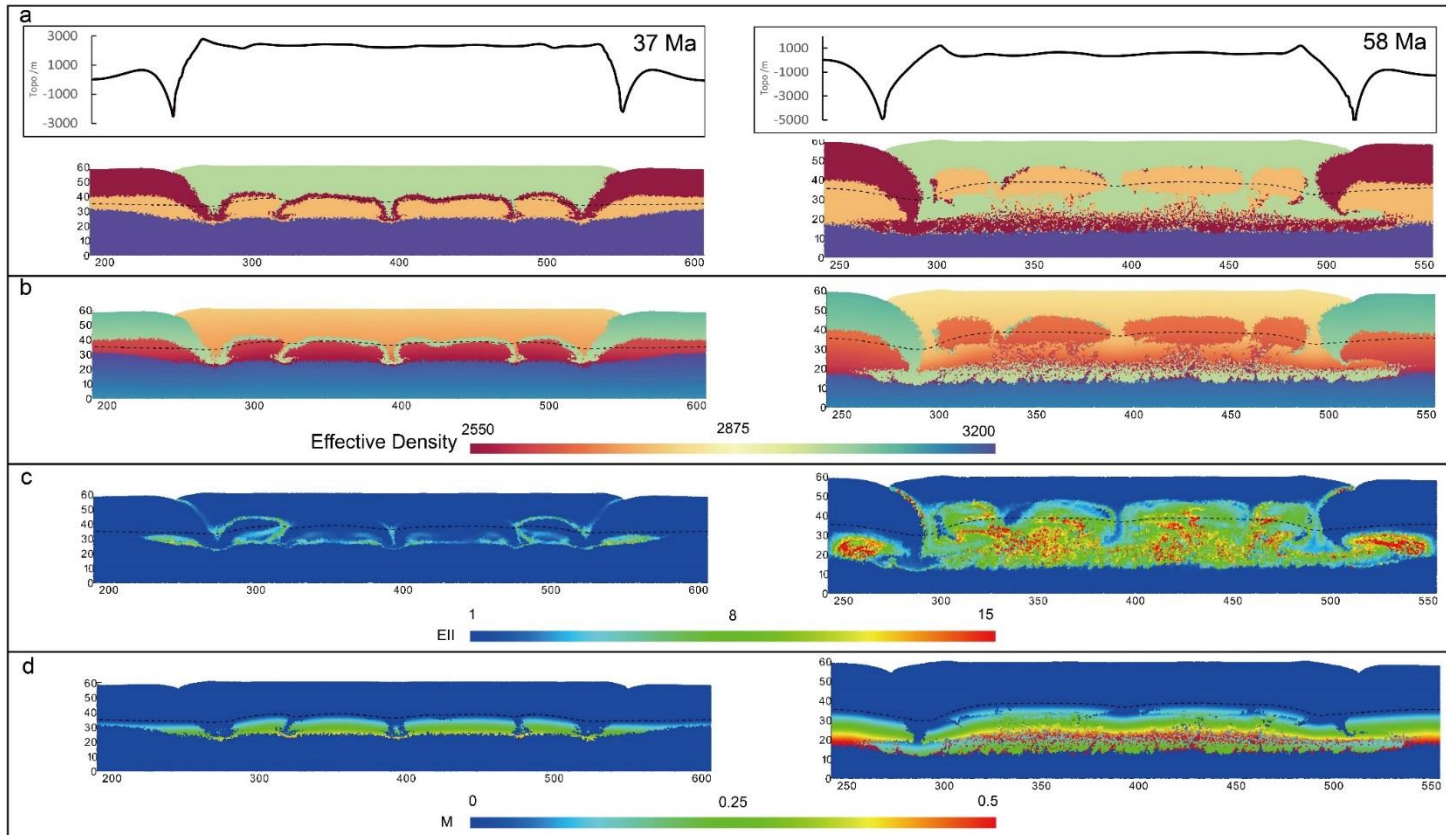


Figure 5. 12: Model M450, the width of sediment is set to 450 km. The solidus temperature of the lower crust is shown in dashed line. At 37 Ma, buoyant lower crustal rocks form four crustal-scale folds. Moderate-high pressure volcano-sedimentary rocks are preserved in three fold hinges. At 58 Ma, partially molten lower crustal rocks ascend into the weak sediment and form four diapirs with different sizes.

5.7. Discussion

5.7.1 The mantle potential temperature

Modern orogenic belts (the Alpine or Himalayan orogenic belts) are the loci of singular mineral transformations, proceeding at High-Pressure and Low-Temperature conditions. The proceeded conditions are within the blueschist and greenschist metamorphic facies series (Maluski and Matte, 1984; Okay, 1989; Maruyama et al., 1996; Prelević et al., 2013). The apparent lack of High-Pressure rocks before the Neoproterozoic time (1000-540 Ma) is still a key debate challenging the existence of modern subduction zones in the Archaean (ca. 4.00-2.50 Ga) and Paleoproterozoic (ca. 2.50-1.80 Ga) times (Ganne et al., 2012).

The mechanical strength of continental lithosphere evolves over geological time and space, and is primarily influenced by the secular cooling effect of T_p (Willett et al., 1993; Burg and Ford, 1997; Anderson, 2005; Mckenzie et al., 2005). The T_p in the WAC during the Eburnean Orogeny, ranges between 1500 and 1600 °C (Figure 5.4). Associating with the indication of a normal T_p cooling rate of 40-60 °C/Gyr (Abbott et al., 1994), this suggests that the T_p could probably reach about 1550-1700 °C in the Archaean time in the WAC. This is in good agreement with the global T_p estimates since ca. 0-4 Ga performed by Herzberg et al. (2010).

The maximum thickness of the lithosphere in West Africa is estimated between 300 and 350 km in the Archaean time and decreased to 200±50 km in the early Proterozoic time (Clouser and Langston, 1990; Qiu et al., 1996; Artemieva and Mooney, 2001). This decrease probably resulted from delamination processes. The thickness of the lithosphere in the early Proterozoic time is roughly in good agreement with the estimated thickness using the pressure of initial melting of primary magmas given in Figure 5.5 (ranging between 3.7 and 5.2 Gpa, corresponding to a depth of about 120-170 km in the WAC). The crust in Archaean province becomes thinner and less dense (De Beer and Meyer, 1984; Durrheim and Mooney, 1994) resulting from the thermal weakening of the underlying convective mantle (Ross et al., 2000; Korenaga, 2006). In some Paleoproterozoic regions, arcs form thickened crust. In the WAC, we suggest that the protracted magmatic activities prior to ca. 2.20 Ga were probably not sufficient to thicken the Birimian crust during the continental plate subduction. This was due to the fact that paleo-subduction slabs commonly dipped steeper (Abbott and Mooney, 1995) and shallower compared to present-day subduction processes (Choukroune et al., 1997; Van Hunen and Van den Berg, 2008). From ca. 2.15 Ga (corresponding to the D1 deformation phase during the Eburnean Orogeny), active margins were dominated by collisional processes (arcs amalgamation) rather than the previously dominant slab-driving subduction (arcs forming) processes (Baratoux et al., 2011; Ganne et al., 2014; Block et al., 2015). The collisional processes were characterized by the extensive occurrences of buckling and

folding resulting from shortening deformation phases (Pons et al., 1995; Pitra et al., 2010). This major geodynamic change further promoted the processes of crustal thickening and led to the formation of over 40 km (Block et al., 2015) thick Birimian crust.

5.7.2 A new tectonic scenario

In the Baoulé-Mossi domain, the dominant structures of greenstone-granitoid belts are shown in Figure 5.13a. The greenstone belts (thus the Ba-KM-GFBF, Ho-BM-OF and LW belts) were intruded and separated by several episodic pulses of granitoid intrusions made of small increments during the Eburnean Orogeny (more details on radiometric ages of granitoids can be found in Baratoux et al., 2011). Different tectonic models used to account for the structural evolution in the Nassian and Western Burkina Faso domains were proposed by Vidal et al. (2009) and Baratoux et al. (2011), respectively (Figures 5.13b and 5.13c). The main difference between the two tectonic models is the role of compressional versus gravitational forces in deforming the greenstone-granitoid belts. The granitoid intrusions between adjacent belts are 30-90 km wide (indicated by yellow dotted ellipses in Figure 5.13a). The mechanisms of the formation of such granitoids and their origins are still an open question due to the debates turning around the geodynamic and tectonic regimes in the WAC.

Our results (Model450, Figure 5.14a) show that four diapirs widely spread in the middle crust and are mechanically capped by the upper crust. The uplift increases in a relatively constant and low rate in the period of t_0 - t_2 (Figure 5.14b), characterizing the process of folding. Subsequently, uplift increases in a high rate as a result of the occurrences of exhumation. High-strain zones ($E_{II} = 0.5$, yellow ellipses in Figure 5.14c, about 30-50 km wide) are observed above the two major diapirs (rise 2 and rise 3). There is an offset of 30-50 km between the diapirs axis and the high strain zones.

According to the numerical results, we here suggest a geodynamic scenario to shed new light on the evolution of greenstone-granitoid belts (Figure 5.15). The model suggests that a very high melt fraction of granitoids (possibly derived from either subducted mélanges, lower crust and/or mantle melting, Moyen, 2011) would be accumulated at depth of subcontinental mantle. Due to the fact that the gravitational instabilities resulting from density and viscosity contrasts (Ganne et al., 2014) become significant as compression continues, the granitoids would ascend and intrude into the upper crust through some potentially weak zones. In our models, high strain zones (Figures 5.7c-5.12c) are largely produced within the diapirs. The diapirs are made of upper solidified lids and lower partially molten materials as a result of the distribution of the solidus temperature of the lower crust (Figures 5.12 and 5.15). This indicates that the granitoids (red flows in Figure 5.15) would canalize along the partially molten parts of diapirs before feeding the upper crust. When the granitoids arrive at the solidified lids of the diapirs (dark blue segments in Figure 5.15), they could not directly intrude the upper crust due

5. A numerical study of exhumation modes in the WAC during regional compression

to the high resistance of solidified lids of diapirs to deformation. Therefore, some potential weaknesses would be required to channelize the granitoids into the upper crust.

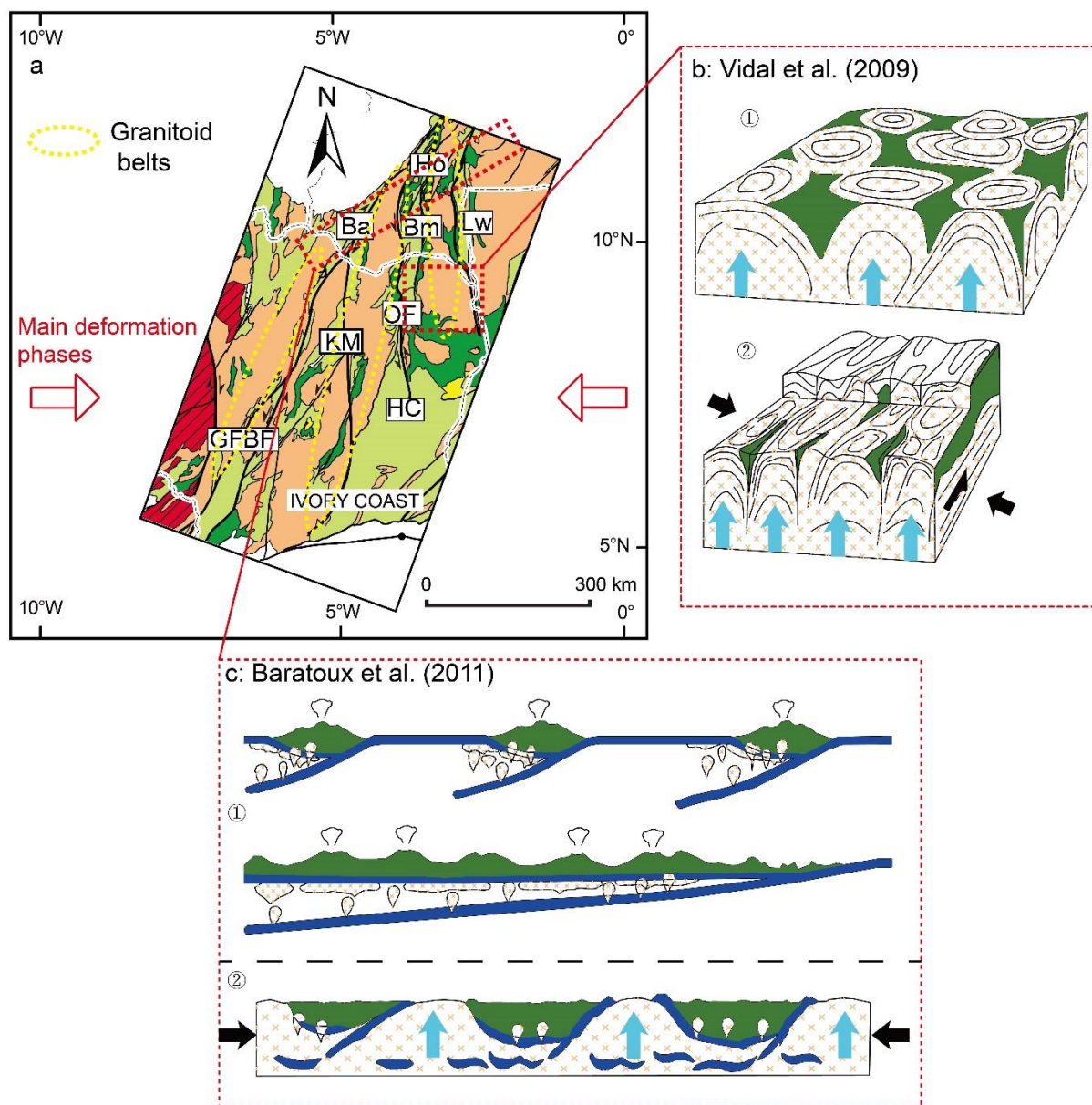


Figure 5. 13: (a) Greenstone-granitoid belts, together with two representative tectonic models (Vidal et al., 2009; Baratoux et al., 2011). Yellow dotted ellipses are used to locate granitoid intrusions. Red arrows represent the orientation of main deformation phases in compression during the Eburnean Orogeny. (b) "Dorm and basin" structure resulting from upwelling diapirs, insights from the study in the Nassian domain (after Vidal et al., 2009). (c) The tectonic model accounting for the evolution of deformation in Western Burkina Faso was suggested by Baratoux et al. (2011).

Over the compressional stage, a large amount of strains are concentrated in volcano-sedimentary rocks which are mostly preserved in between the diapirs. These preserved volcano-sedimentary rocks must be mechanically weak compared to the solidified lids of diapirs (Figures 5.14 and 5.15). Therefore, we

5. A numerical study of exhumation modes in the WAC during regional compression

suggest that the ascending granitoids capped by the solidified lids of diapirs would favour migrating horizontally and intruding into the upper crust via the weakness zones between diapirs (numerical results shown in Figure 5.14, diagram shown in Figure 5.15). When the granitoids pass through the weakness zones, high strain zones (Figure 5.14c) produced above the weakness zones between diapirs in upper crust would become preferential reservoirs/sites (granitoids areas filled by dashes in Figure 5.15) for emplacement of the granitoids (they constitute the so-called granitoid belts).

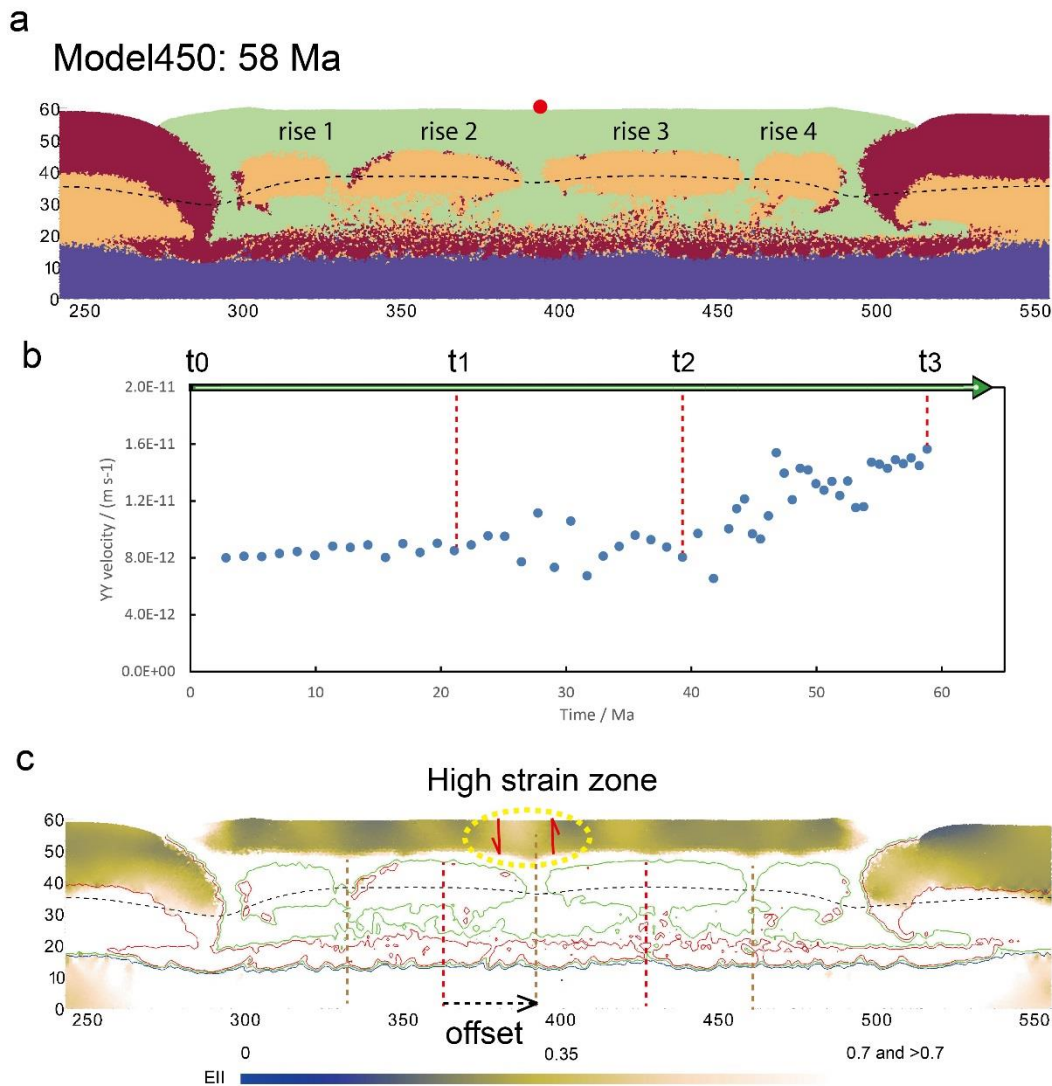


Figure 5. 14: (a) Numerical results of Model450 (see detailed info in Figure 5.12). We shortly name the diapirs as rise 1, rise 2, rise 3 and rise 4 from left to right sides for the purposes of the discussion. The solidus temperature of the lower crust is marked by black dotted line. (b) The impact of the lower crust exhumation on the process of uplift. (Point is indicated by red point in Figure a). (c) The accumulation (EII) of the second invariant of the strain rate is employed to identify fast/slow shear strain rate over time (58 Ma) in the upper crust (about 10-20 km thick). Solid colour lines represent the boundaries of different materials/states. There is an offset of 30-50 km

between diapir axis (in the middle crust) and high strain zones in the upper crust. The high strain zones would favour the emplacement of dome-like granitoid bodies.

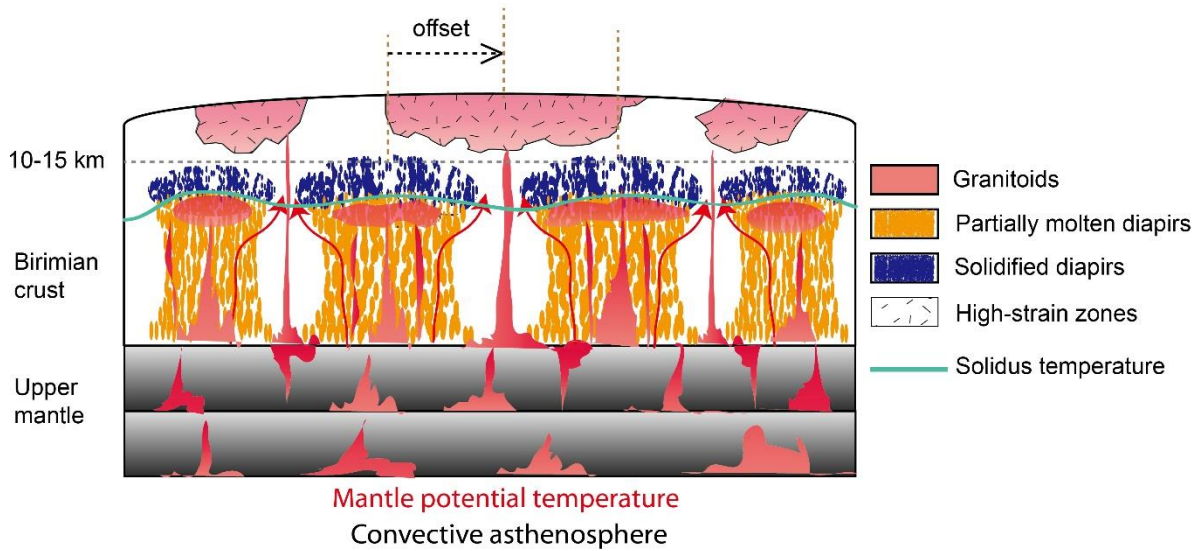


Figure 5. 15: Sketching the scenario of greenstone-granitoid belts during the Eburnean Orogeny. Diapirs are made of upper solidified lids and partially molten lower crust rocks. This feature results from the distribution of solidus temperature of the lower crust (light green line) according to the numerical results in Figure 5.14. We suggest that a series of sheet-like granitoids possibly derived from either subducted mélanges, lower crust and/or mantle melting (Moyen, 2011) accumulated at depths of the subcontinental mantle would canalize along diapirs before feeding the upper crust. When the granitoids arrive at the solidified lids of the diapirs, they would favour migrating horizontally and intruding into the upper crust through weakening zones between the diapirs. This model also suggests a dissymmetry of structures between the upper and middle-lower segments of crust, with the dome-like granitoids overlying high-grade sedimentary synforms and high-grade diapirs underlying low-grade greenstone belts. Red = granitoids; orange= partially molten materials of diapirs (lower part); blue = solidified lids of diapirs (upper segment); light green line = solidus temperature of lower crust (Figure 5.14c).

5.7.3 Implications for the Birimian crust

The granitoids (plutonic activities) play a dominant role in continental growth throughout geological time (Rudnick, 1995; Smithies and Champion, 2000; Martin et al., 2005; Baratoux et al, 2011; Moyen et al., 2011). Granitoids can either be derived from the melting of subduction slabs (Martin, 1986; Martin et al., 2005, 2009), re-melting in the progressively thickened lower mafic crust (Condie, 2005; Zhao et al., 2008; Huang et al, 2009) and mantle melting. However, in the Birimian terrane, the origin of granitoids remains hugely uncertain due to the fact that the geodynamic and tectonic regimes is still a matter of debate. In terms of the spatial-temporal evolution of greenstone-granitoid belts in the WAC, if we agree with the model (Figure 5.15), this indicates that the pluton bodies in this region are assembled by a series of sheet-like intrusions (constituted by many continuous small magmatic pulses).

This sheet-like intrusions model coincides well with our field works according to geochronological data (more detailed radiometric ages of rocks can be found in Baratoux et al., 2011).

This model also suggests that the diapirs (made of lower crustal rocks) produced by Ganne et al. (2014) and by this present work might be widely emplaced in the middle crust. The geometry of the solidified lids of the diapirs would have a significant impact on migration and percolation of granitoids. At the same time, a dissymmetry of structures is suggested between the upper and middle-lower segments of crust, with the dome-like granitoids overlying high-grade sedimentary synforms and high-grade diapirs underlying low-grade greenstone belts (Figure 5.15).

A partial melting zone, fuelled by burial of felsic materials, is partially redistributed as a result of gravitational instabilities in the middle crust. The partially molten rocks (lower crustal sources) blocked at a depth of about 10-15 km in the middle crust, creating a retention zone, which could have contributed to a mechanical decoupling between the upper and middle crust (Vanderhaeghe and Teysier, 2001). Such a partitioning of the crust, preventing the recycling of early formed rocks, could explain the local preservation of cold thermal gradients (10-15 °C/ km) in some parts of the Birimian terranes (Ganne et al., 2012) as well as some archaic feature (dome and basin architecture in the Tera area in Niger). Conversely, this mechanical isolation could have progressively led to a chemical homogenization in the middle and lower parts of the Birimian crust.

5.7.4 Limitations and perspectives

In order to improve the model assumptions, we aim to develop asymmetric models by including asymmetric volcano-sedimentary basins (Maierová et al., 2014). This improvement will help to reveal more realistic patterns of deformation of greenstone-granitoid belts. For partial melting, it was modelled by a linear function of temperature (Gerya et al., 2008; Ganne et al., 2014). In future models, we aim to fully output the metamorphic data calculated with the Perple-x code and directly input it into the numerical model. This can hugely improve the relationship between partial melting and temperature of rocks. In addition, more parametric tests (i.e. viscosity and density contrasts) and field constraints (geophysics, geochemistry, radiometric dating and coupling the upwelling processes of granitoids) should be taken into account in future models.

Regarding the decreasing effect of viscosity due to partial melting, Vanderhaeghe, (2001) revealed that the effective viscosity of partially molten rocks ranges between 10^6 ($M=1$) and 10^{18} Pa s ($M=0.1$). In the present paper, the effective viscosity of partially molten material is still overestimated and ranges between 6×10^{17} Pa s ($M=1$) and 8×10^{18} Pa s ($M=0.1$) (Ganne et al., 2014). According to the difference in viscosity of partially molten rocks between our models and natural cases, the deformation of molten rocks in the models must show more resistance to deformation compared to natural cases (Bittner and

Schmeling, 1995). The overestimated viscosity of the partially molten rocks also indicates that the solidified lids of the diapirs produced in this study (Figure 5.15) may be emplaced in some regions at depths shallower than the depth presented in the model (10-15 kms deep).

High strain zones are always thought to play a significant role in dragging fluid and feeding the upper crust from deeper sources. However, the numerical model presented here still cannot model the transfer process of fluid due to the present software limitation (Feng et al., 2016a, 2016b). This limitation can be improved in the near future if we could employ a two-phase fluid-solid software package (Keller et al., 2013).

5.8 Conclusions

In this study, we reported the T_p estimates for the WAC during the Eburnean Orogeny (ca. 2.20-2.00 Ga). The T_p results yield 1500-1600 °C. The pressures of initial (P_i) and final (P_f) melting yield about 3.7-5.2 GPa (corresponding to a depth of about 120-170 km) and 1-1.3 GPa, respectively. Melt fraction for accumulated fractional melting ranges between 0.29 and 0.34.

In this study, 2D thermo-mechanical models were used to explore the impact of volcano-sedimentary basin on the geometrical evolution of diapirs made of lower crustal rocks under compression. The models show that the thin mafic crust layer beneath the sediment is deformed into a large buckle fold during the early compressional stage, with a constant rate of uplift. Subsequently, relief grows in an increasing rate when the emplacement of diapirs occurs. Finally, we suggest a model to account for the evolution of deformation of greenstone-granitoid belts in the WAC during the Eburnean Orogeny (ca. 2.20-2.00 Ga). This model suggests that, a series of sheet-like granitoid flows possibly derived from subducted mélanges, lower crust and/or mantle melting accumulated at depths of subcontinental mantle would channel along the diapirs before feeding the upper crust. When the granitoids arrive at the solidified lids of diapirs, they would favour migrating horizontally and intruding into the upper crust through the weakening zones between diapirs.

This model also suggests an asymmetry of structures between the upper and middle-lower crust, with the dome-like granitoids overlying high-grade sedimentary synforms and high-grade diapirs underlying low-grade greenstone belts. High grade partially molten rocks may be widely capped by a resistant upper crust at a depth of about 10-15 km in the Leo-Man Shield.

5.9 Acknowledgements

Mark Jessell is warmly thanked for fruitful discussions and encouragements at different stages of the paper. We thank the development teams at the Victorian Partnership for Advanced Computing (VPAC) and Monash University for technical assistance with the software *Underworld*. This work was granted access to the High-Performance Computing resources of both the French supercomputing centre, CCRT of the French Nuclear Agency, under allocations #2014-046351 and #2015-046351 awarded by GENCI (Grand Equipement National de Calcul Intensif), and the regional computing centre, CALMIP in Toulouse, France, under allocation #P1403. We also thank the GEOROC (<http://georoc.mpch-mainz.gwdg.de/georoc/>) and WAXI project groups for kindly providing mafic magma dataset. Figures are plotted using open source package Visit developed by the Lawrence Livermore National Laboratory. X.F. thanks the Chinese Scholarship Council for his PhD scholarship.

5.10 Appendix

Table S1

Table 5.SI. The bulk compositions of original samples used to estimate the T_p in the WAC (around ca. 2.20 - 2.10 Ga).

Reference	Hirdes et al. 2007	Ama Salah et al. 1996	Thomas et al. 2009	Galipp et al. 2003	Ama Salah et al. 1996	Soumaila. 2000	Soumaila. 2000
Sap_ID	1074	AS-393	EC2036	KG 18	AS-5	755	810
Location	Ghana Sefwi Belt	Niger Nigerian iptako	Ghana Wa-Larwa Belt	Ghana Sefwi Belt	Niger Nigerian Liptako	Niger Nigerian Liptako (Zawa Tondi)	Niger Nigerian Liptako (Zawa Tondi)
Rock type	BASALT	BASALT	BASALT	BASALT	BASALT	BASALT	BASALT
lat	6	13.5	9.666	6.08	13.5	14	14
long	-2.8	1.5	-2.46	-2.95	1.5	1	1
SiO ₂	49.34	50.29	50.13	50.62	49.18	50.18	51.06
TiO ₂	0.343	0.31	0.44	0.62	0.28	0.55	0.53
Al ₂ O ₃	14.58	16.25	14.06	14.23	14.03	14.24	13.3
FeO _{Total}	9.09	8.657071	9.4	9.64	10.57303	9.135	8.856
MnO	0.164	0.16	0.162	0.17	0.19	0.16	0.17
MgO	8.64	7.97	9.77	8.62	9.64	9.03	8.79
CaO	13.009	12.84	13.21	12.39	12.66	12.41	11.95
Na ₂ O	2	1.4	1.46	1.85	1.23	1.43	2.42
K ₂ O	0.188	0.01	0.28	0.1	0.08	0.13	0.32
P ₂ O ₅	0.034	0.04	0.03	0.07	0.14	0.16	0.15
LOI	2.1	2.31	0	1.82	1.91	1.47	1.33

5.11 References

- Abbott, D., Burgess, L., Longhi, J., Smith, W. H., 1994. An empirical thermal history of the Earth's upper mantle. *Journal of Geophysical Research* 99, 835-13.
- Abbott, D., Mooney, W., 1995. The structural and geochemical evolution of the continental crust: support for the oceanic plateau model of continental growth. *Reviews of Geophysics* 33, 231-242.
- Agyei Duodu, J., Loh, G.K., Boamah, K.O., 2009. Geological map of Ghana 1:1 000 000. Geological Survey Department of Ghana (GSD).
- Ama Salah, I., Liegeois, J. P., Pouclet, A., 1996. Evolution of a Birimian oceanic island arc of Nigerian Iptako (Sirba): geology, geochronology and geochemistry. *Journal of African earth science* 22, 235-254.
- Amponsah, P.O., Salvi, S., Béziat, D., Siebenaller, L., Baratoux, L., Jessell, M.W., 2015. Geology and geochemistry of the shear hosted Julie deposit, NW Ghana. *Journal of African Earth Science* 112, 505-523.
- Anderson, D. L., 2005. Large igneous provinces, delamination, and fertile mantle. *Elements* 1, 271-275.
- Artemieva, I. M., Mooney, W. D., 2001. Thermal thickness and evolution of Precambrian lithosphere: a global study. *Journal of Geophysical Research: Solid Earth (1978-2012)*, 106 (B8), 16387-16414.
- Baratoux, L., Metelka, V., Naba, S., Jessell, M. W., Grégoire, M., Ganne, J., 2011. Juvenile Paleoproterozoic crust evolution during the Eburnean orogeny (~2.2-2.0Ga), western Burkina Faso. *Precambrian Research* 191, 18-45.
- Bittner, D., Schmeling, H., 1995. Numerical modelling of melting processes and induced diapirism in the lower crust. *Geophysical Journal International* 123, 59-70.
- Block, S., Ganne, J., Baratoux, L., Zeh, A., Parra-Avila, A. L., Jessell, M., Ailleres, L., Siebenaller, L., 2015. Petrological and geochronological constraints on lower crust exhumation during Paleoproterozoic (Eburnean) orogeny, NW Ghana, West African craton. *Journal of Metamorphic Geology* 33, 463-494.
- Boher, M., Abouchami, W., Michard, A., Albarede, F., Arndt, N. T., 1992. Crustal growth in West Africa at 2.1 Ga. *Journal of Geophysical Research: Solid Earth (1978-2012)* 97, 345-369.

5. A numerical study of exhumation modes in the WAC during regional compression

- Bose, P.K., Eriksson, P.G., Sarkar, S., Wright, D.T., Samanta, P., Mukhopadhyay, S., Mandal, S., Banerjee, S., Altermann, W., 2012. Sedimentation patterns during the Precambrian: A unique record? *Marine and Petroleum Geology* 33, 34-68.
- Burg, J. P., Ford, M., 1997. Orogeny through time: an overview. Geological Society, London, Special Publications 121, 1-17.
- Catuneanu, O., Eriksson, P.G., 2007. Sequence stratigraphy of the Precambrian. *Gondwana Research* 12, 560-565.
- Catuneanu, O., Martins-Neto, M. a., Eriksson, P.G., 2005. Precambrian sequence stratigraphy. *Sedimentary Geology* 176, 67-95.
- Chardon, D., Choukroune, P., Jayananda, M., 1996. Strain patterns, décollement and incipient sagducted greenstone terrains in the Archaean Dharwar craton (south India). *Journal of Structural Geology* 18, 991-1004.
- Chardon, D., Peucat, J. J., Jayananda, M., Choukroune, P., Fanning, C. M., 2002. Archaean granite-greenstone tectonics at Kolar (south India): Interplay of diapirism and bulk inhomogeneous contraction during juvenile magmatic accretion. *Tectonics*, 21 (3).
- Choukroune, P., Ludden, J.N., Chardon, D., Calvert, A.J., Bouhallier, H., 1997. Archaean crustal growth and tectonic processes; a comparison of the Superior Province, Canada and the Dharwar Craton, India. *Geological Society Special Publications* 121, 63-98.
- Clouser, R. H. Langston, C. A., 1990. Upper mantle structure of southern Africa from P waves. *Journal of Geophysical Research: Solid Earth (1978-2012)* 95, B11, 17403-17415.
- Condie, K. C., 1994. Greenstones through time. Archaean crustal evolution. Vol. 11. Elsevier Amsterdam, 85-120.
- Condie, K. C., 2005. TTGs and adakites: are they both slab melts? *Lithos* 80, 33-44.
- Condie, K. C., 2013. Plate tectonics & crustal evolution. Elsevier. Pp. 99-104.
- De Beer, J. H., Meyer, R., 1984. Geophysical characteristics of the Namaqua-Natal Belt and its boundaries, South Africa. *Journal of geodynamics* 1, 473-494.
- De Kock, G. S., Armstrong, R. A., Siegfried, H. P., Thomas, E., 2011. Geochronology of the Birim Supergroup of the West African craton in the Wa-Bolé region of west-central Ghana: Implications for the stratigraphic framework. *Journal of African Earth Sciences* 59, 1-40.
- De Smet, J., Berg, A. Van den, Vlaar, N., 1998. Stability and growth of continental shields in mantle convection models including recurrent melt production. *Tectonophysics* 296, 15-29.

- Dioh, E., Béziat, D., Debat, P., Grégoire, M., Ngom, P.M., 2006. Diversity of the Palaeoproterozoic granitoids of the Kédougou inlier (eastern Sénégal): Petrographical and geochemical constraints. *Journal of African Earth Science* 44, 351-371.
- Doumbia, S., Pouclet, A., Kouamelan, A., Peucat, J. J., Vidal, M., Delor, C., 1998. Petrogenesis of juvenile-type Birimian (Paleoproterozoic) granitoids in Central Côte-d'Ivoire, West Africa: geochemistry and geochronology. *Precambrian Research* 123, 47-65.
- Durrheim, R. J., Mooney, W. D., 1994. Evolution of the Precambrian lithosphere: seismological and geochemical constraints. *Journal of Geophysical Research: Solid Earth (1978-2012)*, 99 (B8), 15359-15374.
- Eriksson, P.G., Banerjee, S., Catuneanu, O., Sarkar, S., Bumby, a. J., Mtimkulu, M.N., 2007. Prime controls on Archaean-Palaeoproterozoic sedimentation: Change over time. *Gondwana Research* 12, 550-559.
- Eriksson, P.G., Condie, K.C., Tirsgaard, H., Mueller, W.U., Altermann, W., Miall, a. D., Aspler, L.B., Catuneanu, O., Chiarenzelli, J.R., 1998. Precambrian clastic sedimentation systems. *Sedimentary Geology* 120, 5-53.
- Feng, X., Amponsah, P. O., Martin, R., Ganne, J., Jessell, M. W., 2016a. 3-D numerical modelling of the influence of pre-existing faults and boundary conditions on the distribution of deformation: example of North-Western Ghana. *Precambrian Research* 274, 161-179.
- Feng, X., Jessell, M. W., Amponsah, P. O., Martin, R., Ganne, J., Liu, D., Batt, E. G., 2016b. Effect of strain-weakening on Oligocene-Miocene self-organization of the Australian-Pacific plate boundary fault in southern New Zealand: insights from numerical modelling. *Journal of Geodynamics*, doi: 10.1016/j.jog.2016.03.002.
- Feybesse, J. L., Billa, M., Guerrot, C., Duguey, E., Lescuyer, J. L., Milesi, J. P., Bouchot, V., 2006. The paleoproterozoic Ghanaian province: Geodynamic model and ore controls, including regional stress modeling. *Precambrian Research* 149, 149-196.
- Galipp, K., Klemd, R., Hirdes, W., 2003. Metamorphism and geochemistry of the Paleoproterozoic Birimian Sefwi volcanic belt (Ghana, West Africa). *Geologisches Jahrbuch D111*, 151-191.
- Ganne, J., De Andrade, V., Weinberg, R.F., Vidal, O., Dubacq, B., Kagambega, N., Naba, S., Baratoux, L., Jessell, M., Allibon, J., 2012. Modern-style plate subduction preserved in the Palaeoproterozoic West African craton. *Nature Geoscience* 5, 60-65.
- Ganne, J., Gerbault, M., Block, S., 2014. Thermo-mechanical modeling of lower crust exhumation— Constraints from the metamorphic record of the Palaeoproterozoic Eburnean orogeny, West

- African Craton. *Precambrian Research* 243, 88-109.
- Gerya, T. V., Perchuk, L. L., Burg, J. P., 2008. Transient hot channels: Perpetrating and regurgitating ultrahigh-pressure, high-temperature crust-mantle associations in collision belts. *Lithos* 103, 236-256.
- Gerya, T. V., Yuen, D.A., 2003. Rayleigh - Taylor instabilities from hydration and melting propel "cold plumes" at subduction zones. *Earth and Planetary Science Letters* 212, 47-62.
- Glazner, a. F., Bartley, J.M., Coleman, D.S., Gray, W., Taylor, R.Z., 2004. Are plutons assembled over millions of years by amalgamation from small magma chambers? *GSA Today* 14, 4-11.
- Gorman, B.E., Pearce, T.H., Birkett, T.C., 1978. On the structure of Archaean greenstone belts. *Precambrian Research* 6, 23-41.
- Hein, K. A. A., 2010. Succession of structural events in the Goren greenstone belt (Burkina Faso): implications for West African tectonics. *Journal of African Earth Sciences* 56, 83-94.
- Herzberg, C., 2011. Basalts as temperature probes of Earth's mantle. *Geology* 39, 1179-1180.
- Herzberg, C., Asimow, P. D., 2008. Petrology of some oceanic island basalts: PRIMELT2. XLS software for primary magma calculation. *Geochemistry, Geophysics, Geosystems* 9, Q09001, doi: 10.1029/2008GC002057.
- Herzberg, C., Asimow, P. D., 2015. PRIMELT3 MEGA. XLSM software for primary magma calculation: Peridotite primary magma MgO contents from the liquidus to the solidus. *Geochemistry, Geophysics, Geosystems* 16, 563-578.
- Herzberg, C., Condie, K., Korenaga, J., 2010. Thermal history of the Earth and its petrological expression. *Earth Planetary Science Letters* 292, 79-88.
- Hirdes, W., Davis, D.W., Lüdtke, G., Konan, G., 1996. Two generations of Birimian (Paleoproterozoic) volcanic belts in northeastern Côte d'Ivoire (West Africa): consequences for the "Birimian controversy." *Precambrian Research* 80, 173-191.
- Hirdes, W., Konan, K.G., N'Da, D., Okou, A., Sea, P., Zamble, Z.B., Davis, D.W., 2007. Geology of the Northern Portion of the Oboisso Area, Côte d'Ivoire. Sheets 4A, 4B, 4B BIS, 4. Direction de la Géologie, Abidjan, Côte d'Ivoire and Bundesanstalt für Geowissenschaften und Rohstoffe, Hanover.
- Huang, X. L., Xu, Y. G., Lan, J. B., Yang, Q. J., Luo, Z. Y., 2009. Neoproterozoic adakitic rocks from Mopanshan in the western Yangtze Craton: Partial melts of a thickened lower crust. *Lithos* 112, 367-381.

5. A numerical study of exhumation modes in the WAC during regional compression

- Jessell, M. W., Amponsah, P. O., Baratoux, L., Asiedu, D. K., Loh, G. K., Ganne, J., 2012. Crustal-scale transcurrent shearing in the Paleoproterozoic Sefwi-Sunyani-Comoé region, West Africa. *Precambrian Research* 212-213, 155-168.
- Jessell, M. W., Begg, G. C., Miller, M. S., 2016. The geophysical signatures of the West African Craton. *Precambrian Research* 274, 3-24.
- Keller, T., May, D. A., Kaus, B. J., 2013. Numerical modelling of magma dynamics coupled to tectonic deformation of lithosphere and crust. *Geophysical Journal International* 195, 1406-1442.
- Korenaga, J., 2006. Archaean geodynamics and the thermal evolution of Earth. *Geophysical Monograph-American Geophysical Union* 164, 7-32.
- Leube, A., Hirdes, W., Mauer, R., Kesse, G.O., 1990. The early Proterozoic Birimian Supergroup of Ghana and some aspects of its associated gold mineralization. *Precambrian Research* 46, 139-165
- Lompo, M., 2009. Geodynamic evolution of the 2.25-2.0 Ga Palaeoproterozoic magmatic rocks in the Man-Leo Shield of the West African Craton. A model of subsidence of an oceanic plateau. *Geological Society, London, Special Publications* 323, 231-254.
- Lüdtke, G., Hirdes, W., Konan, G., Koné, Y., Yao, C., Diarra, S., Zamblé, Z., 1998. Géologie de la région Haute Comoé Nord—feuilles Kong (4b et 4d) et Téhini-Bouna (3a à 3d). *Direction de la Géologie Abidjan Bulletin*, 178
- Maierová, P., Lexa, O., Schulmann, K., Štípská, P., 2014. Contrasting tectono-metamorphic evolution of orogenic lower crust in the Bohemian Massif: A numerical model. *Gondwana Res.* 25, 509–521.
- Maluski, H., Matte, P., 1984. Ages of alpine tectonometamorphic events in the northwestern Himalaya (northern Pakistan) by $^{39}\text{Ar}/^{40}\text{Ar}$ method. *Tectonics* 3, 1-18.
- Martin, H., 1986. Effect of steeper Archaean geothermal gradient on geochemistry of subduction-zone magmas. *Geology* 14, 753-756.
- Martin, H., Moyen, J. F., Rapp, R., 2009. The sanukitoid series: magmatism at the Archaean-Proterozoic transition. *Earth and Environmental Science Transactions of the Royal Society of Edinburgh* 100, 15-33.
- Martin, H., Smithies, R. H., Rapp, R., Moyen, J. F., Champion, D., 2005. An overview of adakite, tonalite-trondhjemite-granodiorite (TTG), and sanukitoid: relationships and some implications for crustal evolution. *Lithos* 79, 1-24.
- Maruyama, S., Liou, J.G., Terabayashi, M., 1996. Blueschists and Eclogites of the World and Their Exhumation. *International Geological Review* 38, 485-594.

- Mckenzie, D., Jackson, J., Priestley, K., 2005. Thermal structure of oceanic and continental lithosphere. *Earth and Planetary Science Letters* 233, 337-349.
- Milési, J. P., Ledru, P., Feybesse, J. L., Dommange, A. Marcoux, E., 1992. Early Proterozoic ore deposits and tectonics of the Birimian orogenic belt, West Africa. *Precambrian Research* 58, 305-344.
- Milési, J.P., Feybesse, J.L. Pinna, P. et al., 2004. Geological map of Africa 1:10,000,000, SIGAfrique project. In: 20th Conference of African Geology. BRGM, Orleans, France, 2-7 June. Available at: <http://www.sigafrique.net>.
- Miller, C.F., Watson, E.B., and Harrison, T.M., 1988, Perspectives on the source, segregation and transport of granitoid magmas: *Transactions of the Royal Society of Edinburgh: Earth Sciences* 79, 135-156.
- Moresi, L. N., Solomatov, V. S., 1995. Numerical investigation of 2D convection with extremely large viscosity variations. *Physics of Fluids (1994-present)* 7, 2154-2162.
- Moresi, L., Dufour, F., Mühlhaus, H. B., 2003. A Lagrangian integration point finite element method for large deformation modeling of viscoelastic geomaterials. *Journal of Computational Physics* 184, 476-497.
- Moresi, L., Quenette, S., Lemiale, V., Meriaux, C., Appelbe, B., Mühlhaus, H., 2007. Computational approaches to studying non-linear dynamics of the crust and mantle. *Physics of the Earth and Planetary Interior* 163, 69-82.
- Moyen, J. F., 2011. The composite Archaean grey gneisses: petrological significance, and evidence for a non-unique tectonic setting for Archaean crustal growth. *Lithos* 123, 21-36.
- Oberthür, T., Vetter, U., Davis, D.W., Amanor, J.A., 1998. Age constraints on gold mineralization and Paleoproterozoic crustal evolution in the Ashanti belt of southern Ghana. *Precambrian Research* 89, 129-143.
- Okay, A. I., 1989. Alpine-Himalayan blueschists. *Annual Review of Earth and Planetary Sciences* 17, 55-87.
- Petford, N., Cruden, A. R., McCaffrey, K. J. W., Vigneresse, J. L., 2000. Granite magma formation, transport and emplacement in the Earth's crust. *Nature* 408, 669-673.
- Pons, J., Barbey, P., Dupuis, D. Leger, J.M., 1995. Mechanisms of pluton emplacement and structural evolution of a 2.1 Ga juvenile continental crust: the Birimian of southwestern Niger. *Precambrian Research* 70, 281-301.
- Prelević, D., Jacob, D. E., Foley, S. F., 2013. Recycling plus: a new recipe for the formation of Alpine-

- Himalayan orogenic mantle lithosphere. *Earth and Planetary Science Letters* 362, 187-197.
- Putirka, K. D., Perfit, M., Ryerson, F. J., Jackson, M. G., 2007. Ambient and excess mantle temperatures, olivine thermometry, and active vs. passive upwelling. *Chemical Geology* 241, 177-206.
- Qiu, X., Priestley, K., McKenzie, D., 1996. Average lithospheric structure of southern Africa. *Geophysical Journal International* 127, 563-581.
- Ranalli, G., 1995. *Rheology of the Earth*. Springer Science & Business Media. pp. 413.
- Rey, P. F., Teyssier, C., Whitney, D. L., 2009. The role of partial melting and extensional strain rates in the development of metamorphic core complexes. *Tectonophysics* 477, 135-144.
- Ross, G. M., Eaton, D. W., Boerner, D. E., Miles, W., 2000. Tectonic entrapment and its role in the evolution of continental lithosphere: an example from the Precambrian of western Canada. *Tectonics* 19, 116-134.
- Rudnick, R. L., 1995. Making continental crust. *Nature* 378, 571-577.
- Smithies, R. H., Champion, D. C., 2000. The Archaean high-Mg diorite suite: links to tonalite-trondhjemite-granodiorite magmatism and implications for early Archaean crustal growth. *Journal of Petrology* 41, 1653-1671.
- Soumaila, A., 2000. Etude structurale, pétrographique et géochimique de la ceinture birimienne de Diaborou-Darbani Liptako, Niger occidental (Afrique de l'ouest). (Grenoble Thèses; 94930)
- Tackley, P. J., 2008. Modelling compressible mantle convection with large viscosity contrasts in a three-dimensional spherical shell using the yin-yang grid. *Physics of the Earth and Planetary Interiors* 171, 7-18.
- Thomas, E., De Kock, G.S., Baglow, N., Viljoen, J.H.A., Z.S., 2009. Geological map explanation map sheet 0903B (1:100,000). Mining Sector Support Programme. CGS, BRGM, Geoman, GSD, Accra.
- Thompson, R. N., Gibson, S. A., 2000. Transient high temperatures in mantle plume heads inferred from magnesian olivines in Phanerozoic picrites. *Nature* 407(6803), 502-506.
- Van Hunen, J., Van den Berg, A. P., 2008. Plate tectonics on the early Earth: limitations imposed by strength and buoyancy of subducted lithosphere. *Lithos* 103, 217-235.
- Vanderhaeghe, O., 2001. Melt segregation, pervasive melt migration and magma mobility in the continental crust: the structural record from pores to orogens. *Physics and Chemistry of the Earth, Part A: Solid Earth and Geodesy* 26, 213-223.

5. A numerical study of exhumation modes in the WAC during regional compression

- Vidal, M., Delor, C., Pouclet, A., Simeon, Y., Alric, G., 1996. Evolution géodynamique de l'Afrique de l'Ouest entre 2.2 Ga et 2 Ga; le style archéen' des ceintures vertes et des ensembles sédimentaires birimiens du nord-est de la Côte-d'Ivoire. *Bulletin de la Société géologique de France* 167, 307-319.
- Vidal, M., Gumiaux, C., Cagnard, F., Pouclet, A., Ouattara, G., Pichon, M., 2009. Evolution of a Paleoproterozoic weak type orogeny in the West African Craton (Ivory Coast). *Tectonophysics* 477, 145-159.
- Wang, K., Burov, E., Gumiaux, C., Chen, Y., Lu, G., Mezri, L., Zhao, L., 2015. Formation of metamorphic core complexes in non-over-thickened continental crust: A case study of Liaodong Peninsula (East Asia). *Lithos* 238, 86-100.
- Willett, S., Beaumont, C., Fullsack, P., 1993. Mechanical model for the tectonics of doubly vergent compressional orogens. *Geology* 21, 371-374.
- Zhao, J. H., Zhou, M. F., 2008. Neoproterozoic adakitic plutons in the northern margin of the Yangtze Block, China: partial melting of a thickened lower crust and implications for secular crustal evolution. *Lithos* 104, 231-248.

5. A numerical study of exhumation modes in the WAC during regional compression

Chapter 6

General conclusions and perspectives

6.1 General conclusions

6.1.1 Localization of deformation

Pre-existing faults within the crust acquired from past geological events can play a significant role in initializing the distribution and controlling the evolution of deformation. Such pre-existing faults can offer favoured sites for strain accumulation because of their function as a stress concentrator with respect to the host rock. In this thesis, different orientations of a system of branched strike-slip faults were studied. Under compression boundary conditions, the results show that the internal fault zones as well as the host rocks in between the faults behave as relatively weaker domains than the external regions. Under simple shear boundary conditions, we explored the process of self-organization of the Australian-Pacific plate boundary fault in southern New Zealand. The models show that deformation is focused along narrow high-strain shear zones in the centre of the model when the softening coefficients are high, whereas the strain is more diffuse with many shear zones spread over the model and possibly some high-strain shear zones focused near one border at lower softening coefficients

6.1.2 Exhumation of the lower crust

The emplacement of partially molten lower crust rocks is dominantly driven by the contrasts in density and viscosity compared to surrounding solid rocks. Pre-existing faults are thought to play an important role in influencing and promoting the processes of the emplacement. In this thesis, we also tested the role of pre-existing faults/basin in exhumation of the partially molten lower crust under different boundary conditions (including extension, transtension and compression).

- 1) Under extension, in the Eastern and Western parts of the high grade rock corridors in NW Ghana, partially molten rocks exhumed from the lower into middle-upper crustal levels are interpreted to have been dominantly facilitated by the km-scale high-strain corridors. In the central part of the Bole-Bulenga domain, the high grade rocks are interpreted to have been exhumed as a result of a coupling between two mechanisms: (1) the concentration of partially molten rocks between the Jirapa and Bole-Nangodi faults increases due to the reduction in space from north to south, (2) the concentration of lower partially molten rocks in the central part, as a result of inherited orthogonal (E-W) structures.
- 2) Under transtension, in the Sefwi terrane of SW Ghana, the Kukuom-Juaboso domain (KJD) composed of up to amphibolite-migmatite facies could result from the concentration of upwelling partially molten rocks in the relay zone between the Ketesso and Kenyase shear zones during transtension. The two shear zones probably underwent two main stages for growth and maturation from the D1 to D2 deformation phases. The regional exhumation of

the high grade rocks in the Sefwi terrane probably occurred within a duration of less than 5 Ma.

- 3) Under compression, the role of volcano-sedimentary basin on spatial-temporal evolution of the lower crust exhumation was tested. The models suggest that a series of sheet-like granitoids possibly derived from either subducted mélanges, lower crust and/or mantle melting accumulated at depths of the subcontinental mantle would channel along diapirs before feeding the upper crust. When the granitoids arrive at the solidified lids of the diapirs, they would favour migrating horizontally and intruding into the upper crust through weakening zones between the diapirs. This model also suggests an asymmetry of structures between the upper and middle-lower crust, with the dome-like granitoids overlying high-grade sedimentary synforms and high-grade diapirs underlying low-grade greenstone belts.

6.2 Limitations of the models and Perspectives

For all the models used in this thesis, the geometries of pre-existing shear zones, volcano-sedimentary basins are simplified. These simplifications may result in a reduction in the complexities of the interaction of inherited structures and strain localization compared to natural cases. In addition, all models used a visco-plastic material, in order to better constrain and improve the model, the effect of upper mantle and brittle shell (including elastic behaviour for upper continental crust) of the Earth could be taken into consideration. The numerical models presented here still cannot model fluid transfer processes due to the present limitation of software. This limitation could be improved if we employed a two-phase fluid-solid software package (Keller et al., 2013).

Regarding the decreasing effect of viscosity due to partial melting, Vanderhaeghe, (2001) showed that the effective viscosity of partially molten rocks ranges between 10^6 ($M=1$) and 10^{18} Pa s ($M=0.1$). In the present thesis, the effective viscosity of partially molten material is still overestimated, which ranges between 6×10^{17} Pa s ($M=1$) and 8×10^{18} Pa s ($M=0.1$) (Ganne et al., 2014). According to the difference in viscosity of partially molten rocks between our models and natural cases, the deformation of molten rocks in the models show more resistance to deformation compared to natural cases (Bittner and Schmeling, 1995). In order to improve the setup of the models, further geophysical and geochemical constraints (Moho depth, geochronological and petrological data, viscosity of partially molten rocks, stretching rate et al.) should be included.

6.3 References

- Bittner, D., Schmeling, H., 1995. Numerical modelling of melting processes and induced diapirism in the lower crust. *Geophysical Journal International*, 123, 59-70.
- Ganne, J., Gerbault, M., Block, S., 2014. Thermo-mechanical modeling of lower crust exhumation—

Constraints from the metamorphic record of the Palaeoproterozoic Eburnean orogeny, West African Craton. *Precambrian Research*, 243, 88-109.

Keller, T., May, D. A., Kaus, B. J., 2013. Numerical modelling of magma dynamics coupled to tectonic deformation of lithosphere and crust. *Geophysical Journal International*, 195, 1406-1442.

Vanderhaeghe, O., 2001. Melt segregation, pervasive melt migration and magma mobility in the continental crust: the structural record from pores to orogens. *Physics and Chemistry of the Earth, Part A: Solid Earth and Geodesy*, 26, 213-223.

6.4 Conclusions générales

6.4.1 La localisation de la déformation

L'existence de failles héritées dans la croûte peut jouer un rôle de premier ordre sur l'initialisation, la distribution et le contrôle de la déformation. De telles failles peuvent constituer des sites privilégiés pour l'accumulation de contraintes. Dans cette thèse, différentes orientations pour un système de décrochement en ramification ont été testées. Sous un régime compressif, les résultats montrent que les zones de failles internes, ainsi que les unités de roches présentes entre ces failles réagissent de façon plus fragile que les unités rocheuses présentes à l'extérieur de ces domaines. Pour le cas d'un régime de déformation en cisaillement simple, nous avons exploré le processus de réorganisation qui s'est produit aux limites de deux plaques (i.e. Australie et Pacifique) au sud de la Nouvelle-Zélande. Les modèles montrent que la déformation se concentre le long des zones de cisaillement étroites, situées au centre du modèle, lorsque les coefficients d'amollissement sont élevés. Inversement, la contrainte cisillante ressort de façon plus diffuse à travers le modèle lorsque les coefficients d'amollissement sont faibles. Les cisaillements s'expriment alors sur l'ensemble du modèle bien que les taux de cisaillement restent les plus élevés sur les bordures du modèle.

6.4.2 Exhumation de la croûte inférieure

L'exhumation de roches partiellement fondues issues de la croûte inférieure est guidée préférentiellement par des contrastes de densité et de viscosité avec l'encaissant non-fondu. Les failles héritées sont supposées jouer un rôle important dans les processus de redistribution de matière au sein de cette croûte. Dans cette thèse, nous avons aussi testé le rôle des failles ou des bassins hérités sur l'exhumation de la croûte inférieure partiellement fondue, en tenant compte de différentes conditions aux limites (extension, transtension et compression)

- 1) En contexte extensif, dans les portions Est et Ouest des corridors fortement métamorphisés du Nord-Ouest Ghana, des roches partiellement fondues, issues de la croûte inférieure, ont pu être exhumées au sein des croûtes moyenne à supérieure. Dans la partie centrale du domaine de Bolé-Bulenga, des roches très métamorphisées ont été exhumées grâce au couplage de deux mécanismes: (1) la concentration de roches partiellement fondues entre les failles de

Jirapa et de Bolé-Nangodi; ces failles convergent vers le sud, induisant un rétrécissement de l'espace disponible pour accueillir ce matériel fondu; (2) la concentration de roches partiellement fondues dans la partie centrale, induite par un jeu de failles héritées d'orientation Est-Ouest.

- 2) En contexte de transtension, dans le terrane de Sefwi au Sud-Ouest Ghana, le domaine de Kukuom-Juaboso (KJD), composé majoritairement par des roches à faciès de type amphibolite à migmatitique, semble s'être mis en place sous forme d'intrusions au sein d'une zone relais située entre les zones de cisaillements de Kenyase et de Ketéso. Ces deux zones de cisaillement sont marquées par un stade de croissance puis de maturation qui semblent être reliés aux phases de déformation D1 puis D2 reconnues régionalement. L'exhumation régionale des roches très métamorphisées dans le terrane de Sefwi s'est probablement produite en moins de 5 Ma.
- 3) En régime compressif, l'impact joué par les bassins volcano-sédimentaires sur le processus d'exhumation de la croûte inférieure a été testé numériquement. Les modèles suggèrent que de multiples injections de magmas granitoïdiques, dérivant soit de matériaux subductés, soit d'une fusion de produits crustaux ou de matériel mantellique accumulés en profondeur, ont pu être canalisées au sein de diapirs avant de venir nourrir la croûte supérieure. Lorsque les granitoïdes ont rencontré le toit solidifié des diapirs, ils ont probablement migré latéralement puis sont venus pratiquer une intrusion dans la croûte supérieure via des zones de faiblesse. Ce modèle suggère également une asymétrie des structures entre la croûte supérieure d'une part, et la croûte inférieure à moyenne d'autre part: i.e. (i) les bassins de roches vertes faiblement métamorphisés de la croûte supérieure reposent sur les diapirs métamorphisés et (ii) les bassins de roches vertes très métamorphisés constituent le soubassement des dômes granitoïdiques de la croûte supérieure.

Chapter 7

Appendix

7.1 List of publications associated with this thesis

- Feng, X.**, Amponsah, P. O., Martin, R., Ganne, J., Jessell, M. W., 2016. 3-D numerical modelling of the influence of pre-existing faults and boundary conditions on the distribution of deformation: Example of North-Western Ghana. *Precambrian Research* 274, 161-179.
- Feng, X.**, Jessell, M. W., Amponsah, P. O., Martin, R., Ganne, J., Liu, D., Batt, G. E., 2016. Effect of strain-weakening on Oligocene-Miocene self-organization of the Australian-Pacific plate boundary fault in southern New Zealand: Insights from numerical modelling. *Journal of Geodynamics* 100, 130-143.
- Ganne, J., **Feng, X.**, Rey, P., Andrade, V. D., 2016. Statistical Petrology Reveals a Link Between Supercontinents Cycle and Mantle Global Climate. *American Mineralogist* 101, 2768-2773.
- Ganne, J., Schellart, W. P., Rosenbaum, G., **Feng, X.**, 2017. Probing crustal thickness evolution and geodynamic processes in the past from magma records: An integrated approach. *Special Paper of the Geological Society of America*, 526. DOI: 10.1130/2017. 2526(01).
- Ganne, J., **Feng, X.**, 2017. Primary magmas and mantle temperatures through time? *Geochemistry Geophysics Geosystems*, DOI: 10.1002/2016GC006787.